

Macro-to-Microchannel Transition in Two-Phase Flow and Evaporation

THÈSE N° 4674 (2010)

PRÉSENTÉE LE 30 AVRIL 2010

À LA FACULTÉ SCIENCES ET TECHNIQUES DE L'INGÉNIEUR
LABORATOIRE DE TRANSFERT DE CHALEUR ET DE MASSE
PROGRAMME DOCTORAL EN MÉCANIQUE

ÉCOLE POLYTECHNIQUE FÉDÉRALE DE LAUSANNE

POUR L'OBTENTION DU GRADE DE DOCTEUR ÈS SCIENCES

PAR

Chin Lee ONG

acceptée sur proposition du jury:

Prof. M. Parlange, président du jury
Prof. J. R. Thome, directeur de thèse
Dr G. P. Celata, rapporteur
Prof. M. E. Poniewski, rapporteur
Dr J. Van Herle, rapporteur



ÉCOLE POLYTECHNIQUE
FÉDÉRALE DE LAUSANNE

Suisse
2010

Acknowledgement

This research study has been carried out at the Laboratory of Heat and Mass Transfer (LTCM) under the supervision of Prof. John R. Thome. This research project is financially supported by the Swiss National Science Foundation (SNSF) through FNS Grant Nos. 200021-107420/1 and 200020-119652/1.

I am heartily thankful to Prof. John R. Thome, for his encouragement, support and guidance from the beginning till the end of this research campaign. He has made available his support in many ways to make this research campaign a success, including the constructive discussions during the preparation this manuscript. I am equally grateful to Prof. M. Parlange, Prof. M. E. Poniewski, Dr. Gian Piero Celata and Dr. Jan Van Herle for their valuable time in reading this manuscript, together with their constructive remarks and suggestions.

It is also my pleasure to thank Mr. Laurent Chevalley, for his professional technical experience in making this experimental campaign a success. I owe the success of the experimental campaign fully to his expertise in fabricating the test section, the excellent modification and the regular maintenance work performed on the test facility.

I would also like thank Dr. Andrea Cioncolini for his collaboration in performing the statistical comparison of the two-phase pressure drop data.

Finally, I would like to thank my family members, colleagues and friends for their continuous motivation and support. I joyfully send my regards and blessings to all of those who supported me in any respect during the tenure of this research project.

Abstract

Continuous development of highly efficient and compact cooling elements are driven by extensive developments of Micro-Electro-Mechanical Systems (MEMS) devices such as microprocessors or micro high-powered laser systems. As microprocessors continue to head in the direction of miniaturization, it was quickly realized that the major obstacle to overcome was 'heat'. This justified the need for the development of a new generation of liquid cooling technologies that involves phase-change processes. However, significant differences in two-phase transport phenomena have been reported in the microscale sized channels as compared to conventional macroscale channels. The classification of macroscale, mesoscale and microscale channels with respect to two-phase processes is still an open question.

This research project focuses on investigating the macro-to-microscale transition during flow boiling in small scale channels of various size and refrigerants to investigate the effects of channel confinement on flow boiling heat transfer, two-phase flow patterns, pressure drop, critical heat flux and liquid film stratification in a single circular horizontal channel. In this project, we systematically investigated the trends observed in the heat transfer data, pressure drop, critical heat flux and film stratifications for wide range of conditions as a function of flow pattern, creating a uniquely comprehensive experimental database for R134a (high pressure), R236fa (medium pressure) and R245fa (low pressure) in the 1.03, 2.20 and 3.04 *mm* channels. From a heat transfer viewpoint, the prediction of the heat transfer requires first the prediction of the two-phase flow regimes in these small scale channels. So, in that respect an improved flow pattern map has been proposed and by determining the flow patterns transitions existing under different conditions, the effects of the flow regimes and channel dimensions on flow boiling heat transfer is thus explained. A flow pattern based heat transfer prediction model, i.e. the three-zone model showed good agreement in the prediction of heat transfer coefficients corresponding to the isolated bubble (IB) and coalescing bubble (CB) flows. As for the two-phase pressure drops, various statistical comparisons have been made by comparing the pressure drop database with various macroscale and microscale prediction methods, finding that three macroscale and two microscale methods predicted the pressure drop database with good accuracy. From this research, a distinctive peak in the CHF has been identified when comparing the experimental CHF database for 0.50, 0.80, 1.03, 2.20 and 3.04 *mm* channels (the first two from previous study). A new CHF prediction method was developed that is applicable for the CHF prediction of single, square multi-microchannels and split flow multi-channels. Finally, the processing of the high speed flow visualization images provided the interpretation of the lower threshold of the macro-microscale transition. As an approximate rule, the lower threshold of macro-scale flow is $Co = 0.3-0.4$ while the

upper threshold of the symmetric microscale flow is $Co \approx 1$.

Keywords: two-phase flow, macroscale, microscale, transition, confinement, flow boiling, heat transfer, pressure drop, critical heat flux.

Version Abrégée

Le développement continu des systèmes de refroidissement compacts et performants est motivé par l'évolution des Systèmes Micro-Electro-Mécaniques Systems (MEMS) tels que les microprocesseurs ou les microsystèmes de laser haute puissance. Comme la tendance actuelle en matière de microprocesseur est la miniaturisation, l'obstacle majeur à surmonter s'est vite révélé être la "chaleur". Cela explique la nécessité de développer une nouvelle génération de systèmes de refroidissement liquide basés sur un processus de changement de phase. Toutefois, des différences significatives dans les phénomènes diphasiques ont été rapportées entre les micro-canaux et les macro-canaux conventionnels. La classification des macro-, méso- et micro-canaux vis-à-vis des phénomènes de changement phase est toujours une question ouverte.

Ce projet de recherche est axé sur l'étude de la transition entre les échelles macro et micro lors des écoulements en ébullition pour des canaux à petite échelle pour diverses tailles et réfrigérants afin d'étudier l'effet du confinement sur le transfert de chaleur, les modes d'écoulement diphasiques, les pertes de charge, le flux de chaleur critique et la stratification du film liquide dans un tube circulaire. Lors de ce projet, les tendances observées dans les données de transfert de chaleur, pertes de pression, flux de chaleur critique et stratification de film liquide ont été systématiquement examinées pour une vaste gamme de conditions en fonction de la configuration de l'écoulement, créant ainsi une base de données expérimentales complète et unique pour les fluides R134a (haute pression), R236fa (moyenne pression) et R245fa (basse pression) dans des tubes de diamètres $D_{in}=1.03, 2.20$ et 3.04 mm. Du point de vue du transfert de chaleur, la prédiction du coefficient de transfert de chaleur nécessite tout d'abord la prédiction des régimes d'écoulement diphasiques dans le tube. Dans ce sens, une version améliorée de la carte d'écoulement en micro-canaux a été proposée et par la prédiction des transitions entre les différents régimes d'écoulement existant selon différentes conditions, les effets des régimes d'écoulement et des dimensions de canal sur le transfert de chaleur en ébullition ont été ainsi expliqués. Un modèle de prédiction de transfert de chaleur basé sur les régimes d'écoulement, à savoir le modèle à trois zones, a montré de bons résultats pour la prédiction des coefficients de transfert de chaleur correspondant aux écoulement IB et CB. Pour les pertes de pression diphasiques, diverses comparaisons statistiques ont été faites entre les bases de données obtenues et les différentes méthodes de prévision existantes pour les échelles micro et macro. Lors de cette étude, un pic distinctif pour le flux de chaleur critique (CHF) a été identifié en comparant les bases de données expérimentales obtenues pour des canaux de diamètres $D_{in}=0.50, 0.80, 1.03, 2.20$ et 3.04 mm. Une nouvelle méthode de prévision du CHF a été développée et est applicable pour la prédiction du CHF pour des mono- et multi-microcanaux à écoulement simple ou séparé. Enfin, le

traitement d'image des écoulements enregistrés à haute vitesse a permis l'interprétation du seuil inférieur de la transition macro/micro. En première approximation, le seuil inférieur de l'échelle macro correspond à un nombre de confinement de $Co=0.3 - 0.4$, alors que le seuil supérieur de l'échelle micro correspond à $Co \approx 1$.

Mots clés: d'écoulement diphasiques, macro, micro, transition, confinement, écoulements en ébullition, transfert de chaleur, pertes de pression, flux de chaleur critique.

Contents

Acknowledgement	iii
Abstract	v
Version Abrégée	vii
Nomenclature	xxv
1 Introduction	1
1.1 Overview	1
1.2 Research Objective	2
2 State of the Art Review	5
2.1 Overview	5
2.2 Macro-Microscale Transition Criteria	5
2.2.1 Channel Size Classifications	5
2.2.2 Bubble Confinement	6
2.2.3 Bubble Departure Diameter	8
2.3 Flow Boiling Heat Transfer	10
2.3.1 Heat Transfer Mechanisms	10
2.4 Two-Phase Flow Patterns	20
2.4.1 Macroscale Two-Phase Flow and Flow Maps	21
2.4.2 Microscale Two-Phase Flow and Flow Maps	22
2.5 Two-Phase Pressure Drops	28
2.6 Critical Heat Flux	31
3 Experimental Test Facility and Data Reduction Methods	35

3.1	Test Facility Description	35
3.2	The Reservoir Loop	36
3.3	The Pump Loop	36
3.4	The Test Section	37
3.4.1	Heat Transfer Measurements	38
3.4.2	Pressure Drop Measurements	40
3.4.3	Optical Measurement Technique	40
3.4.4	Flow Pattern Visualization	41
3.4.5	Critical Heat Flux	41
3.4.6	Film Thickness Measurement	41
3.5	Data Reduction	42
3.5.1	Single-Phase Validation	42
3.5.2	Inner Wall Temperature	43
3.5.3	Single-Phase Heat Transfer and Pressure Drop	44
3.5.4	Two-Phase Heat Transfer and Pressure Drop	45
3.6	Experimental Uncertainties	45
3.6.1	Thermocouple Uncertainty	46
3.6.2	Data Acquisition System Uncertainty	48
3.6.3	Mass Flow Meter Uncertainty	48
3.6.4	Absolute and Differential Pressure Transducers	48
3.6.5	Channel Diameter and Heated Length	48
3.6.6	Surface Roughness	49
3.6.7	Fluid Property Regression	50
3.6.8	Random Uncertainties	50
3.6.9	Total Measurement Uncertainties	51
4	Two-Phase Flow Patterns	53
4.1	Experimental Procedure	53
4.2	Two-Phase Flow Patterns	53
4.2.1	Effects of Mass Velocity	57
4.3	Experimental Flow Pattern Transitions	58
4.3.1	Effects of Channel Confinement	61

4.3.2	Effects of Fluid Properties	68
4.3.3	Effects of Saturation Temperature	72
4.4	Flow Pattern Maps Comparisons	73
4.5	New Macro-Micro Flow Pattern Map	77
4.6	Summary	80
5	Flow Boiling Heat Transfer	81
5.1	Single-Phase Validation	81
5.2	Flow Boiling Heat Transfer	82
5.2.1	Flow Boiling Curves	82
5.2.2	Effects of Channel Confinement	85
5.2.3	Effects of Fluid Properties	92
5.2.4	Effects of Mass Velocity	99
5.2.5	Effects of Saturation Temperature	104
5.2.6	Effects of Inlet Sub-cooling	110
5.2.7	Discussion of Heat Transfer Results	113
5.3	Heat Transfer Prediction Method Comparisons	114
5.3.1	The Three-Zone Heat Transfer Model	125
6	Two-Phase Pressure Drop	133
6.1	Single-Phase Validation	133
6.2	Adiabatic Two-Phase Pressure Drops	135
6.2.1	Effects of Channel Confinement	135
6.2.2	Effects of Fluid Properties	137
6.2.3	Effects of Saturation Temperature	140
6.2.4	Effects of Mass Mass Velocity	140
6.3	Two-Phase Pressure Drops Comparison	142
6.4	Summary	150
7	Film Thickness Measurement	151
7.1	Objective	151
7.2	Experimental Setup	151
7.3	Image Processing Algorithm	152

7.4	Calibration	152
7.5	Effect of Mass Velocity	153
7.6	Film Thickness Comparison	156
7.7	Summary of Macro-to-Microscale Transition	164
8	Critical Heat Flux	165
8.1	Experimental CHF Results	165
8.1.1	Effects of Mass Velocity and Channel Diameter	166
8.1.2	Effects of Saturation Temperature	167
8.1.3	Effects of Fluid Properties	173
8.1.4	Effects of Sub-cooling	176
8.1.5	Effects of Flow Pattern	177
8.2	Comparison of Results to Existing CHF Methods	177
8.3	New CHF correlation	180
9	Conclusions and Recommendations	185
9.1	Conclusions	185
9.1.1	Two-Phase Flow Patterns	185
9.1.2	Flow Boiling Heat Transfer	186
9.1.3	Two-Phase Pressure Drops	187
9.1.4	Film Thickness Measurements	187
9.1.5	Critical Heat Flux	187
9.2	Recommendations	188
	Bibliography	189
	Curriculum Vitae	199

List of Figures

- 1.1 Heat transfer for various coolant and heat transfer modes 2
- 2.1 Knudsen number ranges for various types of flow for Harley [1] 6
- 2.2 Channel classification proposed by Kandlikar [2] 6
- 2.3 Macro-microscale threshold diameter for (a) R134a, (b) R236fa and (c) R245fa as a function of reduced pressure. 9
- 2.4 Schematic of macroscale vertical in-tube flow boiling process adopted from Steiner [3] 11
- 2.5 Geometrical illustration of the liquid-vapor regions, stratified and dry angles from Kattan et al. [4] 12
- 2.6 Refrigerant R22, $D_{in}=10.7\text{ mm}$, $T_{sat}=5\text{ }^{\circ}\text{C}$, $q=10.0\text{ kW/m}^2$ at: (a) $G=150\text{ kg/m}^2\text{s}$ and (b) $G=250\text{ kg/m}^2\text{s}$ 12
- 2.7 Experimental heat transfer coefficients vs. vapor quality for R22, R134a and R404A: (a) Effects of heat flux and (b) Effects of mass flux. 13
- 2.8 Flow boiling heat transfer results from Lazarek et al. [5] 14
- 2.9 Heat transfer results of Lin et al. [6] for R141b in the 1.10 mm channel, $Co=1.1$: (a) $G=365\text{ kg/m}^2\text{s}$ and (b) $G=505\text{ kg/m}^2\text{s}$ 15
- 2.10 Heat transfer results of Lin et al. [6] for R141b in the 3.60 mm channel, $Co=0.33$: (a) $G=50\text{ kg/m}^2\text{s}$ and (b) $G=130\text{ kg/m}^2\text{s}$ 16
- 2.11 Flow boiling heat transfer results of Bao et al. [7] for (a) Effects of heat flux and (b) Effects of mass flux. 17
- 2.12 Flow boiling results of Ohwaib et al. [8] for R134a at $T_{sat}=34\text{ }^{\circ}\text{C}$ 18
- 2.13 Experimental boiling heat transfer of Isobutane by Khobandeh [9]. 18
- 2.14 Heat and mass flux effects on the heat transfer coefficient for R134a in a: (a) $D_{in}=3.10\text{ mm}$, (b) $D_{in}=1.12\text{ mm}$ and (c) $D_{in}=0.51\text{ mm}$ channel. 19
- 2.15 Heat transfer results comparison of Consolini [10] for (a) R236fa and (b) R134a in the 0.51 mm channel at $T_{sat}=31\text{ }^{\circ}\text{C}$ with $\Delta T_{sub}=2\text{ K}$ 20
- 2.16 Illustration of the sequence of two-phase flow patterns during evaporation from Collier and Thome [11]. 21

2.17	Diabatic flow pattern map for flow boiling of water in a 15×10 mm channel from Sato et al. [12] showing the transition lines.	22
2.18	Flow pattern map of Wojtan et al. [13] for R22 in the 13.84 mm channel at $T_{sat}=5$ °C and $G=100$ kg/m ² s.	23
2.19	Illustration of the two-phase flow regimes from Kawaji et al. [14]; (a) Minichannel flow patterns and (b) Microchannel flow patterns.	24
2.20	Flow pattern map of Suo [15].	24
2.21	Flow pattern map comparison for circular and near-circular channels with $D_h \leq 1$ mm from Akbar et al. [16].	26
2.22	Vertical two-phase flow regimes from Chen et al. [17] at 10 bar for the (a) 1.10 mm and (b) 4.26 mm channel.	27
2.23	Flow pattern map simulation for $q=10.0$ kW/m ² , $T_{sat}=31$ °C with $T_{sub}=4$ K for (a) R134a and (b) R236fa.	28
2.24	Experimental adiabatic two-phase pressure drop data of Revellin et al. [18] as a function of: (a) channel diameter, (b) mass velocity, (c) fluid properties and (d) saturation temperature.	29
2.25	Channel diameter effect on CHF from Bergles [19].	31
2.26	Effect of sub-cooling and mass velocity on CHF from Kandlikar [20] with additional data from Bergles [21].	32
2.27	Effect of tube diameter on subcooled flow boiling CHF at high mass flux by Nariai [22].	33
2.28	Experimental CHF data of Wojtan et al. [23], (a)Effect of channel diameter, (b)Effect of heated length, (c)Effect of saturation temperature and (d)Effect of working fluid.	34
3.1	Schematic view of the experimental facility in reservoir mode.	37
3.2	Schematic view of the experimental facility in pump mode.	38
3.3	A 3-dimensional view of the test section.	39
3.4	Schematic of the test section configuration with instrumentation.	40
3.5	A magnified image of the surface roughness for the $D_{in}=1.03$ mm channel.	49
4.1	Probability Density Function for R236fa in the $D_{in}=1.03$ mm channel at $T_{sat}=31$ °C, $G=200$ kg/m ² s and $T_{in}=27$ °C; (a) Isolate bubble, (b) Coalescing bubble, (c) Wavy-annular, (d) Smooth-annular flow, (e) Isolate bubble PDF, (f) Coalescing bubble PDF, (g) Wavy-annular PDF and (h) Smooth-annular flow PDF.	54

- 4.2 Flow patterns observed for R236fa in the $D_{in}=1.03$ mm channel at $T_{sat}=31$ °C, $G=201$ kg/m²s, $T_{in}=27$ °C and $Co=0.85$; (a) $q=2.95$ kW/m², $x=0.034$ (b) $q=9.6$ kW/m², $x=0.21$, (c) $q=20.1$ kW/m², $x=0.48$ and (d) $q=37.5$ kW/m², $x=0.92$ 55
- 4.3 Flow patterns observed for R236fa in the $D_{in}=3.04$ mm channel at $T_{sat}=31$ °C, $G=405$ kg/m²s, $T_{in}=27$ °C and $Co=0.28$; (a) $q=7.9$ kW/m², $x=0.051$ (b) $q=12.1$ kW/m², $x=0.103$, (c) $q=29.1$ kW/m², $x=0.314$ and (d) $q=63.8$ kW/m², $x=0.74$ 56
- 4.4 Flow patterns for R134a, $D_{in}=2.20$ mm channel at $T_{sat}=31$ °C, $G=307$ kg/m²s, $T_{in}=27$ °C and $Co=0.37$; (a) $q=3.5$ kW/m², $x=0.013$ (b) $q=5.2$ kW/m², $x=0.033$, (c) $q=9.4$ kW/m², $x=0.094$, (d) $q=19.0$ kW/m², $x=0.19$, (e) $q=36.0$ kW/m², $x=0.44$ and (f) $q=65.7$ kW/m², $x=0.81$ 56
- 4.5 Flow patterns for R134a, $D_{in}=3.04$ mm channel at $T_{sat}=31$ °C, $G=299$ kg/m²s, $T_{in}=27$ °C and $Co=0.27$; (a) $q=6.6$ kW/m², $x=0.05$, (b) $q=21.4$ kW/m², $x=0.258$, (c) $q=34.7$ kW/m², $x=0.44$ and (d) $q=60.4$ kW/m², $x=0.80$ 57
- 4.6 Flow patterns for R245fa, $D_{in}=2.20$ mm channel at $T_{sat}=31$ °C, $G=302$ kg/m²s, $T_{in}=27$ °C and $Co=0.46$; (a) $q=4.3$ kW/m², $x=0.014$ (b) $q=6.04$ kW/m², $x=0.03$, (c) $q=11.0$ kW/m², $x=0.09$, (d) $q=17.7$ kW/m², $x=0.18$ and (e) $q=56.7$ kW/m², $x=0.74$ 57
- 4.7 Flow patterns for R245fa, $D_{in}=3.04$ mm channel at $T_{sat}=31$ °C, $G=298$ kg/m²s, $T_{in}=27$ °C and $Co=0.34$; (a) $q=7.0$ kW/m², $x=0.058$ (b) $q=11.2$ kW/m², $x=0.11$, (c) $q=16.3$ kW/m², $x=0.17$, (d) $q=27.9$ kW/m², $x=0.314$ and (e) $q=62.3$ kW/m², $x=0.75$ 58
- 4.8 Flow patterns for R245fa, $D_{in}=3.04$ mm channel at $T_{sat}=31$ °C, $G=602$ kg/m²s, $T_{in}=27$ °C and $Co=0.34$; (a) $q=10.7$ kW/m², $x=0.038$ (b) $q=15.5$ kW/m², $x=0.06$, (c) $q=27.4$ kW/m², $x=0.13$ and (d) $q=82.3$ kW/m², $x=0.46$. 58
- 4.9 Experimental flow pattern transition lines for R236fa, $D_{in}=1.03$ mm channel at $T_{sat}=31$ °C, $T_{in}=27$ °C and $Co=0.83$ 59
- 4.10 Experimental flow pattern transition lines for R134a, $D_{in}=2.20$ mm channel at $T_{sat}=31$ °C, $T_{in}=27$ °C and $Co=0.36$ 60
- 4.11 Experimental flow pattern transition lines for R134a, $D_{in}=3.04$ mm channel at $T_{sat}=31$ °C, $T_{in}=27$ °C and $Co=0.27$ 60
- 4.12 Flow pattern transition lines for R134a, $T_{sat}=31$ °C and $T_{in}=27$ °C; (a) $D_{in}=0.50, 0.80, 1.03$ and 2.20 mm and (b) $D_{in}=2.20$ and 3.04 mm. (The symbols represent the transition lines observed in the database and not the data points) 62
- 4.13 Flow pattern transition lines for R236fa and R245fa at $T_{sat}=31$ °C and $T_{in}=27$ °C; (a) R236fa and (b) R245fa. (The symbols represent the transition lines observed in the database and not the data points) 63

4.14	R134a flow patterns and transition lines with superficial phase velocities as coordinates for $T_{sat}=31\text{ }^{\circ}\text{C}$ and $T_{in}=27\text{ }^{\circ}\text{C}$; (a) $D_{in}=1.03\text{ mm}$, $Co=0.78$, (b) $D_{in}=2.20\text{ mm}$, $Co=0.36$ and (c) $D_{in}=3.04\text{ mm}$, $Co=0.27$	65
4.15	R236fa flow patterns and transition lines with superficial phase velocities as coordinates for $T_{sat}=31\text{ }^{\circ}\text{C}$ and $T_{in}=27\text{ }^{\circ}\text{C}$; (a) $D_{in}=1.03\text{ mm}$, $Co=0.83$, (b) $D_{in}=2.20\text{ mm}$, $Co=0.39$ and (c) $D_{in}=3.04\text{ mm}$, $Co=0.28$	66
4.16	R245fa flow patterns and transition lines with superficial phase velocities as coordinates for $T_{sat}=31\text{ }^{\circ}\text{C}$ and $T_{in}=27\text{ }^{\circ}\text{C}$; (a) $D_{in}=1.03\text{ mm}$, $Co=0.99$, (b) $D_{in}=2.20\text{ mm}$, $Co=0.46$ and (c) $D_{in}=3.04\text{ mm}$, $Co=0.34$	67
4.17	Flow patterns and transition lines for R134a, R236fa and R245fa at $T_{sat}=31\text{ }^{\circ}\text{C}$ and $T_{in}=27\text{ }^{\circ}\text{C}$; (a) $D_{in}=1.03\text{ mm}$ and (b) $D_{in}=2.20\text{ mm}$. (The symbols represent the transition lines observed in the database and not the data points)	69
4.18	Flow patterns transition lines based on superficial Weber numbers in the $D_{in}=1.03\text{ mm}$, $T_{sat}=31\text{ }^{\circ}\text{C}$; (a) R134a, (b) R245fa.	70
4.19	Flow patterns transition lines based on superficial Weber numbers in the $D_{in}=2.20\text{ mm}$, $T_{sat}=31\text{ }^{\circ}\text{C}$; (a) R134a, (b) R245fa.	71
4.20	Flow patterns and transition lines for R134a, R236fa and R245fa for $T_{sat}=25$, 31 and $35\text{ }^{\circ}\text{C}$; (a) R134a and (b) R245fa. (The symbols represent the transition lines observed in the database and not the data points)	72
4.21	Extrapolation of the macroscale flow pattern map of Wojtan [13] for R134a, $T_{sat}=31\text{ }^{\circ}\text{C}$; (a) $D_{in}=1.03\text{ mm}$ and (b) $D_{in}=3.04\text{ mm}$	74
4.22	Extrapolation of the microscale flow pattern map of Revellin [24] for the $D_{in}=1.03\text{ mm}$ channel; (a) R134a, (b) R236fa and (c) R245fa.	75
4.23	Flow pattern transition lines of Yang [25] for R134a; (a) $D_{in}=2.20\text{ mm}$ and (b) $D_{in}=3.04\text{ mm}$	76
4.24	Comparison of the microscale flow pattern map of Revellin [24] and the new flow pattern map correlation for R134a, $D_{in}=0.51\text{ mm}$, $T_{sat}=31\text{ }^{\circ}\text{C}$	78
4.25	(a) R134a, $D_{in}=2.20\text{ mm}$ and (b) R236fa, $D_{in}=3.04\text{ mm}$	79
5.1	Single-phase experimental heat losses compared to predicted heating efficiency for R134a in the $D_{in}=1.03\text{ mm}$ channel.	82
5.2	(a) Sub-cooled liquid heat transfer results for R134a in the $D_{in}=1.03\text{ mm}$ channel and (b) Experimental Nusselt numbers versus Gnielinski [26] correlation.	83
5.3	(a) Sub-cooled liquid heat transfer results for R245fa in the $D_{in}=1.03\text{ mm}$ channel and (b) Experimental Nusselt numbers versus Gnielinski [26] correlation.	83

5.4	Boiling curve for the last thermocouple at heated length location of $Z=157$ mm in the $D_{in}=1.03$ mm channel; (a) R134a and (b) R245fa.	84
5.5	Heat transfer coefficients for R134a at $T_{sat}=31$ °C; (a) $D_{in}=1.03$ mm channel, $Co=0.78$, (b) $D_{in}=2.20$ mm channel, $Co=0.36$ (c) $D_{in}=3.04$ mm channel, $Co=0.27$	87
5.6	Heat transfer coefficients for R236fa at $T_{sat}=31$ °C; (a) $D_{in}=1.03$ mm channel, $Co=0.83$, (b) $D_{in}=2.20$ mm channel, $Co=0.39$ (c) $D_{in}=3.04$ mm channel, $Co=0.28$	88
5.7	Heat transfer coefficients for R245fa at $T_{sat}=31$ °C; (a) $D_{in}=1.03$ mm channel, $Co=0.99$ and (b) $D_{in}=2.20$ mm channel, $Co=0.46$	89
5.8	Heat transfer coefficients for R236fa in the $D_{in}=1.03$ mm channel at $T_{sat}=31$ °C, $Co=0.83$; (a) $G=201$ kg/m ² s and (b) $G=499$ kg/m ² s.	91
5.9	Heat transfer coefficients for R245fa in the $D_{in}=1.03$ mm channel at $T_{sat}=31$ °C, $Co=0.99$; (a) $G=199$ kg/m ² s and (b) $G=498$ kg/m ² s.	92
5.10	Comparison of refrigerant properties at $T_{sat}=31$ °C.	92
5.11	Heat transfer comparison for R134a, R236fa and R245fa in the $D_{in}=1.03$ mm channel at $T_{sat}=31$ °C, $G \approx 200$ kg/m ² s; (a) $Co=0.78$, (b) $Co=0.83$ and (c) $Co=0.99$	94
5.12	Heat transfer comparison for R134a, R236fa and R245fa in the $D_{in}=1.03$ mm channel at $T_{sat}=31$ °C, $G \approx 500$ kg/m ² s; (a) $Co=0.78$, (b) $Co=0.83$ and (c) $Co=0.99$	95
5.13	Heat transfer comparison for R134a, R236fa and R245fa in the $D_{in}=2.20$ mm channel at $T_{sat}=31$ °C, $G \approx 500$ kg/m ² s; (a) $Co=0.36$, (b) $Co=0.39$ and (c) $Co=0.46$	97
5.14	Heat transfer comparison for R134a, R236fa and R245fa in the $D_{in}=3.04$ mm channel at $T_{sat}=31$ °C, $G \approx 500$ kg/m ² s; (a) $Co=0.27$, (b) $Co=0.28$ and (c) $Co=0.34$	98
5.15	Mass velocity effects on heat transfer for R134a in the $D_{in}=1.03$ mm channel at $T_{sat}=31$ °C, $Co=0.78$; (a) $G \approx 800$ kg/m ² s and (b) $G \approx 1000$ kg/m ² s.	99
5.16	Mass velocity effects on heat transfer for R134a, R236fa and R245fa in the $D_{in}=1.03$ mm channel at $T_{sat}=31$ °C; (a) R134a, $Co=0.78$, (b) R236fa, $Co=0.83$ and (c) R245fa, $Co=0.99$	101
5.17	Mass velocity effects on heat transfer for R134a and R236fa in the $D_{in}=2.20$ mm channel at $T_{sat}=25$ °C; (a) R134a, $Co=0.38$ and (b) R236fa, $Co=0.40$	102
5.18	Mass velocity effects on heat transfer for R134a, R236fa and R245fa in the $D_{in}=3.04$ mm channel at $T_{sat}=31$ °C; (a) R134a, $Co=0.27$, (b) R236fa, $Co=0.28$ and (c) R245fa, $Co=0.34$	104
5.19	Heat transfer coefficients for R236fa at $G \approx 300$ kg/m ² s; (a) $T_{sat}=31$ °C, $Co=0.83$ and (b) $T_{sat}=35$ °C, $Co=0.81$	105

5.20	Heat transfer coefficients for R245fa at $G \approx 400 \text{ kg/m}^2\text{s}$; (a) $T_{sat}=31 \text{ }^\circ\text{C}$, $Co=0.99$ and (b) $T_{sat}=35 \text{ }^\circ\text{C}$, $Co=0.97$	106
5.21	Heat transfer coefficients for R134a in the $D_{in}=2.20 \text{ mm}$ channel for $G \approx 300 \text{ kg/m}^2\text{s}$; (a) $T_{sat}=25 \text{ }^\circ\text{C}$, $Co=0.38$, (b) $T_{sat}=31 \text{ }^\circ\text{C}$, $Co=0.36$ and (c) $T_{sat}=35 \text{ }^\circ\text{C}$, $Co=0.35$	108
5.22	Heat transfer coefficients for R236fa in the $D_{in}=2.20 \text{ mm}$ channel for $G \approx 500 \text{ kg/m}^2\text{s}$; (a) $T_{sat}=25 \text{ }^\circ\text{C}$, $Co=0.40$, (b) $T_{sat}=31 \text{ }^\circ\text{C}$, $Co=0.39$ and (c) $T_{sat}=35 \text{ }^\circ\text{C}$, $Co=0.38$	109
5.23	Sub-cooling effects the on heat transfer coefficient for R134a at $T_{sat}=31 \text{ }^\circ\text{C}$; (a) $D_{in}=1.03 \text{ mm}$ channel, $Co=0.78$ and (b) $D_{in}=3.04 \text{ mm}$ channel, $Co=0.27$	110
5.24	Sub-cooling effects on the heat transfer coefficient for R236fa at $T_{sat}=31 \text{ }^\circ\text{C}$; (a) $D_{in}=1.03 \text{ mm}$ channel, $Co=0.83$ and (b) $D_{in}=3.04 \text{ mm}$ channel, $Co=0.28$	111
5.25	Sub-cooling effects on the heat transfer coefficient for R236fa in the $D_{in}=2.20 \text{ mm}$ channel; (a) $T_{sat}=25 \text{ }^\circ\text{C}$, $Co=0.40$, (b) $T_{sat}=31 \text{ }^\circ\text{C}$, $Co=0.39$ and (c) $T_{sat}=35 \text{ }^\circ\text{C}$, $Co=0.38$	112
5.26	Experimental heat transfer coefficient comparison with Lazarek et al. [5] correlation for R134a, R236fa and R245fa; (a) $D_{in}=1.03 \text{ mm}$ channel, (b) $D_{in}=2.20 \text{ mm}$ and (c) $D_{in}=3.04 \text{ mm}$ channel.	115
5.27	Experimental heat transfer coefficient comparison with Tran et al. [27] correlation for R134a, R236fa and R245fa; (a) $D_{in}=1.03 \text{ mm}$ channel, (b) $D_{in}=2.20 \text{ mm}$ and (c) $D_{in}=3.04 \text{ mm}$ channel.	117
5.28	Experimental heat transfer coefficient comparison with Garimella et al. [28] correlation for R134a, R236fa and R245fa; (a) $D_{in}=1.03 \text{ mm}$ channel, (b) $D_{in}=2.20 \text{ mm}$ and (c) $D_{in}=3.04 \text{ mm}$ channel.	119
5.29	Experimental heat transfer coefficient comparison with Liu & Winterton [29] correlation for R134a, R236fa and R245fa; (a) $D_{in}=1.03 \text{ mm}$ channel, (b) $D_{in}=2.20 \text{ mm}$ and (c) $D_{in}=3.04 \text{ mm}$ channel.	120
5.30	Experimental heat transfer coefficient comparison with Saitoh et al. [30] correlation for R134a, R236fa and R245fa; (a) $D_{in}=1.03 \text{ mm}$ channel, (b) $D_{in}=2.20 \text{ mm}$ and (c) $D_{in}=3.04 \text{ mm}$ channel.	122
5.31	Comparison of the current experimental heat transfer data for CB flow with the new Consolini et al. [31,32] coalescing bubble heat transfer model for R134a, R236fa and R245fa; (a) $D_{in}=1.03 \text{ mm}$ channel, (b) $D_{in}=2.20 \text{ mm}$ and (c) $D_{in}=3.04 \text{ mm}$ channel.	124
5.32	Comparison of the current experimental heat transfer data with the Thome et al. three-zone model for R134a, R236fa and R245fa; (a) $D_{in}=1.03 \text{ mm}$ (IB and CB flow), (b) $D_{in}=2.20 \text{ mm}$ (IB and CB flow) and (c) $D_{in}=3.04 \text{ mm}$ channel (S-P and CB flow)	127

5.33	Comparison of the current experimental heat transfer data for CB flow with the Thome et al. [33, 34] heat transfer model for R134a, R236fa and R245fa; (a) $D_{in}=1.03\text{ mm}$ and (b) $D_{in}=2.20\text{ mm}$ channel.	128
5.34	Comparison of the current CB flow experimental heat transfer data with the Thome et al. three-zone model for R134a, R236fa and R245fa; (a) $D_{in}=1.03\text{ mm}$ (CB flow), (b) $D_{in}=2.20\text{ mm}$ (CB flow) and (c) $D_{in}=3.04\text{ mm}$ channel (S-P and CB flow).	131
6.1	(a) Single-phase friction factor for R134a in the $D_{in}=1.03\text{ mm}$ channel and (b) Experimental versus Prediction.	134
6.2	(a) Single-phase friction factor for R245fa in the $D_{in}=1.03\text{ mm}$ channel and (b) Experimental versus Prediction.	134
6.3	Two-phase pressure drops for R236fa in the $D_{in}=1.03$ and 3.04 mm channels at $T_{sat}=31\text{ }^{\circ}\text{C}$; (a) $D_{in}=1.03\text{ mm}$, $Co=0.83$ and (b) $D_{in}=3.04\text{ mm}$, $Co=0.28$	135
6.4	Two-phase pressure drops for R236fa in the $D_{in}=1.03$ and 3.04 mm channels at $T_{sat}=31\text{ }^{\circ}\text{C}$; (a) $D_{in}=1.03\text{ mm}$, $Co=0.99$ and (b) $D_{in}=3.04\text{ mm}$, $Co=0.34$	136
6.5	Two-phase pressure drops for R134a, R236fa and R245fa in the $D_{in}=1.03\text{ mm}$ channel at $T_{sat}=31\text{ }^{\circ}\text{C}$; (a) R134a, (b) R236fa and (c) R245fa.	138
6.6	Two-phase pressure drops for R134a, R236fa and R245fa in the $D_{in}=3.04\text{ mm}$ channel at $T_{sat}=31\text{ }^{\circ}\text{C}$; (a) R134a, (b) R236fa and (c) R245fa.	140
6.7	Two-phase pressure drops for R236fa in the $D_{in}=2.20\text{ mm}$ channel; (a) $T_{sat}=25\text{ }^{\circ}\text{C}$ and (b) $T_{sat}=31\text{ }^{\circ}\text{C}$	141
6.8	Homogeneous Cicchitti prediction: 76.9% data within $\pm 50\%$ prediction (MAE of 31.4%).	143
6.9	Homogeneous Owens prediction: 70.1% data within $\pm 50\%$ prediction (MAE of 35.2%).	143
6.10	Homogeneous McAdams prediction: 57.4% data within $\pm 50\%$ prediction (MAE of 46.8%).	144
6.11	Homogeneous Duckler prediction: 46.8% data within $\pm 50\%$ prediction (MAE of 50.5%).	144
6.12	Lockhart-Martinelli prediction: 75.6% data within $\pm 50\%$ prediction (MAE of 40.5%).	145
6.13	Baroczy-Chisholm prediction: 83.3% data within $\pm 50\%$ prediction (MAE of 29.6%).	145
6.14	Friedel prediction: 78.1% data within $\pm 50\%$ prediction (MAE of 34.2%).	146
6.15	Muller-Steinhagen and Heck prediction: 74.2% data within $\pm 50\%$ prediction (MAE of 35.6%).	146

6.16	Mishima Hibiki prediction: 61.4% data within ± 50 % (MAE of 44.4%).	148
6.17	Zhang Mishima prediction: 70.3% data within ± 50 % (MAE of 42.7%).	148
6.18	Sun-Mishima prediction: 72.6% data within ± 50 % (MAE of 39.3%).	149
6.19	Tran et al. prediction: 42.8% data within ± 50 % (MAE of 71.6%).	149
7.1	Full liquid image calibration for the $D_{in}=1.03$ mm channel.	153
7.2	Top and bottom liquid film thickness for R236fa in the $D_{in}=1.03$ mm channel at $T_{sat}=31$ °C, $G=603$ kg/m ² s; a) $q=7.1$ kW/m ² , $x=0.03$, (b) $q=10.3$ kW/m ² , $x=0.06$, (c) $q=13.9$ kW/m ² , $x=0.09$ and (d) $q=23.2$ kW/m ² , $x=0.16$	154
7.3	Top and bottom liquid film thickness for R245fa in the $D_{in}=1.03$ mm channel at $T_{sat}=31$ °C, $G=599$ kg/m ² s; a) $q=9.9$ kW/m ² , $x=0.04$, (b) $q=11.5$ kW/m ² , $x=0.05$, (c) $q=17.8$ kW/m ² , $x=0.08$ and (d) $q=22.6$ kW/m ² , $x=0.11$	155
7.4	Top and bottom liquid film thickness for R236fa in the $D_{in}=1.03$ mm channel at $T_{sat}=31$ °C, $G=100$ kg/m ² s; a) $q=5.1$ kW/m ² , $x=0.208$, (b) $q=7.9$ kW/m ² , $x=0.33$, (c) $q=11.3$ kW/m ² , $x=0.49$ and (d) $q=15.2$ kW/m ² , $x=0.69$	157
7.5	Top and bottom liquid film thickness for R245fa in the $D_{in}=1.03$ mm channel at $T_{sat}=31$ °C, $G=100$ kg/m ² s; a) $q=5.4$ kW/m ² , $x=0.16$, (b) $q=12.1$ kW/m ² , $x=0.41$ and (c) $q=15.9$ kW/m ² , $x=0.57$	159
7.6	Top and bottom liquid film thickness for R236fa in the $D_{in}=1.03$ mm channel at $T_{sat}=31$ °C, $G=200$ kg/m ² s; a) $q=7.9$ kW/m ² , $x=0.16$, (b) $q=11.2$ kW/m ² , $x=0.25$, (c) $q=13.2$ kW/m ² , $x=0.29$, (d) $q=15.2$ kW/m ² , $x=0.35$, (e) $q=20.1$ kW/m ² , $x=0.48$ and (f) $q=31.1$ kW/m ² , $x=0.68$	161
7.7	Top and bottom liquid film thickness for R245fa in the $D_{in}=1.03$ mm channel at $T_{sat}=31$ °C, $G=199$ kg/m ² s; a) $q=9.6$ kW/m ² , $x=0.15$, (b) $q=15.0$ kW/m ² , $x=0.26$, (c) $q=17.6$ kW/m ² , $x=0.31$, (d) $q=22.5$ kW/m ² , $x=0.41$ and (e) $q=25.4$ kW/m ² , $x=0.46$	163
8.1	CHF criteria for R134a in the $D_{in}=1.03$ mm channel at $T_{sat}=31$ °C and $G=928$ kg/m ² s.	166
8.2	CHF comparison for R134a, R236fa and R245fa in the $D_{in}=1.03, 2.20, 3.04$ mm channels at $T_{sat}=31$ °C; (a) R134a, (b) R236fa and (c) R245fa.	169
8.3	CHF comparison for R134a in the $D_{in}=0.51, 0.79, 1.03, 2.20, 3.04$ mm channels at $T_{sat}=31$ °C.	169
8.4	Effects of saturation temperature for R134a, R236fa and R245fa in the $D_{in}=2.20$ mm channel at $T_{sat}=25, 31, 35$ °C; (a) R134a, (b) R236fa and (c) R245fa.	171
8.5	CHF comparison for R134a and R236fa in the $D_{in}=3.04$ mm channel at $T_{sat}=31, 35$ °C; (a) R134a and (b) R236fa.	172

8.6	CHF comparison for R134a, R236fa and R245fa at $T_{sat}=31^{\circ}C$; (a) $D_{in}=1.03$ mm, (b) $D_{in}=2.20$ mm and (c) $D_{in}=3.04$ mm.	174
8.7	CHF comparison for R134a, R236fa and R245fa in the $D_{in}=2.20$ and 3.04 mm channels; (a) $D_{in}=2.20$ mm, $T_{sat}=25^{\circ}C$ and (b) $D_{in}=3.04$ mm, $T_{sat}=35^{\circ}C$	175
8.8	Effects of sub-cooling on CHF in the $D_{in}=3.04$ mm channel.	176
8.9	Comparison of the Wojtan et al. [23] correlation with the current experimental CHF data.	177
8.10	Comparison of the Qi et al. [35] correlation with the current experimental CHF data.	178
8.11	Comparison of the Mudawar et al. [36] correlation with the current experimental CHF data.	178
8.12	Comparison of the Katto et al. [37] correlation with the current experimental CHF data.	179
8.13	Comparison of the Katto et al. [37] correlation with the current experimental CHF data for various fluids.	179
8.14	Comparison of the new CHF correlation with the experimental CHF data.	181
8.15	Fluid comparison with the new CHF correlation.	181
8.16	Comparison of the new CHF correlation with the experimental data of Park [38].	182
8.17	Comparison of the new CHF correlation with the CHF experimental data of Bruno et al. [39] for silicon multi micro-channels.	182
8.18	Comparison of the new CHF correlation with the split flow CHF experimental data of Mauro et al. [40].	183
8.19	Experimental CHF data comparison for water with the new CHF correlation.	184
9.1	Macro-microscale transition criterion: Current study, Li et al. [41] and Cheng et al. [42].	186

List of Tables

- 3.1 The test section diabatic and adiabatic lengths 41
- 3.2 Regression error of the thermocouples used in the current experiments. . . 47
- 3.3 The uncertainties of the channel diameter and heated length 49
- 3.4 The root mean square values of the surface roughness. 50
- 3.5 Uncertainty range for the $D_{in}=1.03, 2.20$ and 3.04 *mm* channels. 52

- 4.1 A summary of the experimental confinements numbers at $T_{sat}=31$ °C for
the $D_{in}=2.20$ and 3.04 *mm* channel. 78

- 5.1 Minimum film thickness, δ_{min} for the $D_{in}=1.03, 2.20$ and 3.04 *mm* channels.129

- 8.1 Applicability range of the new CHF correlation. 180
- 8.2 Experimental CHF data comparison with the newly proposed CHF corre-
lation. 183

Nomenclature

Symbols	Description	SI units
Roman		
A	area	$[m^2]$
C_p	specific heat at constant pressure	$[J/kgK]$
CB	coalescing bubble	
CHF	critical heat flux	$[W/m^2]$
D	channel diameter	$[m]$
f	friction factor	-
f_{ps}	frames per second	-
f_{opt}	optimum pair frequency	-
F	force	$[N]$
g	acceleration due to gravity (9.81)	$[m^2/s]$
G	mass velocity	$[kg/m^2s]$
h	heat transfer coefficient	$[W/m^2K]$
H	enthalpy	$[J/kg]$
H_{lv}	latent heat	$[J/kg]$
I	current	$[A]$
IB	isolated bubble	-
L	Length	$[m]$
\dot{m}	mass flow rate	$[kg/s]$
M	molecular weight	$[kg/kmol]$
MAE	mean absolute error ($\text{abs}(\frac{\text{prediction}-\text{experimental}}{\text{experimental}})$)	-
n_f	dimensionless exponent	-
P	pressure	$[Pa]$
PDF	probability density function	-
q	heat flux	$[W/m^2]$
q_{ref}	reference heat flux	$[W/m^2]$
q'''	rate of energy generation per unit volume	$[W/m^3]$
Q	heat rate	$[J/s]$
r	radial coordinate	-
rms	root mean square	-
R	radius	$[m]$
R^2	residuals	-
S	standard deviation	-
T	temperature	$[^\circ C]$
$\Delta(V)$	voltage drop	$[V]$
V	Volume	$[m^3]$
x	vapor quality	-
X	X pixel coordinate	-
Y	Y pixel coordinate	-
$\Delta(z)$	discretized axial distance	$[m]$

Symbols	Description	SI units
Greek		
α	thermal diffusivity	$[m^2/s]$
β	volumetric thermal expansion coefficient	$[1/K]$
δ	falling film thickness	$[m]$
η	heating efficiency	-
μ	dynamic viscosity [Pa.s]	$[kg/ms]$
ν	kinematic viscosity	$[m^2/s]$
ρ	density	$[kg/m^3]$
σ	surface tension	$[N/m]$
τ	pair period	-
ε	relative heat loss	-
κ	thermal conductivity	$[W/mK]$
ξ	singular loss coefficient	-
∞	ambient	-
Subscripts		
<i>adb</i>	adiabatic	-
<i>cap</i>	capillary	-
<i>crit</i>	critical	-
<i>db</i>	diabatic	-
<i>diff</i>	differential	-
<i>ev</i>	evaporator	-
<i>fr</i>	frictional	-
<i>GS</i>	gas superficial	-
<i>in</i>	inner	-
<i>l</i>	liquid	-
<i>LO</i>	liquid only	-
<i>VO</i>	vapor only	-
<i>LS</i>	liquid superficial	-
<i>out</i>	outer	-
<i>ph</i>	pre-heater	-
<i>ref</i>	reference	-
<i>sat</i>	saturation	-
<i>sp</i>	single-phase	-
<i>th</i>	threshold	-
<i>TS</i>	test section	-
<i>v</i>	vapor	-
<i>wall</i>	wall	-

**Dimensionless
numbers**

Bo	Boiling number $(\frac{q}{Gh_{lv}})$	-
Bo	Bond number $(\frac{g(\rho_l - \rho_v)D_{in}^2}{\sigma})$	-
Bi	Biot number $(\frac{hD_{in}}{\kappa_{wall}})$	-
Co	Confinement number $(\frac{1}{D_{in}} \sqrt{\frac{\sigma}{g(\rho_l - \rho_v)}})$	-
$Eö$	Eötvös number $(\frac{g(\rho_L - \rho_G)d_{in}^2}{8\sigma})$	-
Fr	Froude number $(\frac{G^2}{\rho_L^2 g D_{in}})$	-
Nu	Nusselt number $(\frac{hD_{in}}{\kappa_{fluid}})$	-
Pr	Prandtl number $(\frac{\mu c_p}{\kappa_{fluid}})$	-
Ra	Rayleighs number $(\frac{g\beta(T - T_\infty)D^3}{\nu\alpha})$	-
Re	Reynolds number $(\frac{GD_{in}}{\mu})$	-
We	Weber number $(\frac{G^2 D_{in}}{\sigma\rho})$	-

Chapter 1

Introduction

1.1 Overview

Liquid-vapor phase change processes provide numerous advantages for many technological applications. These phase change phenomena associated with boiling and condensation occur in numerous heat transfer and fluid mechanic applications due to their highly advantageous thermodynamic efficiency. The inclusion of these technological applications stretch from nuclear, aerospace, automotive and refrigeration industries to microelectronics thermal management systems. It is widely anticipated that the heat dissipation per unit volume for micro devices will rise further in the near future, thus justifying the need for more energy efficient cooling with higher heat removal characteristics.

The need for high heat flux dissipation technologies involving phase change processes for these microelectronics have become a challenging task for heat transfer engineers. Two-phase heat sinks for microcooling systems such as those described in Jiang et al. [43], [44] are compact in size but must be able to achieve high heat transfer rates associated with flow boiling heat transfer of the refrigerant/coolant through latent heat of vaporization. As a consequence, the rapid advancements in microfabrication technologies are creating a worldwide redirection of liquid-vapor phase change research and development from the conventional macroscale to the microscale transport phenomena.

According to Thome [45], the '*best*' cooling process involves forced flow boiling processes to achieve high heat dissipation efficiency. In comparison, thermal heat dissipation through latent heat of vaporization is on the order of ≈ 100 times higher than the sub-cooled liquid specific heat. Literature reviews have shown that flow boiling offers high heat flux dissipation capabilities at moderate wall superheats. Another significant advantage of microscale in-tube flow boiling heat transfer includes a low refrigerant/coolant charge and mass flow rate but a significantly larger mass flow rate per unit flow area. Fig. (1.1) illustrates the comparison of various cooling techniques by Lin et al. [46]. From this, it is clear that the prospect of confined flow boiling in future Micro-Thermal-Management Systems (MTMS) holds the promise of solving the upcoming technological void for the commercial electronics cooling industry.

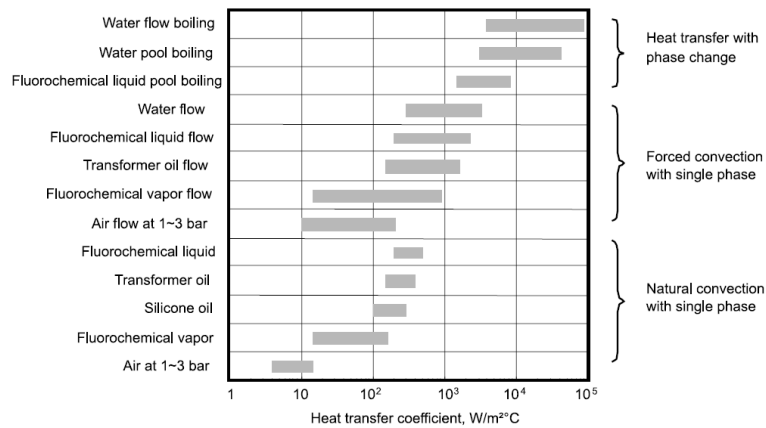


Figure 1.1: Heat transfer for various coolant and heat transfer modes

Significant advances have been made since the 1950s to successfully develop an understanding of the macroscale flow boiling heat transfer phenomena. However, major differences in the transport phenomena have been reported in the microscale in comparison to the macroscale. Hence, this brings up the question of channel size and the proper definition of macroscale and microscale in two-phase processes and the need to address flow boiling processes in the transition from macro to microscale. Most macroscale heat transfer prediction methods and theories, two-phase flow pattern maps and pressure drop prediction methods from literature are inadequate to describe the flow boiling process in the microscale. The failure of these methods to accurately predict the heat transfer coefficient, pressure drop and flow regimes in microscale channels allows only part of the macroscale knowledge to be transferred to microscale studies. As discussed, this is due to significant differences in the phase change phenomena in the macro-micro transition region. In brief, many extrapolation of macroscale models to microscale boiling conditions were performed without a sound physical basis and clear understanding of the fundamental issues representing two-phase flow and heat transfer in microscale channels. Despite numerous investigations in this field for nearly thirty years since the first experiments by Lazarek et al. [5], the characteristics of two-phase heat transfer and the transport phenomena in these small scale channels have yet to be well clarified.

1.2 Research Objective

This research project focuses on investigating the macro-to-microscale confinement effects of channel dimensions and refrigerant fluid properties on flow boiling heat transfer, two-phase flow patterns, pressure drop, critical heat flux and liquid film stratification in a single circular channel. In 'true' evaporative flow boiling in microscale channels, the influence of gravity becomes irrelevant compared to the surface tension effects. The confinement number accounts for the ratio of gravity and surface tension forces, becoming macroscale for $Co < 0.5$ and $Co > 0.5$ for microscale, where Co is defined as $Co = \frac{1}{D_{in}} \sqrt{\frac{\sigma}{g(\rho_l - \rho_v)}}$. For this investigation, flow boiling experiments have been conducted

for three refrigerants (R134a - high pressure, R236fa - medium pressure and R245fa - low pressure) in a single circular channel with 1.03, 2.20 and 3.04 *mm* internal diameters. Experimental and theoretical investigations have been made for a mechanistic classification of two-phase flow systems into the macroscale (conventional channels), miniscale (mesoscale) and microscale flows and is discussed in the following chapters. The test conditions were manipulated so as to obtain all three regimes according to the tentative confinement number transition criterion, $Co = 0.5$, proposed by Lin et al. [6]. Other dimensionless parameters such as the Weber and Capillary number that account for the relation between surface tension, inertia and viscous forces have proven to be of relevant importance in explaining the complex hydrodynamic features of this transitional flow boiling phenomena. Throughout this experimental campaign, a systematic investigation of the trends in heat transfer, pressure drop, two-phase flow patterns, critical heat flux, void fraction and liquid film stratifications for a wide range of conditions as a function of flow pattern has been undertaken to generate a uniquely comprehensive experimental database to then be used in the analysis for defining an improved macro-to-micro transition criterion.

The contents of this manuscript are organized into the following chapters:

1. Chapter 1 - Introduction
2. Chapter 2 - State of the Art Review
3. Chapter 3 - The Experimental Campaign
4. Chapter 4 - Two-Phase Flow Patterns
5. Chapter 5 - Flow Boiling Heat Transfer
6. Chapter 6 - Two-Phase Pressure Drop
7. Chapter 7 - Optical Film Thickness Measurement Measurement
8. Chapter 8 - Critical Heat Flux
9. Chapter 9 - Conclusion and Recommendation

Chapter 2

State of the Art Review

2.1 Overview

Flow boiling heat transfer researchers are in a '*dilemma*' on how to classify the channel dimensions according to macroscale, miniscale and microscale channels. There is no proven criterion in the literature to define the difference among macroscale (or macrochannels), miniscale (minichannels) and microscale (microchannels). In other words, there is no established universal agreement or available definition in literature to clearly predict the transition in the flow characteristics and heat transfer trends when decreasing the channel diameter to very small sizes. In this chapter, reviews of macro-microscale transition criteria flow boiling heat transfer, two-phase flow pattern maps, two-pressure drops and critical heat flux are presented. The reason is that all of these experimental parameters will be measured in the experimental part of this thesis and then be used as "clues" to determine or identify the macro-microscale general transition criterion.

2.2 Macro-Microscale Transition Criteria

Several macro-to-microscale transition criteria have however been proposed by independent researchers ranging from physical channel size classifications to approaches based on bubble confinement and bubble departure diameter. These criteria are so far not of proven utility. Representative work to determine the transition criteria in two-phase flow have been briefly reviewed and are presented in the following sections of this chapter.

2.2.1 Channel Size Classifications

Single-phase gas flows on the other hand can be classified based on rarefaction effects based on the Knudsen number, Kn as shown in Fig. (2.1). Fixed channel classifications have been proposed by independent researchers based on the physical size of the channels. Mehendale et al. [47] proposed the following classification : microchannels for a size range $1 \mu\text{m} - 100 \mu\text{m}$, mesochannels for channel sizes from $100 \mu\text{m}$ to 1.0 mm , compact channels from 1.0 mm to 6.0 mm and macrochannels for all channel sizes exceeding 6.0 mm .

Kandlikar et al. [2] instead proposed another criteria for macro-microscale channel classification based on flow considerations. The author proposed that conventional channels are identified as those with hydraulic diameters of 3.0 mm or larger while minichannels have been classified for those with hydraulic diameters of $200 \text{ }\mu\text{m}$ to 3.0 mm . Microchannels are those smaller than $200 \text{ }\mu\text{m}$, and so on as shown in Fig. (2.2).

The Kandlikar et al. recommended the in above criteria for both liquid and two-phase flow applications to provide uniformity in channel classification. The following classification is presented in Fig. (2.2). Shah [48] characterized compact heat exchangers as exchangers with surface-to-volume ratio $> 700 \text{ m}^2/\text{m}^3$, which translates to a threshold diameter for the macro-micro transition of $< 6.0 \text{ mm}$ irrespective of the fluid properties.

Range of Knudsen numbers	Type of flow
$0.001 > \text{Kn}$	Continuum flow: no rarefaction effects
$0.1 > \text{Kn} > 0.001$	Slip flow: rarefaction effects that can be modeled with a modified continuum theory accounting for wall slip
$10 > \text{Kn} > 0.1$	Transition flow: a type of flow between slip flow and free molecular flow that is analyzed statistically, i.e., with Boltzman equation
$\text{Kn} > 10$	Free molecular flow: motion of individual molecules must be modeled and then treated statistically

Figure 2.1: Knudsen number ranges for various types of flow for Harley [1]

Conventional Channels:	$D_h > 3 \text{ mm}$
Minichannels:	$3 \text{ mm} \geq D_h > 200 \text{ }\mu\text{m}$
Microchannels:	$200 \text{ }\mu\text{m} \geq D_h > 10 \text{ }\mu\text{m}$
Transitional Channels:	$10 \text{ }\mu\text{m} \geq D_h > 0.1 \text{ }\mu\text{m}$
Transitional Microchannels:	$10 \text{ }\mu\text{m} \geq D_h > 1 \text{ }\mu\text{m}$
Transitional Nanochannels:	$1 \text{ }\mu\text{m} \geq D_h > 0.1 \text{ }\mu\text{m}$
Molecular Nanochannels:	$0.1 \text{ }\mu\text{m} \geq D_h$

Figure 2.2: Channel classification proposed by Kandlikar [2]

2.2.2 Bubble Confinement

The bubble confinement approach is based on the confined growth of a bubble in small channels. The role of surface tension forces becomes important and the gradual *imminent* suppression of the gravity forces increases as the channel size decreases. Kew et al. [49] performed flow boiling experiments for single channels with internal diameters of 1.10, 1.80, 2.80 and 3.60 mm and for a square channel of $2.0 \times 2.0 \text{ mm}$ as part of a compact heat exchanger study. They proposed bubble growth confinement within a channel for

the distinction of macro-and-microscale channels in the form of a Confinement number, Co :

$$Co = \frac{1}{D_{in}} \sqrt{\frac{\sigma}{g(\rho_l - \rho_v)}} \quad (2.1)$$

They set the threshold at $Co=0.5$ where $Co > 0.5$ is for microscale and $Co < 0.5$ for macroscale.

Triplett et al. [50], who have systematically investigated capillary gas-liquid two-phase flows in 1.10 and 1.49 mm circular microchannels, proposed two-phase flows smaller than the order of the capillary length as the threshold of microchannel flows. In continuation, Brauner et al. [51] investigated the effect of channel diameter on the mechanisms leading to adiabatic flow pattern transitions in single channels and proposed the role of the dimensionless Eötvös number $Eö$ for the macro-micro threshold. The Eötvös number is similar to the Bond number Bo and represents the ratio of buoyancy force to surface tension forces. The Eötvös number is defined as:

$$Eö = \frac{g(\rho_l - \rho_v)d_{in}^2}{8\sigma} \quad (2.2)$$

They showed that the $Eö$ number plays an important role in dictating the relevant characteristics in dispersed flows and the wall wetting characteristics in separated flows. In conclusion, they proposed an $Eö \sim 0.2$ as the characteristic threshold value for microscale flows.

Li et al. [41] conducted an experimental investigation to determine the channel size effects on two-phase flow regimes for in-tube condensation. They studied the effects of gravity by investigating the transition from asymmetric flow to symmetric flow. The authors subdivided the flow distribution characteristics and proposed the following criteria for the mini-to-microscale transition. The threshold diameter is defined as $d_{th} = 1.75L_{cap}$ and the critical diameter as $d_{crit} = 0.224L_{cap}$. The capillary length is defined as:

$$L_{cap} = \sqrt{\frac{\sigma}{g(\rho_l - \rho_v)}} \quad (2.3)$$

Their observations, based on the flow regime with respect to the internal tube diameter d_{in} , are described as follows:

1. $d_{in} < d_{crit}$: Gravity forces are insignificant compared to surface tension forces. The flow regimes are symmetrical.
2. $d_{crit} < d_{in} < d_{th}$: Gravity and surface tension forces are equally dominant. A slight stratification of the flow distribution is observed.
3. $d_{th} < d_{in}$: Gravity forces are dominant and the flow regimes are similar to macroscale flows.

Similarly, a subsequent review by Cheng et al. [42] classified the work of Li et al. [41] on phase change heat transfer into Microchannel, Mesochannel and Macrochannel in terms of the Bond number, Bo . They proposed the following classifications:

1. $Bo < 0.05$: Microscale flow and the effect of gravity can be neglected.
2. $0.05 < Bo < 3.0$: Mesoscale flow where surface tension is dominant and gravity effects are small.
3. $Bo > 3.0$: Macroscale flow where gravity forces are dominant.

Review Summary

In summary, the dimensionless numbers such as the Eötvös number ($Eö$), Bond number (Bo) and the Confinement number (Co) are interrelated as:

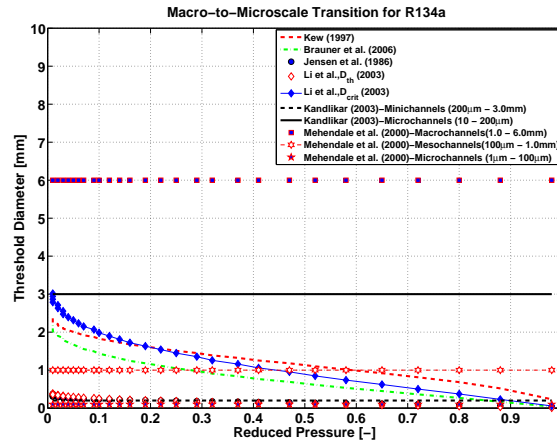
$$Eö = \frac{Bo}{8} = \frac{1}{8Co^2} \quad (2.4)$$

The Confinement number, Co is adopted for use here in this manuscript as it accounts for confined flow boiling occurring in these small scale channels. The Confinement number, Co is defined as the bubble capillary length over the channel size. Upon the onset of bubble nucleation, the bubble grows and becomes confined when the bubble diameter reaches the channel size. The bubble will then continue to grow in length in the stream wise direction resulting in elongated bubbles observed in small scale confined channels. This acknowledges the importance of scaling effects in terms of forces and the bubble geometry.

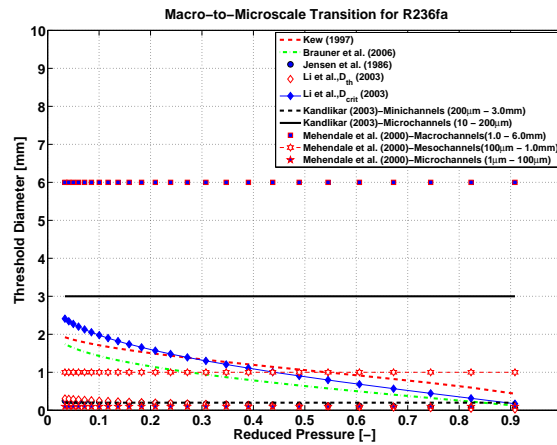
2.2.3 Bubble Departure Diameter

Jacobi et al. [52] proposed a heat transfer model based on elongated bubble flow in microscale channels. Their assumption is that microscale flow is reached when the bubble growth diameter reaches the tube internal diameter followed by subsequent detachment from the wall surface. In their heat transfer model, the critical bubble radius is evaluated using the effective nucleation wall superheat. A comprehensive macro-microscale transition review by Thome [53] proposed the use of nucleate pool boiling bubble detachment due to the lack of availability of methods to predict bubble departure diameters for confined bubble flow. Various expressions and correlations have been proposed by independent researchers to predict the bubble departure diameter during nucleate pool boiling. This includes the Fritz [54] study, Nishikawa et al. [55], [56], Kutateladze et al. [57] and Jensen et al. [58].

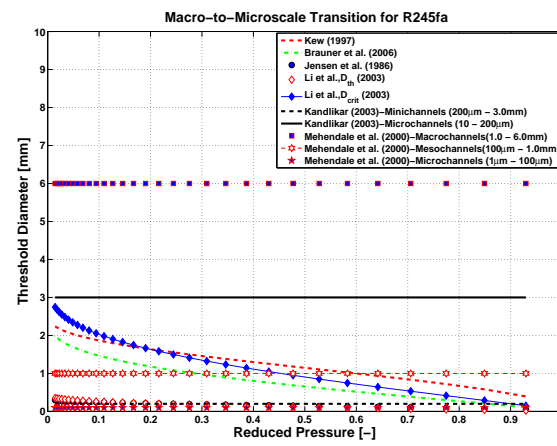
The various approaches proposed by individual researchers in the previous sections have been compared for the three fluids tested in the present study, plotted as refrigerants a function of threshold diameter vs. reduced pressure. Fig. (2.3) illustrates the possible range of macro-microscale transition threshold diameters for R134a, R236fa and R245fa. All of these methods can be considered to be preliminary since none have been systematically validated.



(a)



(b)



(c)

Figure 2.3: Macro-microscale threshold diameter for (a) R134a, (b) R236fa and (c) R245fa as a function of reduced pressure.

2.3 Flow Boiling Heat Transfer

This section addresses the in-tube flow boiling heat transfer mechanisms and the heat transfer trends during flow boiling in small scale channels. A comprehensive review of several experimental flow boiling studies by different researchers is presented here. From the literature, experimental results from different researchers can hardly be compared against one or another since there is not any accepted benchmark among these researchers on the issue of the dominant heat transfer mechanisms during flow boiling heat transfer in small channels. In other words, researchers are in somewhat of a *dilemma* to conclude which is the dominant heat transfer mechanism in these channels. Thus, the flow boiling heat transfer mechanisms have been classified by independent two-phase flow boiling researchers into three different categories: (i) nucleate boiling dominant which is heat flux dependent, (ii) convective boiling dominant with the heat transfer coefficient dependent on mass flux and vapor quality but not heat flux and (iii) thin film evaporation of the liquid film around elongated bubble flows which is heat flux dependent.

2.3.1 Heat Transfer Mechanisms

Macroscale Flow Boiling

Flow boiling research studies in the 1950s and 1960s have recognized that the heat transfer coefficient in macroscale flow boiling is an interaction of nucleate and convective boiling. In-tube flow boiling of refrigerants in macroscale or (*conventional*) channels can thus be classified according to nucleate boiling relating to the formation of vapor bubbles at the tube wall surface and convective boiling in which the heat is transferred through conduction and convection through a thin liquid film with continuous evaporation at the liquid-vapor interface. It is often assumed for simplicity that only one of the boiling types occurs at once and that the mechanism switches from one type of flow boiling to the other at some point. In fact, the flow mechanisms can coexist as the thermodynamic vapor quality increases where convective boiling gradually supplants nucleate boiling. Thus, nucleate and convective boiling components can be superimposed by a very complex mechanism. Steiner et al. [3] studied the fundamental characteristics of flow boiling in vertical tubes and suggested that convective boiling is the only mechanism for heat fluxes below the onset of boiling where the heat transfer coefficient is independent of heat flux over a wide range of vapor quality. For fully developed nucleate boiling at high heat fluxes, the heat transfer coefficient is virtually independent on mass flux and vapor quality. A typical schematic representation of the in-tube flow boiling process is illustrated in Fig. (2.4):

1. At the vapor quality of $x = 0$, the onset of nucleate boiling is reached and the heat transfer coefficient corresponds to the respective heat fluxes.
2. At low heat fluxes, convective boiling is significant and becomes the dominant mechanism with increasing vapor quality.

3. At intermediate heat fluxes, the heat transfer coefficient is largely independent of vapor quality before converging into a single value at higher vapor qualities where convective boiling becomes dominant. The nucleate boiling coefficient values increase with increasing saturation pressure.

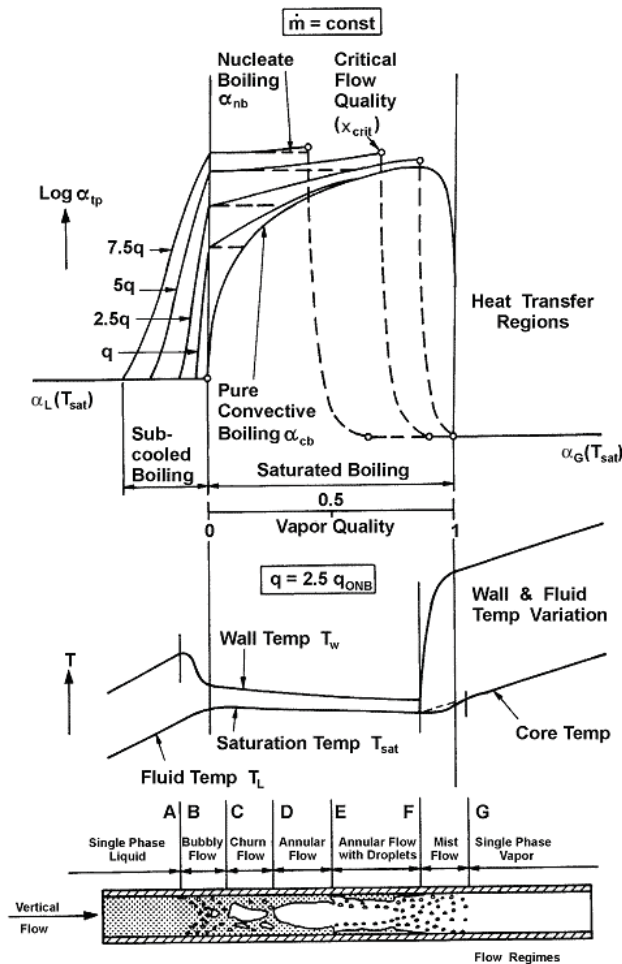


Figure 2.4: Schematic of macroscale vertical in-tube flow boiling process adopted from Steiner [3]

Kattan et al. [4, 59, 60] performed in-tube flow boiling experiments for five refrigerants, (R134a, R-123, R-402A, R-404A and R-502) in a 11.9 mm copper tube for a wide range of parameters to study the effects of local flow patterns on flow boiling heat transfer. In this pioneering work, the authors proposed a flow boiling model that takes a more fundamental approach in predicting the local heat transfer coefficients by incorporating a simplified flow structure into the heat transfer prediction as a function of the local flow pattern, i.e. Stratified–wavy, fully Stratified, Intermittent and Annular flows. Fig. (2.5) illustrates the simplified two-phase flow structure used in their heat transfer prediction model.

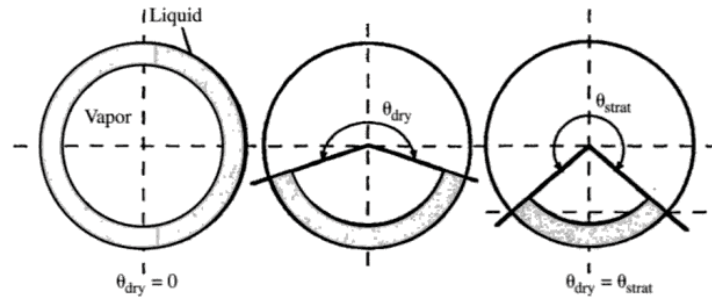


Figure 2.5: Geometrical illustration of the liquid-vapor regions, stratified and dry angles from Kattan et al. [4]

In continuation, Wojtan et al. [13] performed flow boiling tests for R22 and R410A in horizontal tubes with 8.0 and 13.84 mm internal diameters. Upon completion of their work, they have implemented several important modifications to the flow pattern map of Kattan et al. [4] by subdividing the stratified–wavy region into three subzones: Slug, Slug/Stratified-wavy and Stratified–wavy flow and the extension of the heat transfer prediction model to include dryout and mist flow by addition of the annular-to-dryout and dryout-to-mist flow transition lines. Fig. (2.6) illustrates the comparison of their new prediction method and new macroscale flow pattern map with the flow boiling experimental data of Lallemand et al. [61] for refrigerant R22 in a 10.7 mm internal diameter tube.

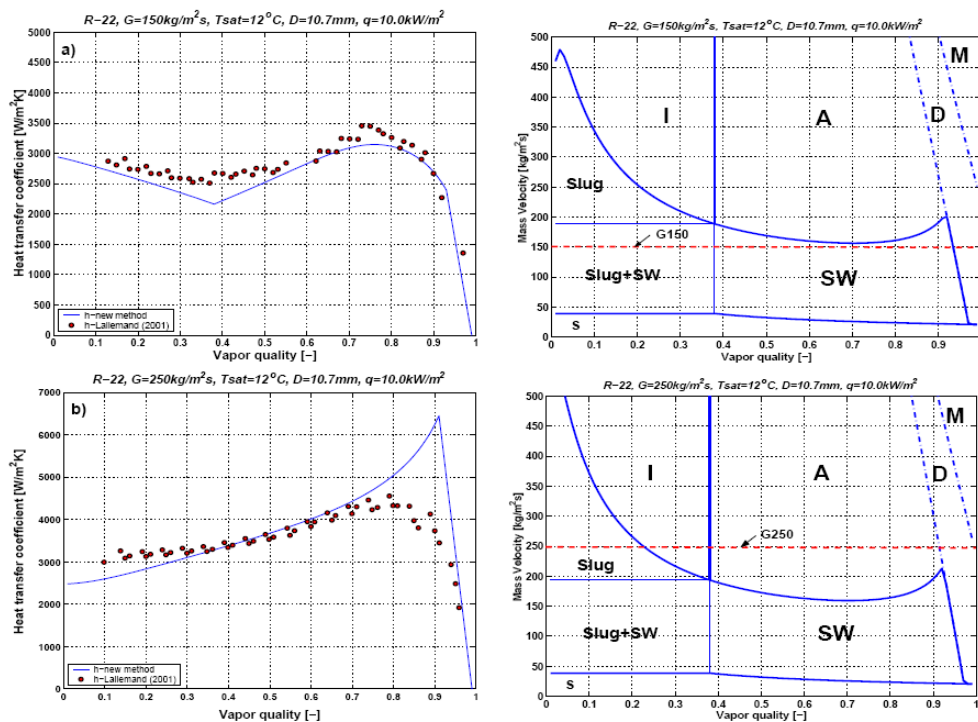


Figure 2.6: Refrigerant R22, $D_{in}=10.7$ mm, $T_{sat}=5$ °C, $q=10.0$ kW/m² at: (a) $G=150$ kg/m²s and (b) $G=250$ kg/m²s

Jabardo et al. [62] experimentally investigated convective boiling for refrigerants R22, R134a and R404A in a copper channel with an internal diameter of 12.70 mm. From their experimental observations, they observed the influence of physical parameters such as mass flux and heat flux on their in-tube flow boiling heat transfer results. The flow boiling heat transfer data obtained by Jabardo et al. [62] are shown in Fig. (2.7).

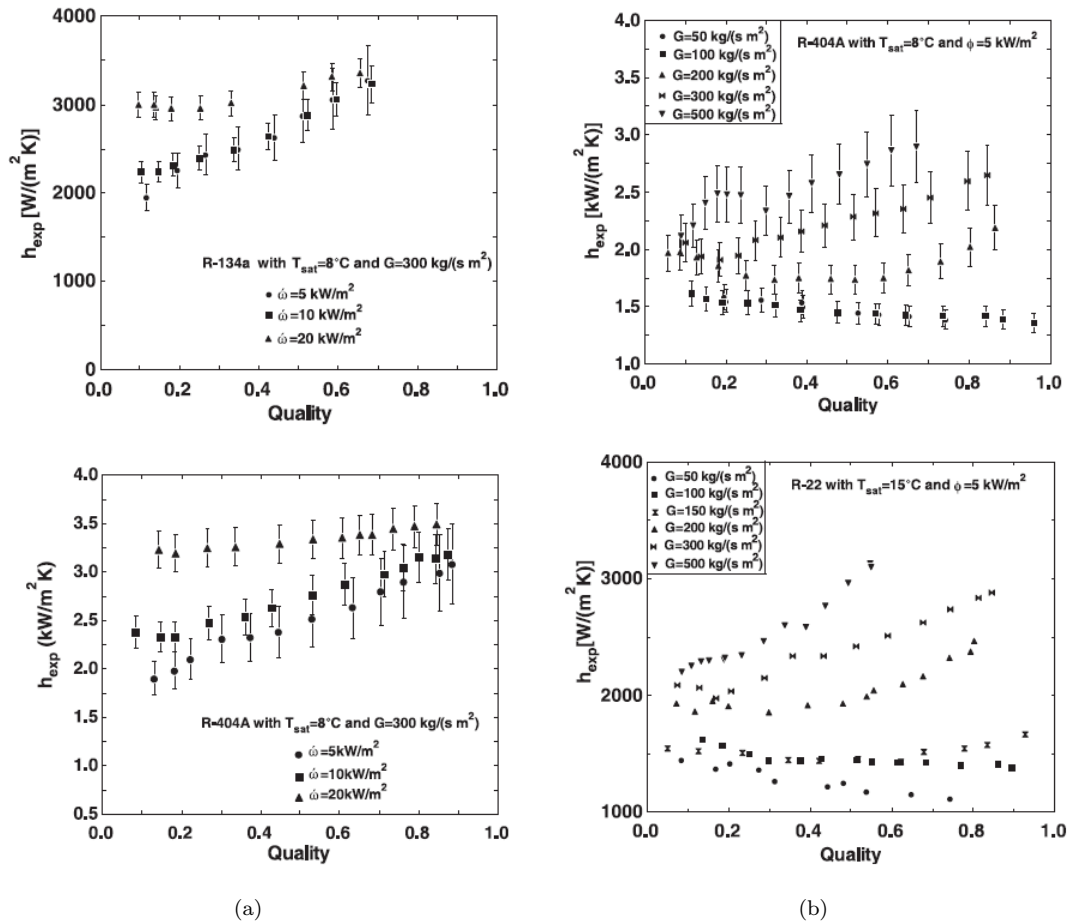


Figure 2.7: Experimental heat transfer coefficients vs. vapor quality for R22, R134a and R404A: (a) Effects of heat flux and (b) Effects of mass flux.

Microscale Flow Boiling

Pioneering work on microscale flow boiling heat transfer was performed by Lazarek et al. [5] for R-113 in a round tube with an internal diameter of 3.1 mm. From their experimental data, the authors found that the local heat transfer coefficient was independent of quality in the saturated boiling region as presented in Fig. (2.8). The strong influence of heat flux on the local heat transfer coefficient up to vapor quality with negligible influence of quality suggest that nucleate boiling was the dominant heat transfer mechanism and that pure convective boiling did not exist for the range of parameters they investigated.

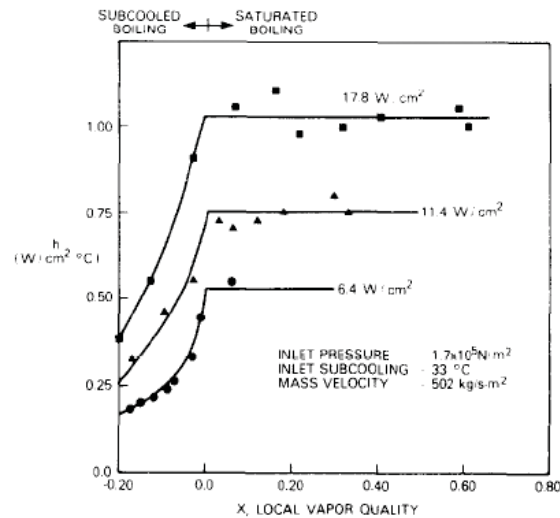
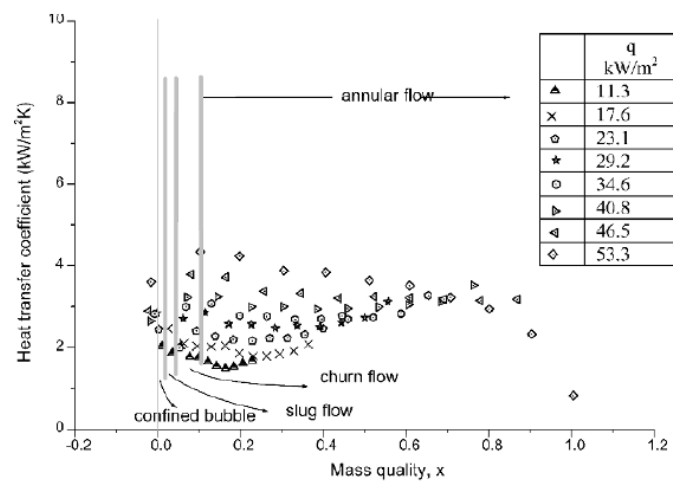


Figure 2.8: Flow boiling heat transfer results from Lazarek et al. [5]

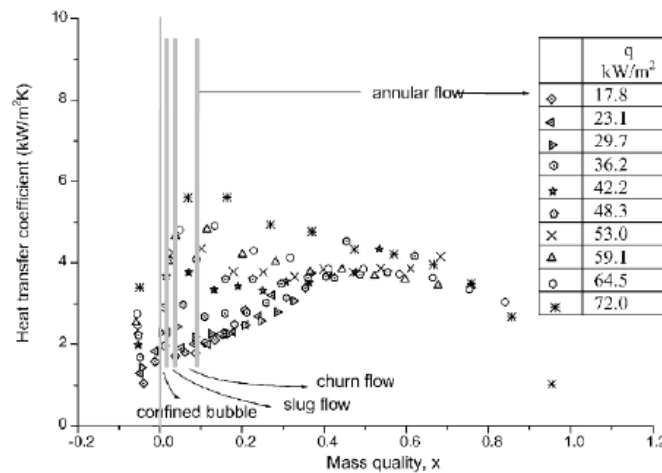
Other researchers, Kew et al. [49], conducted flow boiling experiments of R141b in channels with internal diameters of 1.39, 2.87 and 3.69 *mm*. From their experimental flow boiling results, the heat transfer coefficients for the 3.69 and 2.87 *mm* illustrate trends similar to those observed in conventional macroscale channels. However, the trends are less apparent for the smaller 1.39 *mm* channel where the heat transfer trend falls rapidly at higher quality for the two values of mass flux tested. The authors then concluded that the effect of confinement is significant in such that channels with confinement number, $Co > 0.5$ is termed microscale channels and vice versa $Co < 0.5$ for macroscale channels. For channels with $Co < 0.5$, they concluded without physical observation, however that the boiling mechanism was predominantly nucleate as it showed a strong dependence on heat flux but not on quality. Furthermore, their heat transfer coefficients are a function of heat flux at low vapor quality, but the trend changes and becomes independent of heat flux at higher vapor qualities. On the other hand, the authors also showed that the flow regimes in small channels differed slightly from those observed in large channels which are defined as: isolated bubble, confined bubble and annular-slug flow. In summary, they also showed that established correlations developed for large tubes did not extrapolate well to small tubes.

Continuing the earlier work of Kew et al. [49], Lin et al. [6] conducted another set of flow boiling experiments with refrigerant R141B in circular tubes of 1.10, 1.80, 2.80 and 3.60 *mm* and a 2.0 x 2.0 *mm* square channel. From the experimental trends, the authors concluded that flow boiling in small channels can be divided into a nucleate boiling dominant region at low vapor quality range and a convective boiling dominant region at higher vapor qualities. The heat transfer coefficient is observed to increase dramatically from the single phase liquid coefficient to a peak vapor quality of $x \approx 0.05 - 0.1$, corresponding to confined slug flow. The heat transfer values in this region increase with heat flux for all range of mass flux tested and this corresponds similarly to the nucleate boiling region observed in large channels. However, the reduction of the heat transfer coefficient values thereafter at higher vapor qualities differ from conventional macroscale theories. The

authors explained that this might be due to a higher pressure gradient observed during flow boiling in these small channels, with the nucleate boiling contribution expected to decrease with reduced pressure as can be explained by Cooper correlation for pool boiling. In the convective boiling region, the heat transfer coefficient is found to be independent of heat flux but increases with increasing vapor quality. The local heat transfer coefficients increase and converge at higher vapor qualities in the annular flow regime, suggesting convective boiling dominance in this region. When the vapor quality approaches unity, partial dryout is encountered and a significant drop in the heat transfer coefficient is observed. This drove the authors to conclude that both nucleate and convective boiling is dominant in small channels. Studies at higher confinement by Moriyama et al. [63], i.e. $Co > 10$ concluded that evaporative heat transfer is predominantly convective by conduction through a thin liquid layer of liquid on the heated surface.



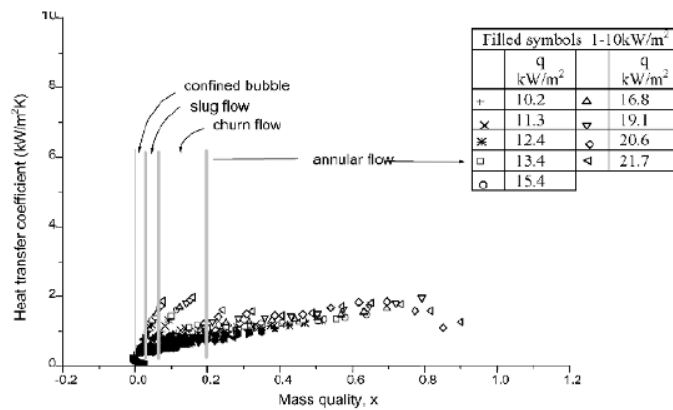
(a)



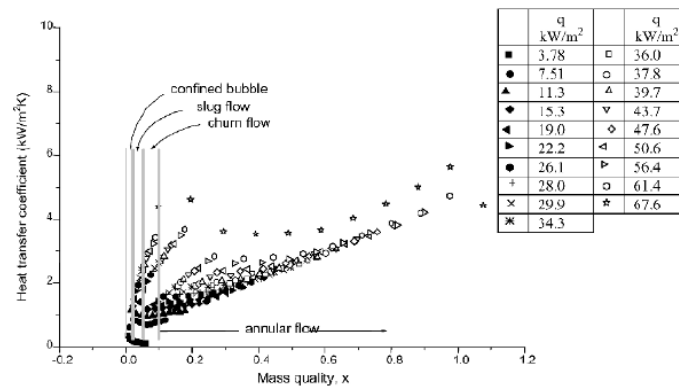
(b)

Figure 2.9: Heat transfer results of Lin et al. [6] for R141b in the 1.10 mm channel, $Co=1.1$: (a) $G=365 \text{ kg/m}^2\text{s}$ and (b) $G=505 \text{ kg/m}^2\text{s}$.

Bao et al. [7] also studied flow boiling heat transfer experiments for R11 and HCFC123 in



(a)



(b)

Figure 2.10: Heat transfer results of Lin et al. [6] for R141b in the 3.60 mm channel, $Co=0.33$: (a) $G=50 \text{ kg/m}^2\text{s}$ and (b) $G=130 \text{ kg/m}^2\text{s}$.

a smooth copper tube with an internal diameter of 1.95 mm for different heat fluxes, mass fluxes and system pressures. Referring to Fig. (2.11)a, the local heat transfer increases with heat flux for both the refrigerants while the effect of mass flux and vapor quality is small as shown in Fig. (2.11)b. Thus, the local heat transfer coefficient appeared to be a strong function of heat flux and system pressure but minor effects of mass flux and vapor quality for the range of parameters examined. Applying macroscale logic, they thus suggested that the dominant heat transfer mechanism is via nucleate boiling while convective boiling is insignificant.

Ohwaib et al. [8] performed flow boiling experiments of R134a in a uniformly heated vertical microchannel with internal diameters of 1.70, 1.22 and 0.83 mm to investigate channel effects on flow boiling heat transfer. From their experiments, the authors discovered that the heat transfer coefficient is highly dependent on heat flux but only varies slightly with mass flux and vapor quality, for values $x < 0.60$. They then concluded that the contribution of forced convection heat transfer to the overall transfer rate is small given the dominance of nucleate boiling. Finally, the authors also found that flow boiling heat transfer coefficients are higher for smaller diameter channels as shown in Fig. (2.12).

The higher heat transfer trend was also reported by Yan et al. [64] who found that the flow boiling heat transfer coefficients obtained from their 2.0 mm channel were 30-80% higher in value when compared to larger channels ($D_{in} > 8.0$ mm) reported in the literature. Investigating further, Callizo et al. [65] performed similar flow boiling tests with R134a in a vertical 640 μm channel with a heated length of 613 mm and observed that the heat transfer coefficient increased with heat flux but did not change with quality when $x < 0.45 - 0.50$. Increasing in quality, a decreasing heat transfer coefficient trend was observed and the effects of heat flux diminished. The authors explained that the drop in the heat transfer trend at higher qualities was due to the presence of intermittent dryout with extreme wall temperature fluctuations downstream of the channel. On the other hand, it was observed that the dependence of the heat transfer coefficients on vapor quality shifted to lower values of x with increasing heat flux. The authors then arrived to the conclusion that the local and averaged heat transfer coefficient is a strong function of heat flux and is essentially independent of the mass flux for values of $x < 0.5$ for the 0.63 mm channel.

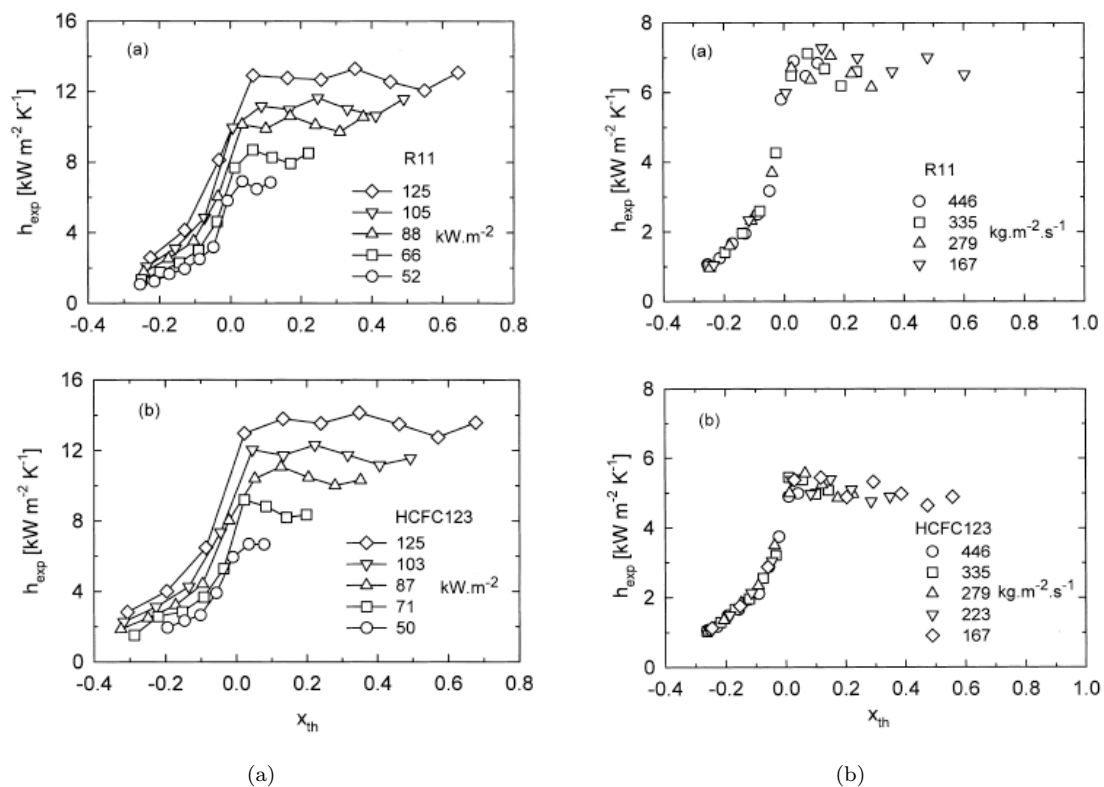


Figure 2.11: Flow boiling heat transfer results of Bao et al. [7] for (a) Effects of heat flux and (b) Effects of mass flux.

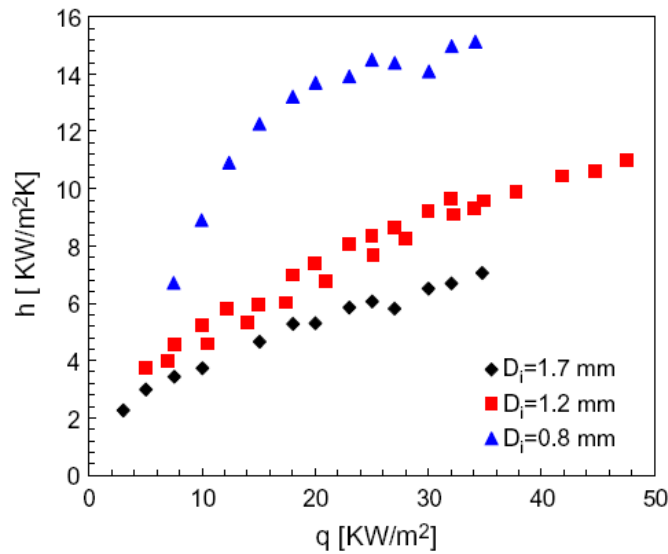


Figure 2.12: Flow boiling results of Ohwaib et al. [8] for R134a at $T_{sat}=34$ °C.

Khodabandeh [9] conducted flow boiling experiments with isobutane in multichannel evaporators with hydraulic diameters of 1.10, 1.50, 1.90, 2.50 and 3.50 mm to investigate the effects of channel size, fluid properties, surface wall structures, heat flux, system pressure, mass flux and channel length on the heat transfer coefficient in a thermosyphon loop. From his experimental database, no clear trend on the influence of tube diameter on heat transfer coefficient can be seen. Thus, the author hypothesized that the influence of channel diameter on heat transfer is small or negligible as long as nucleate boiling remains the dominant mechanism and a weak dependency of heat transfer coefficient on vapor quality and mass flux is observed. The heat transfer coefficient is also observed to increase with increasing system pressure and confirms the findings of other researchers. The reported flow boiling heat transfer results for the various channel diameters is illustrated in Fig. (2.13).

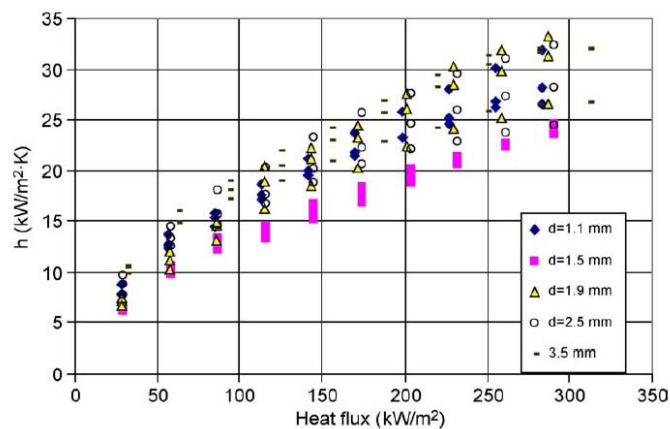


Figure 2.13: Experimental boiling heat transfer of Isobutane by Khobandeh [9].

Fig. (2.14) shows the experimental flow boiling results of Saitoh et al. [66] for R134a in a horizontal channel with internal diameters of 0.51, 1.12 and 3.10 mm channels. From their results, all three channels showed strong effects of heat flux signifying the dominance of nucleate boiling as concluded by the authors. On the issue of forced convective boiling, the authors observed that the 3.10 mm channel exhibits the strongest effect of mass flux on the heat transfer coefficient as compared with the 1.10 mm channel while surprisingly less significant effect exist on mass flux for the 0.51 mm channel. The onset of dryout is also observed to occur earlier in the lower vapor quality region with decreasing channel diameter. The authors then established the conclusion that convective boiling dominance effectively decreases with decreasing channel diameter.

Similar experiments were conducted by Consolini [10] on stable two-phase micro-channel flows for R134a, R236fa and R245fa in a single microchannel with 0.51 and 0.79 mm internal diameters. The tests gave clear indications as to the different parameters that govern the heat transfer process in these small scale channels. The heat transfer coefficients for R134a and R236fa have shown a stronger dependency on heat flux compared to R245fa which exhibits higher surface tension characteristics. At low vapor qualities, the heat transfer coefficients are heat flux dependent but diminishes at the higher vapor qualities converging monotonically at higher vapor quality regions. The heat transfer results are shown in Fig. (2.15).

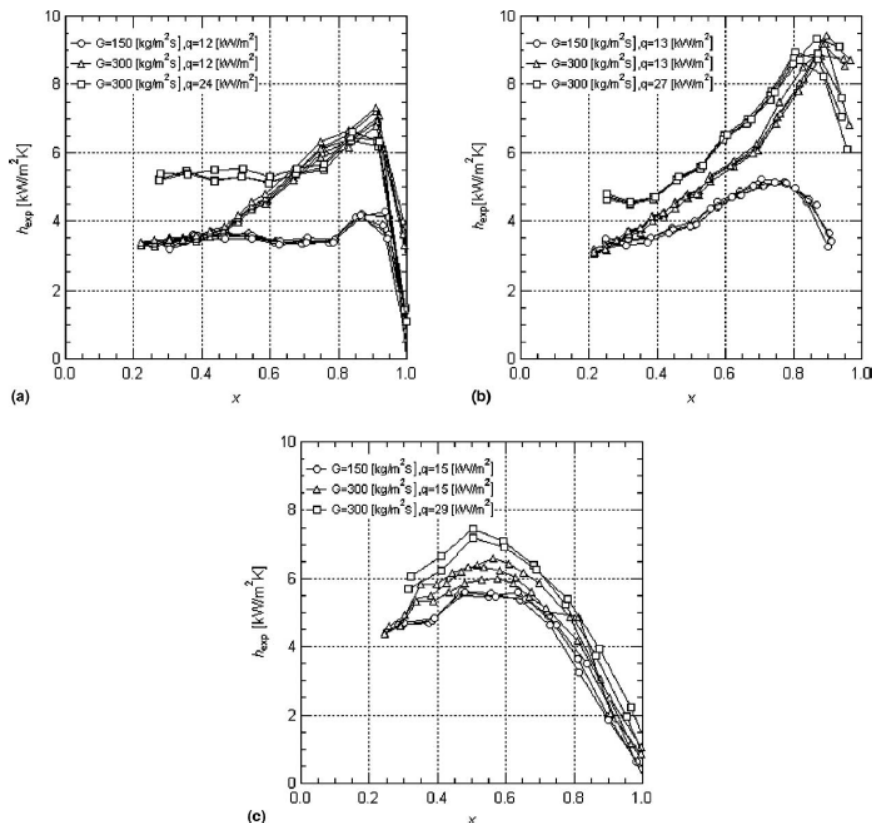


Figure 2.14: Heat and mass flux effects on the heat transfer coefficient for R134a in a: (a) $D_{in}=3.10 \text{ mm}$, (b) $D_{in}=1.12 \text{ mm}$ and (c) $D_{in}=0.51 \text{ mm}$ channel.

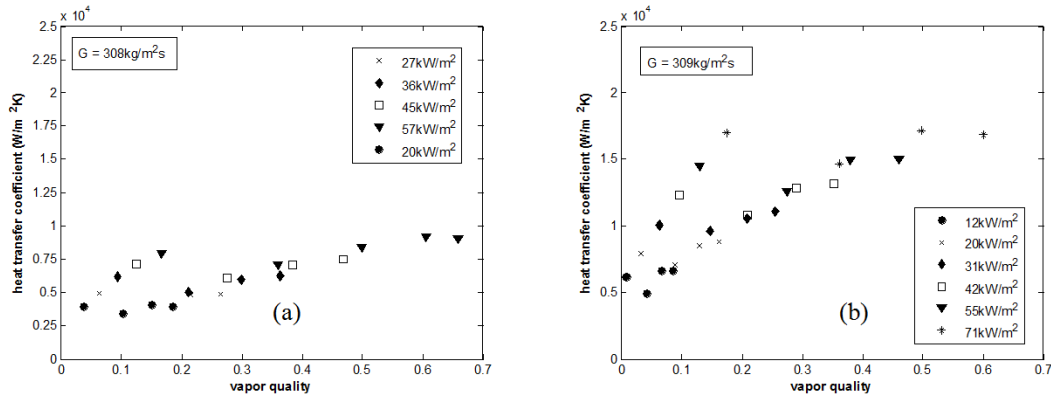


Figure 2.15: Heat transfer results comparison of Consolini [10] for (a) R236fa and (b) R134a in the 0.51 mm channel at $T_{sat}=31 \text{ }^\circ\text{C}$ with $\Delta T_{sub}=2 \text{ K}$.

Review Summary

In summary, all the experimental work reviewed here showed significant effects of heat flux on the heat transfer coefficient while the influence of forced convective boiling on heat transfer is reported to be insignificant in small scale confined channels except for the experimental results obtained by Lin et al. [6]. The increasing heat transfer trend in the annular flow regime suggests that forced convection might still be dominant in confined channels. On the other hand, there is no universal agreement among the researchers reviewed here regarding the effect of channel size on the heat transfer coefficient, i.e. when do these trends change from macroscale to microscale?. However, a tentative conclusion can be drawn on the dryout phenomena occurring at earlier vapor qualities when confinement increases. The experimental data of Consolini [10] under stable two-phase microchannel flows indicated the importance of the fluid properties on the flow boiling heat transfer process in confined microscale channels. The heat transfer mechanisms in microchannels are typically assumed to be similar to those in macrochannels, with the exception of the appearance of the thin film evaporation mechanism of Jacobi and Thome [52]. Furthermore, extrapolation of macroscale flow boiling methods to microscale has been shown to not be very accurate.

2.4 Two-Phase Flow Patterns

Due to significant observed differences between the macroscale and microscale phase change phenomena, it has been conclusively shown that applying or extrapolating two-phase macroscale methods in heat transfer and flow maps to the microscale as *'unrealistic'*. In transiting from macroscale to microscale flows, gravity dominance is successively overcome by surface tension forces and thus result in the gradual suppression of certain macroscale flow regime. Two-phase flow pattern transitions do not occur abruptly but in a gradual manner due to diminishing gravity forces when channel size decreases. While

gravity plays an important role in the macroscale, it has less effect in the microscale due to the contrasting effects of surface tension. Evidently, the gradual suppression of one macroscale flow regime (stratified flow) and the convergence of the intermittent flow regime (slug, plug and stratified wavy) into the elongated bubble regime in microscale supports the idea of a macro-microscale transition in between. The state-of-the-art review of two-phase flow patterns and flow patterns maps occurring in macroscale and microscale channels is presented in the following sub-sections.

2.4.1 Macroscale Two-Phase Flow and Flow Maps

In general, the type of two-phase flow pattern observed in a channel depends on the respective distribution of the different phases taking a particular configuration. Distinguishing criteria, such as the relative importance of various forces, e.g. inertia, viscosity, buoyancy and surface tension effects, all play an important role concerning the motion of the liquid and vapor phases flowing in the conduit. A schematic of evaporative flow patterns occurring in a horizontal tube is illustrated in Fig. (2.16).

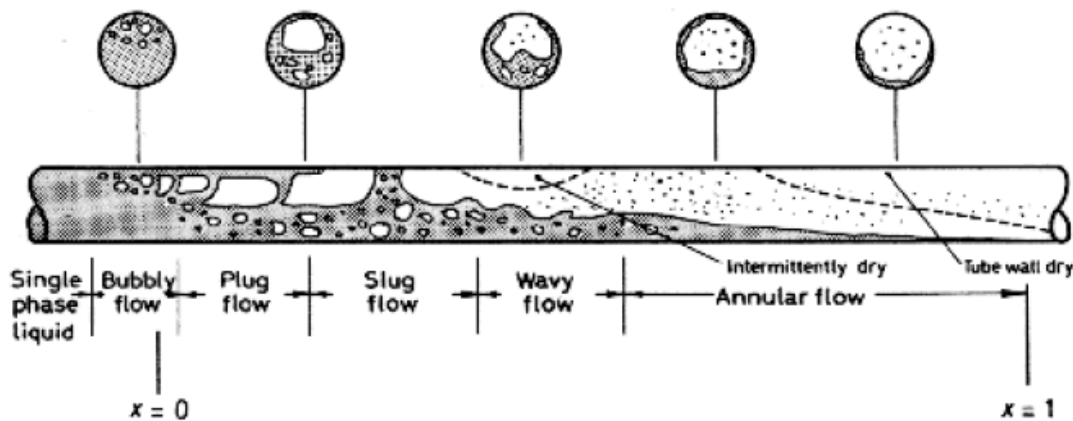


Figure 2.16: Illustration of the sequence of two-phase flow patterns during evaporation from Collier and Thome [11].

Numerous studies concerning two-phase flow patterns in macroscale channels have been published to date. The studies of two-phase flow pattern transitions have led to various developments of flow pattern prediction maps occurring during diabatic and adiabatic flow conditions in large channels. These include the adiabatic flow maps proposed by Hewitt et al. [67], Baker [68], Taitel et al. [69] and diabatic flow pattern maps proposed by Sato et al. [12], Kattan et al. [4] and Wojtan et al. [13].

Sato et al. [12, 70] for example investigated saturated flow boiling of water in a vertical rectangular cross section of internal diameter $15 \times 10 \text{ mm}$ and with a heated length of 1000 mm . From their experimental observations, the flow patterns are classified into bubbly, slug, slug–annular, annular and annular–bubbly flow. The authors arrived at a general conclusion that the flow pattern transitions occur at lower quality as heat flux, mass flux or the heated length increases. They explained that the reason for such

transitions are qualitatively related to the bubble coalescence process and the effect of the subcooled void being more pronounced than that of the saturated boiling length at higher mass flux. The authors also concluded that flow pattern transitions occur faster for smaller channels namely because the bubbles fill easier the channel and thus transition occurs faster. Such tendency is perhaps obvious since the given heat per unit mass flow per unit time $4qL/GD$ becomes larger and the amount of vapor generated increases for smaller channels. Fig. (2.17) shows the flow pattern data of Sato et al. [12] for water with transitions lines included.

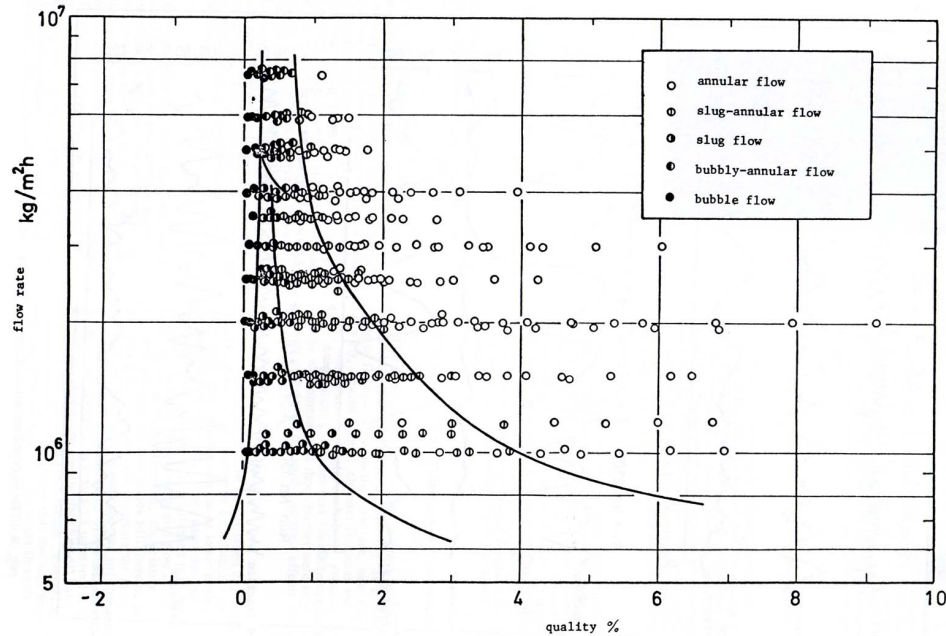


Figure 2.17: Diabatic flow pattern map for flow boiling of water in a $15 \times 10 \text{ mm}$ channel from Sato et al. [12] showing the transition lines.

Fig. (2.18) illustrates the flow pattern map proposed by Wojtan et al. [13] for evaporative flows in horizontal channels. From experimental measurements and trends observed in the dynamic void fraction, the stratified-wavy region has been modified from the Kattan et al. [4] flow map and subdivided into three zones: slug, slug/stratified-wavy and stratified-wavy. The intermittent-annular flow transition line has also been adjusted for vapor qualities below x_{IA} . The authors claimed that these modifications provided a more accurate prediction of the flow regimes below G_{wavy} and significantly improved the identification of the inception of the dryout phenomenon.

2.4.2 Microscale Two-Phase Flow and Flow Maps

This section presents a brief review emphasizing the numerous mini and microscale adiabatic and diabatic two-phase flow pattern studies to date. For simplicity reasons, only selected representative studies involving miniscale(mesoscale) and microscale flow patterns will be discussed. Kawaji et al. [14] presented a comparative review of adiabatic two-phase

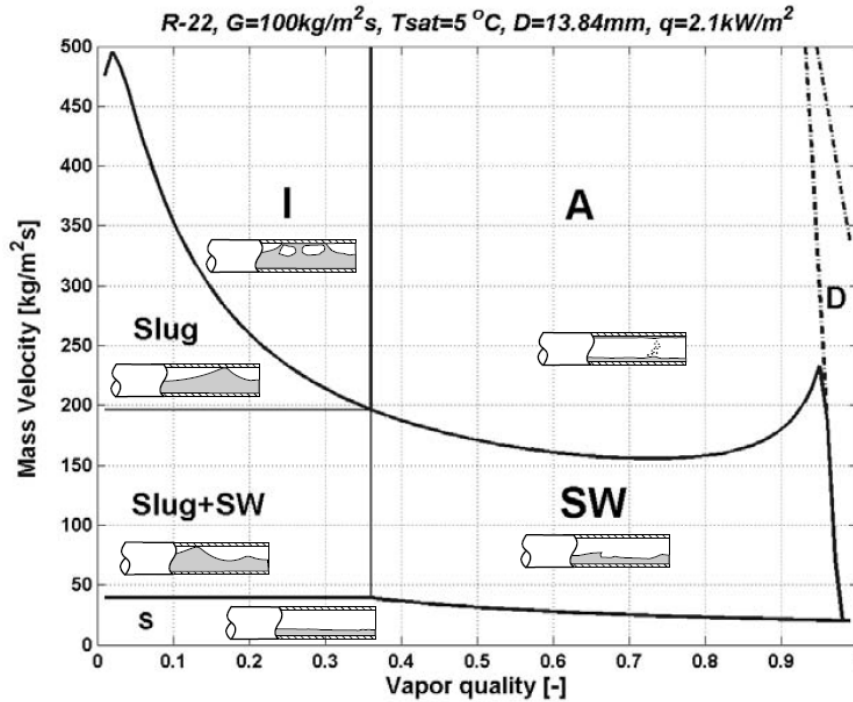


Figure 2.18: Flow pattern map of Wojtan et al. [13] for R22 in the 13.84 mm channel at $T_{sat}=5\text{ }^{\circ}\text{C}$ and $G=100\text{ kg/m}^2\text{s}$.

flow patterns and suggested that two-phase flows in macrochannels and minichannels appear to exhibit morphological similarity. The author's judgement is based on the work done by Triplett et al. [50], Damianides et al. [71] and Fukano et al. [72]. Reviewing the work done by Serizawa et al. [73], Kawahara et al. [74] and Chung et al. [75], the author then pointed out the significant difference in the observed two-phase flow patterns unique to microchannels. Schematics of minichannel and microchannel flow are illustrated in Fig. (2.19). Here the use of the term "minichannels" is loosely given to flows thought to be in the transition state between macroscale and microscale flow.

The pioneering work of Suo [15] involving gas-liquid two-phase flow pattern observations in capillary tubes provided the first insight of the two-phase distribution in microscale channels. The author conducted adiabatic two-phase experiments with air–water, water–nitrogen and N_2 –heptane with nitrogen in channels with internal diameters of 1.03 and 1.60 mm for capillary numbers of $Ca=0 - 0.04$. They concluded from their experimental observations that only three distinct flow patterns can be identified : bubbly–slug, slug and annular flow. The flow pattern map proposed by Suo [15] as a function of capillary number, Ca and volumetric quality is shown in Fig. (2.20).

A two-phase flow pattern study under microgravity conditions by Zhao et al. [76], Rezkallah [77] and then later by Lowe et al. [78] concerned a 9.525 mm diameter channel. The authors proposed a two-phase flow transition model for channels under microgravity conditions based on various Weber numbers. The authors argued that inertia and surface tension forces are the dominant forces as opposed to buoyancy for microgravity flows and

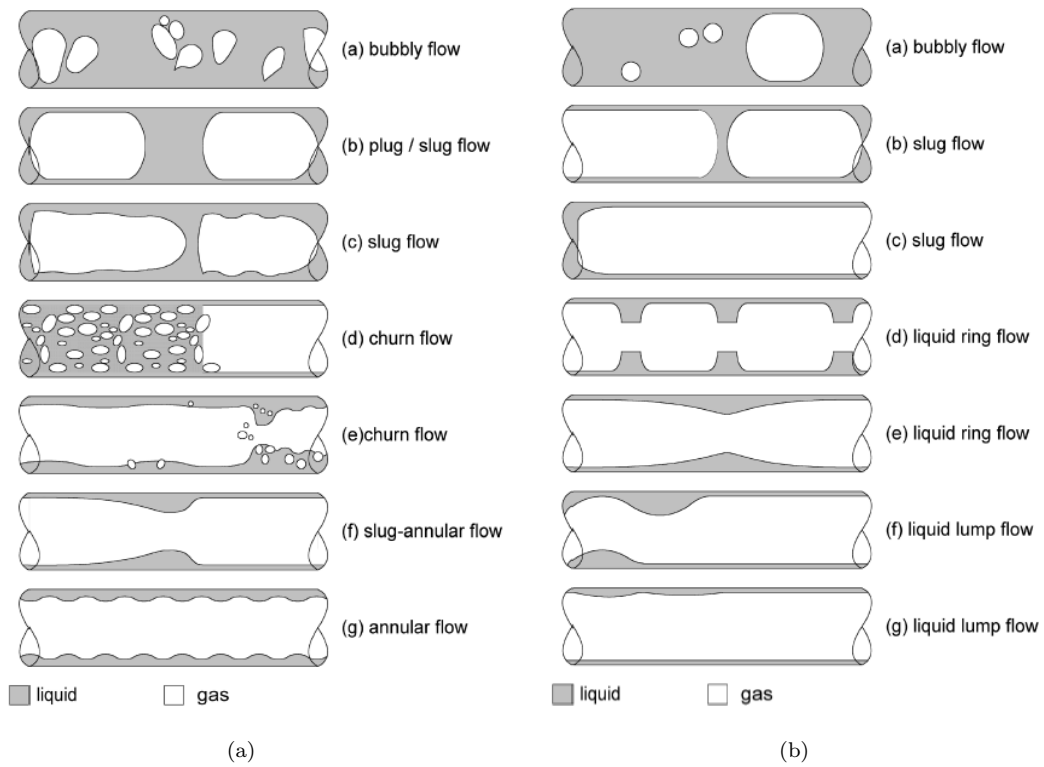


Figure 2.19: Illustration of the two-phase flow regimes from Kawaji et al. [14]; (a) Minichannel flow patterns and (b) Microchannel flow patterns.

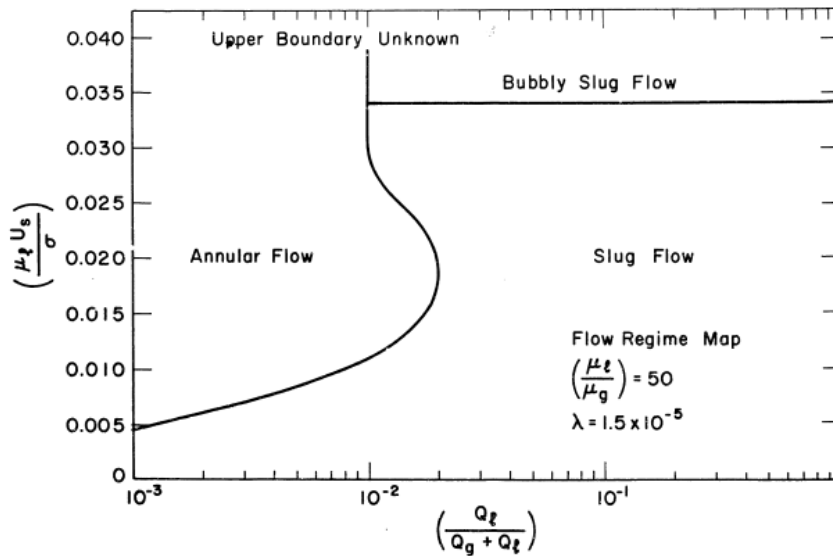


Figure 2.20: Flow pattern map of Suo [15].

thus used these new Weber numbers for the correlation of the flow regime transitions. The proposed flow pattern map can be divided into three distinct zones, namely the sur-

face tension dominated zones such as the bubbly and slug regimes, an inertia dominated zone corresponding to the annular flow regime and a transition zone when both surface tension and inertia forces exhibit comparable dominance.

Triplett et al. [50,79] investigated gas-liquid two-phase flow in circular and semi-triangular cross section channels and proposed a graphical flow pattern map in terms of superficial velocities. Five flow patterns were identified in their experiments : bubbly, slug, churn, slug–annular and annular flows. The authors then compared their flow pattern map against those of Suo [15] and Taitel et al. [69] (a macroscale map) with little success but obtained better agreement when compared to experimental flow pattern maps of Damianides et al. [71] and Fukano et al. [72].

Based on available adiabatic experimental flow pattern transition data, Akbar et al. [16] examined the feasibility of a Weber number based flow pattern map following the methodology adopted by Lowe et al. [78] and Rezkallah [77]. The authors then proposed a flow pattern map that is divided into four zones, namely surface tension dominated, annular, froth and transition boundary zone. The recommended flow pattern transition lines are represented by the following expressions:

1. The surface tension dominated zone:
by $We_{LS} \leq 3.0$ and $We_{GS} \leq 0.11We_{LS}^{0.315}$
by $We_{LS} > 3.0$ and $We_{GS} \leq 1.0$
2. Annular flow (inertia dominated zone 1):
by $We_{LS} \geq 11We_{LS}^{0.14}$ and $We_{GS} \leq 3.0$
3. Dispersed flow (inertia dominated zone 2):
by $We_{LS} > 3.0$ and $We_{GS} > 1.0$
4. Transition zone (remaining space)

Fig. (2.21) illustrates the comparison of numerous flow pattern maps proposed by researchers discussed earlier. The graph shows a general qualitative trend of a agreement between the various map but a significant quantitative difference (remembering that the maps are on a log–log scale). Also, they concluded that non-circular channels with sharp corners might support somewhat different flow regimes and transition boundaries as compared to near circular channels thus signifying the effects of channel shapes on flow regime transitions.

Chen et al. [17] studied flow boiling heat transfer with R134a as the working fluid in a vertical channel with 1.10, 2.01, 2.88 and 4.26 mm inner diameters for a pressure range of 6–14.0 bar for different mass fluxes. From their experimental observations, the flow patterns in the 2.80 and 4.26 mm channel did not exhibit common flow characteristics encountered in small tubes. However, the 1.10 mm channel did show small scale flow characteristics as reported in previous studies. The authors also arrived at the conclusion

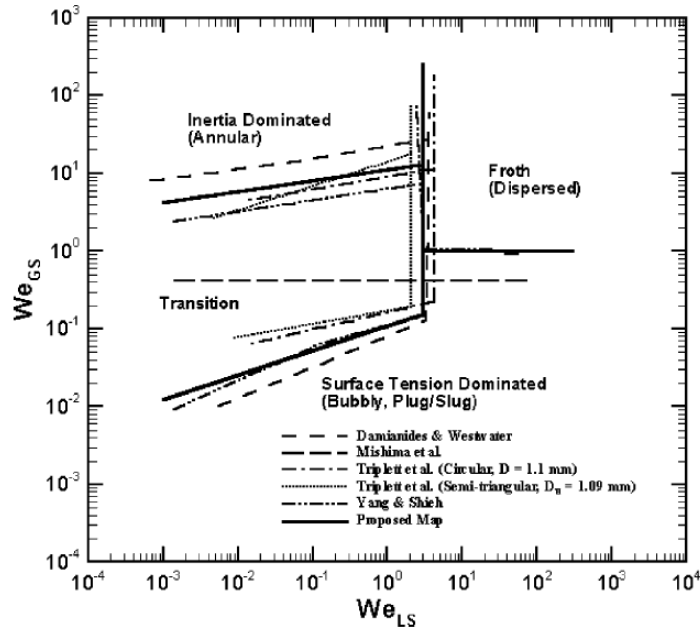


Figure 2.21: Flow pattern map comparison for circular and near-circular channels with $D_h \leq 1$ mm from Akbar et al. [16].

that the transition boundaries of slug/churn and churn/annular flow shifts to higher vapor qualities when channel diameter decreases. The flow transition boundaries for slug/churn and churn/annular have also been observed to shift significantly to lower vapor qualities as the mass flux increases, thus signifying the dependence of mass flux on flow regime transitions. The study of Chen et al. [17] on the effect of channel diameter on flow pattern transitions is thus in full contradiction with the results obtained from the condensation study of Coleman et al. [80] and the flow evaporation study of Revellin et al. [24] for R134a and R245fa in a 0.5 and 0.8 mm channel. Notably, the current experimental flow patterns obtained and presented later in this thesis for the 1.03 mm channel, presented also in Ong et al. [81] showed an expansion of the annular flow regime when channel confinement increases, and not a decrease. Thus, nearly all small channel studies point to an increased dominance of the annular flow regime at the expense of the others.

The flow regimes observed in the current experiments for the 1.03 mm channel are bubbly flow with buoyancy effects, elongated bubble (slug) flow, churn, annular, and mist flow at very high vapor qualities. No stratified flows were observed. On the other hand, the CB/Annular transition of Revellin et al. [24] developed mainly for R134a did not work as well for the fluids R236fa and R245fa as their map was only based on mass flux above $G = 350$ kg/m². Based on this new larger database for these three fluids in diameters for 0.509 to 1.030 mm channels, their IB/CB and CB/Annular transition expression has been modified to account for the effects of reduced pressure of these two refrigerants to this larger channel. A simulation of the newly proposed IB/CB transition lines for R134a and R236fa with internal diameters of 0.50, 0.80 and 1.03 mm is presented in Fig. (2.23).

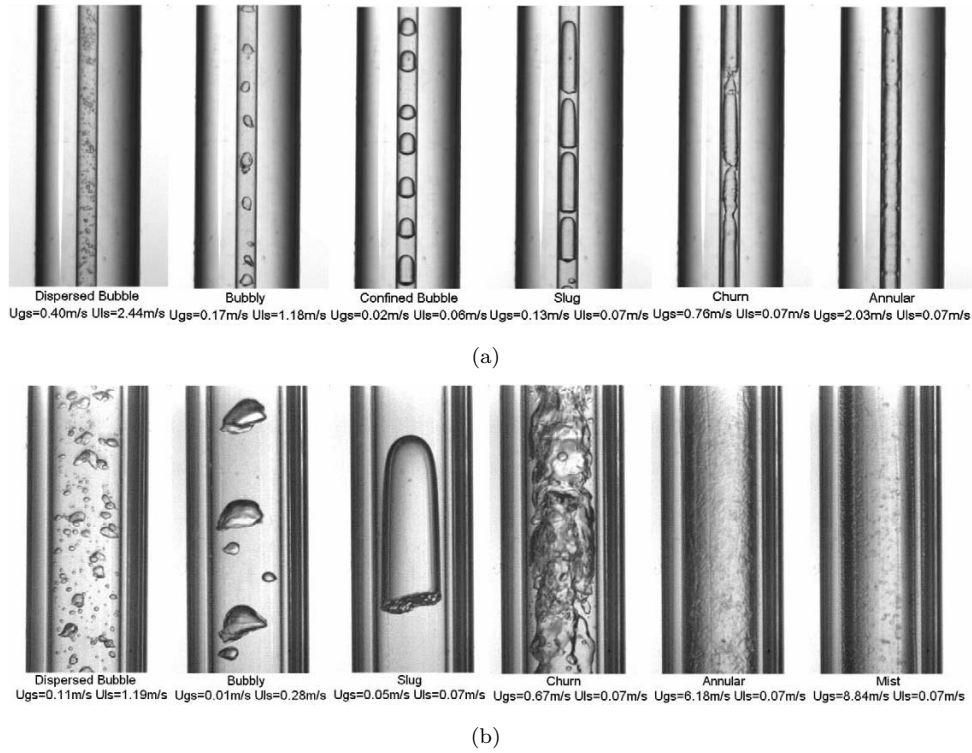
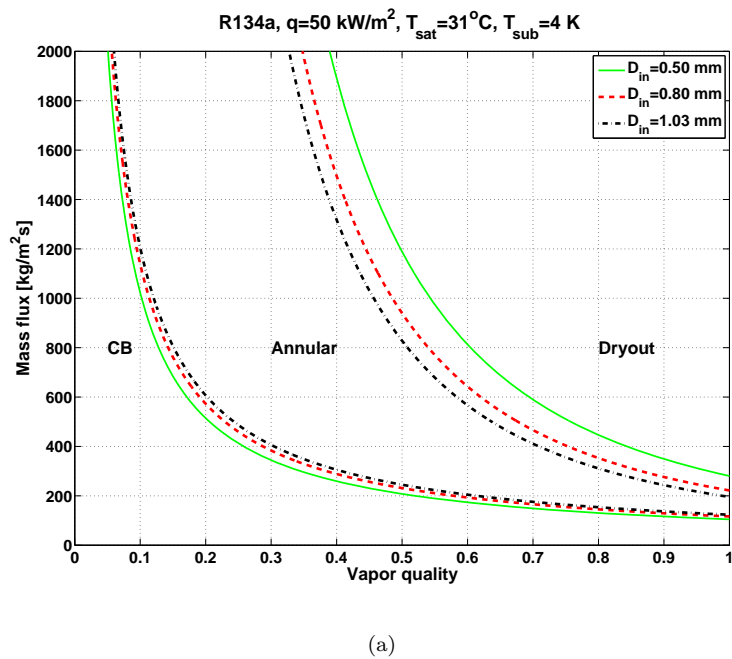
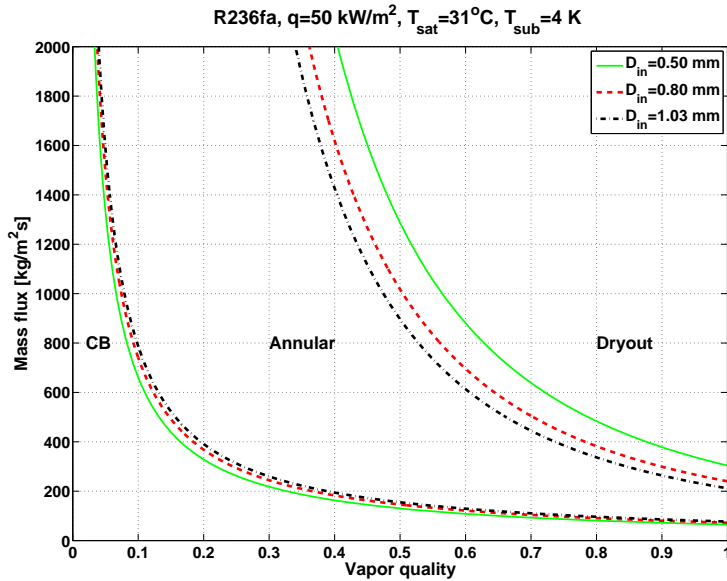


Figure 2.22: Vertical two-phase flow regimes from Chen et al. [17] at 10 bar for the (a) 1.10 mm and (b) 4.26 mm channel.





(b)

Figure 2.23: Flow pattern map simulation for $q=10.0\text{ kW/m}^2$, $T_{\text{sat}}=31\text{ }^\circ\text{C}$ with $T_{\text{sub}}=4\text{ K}$ for (a) R134a and (b) R236fa.

Review Summary

In summary, two-phase flow regimes for macroscale, miniscale and microscale have been observed and analyzed. It is clear from the studies of all the researchers discussed earlier that the dominance of surface tension forces is more important in small scale channels, gradually suppressing the gravity forces when channel size decreases. The fluid properties also play an important role in the flow pattern transitions from one regime to another as illustrated in Fig. (2.23). The suppression of the stratified flow regime and the convergence of the macroscale intermittent flow regime into the elongated bubble flow regime in microscale supports the idea of a macro-microscale transition in between. In 'true' microchannel flow, the isolated and coalescing bubble regime is therefore gradually suppressed, such as the annular flow region that spans over an ever wider range of vapor quality before reaching the onset of dryout.

2.5 Two-Phase Pressure Drops

This section presents and discusses the experimental investigations on the variation of frictional two-phase pressure drop as a function of mass flux, channel diameter, heated length and saturation pressure. Bergles et al. [82] performed experimental flow boiling tests with water to identify the importance of parameters affecting pressure drop in small channels during highly subcooled boiling. The experimental results indicated that the two-phase pressure drop is highly dependent on mass flux, the heated length, saturation pressure and inlet subcooling. The authors then concluded that the two-phase pressure

drop is directly proportional to mass flux and heated length but inversely proportional to the tube diameter.

Revellin et al. [18], on the other hand performed adiabatic two-phase pressure drop measurements for R134a and R245fa in a single microchannel of internal diameters, $D_{in}=0.509$ and 0.790 mm. From their experimental observations, the authors concluded that the two-phase pressure drop is inversely proportional to channel diameter and is directly proportional to mass velocity. The frictional two-phase pressure drop was also observed to decrease with saturation temperature. Finally, the authors concluded that the refrigerant properties play an important role on the two-phase frictional pressure drop, with R245fa registering a higher frictional pressure drop in comparison with R134a. The high relative liquid-vapor phase density difference for R245fa together with the combined effect of this fluids high viscosity explains the higher two-phase frictional pressure drop observed for this fluid.

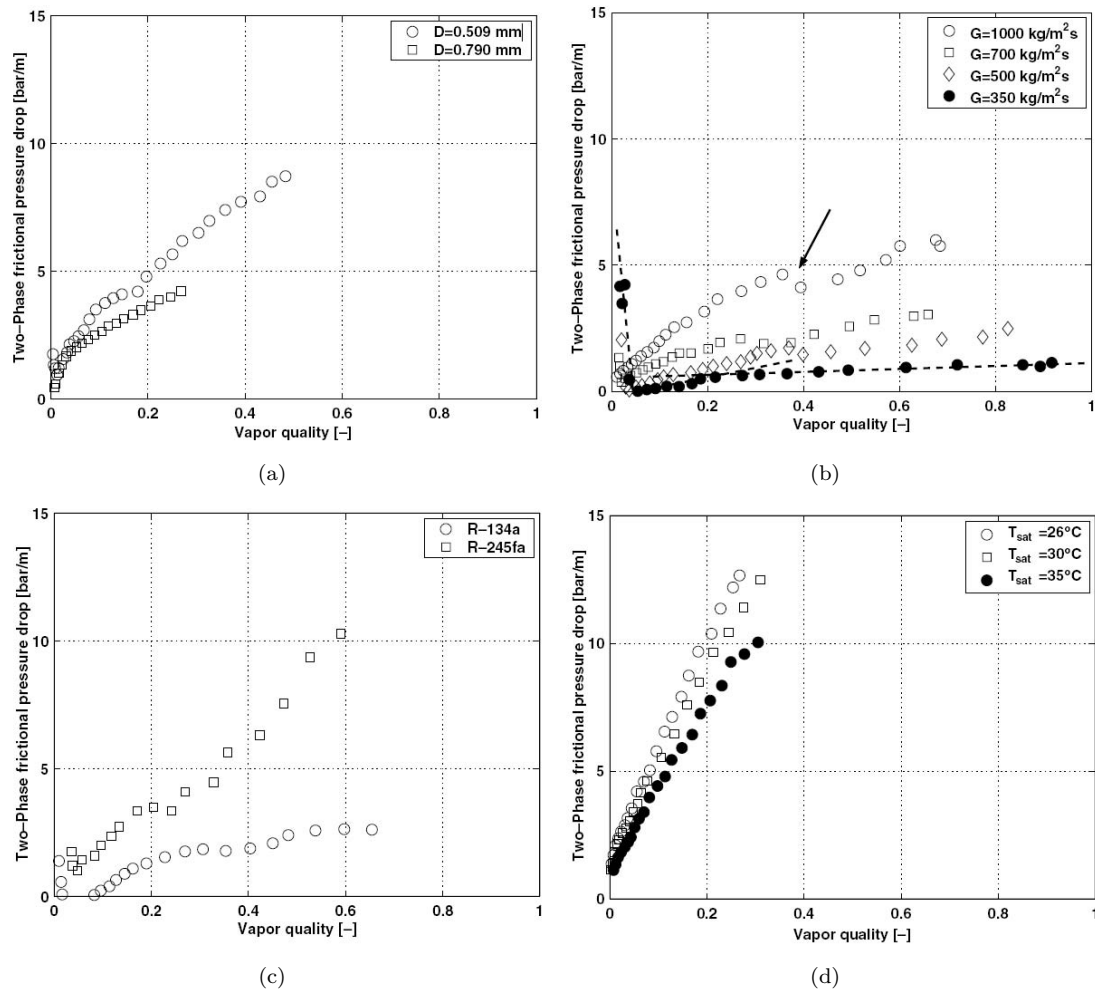


Figure 2.24: Experimental adiabatic two-phase pressure drop data of Revellin et al. [18] as a function of: (a) channel diameter, (b) mass velocity, (c) fluid properties and (d) saturation temperature.

Pehlivan et al. [83] also investigated two-phase pressure drops and two-phase flow characteristics of air/water in a single channel with diameters of 0.80, 1.00 and 3.00 *mm*. Their pressure drop data were compared to prediction methods available in literature and the authors concluded that the homogeneous [11] and Chisholm [84] method best predicted their 0.80 and 1.00 *mm* data. The authors explained that their measurement errors increased as the channel diameter decreased, leading to the conclusion that comparisons with the homogeneous model lose its accuracy. This view is supported by Kandlikar [85] who proposed that more accurate flow boiling pressure drop data as a function of quality, heat flux, mass flux and various channel dimensions are required to establish a clear indication of two-phase pressure drops in mini and microscale channels.

The flow boiling pressure drop data of Tran et al. [86] for three refrigerants R134a, R12 and R113 in two round tubes of diameter 2.46 and 2.92 *mm* showed that two-phase pressure drops increased with mass flux but decreased with increasing saturation. However, the results were not successfully predicted by state-of-the-art correlations available in literature. They suggested the reason for the failure of conventional channel correlations for their data as mainly due to the different flow behavior in these small channels. The coalesced bubbles are confined, elongated and slide over the thin film with additional friction as they flow downstream as opposed in large tube flows where the bubbles grow and flow along the tube without restrictions. The authors then proposed a new correlation for two-phase frictional pressure drop that takes into account the effects of surface tension and channel size. They claimed that the correlation is valid for smooth channels for up to channel diameters of 3.00 *mm* for their refrigerants tested. Quibén et al. [87] proposed the development of a new phenomenological two-phase pressure drop model based on the local flow patterns using the Wojtan et al. [13] flow pattern map. Revellin et al. [88] compared experimental frictional pressure drop database for smooth tubes from literature and claimed that the model of Quibén et al. [87] and Grönnerud et al. [89] displayed good prediction of the experimental data to within $\pm 30\%$ error band.

Review Summary

Numerous macro and microscale frictional pressure drop prediction methods have been presented to date in literature. However, no universal pressure drop prediction methods can be deemed reliable to predict two-phase pressure drops down to the microscale. A review by Ribatski et al. [90] showed that one macroscale method by Müller-Steinhagen et al. [91] and two microscale methods, namely homogeneous [11] and Mishima et al. [92] best predicted their large experimental database obtained from the literature. Our current pressure drop data for the $D_{in}=1.03, 2.20$ and 3.04 *mm* for the three refrigerants will be presented and compared with macroscale and microscale prediction methods in Chapter 6 - Two-Phase Pressure Drops.

2.6 Critical Heat Flux

The occurrence of critical heat flux, (CHF) is regarded as an undesirable condition that cause results in overheating of a heated channel wall, in this case two-phase evaporators. With progressive development in MEMs technology, the need to develop these high heat flux dissipation technologies for microelectronics have become a challenging task. This brings about the question on the effects of channel size and fluid properties on CHF.

Regarding CHF tests, Bergles et al. [19] experimentally investigated subcooled CHF for flow boiling of water in channel diameters ranging from 0.30 – 2.70 *mm* for a wide range of subcooling, mass flux, channel lengths and pressure. From the experiments, the authors discovered that CHF increased by a factor of two when channel size decreased from 2.70 *mm* to 0.30 *mm*. CHF was also found to increase with increased subcooling and mass flux in a non-linear fashion. However, CHF was found to be higher only for a heated length with $L/D \leq 10$ and weakly dependent on system pressure. Fig. (2.25) shows the experimental CHF results and CHF predictions of Bergles et al. [19].

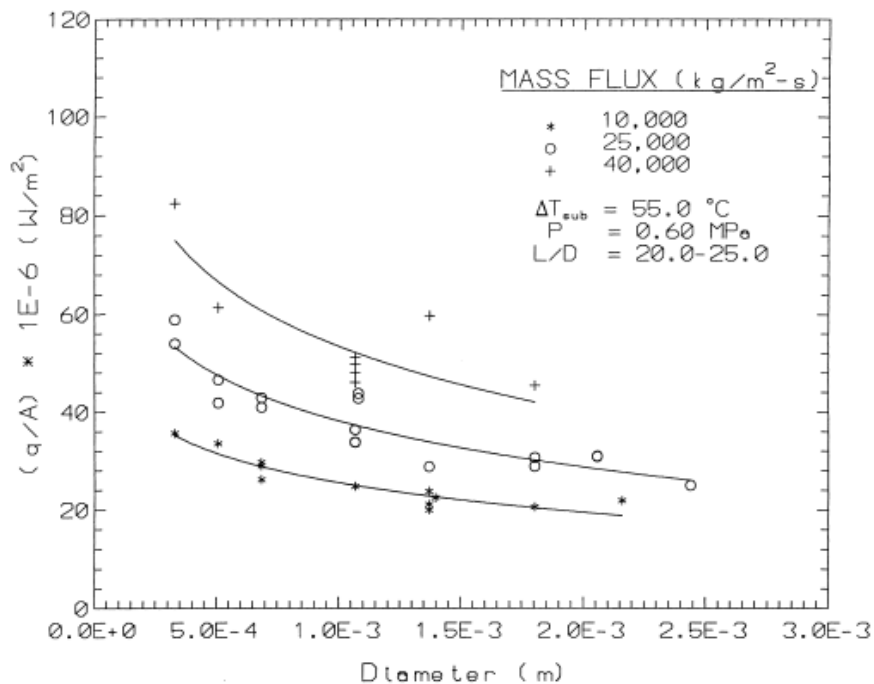
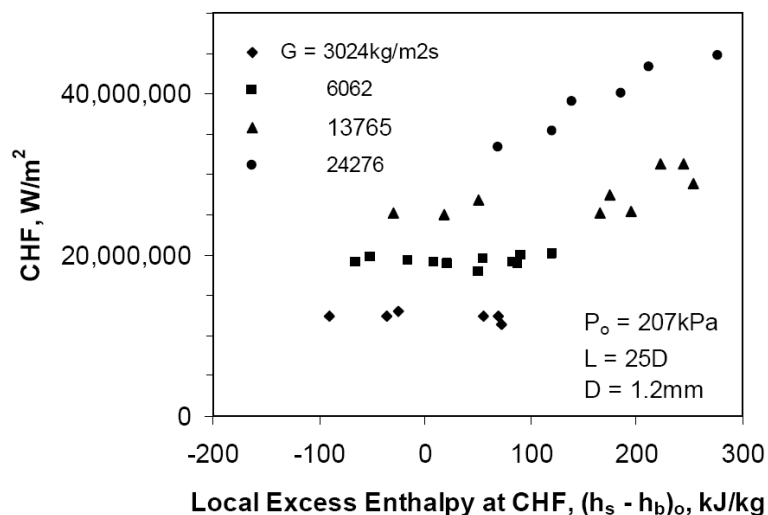


Figure 2.25: Channel diameter effect on CHF from Bergles [19].

Celata and coworkers [93,94] also studied flow boiling of water in small diameter channels and arrived at the same conclusion with increasing CHF for smaller channels. However, they also observed that the CHF value increased with channel diameter until a threshold value of $D_{in}=0.70\text{ mm}$ and then remained practically constant and independent of the channel diameter. The authors claimed that this is due to a change in the critical boiling mechanism, from liquid sublayer dryout for large channels to flooding of the vapor phase in the entire channel. This flooding phenomena means actually the bubble confinement which anticipates the CHF, which is an inverse function of the system pressure (size of the bubble).

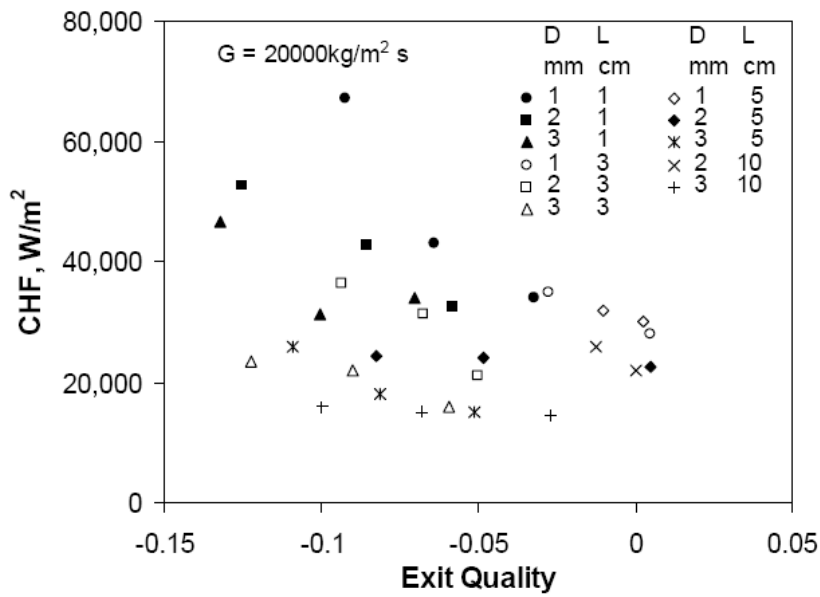
According to Bergles [21,95,96], the channel size effect on subcooled CHF is due to greater influence on the bubble boundary layer in small scale channels, notably in transition from miniscale to microscale channels. Bergles [21] concluded that as the L/D increases, the CHF decreases and becoming independent on $L/D > 30$. The author also concluded that CHF increases with decreasing channel size and with increasing mass flux, but the effect becomes less significant for tube sizes above $D_{in}=5\text{ mm}$. In miniscale channels, the bubble boundary layer occupies a larger proportion of the cross-section, reaching CHF only when the bubble boundary layer breaks down. As for microscale channels, the bubbles agglomerate and fill the channel, reaching CHF when the liquid film between the bubble and the wall ruptures. This CHF case is expected to be lower than of the boundary layer case, due to the variation in nucleation and agglomeration of the bubble. In this case, the hydrodynamic theory breaks down and this explains the attained lower CHF values while the channel gap decreases.



(a)

Figure 2.26: Effect of sub-cooling and mass velocity on CHF from Kandlikar [20] with additional data from Bergles [21].

Nariai [22] conducted experiments to study the effect of tube diameter, tube length and mass flux on CHF. The author found that CHF increases with a decrease in both the channel diameter and length. At low mass flux however, both effects disappear for suffi-



(a)

Figure 2.27: Effect of tube diameter on subcooled flow boiling CHF at high mass flux by Nariai [22].

ciently high values of length and diameter. Fig. (2.27) illustrates the experimental CHF results of Niriai [22] for water.

Roach et al. [97] experimentally studied CHF associated with flow boiling of sub-cooled water in circular tubes of channel diameter $D_{in}=1.17$ and 1.45 mm with $L/D_{in}=110$. The authors observed that CHF increased with increasing channel diameter, mass flux and pressure. Oh et al. [98], on the other hand conducted subatmospheric experiments with water in a single rectangular aluminum heated channel. The CHF results were found to increase with mass flux in an almost linear fashion. The authors also found the relation between sub-cooling and CHF to be linear although the effect was not so significant. Another researcher, Jiang et al. [43] conducted CHF studies with water in an array of grooved microchannels of hydraulic diameter of $D_h=40$ μm . The authors found that the CHF was a function of flow rate and increased linearly with an increase in the rate of flow.

Regarding saturated CHF in small channels, a number of studies have investigated the salient trends. For instance, Wojtan et al. [23] investigated saturated critical heat flux for R134a and R245f in a single, uniformly heated microchannel with channel diameters of 0.50 and 0.80 mm. The authors performed CHF tests for a wide range of conditions to investigate the effects of mass flux, heated length, fluid properties, saturation temperature and inlet subcooling. The authors observed a strong dependence of CHF on mass velocity, channel diameter and heated length with no influence of small levels of inlet liquid subcooling. In summary, the authors found the lowest CHF value for the smaller 0.50 mm channel, a higher CHF value corresponding to a shorter heated length, a slightly

higher CHF value for higher saturation temperatures at high mass velocities and concluding that R245fa exhibited a higher CHF than R134a. Some of the experimental results of Wojtan et al. [23] are depicted in Fig. (2.28).

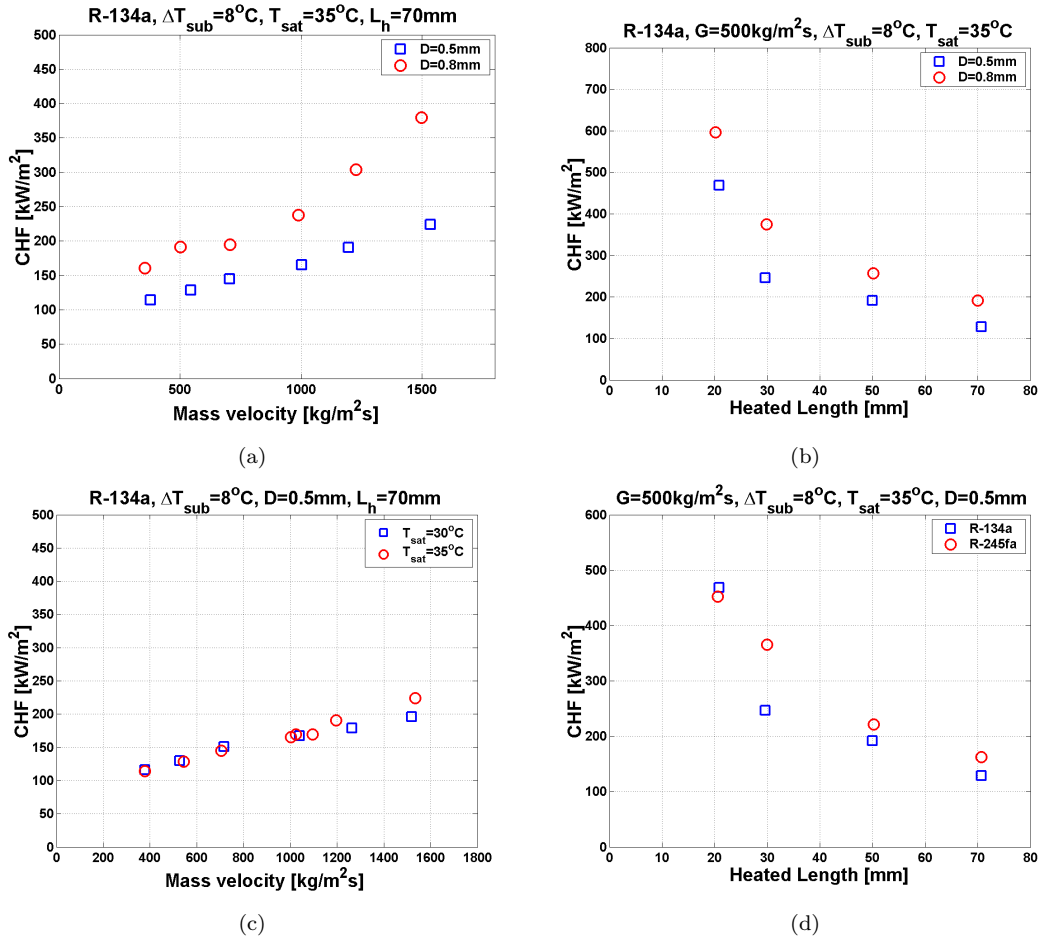


Figure 2.28: Experimental CHF data of Wojtan et al. [23], (a)Effect of channel diameter, (b)Effect of heated length, (c)Effect of saturation temperature and (d)Effect of working fluid.

Review Summary

Briefly summarizing, the subcooled CHF experimental results acquired by two independent studies showed increasing CHF value with decreasing channel diameter and increasing mass flux, Wojtan et al. [23] and others have reported decreasing CHF values with decreasing channel diameters for saturated CHF conditions. For saturated CHF, to be measured experimentally in this thesis, more data are required to investigate the macro-microscale transition to see if there is such a transition or not.

Chapter 3

Experimental Test Facility and Data Reduction Methods

This chapter describes the experimental test facility, the test section, the data reduction procedures and the instrumentation used for the present flow boiling experiments on heat transfer, diabatic and adiabatic pressure drops, optical two-phase flow characterizations, high speed two-phase flow visualizations and liquid film thickness measurements. This experimental campaign involves forced flow evaporation tests of R134a, R236fa and R245fa in circular channels of 1.03, 2.20 and 3.04 *mm* inner diameters. The present study serves to investigate the effects of channel size and fluid properties on flow boiling heat transfer, both diabatic and adiabatic pressure drops, two-phase flow patterns and an optical set-up to determine the bubble frequency, bubble velocity, bubble coalescence rate and void fraction in these minichannels. The existing microchannel test rig at LTCM has been modified from its original configuration and adapted to accommodate the new minichannel two-phase flow boiling experiments.

The experimental facility has two operational modes: (i) the reservoir mode where the flow is driven by pressure difference between the two temperature/pressure controlled reservoirs, (ii) the pump mode to drive the refrigerant flow. The mode of operation for the tests is selected based on the test condition, with the reservoir mode being used for low mass velocity runs and the pump mode at higher mass flow runs. As discussed later in the flow boiling heat transfer and two-phase pressure drop chapter, the experimental results acquired using the pump and reservoir mode showed good agreement and repeatability. The experimental data have been acquired with a data acquisition system of National Instruments. An independent LabView 7.0 interface was developed for data acquisitions and test condition regulation purposes. A detailed description of the test facility in both operation modes is presented in the next sections of this chapter.

3.1 Test Facility Description

The entire microchannel test facility consists of two reservoir tanks connected to two separate 2 *kW* series RK-20KP LAUDA thermostats, a micromotion Elite CMF010 Coriolis mass flow meter for mass flow rate measurements, a tube-in-tube heat exchanger to set

the test section inlet subcooling, a Swagelok throttle valve to ensure stable two-phase flow and mass flow regulation into the test section, a condenser, two separate Sorensen power supplies for direct current heating, a condenser, a 60 μm filter, a tube annulus heat exchanger for adequate pump inlet subcooling and a magnetic gear pump. A liquid phase sensor is located immediately upstream of the micropump and the coriolis mass flow meter to detect vapor flashing. If vapor presence is detected, the power supply to the test section and the micropump is automatically terminated to avoid equipment damage and test section burnout. As a precaution, a sight glass is installed upstream of the coriolis mass flow meter and the test section inlet for visual inspection of the flow.

3.2 The Reservoir Loop

The schematic diagram of the test rig operating in the reservoir mode is shown in Fig. (3.1). Before each test run, the pump is used to refill the refrigerant from the cold reservoir into the hot reservoir. Once the recharging procedure is completed, the two reservoirs are then isolated by closing the reservoir bypass valve and then leaving the reservoirs to equilibrate to their respective temperatures, maintained by the separate LAUDA thermostats. The hot reservoir is maintained at a higher temperature while the latter cold reservoir is maintained at a lower temperature. The pressure difference between the two reservoirs then drives the refrigerant flow from the hot reservoir through the test section and to the cold reservoir. For each increase in power input, the throttle valve and the cold reservoir temperature is re-adjusted lower to obtain the desired mass flow and set the evaporator outlet saturation condition. The reservoir mode is used for low mass and heat flux tests as it delivers the advantage of rapid stabilization of the experimental condition, i.e. flow boiling experiments in the $D_{in}=1.03\text{ mm}$ channel for $G=100-1000\text{ kg/m}^2\text{s}$ and $G=100-300\text{ kg/m}^2\text{s}$ for the $D_{in}=2.20$ and 3.04 mm channels. The pump mode of operation is selected for the remaining experimental runs, i.e. $G=1100-1500\text{ kg/m}^2\text{s}$ for the $D_{in}=1.03\text{ mm}$ channel and $G=400-1500\text{ kg/m}^2\text{s}$ for the $D_{in}=2.20$ and 3.04 mm channels.

3.3 The Pump Loop

The test facility schematic of the test facility operating in the pump mode is shown in Fig. (3.2). For the pump mode, the cold reservoir is connected to the main refrigerant loop and maintained at the required saturation condition with a LAUDA thermostat. A tube-in-tube chiller is installed at the pump inlet to ensure adequate refrigerant flow subcooling to avoid cavitation in the pump. A pump outlet bypass valve is used to regulate the refrigerant mass flow into the main test loop and to provide stable flow. The pump is fastened onto the ground using four vibration dampers to dampen the oscillations caused by the pump motor. Two vibration damping hoses are also each mounted to the inlet and outlet of the pump to further suppress any possible oscillations and thus providing the assurance of a fully stable flow. The heat exchanger before the test section is used to subcool or preheat (depending on the test conditions) the refrigerant

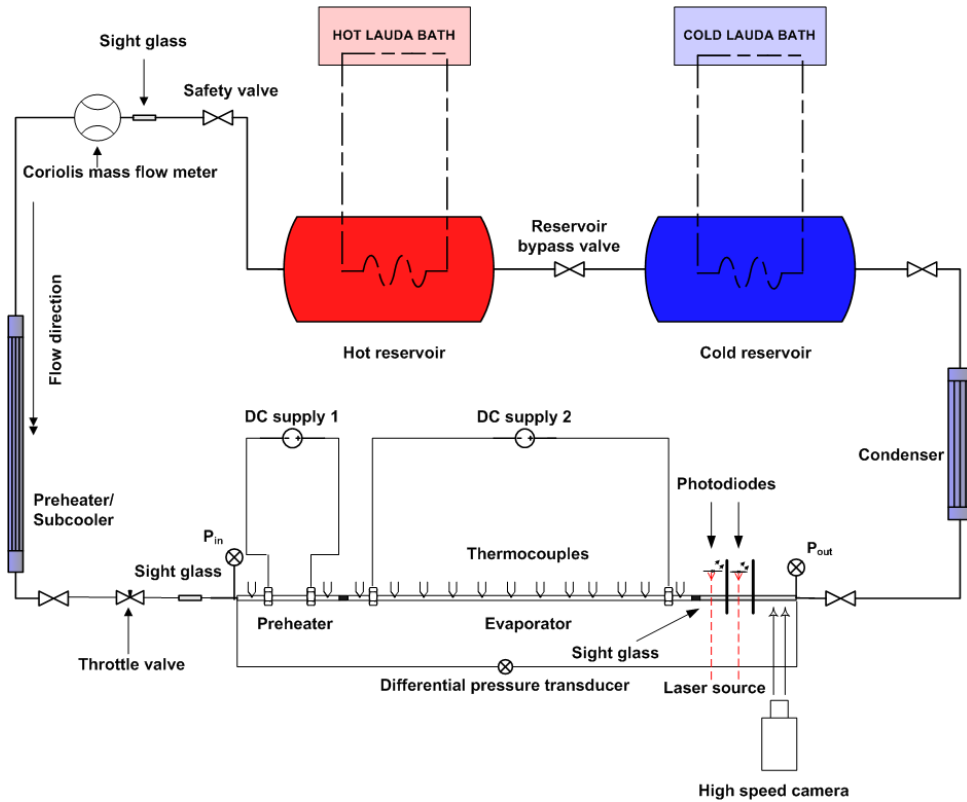


Figure 3.1: Schematic view of the experimental facility in reservoir mode.

before it enters the test section. Another test section preheater is then used to accurately regulate the degree of subcooling of the fluid entering the evaporator. Exiting the test section, the saturated liquid-vapor refrigerant flows into a condenser, where it is fully condensed and filtered before re-entering the pump. For all the tests conditions, the saturation temperature is regulated at the evaporator outlet. After each power increment to the evaporator, the saturation temperature/pressure of the cold reservoir (with a $-15\text{ }^{\circ}\text{C}$ limit) has to be reduced to compensate for the heat input. However, the cold reservoir is always maintained above atmospheric pressure to avoid any problem of air leakage into the refrigerant loop as a precaution for all conditions. For R134a at high mass flux and heat flux conditions, the cold reservoir will be gradually reduced for each gradual heat input until reaching the $-15\text{ }^{\circ}\text{C}$ limit, corresponding to a saturation pressure of 1.639 bar. However, the minimum cold reservoir temperature is higher for R236fa and R245fa due to the lower saturation pressures of these two fluids, corresponding to $0\text{ }^{\circ}\text{C}$ (1.0757 bar) and $15\text{ }^{\circ}\text{C}$ (1.0175 bar), respectively.

3.4 The Test Section

The test sections constructed for the flow boiling experiments are comprised of a preheater and an evaporator, both constructed from the same thin wall AISI 304 stainless steel tubing and a 100 mm long Borosilicate sight glass located at the channel exit for flow

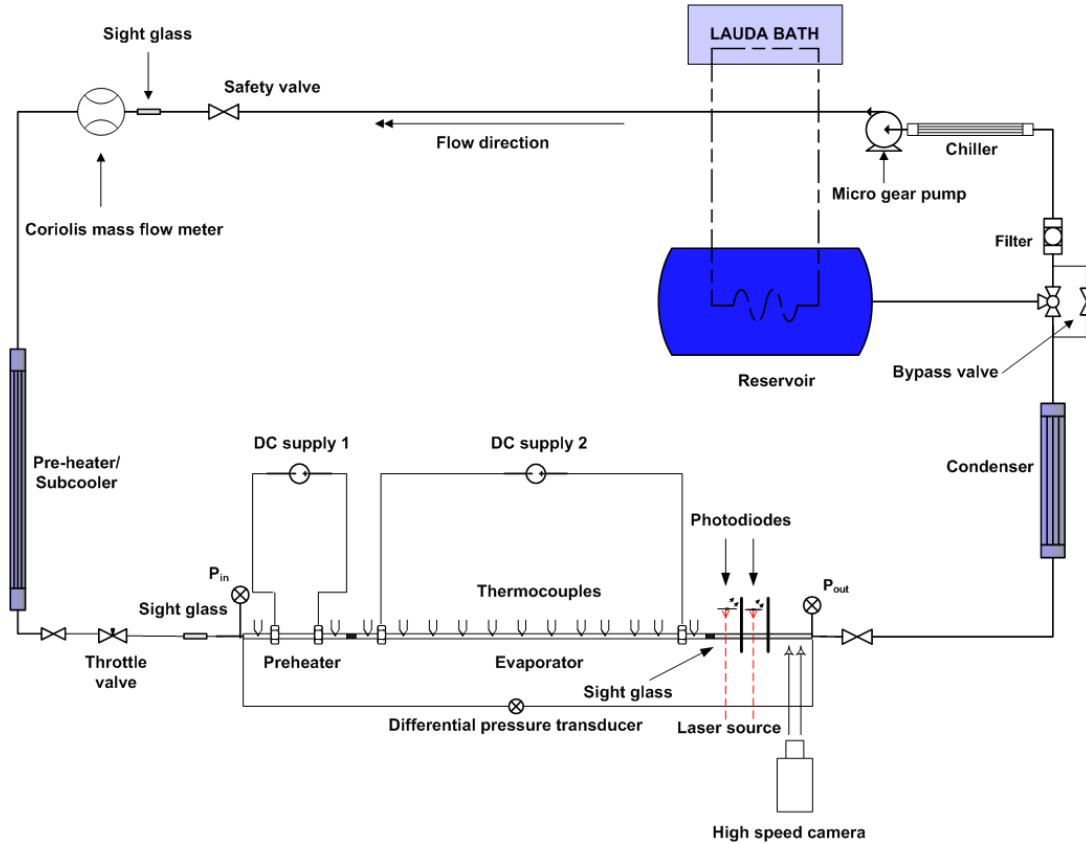


Figure 3.2: Schematic view of the experimental facility in pump mode.

visualization. The test sections are manufactured to assure precise alignment of the preheater, evaporator and the sight glass to avoid inducing a flow disturbance. Two pairs of copper electrodes are installed on the preheater and evaporator, connected to separate *Sorensen* DC power supplies for electrical heating (direct current). The heated length of the preheater is maintained at a length/diameter ratio of ≈ 50 while a ratio of ≈ 180 is used for the evaporator. The preheater section is used to regulate the degree of subcooling for the fluid entering the evaporator and to allow investigation of subcooling on flow boiling heat transfer. The sight glass located downstream of the evaporator allows adiabatic flow pattern visualizations. A 3-dimensional view of the test section is shown in Fig. (3.3) and a schematic drawing is shown in Fig. (3.4).

3.4.1 Heat Transfer Measurements

Type K $250 \mu m$ thermocouples are used for the heat transfer measurements during the experimental campaign. These thermocouples are sheathed and prevent electrical contact with the outside surface of the test sections. All thermocouples were calibrated in the lab before use. The thermocouples are wall mounted, firmly attached to the wall with small elastic O-rings for external wall temperature measurements. The size of O-rings used for fastening the thermocouples have a internal diameter of $750 \mu m$, $1.50 mm$ and $2.50 mm$ respectively. Table 3.1 gives the relevant sectional lengths. The thermocouples along the

heated channel length are positioned equally spaced apart, with 15 mm spacing for the 1.03 mm channel, 30 mm spacing for the 2.20 mm channel and 45.0 mm for the 3.04 mm channel. The first and last thermocouple are positioned at distinct positions away from the electrodes to avoid wall temperature measurements becoming affected by axial heat conduction. Additional thermocouples are attached to the wall of the adiabatic inlet and outlet of the evaporator for fluid temperature measurements. Similarly another two K-type 2 mm thermocouples are positioned at inlet and outlet of the test section, fully immersed in the liquid for direct fluid temperature measurements. One wall thermocouple is used for temperature measurement in each location for the 1.03 mm channel (at the top) while two side wall mounted thermocouples are used for 2.20 and 3.04 mm channels. Both the preheater and evaporator for all the test sections are thermally insulated by an insulating layer of Aeroflex foam fully sealed to reduce natural convection heat losses to the ambient. Single-phase experiments are performed to validate the test section and to access longitudinal conductive and natural convective heat losses (discussed later).

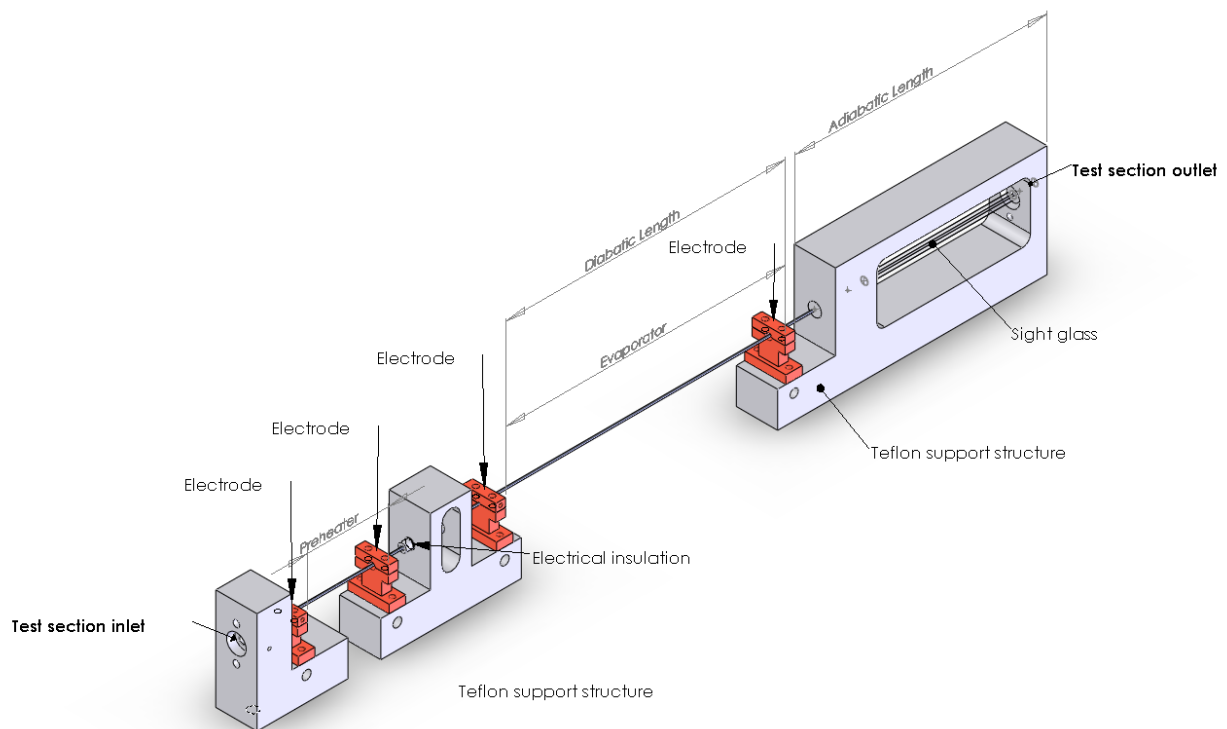


Figure 3.3: A 3-dimensional view of the test section.

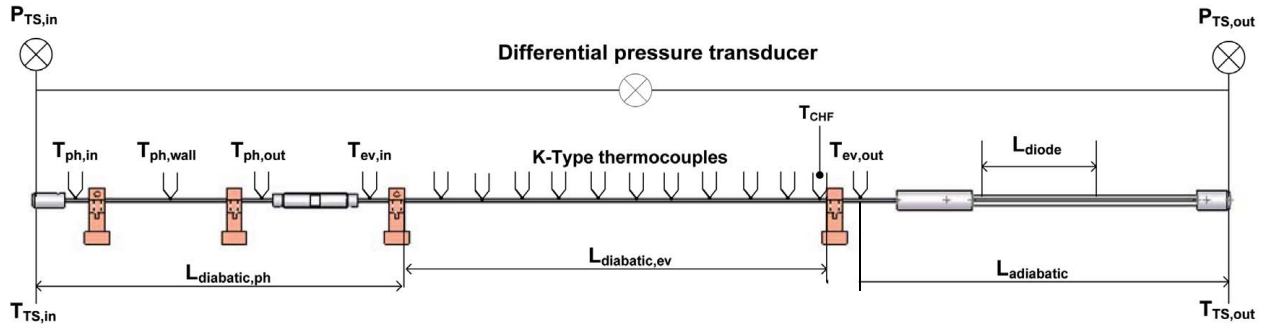


Figure 3.4: Schematic of the test section configuration with instrumentation.

3.4.2 Pressure Drop Measurements

Two calibrated *Keller* piezoelectric absolute pressure transducers *Series – 33X* with a range of 0-10 *bar* are placed at the test section inlet and outlet for saturation pressure measurements. The test section outlet pressure transducer accuracy has also been verified with the saturation value given by the test section outlet thermocouple in two-phase flows. Another *Keller* differential pressure transducer *SeriesPD – 39X* with a range of 0-5 *bar* is used to independently measure the pressure drop across the test section. The adiabatic pressure drop across the sight glass is then evaluated from the saturation temperature measurements at the evaporator outlet ($T_{ev,outlet}$) and test section outlet ($T_{TS,outlet}$). The diabatic pressure drop for the evaporator is then evaluated by subtracting the single phase pressure drop across the preheater. Refer to Fig. (3.4) for more detailed information.

3.4.3 Optical Measurement Technique

The optical measurement technique developed by Revellin et al. [99] has been implemented for objective classification of two-phase flow patterns in these channels. The setup consists of two low powered laser beams, with a power less than 1 *mW*, focused by two separate lenses utilizing two micropositioning systems. The laser beams are directed through the sight glass to two photodiodes located on the rear side of the glass channel. For two-phase flow, the refractive index difference between liquid and vapor refracts the laser beam's angle of incidence, resulting in a drop in light intensity detected by the photodiode, thus registering a lower voltage signal. The photodiodes at the opposite side of the sight glass measure the light intensity via voltage signals acquired at a scan rate of 10,000 *Hz* over 5 seconds. The laser beams and the photodiode are first calibrated in full liquid flow before initiating two-phase flow visualization. Obtaining the Probability Density Function (PDF) of the measured photodiode voltage signals in correspondence with the flow regimes enable classification of the corresponding flow patterns and their transitions. The results are discussed in further detail in Chapter 4.

3.4.4 Flow Pattern Visualization

To complement the measurements acquired with the optical technique, flow visualization videos are acquired through the use of a PHOTRON Ultima APX high speed, high resolution camera. The camera is positioned at the inlet of the sight glass to acquire flow regime videos directly at the exit of the evaporator at a rate of 4,000 to 10,000 *fps* for mist flow.

3.4.5 Critical Heat Flux

A K-type 250 μm thermocouple is positioned at the top of the channel for critical heat flux measurements, located just 1.0 *mm* from the evaporator outlet electrode. For consistency reasons, the critical heat flux (CHF) criteria used by Revellin. [100] is adopted in this current experimental campaign. The CHF criteria is assumed to be reached when the wall superheat exceeds 40 *K* during small increments in heat flux. The supplied power to the electrodes is automatically cut once the CHF criteria is reached to avoid test section burnout.

3.4.6 Film Thickness Measurement

High speed images of the flow visualization videos were acquired through the use of a PHOTRON Ultima APX high speed camera, positioned at the inlet of the sight glass. A continuous halogen light source was positioned at the rear side of the sight glass at mid-plane to provide sufficient background lighting for the high speed video acquisition. A diffusive filter paper is positioned between the light source and sight glass to diffuse the light source and to obtain a soft lighting effect. The high speed videos were acquired at a rate of 4,000 *fps* and then post processed with a MATLAB image processing code to detect the liquid-vapor bubble interface and compute the top and bottom liquid layer film thickness in terms of the number of image pixels. The image processing technique is presented later in Chapter 7.

D_{int} (<i>mm</i>)	1.03	2.20	3.04
$L_{diabatic,ph}$ (<i>mm</i>)	157.50 \pm 0.1	201.10 \pm 0.1	241.60 \pm 0.1
$L_{adiabatic}$ (<i>mm</i>)	140.5 \pm 0.1	131.30 \pm 0.1	149.50 \pm 0.1
$L_{evaporator}$ (<i>mm</i>)	180.00 \pm 0.1	381.00 \pm 0.1	540.00 \pm 0.1
L_{total} (<i>mm</i>)	478.00	713.40	931.10

Table 3.1: The test section diabatic and adiabatic lengths

3.5 Data Reduction

The following subsections describe the thermal loss assessment and the data reduction methods used in the evaluation of heat transfer and pressure drop measurements for the experimental campaign.

3.5.1 Single-Phase Validation

Single-phase experiments were carried out on each test section prior to the boiling tests to evaluate the thermal losses. The evaporator wall temperatures were kept below T_{sat} in all single-phase tests to avoid subcooled boiling in the evaporator. The heat loss is mainly due to axial conduction of heat at the inlet and outlet of the evaporator and natural convective losses of heat to the ambient along the length to the test section. The channel length was discretized into 10 individual sections to evaluate the local air-side Nusselt numbers. The total heat losses are the sum of:

$$Q_{loss} \cong Q_{convection} + Q_{conduction} \quad (3.1)$$

The local external natural convection Nusselt numbers for each section were estimated with the correlation proposed by Churchill et al. [101] while axial conduction losses were estimated by evaluating the Biot number with the in-tube convection coefficient obtained from the correlation of Gnielinski [26]. The heating efficiency, η and the axial conduction losses are estimated by:

$$\eta = 1 - \varepsilon_{conduction} - \varepsilon_{convection} \quad (3.2)$$

where

$$\varepsilon_{conduction} = \frac{Q_{conduction}}{\Delta VI} \quad (3.3)$$

$$\varepsilon_{convection} = \frac{Q_{convection}}{\Delta VI} \quad (3.4)$$

and ΔVI is the Joule heating applied electrically by DC current.

$$\varepsilon_{conduction} = \frac{2 \cosh \sqrt{Bi} - 1}{\sqrt{Bi} \sinh \sqrt{Bi}} \quad (3.5)$$

The natural convection losses are estimated by using:

$$Nu_{\infty,1} = \left\{ 0.60 + \frac{0.387 Ra_D^{1/6}}{[1 + (\frac{0.559}{Pr})^{9/16}]^{8/27}} \right\}^2 \text{ for } Ra_D \leq 10^{12} \quad (3.6)$$

where

$$Ra_D = \frac{g\beta(T_{wall,ext} - T_{\infty})T^3}{\nu\alpha} \quad (3.7)$$

$$\varepsilon_{convection} = \frac{\pi\kappa_{\infty}}{\Delta VI} \sum_{i=1}^{10} Nu_{\infty,1}(T_{wall,in} - T_{\infty})\Delta z_i \quad (3.8)$$

The fluid temperature rise across the heated length provides the heat input into the refrigerant flow, $Q_{effective}$ calculated using

$$Q_{effective} = \dot{m}C_p(T_{fluid,outlet} - T_{fluid,inlet}) \quad (3.9)$$

The measured $Q_{effective}$ is compared with the heat input ΔVI , and then readjusted to account for the predicted heat losses due to conduction and convection. This allows the estimation of the actual heat input to the fluid, $Q_{effective}$.

3.5.2 Inner Wall Temperature

The inner wall temperature $T_{wall,in}$ is back calculated from the measured wall temperature $T_{wall,out}$ with the assumption of uniform heat generation in a one-dimensional cylindrical geometry due to the electrical heating. The channel wall property is assumed to be constant with uniform volumetric heat generation and a diabatic outer wall boundary condition. The general solution for the temperature distribution in a radial system is described by:

$$T(r) = -\frac{q'''}{4\kappa}r^2 + C_1 \ln r + C_2 \quad (3.10)$$

Applying the boundary condition for the outer wall with outer radius, $r = R$ gives

$$-\kappa \frac{dT}{dr} \Big|_R = h_\infty(T_R - T_\infty) \quad (3.11)$$

Substituting the equation into the general solution, it follows that

$$-\frac{q'''}{2}R + \frac{C_1\kappa}{R} = h_\infty(T_\infty - T_R) \quad (3.12)$$

Re-arranging the equation, the constants C_1 and C_2 are rewritten as

$$C_1 = \frac{q'''}{2\kappa}R^2 + \frac{h_\infty R}{\kappa}(T_\infty - T_R) \quad (3.13)$$

$$C_2 = T_R + \frac{q'''}{4\kappa}R^2 - \left[\frac{q'''}{2\kappa}R^2 + \frac{h_\infty R}{\kappa}(T_\infty - T_R) \right] \ln R \quad (3.14)$$

The wall heat flux, q is then determined as

$$q = -\kappa \frac{dT}{dr} \Big|_{r=R} = -\frac{q'''}{2R}(R^2 - R_o^2) + \frac{h_\infty R}{R_o}(T_R - T_\infty) \quad (3.15)$$

Simplifying, it follows that

$$q = -\frac{P}{2\pi R_o L_{ev}} + \frac{h_\infty R}{R_o}(T_R - T_\infty) \quad (3.16)$$

3.5.3 Single-Phase Heat Transfer and Pressure Drop

For single-phase experiments with a uniform wall heat flux, the fluid temperature rise along the evaporator is linear and thus can be determined from the inlet and outlet fluid temperature measurements. Thus, the heat transfer coefficient for each thermocouple location is determined from Newton's law of cooling:

$$h = \frac{q}{T_{wall,in} - T_{fluid}} \quad (3.17)$$

The single-phase pressure drop across the evaporator is calculated by subtracting the total measured pressure loss with the calculated single-phase pressure drop across the preheater and the *adiabatic* sight glass.

$$\Delta P_{ev} = \Delta P_{diff} - \Delta P_{sp,ph} - \Delta P_{sp,adb} \quad (3.18)$$

As the test section is fixed in a horizontal configuration, the effect of gravitational pressure loss is nil and the general form for total single-phase pressure loss across the evaporator is evaluated as:

$$\Delta P_{ev} = \Delta P_{fr} + \Delta P_{singular} \quad (3.19)$$

with the frictional pressure drop, P_{fr} being defined as:

$$\Delta P_{fr} = -\frac{G^2}{2\rho_l} 4f \frac{L_{ev}}{D_{in}} \quad (3.20)$$

and

$$\Delta P_{sing} = -\frac{G^2}{2\rho_l} \xi \quad (3.21)$$

Rearranging the equations, the dimensionless form of the single-phase experimental pressure loss is expressed as:

$$\Delta P_{ev} \frac{2\rho_l D_{in}}{G^2 L_{ev}} = 4f + \xi \frac{D_{in}}{L_{ev}} \quad (3.22)$$

The single-phase pressure loss due to contraction and expansion at the inlet and outlet manifold is accounted for by evaluating the single-phase loss coefficient ξ in laminar flow tests, which is independent of the Re number but is a function of the geometry. Multiplying the RHS by Re , the equation becomes:

$$4f Re + \xi \frac{D_{in}}{L_{ev}} Re = a + b Re \quad (3.23)$$

where $a = 4f$ and the constant term $b = \xi \frac{D_{in}}{L_{ev}}$. The results are then plotted against Re to evaluate the singular pressure coefficient, allowing the Fanning friction factor to be evaluated. The measured experimental friction factors are then compared to correlations available from literature, which is discussed in further detail in Chapter 6.

3.5.4 Two-Phase Heat Transfer and Pressure Drop

For flow boiling experiments, the liquid refrigerant enters the evaporator in a subcooled condition with the subcooled length, L_{sat} evaluated by the following energy balance:

$$L_{sat} = \frac{\dot{m}C_p}{q\pi D_{in}} (T_{sat} - T_{fluid,inlet}) \quad (3.24)$$

The saturation pressure, P_{sat} is calculated by evaluating the single-phase pressure drop across the preheater and the subcooled length from,

$$P_{sat} = P_{TS,inlet} - \frac{G^2}{2\rho_l} 4f \frac{L_{sat} + L_{ph}}{D_{in}} \quad (3.25)$$

The local fluid temperature in the subcooled region of the evaporator is evaluated via an energy balance expressed as:

$$T_{fluid} = T_{fluid,inlet} + \frac{q\pi D_{in} L_{sat}}{\dot{m}C_p} \quad (3.26)$$

As for the saturated region, the fluid temperature is deduced from the local saturation pressure with the assumption of a linear pressure drop for $L > L_{sat}$ so that:

$$P_{sat}(L) = P_{ev,outlet} + \frac{P_{sat} - P_{ev,outlet}}{L_{sat} - L_{ev}} (L - L_{ev}) \quad (3.27)$$

and

$$T_{fluid}(L) = T_{sat}(P_{sat}(L)) \quad (3.28)$$

The thermodynamic vapor quality in the saturated region is expressed in terms of the local enthalpy where H is the local enthalpy determined through the energy balance, H_L is the specific enthalpy of the saturated liquid and H_{LV} is the latent heat of vaporization:

$$x = \frac{H - H_l}{H_{lv}} \quad (3.29)$$

The *diabatic* pressure drop consists of the single phase pressure loss for the subcooled length and the saturated length. The *diabatic* pressure drop across the evaporator is defined as

$$\Delta P_{diabatic} = P_{TS,inlet} - \frac{G^2}{2\rho_l} 4f \left(\frac{L_{ph}}{D_{in}} \right) - P_{ev,outlet} \quad (3.30)$$

while the *adiabatic* pressure drop across the sight glass is

$$\Delta P_{adiabatic} = \Delta P_{diff} - \frac{G^2}{2\rho_l} 4f \left(\frac{L_{ph}}{D_{in}} \right) - \Delta P_{diabatic} \quad (3.31)$$

3.6 Experimental Uncertainties

This section describes the various terms and the methods used in the estimation of the measurement uncertainties, the dominant source of error and the effects on the test results. As the uncertainty in a measurement has no definite value, the uncertainty in the

measured result can take on different values, depending on the terms considered. This uncertainty evaluation is referenced to the ASME Instruments and Apparatus Supplements (PTC 19.1) [102] and to the ASME Performance Test Codes in accordance with accepted practice. As the measurement consists of the combination of the true value plus the total measurement error, the total measurement uncertainty is the combination of the following two components, *systematic uncertainty* due to the uncertainty in the measuring instrument itself and *random uncertainty* introduced by variations and scatter in measurements. Hence, the sources of uncertainty in our measurement process are arbitrary classified as: (i) calibration uncertainty, (ii) data acquisition uncertainty and (iii) data reduction technique uncertainties. The estimation of uncertainty in the quantities measured is firstly determined and propagated to produce the final uncertainty in the results with propagation of errors theory. The general formula based on the first-order Taylor series expansion of functions of many variables with independent and random uncertainties $\sigma_x, \dots, \sigma_z$ is

$$\sigma_f^2 = \sigma_x^2 \left(\frac{\partial f}{\partial x} \right)^2 + \sigma_y^2 \left(\frac{\partial f}{\partial y} \right)^2 + \sigma_z^2 \left(\frac{\partial f}{\partial z} \right)^2 + \dots \quad (3.32)$$

and the total uncertainty is

$$\sigma_f \leq \sigma_x \left| \left(\frac{\partial f}{\partial x} \right) \right| + \dots + \sigma_z \left| \left(\frac{\partial f}{\partial z} \right) \right| \quad (3.33)$$

The *systematic uncertainty* of the instrumentation is discussed in further detail in the following sections.

3.6.1 Thermocouple Uncertainty

The thermocouple measurement uncertainty is estimated by considering the precision thermometer's systematic error and the standard errors from the linear least square curve fitting method. The thermocouples are calibrated with a 2 °C temperature step from 20 to 60 °C in a constant thermal LAUDA bath with a ATP 4200 precision thermometer equipped with two temperature reference probes. The calibration step is deliberately chosen to yield reasonable data points to reduce the standard errors of the calibration. All the thermocouples are connected to a NI-DAQ chassis SCXI-1000 with SCXI-1102 module slots and SCXI-1303 terminal block. The data are acquired at 5000 Hz and the temperature is taken as the mean value of one hundred samples corresponding to 0.02 s. The standard deviation was used to calculate the uncertainties in reference to Kline et al. [103] and Moffat [104, 105]. In all cases, the data are acquired only at a steady state condition, which is when the absolute mean temperature difference satisfies, $\Delta T_{mean} < 0.002 K$. The ATP 4200 precision thermometer has a reported systematic error from the manufacturer specifications of 0.01 °C for a temperature operating range from -200 °C up to +962 °C. The standard error of the thermocouples is computed by evaluating the sum of the squares of the offsets "*residuals*", R^2 , for a set of $N = 41$ calibration step points. In theory from Weisstein [106], the sum of the squares of the vertical deviations R^2 of a set of N data points from a function f is shown in Eq. (3.35). For the condition of R^2 to be a minimum, the following has to be satisfied.

$$\frac{\partial(R^2)}{\partial a_i} = 0 \quad (3.34)$$

for $i = 1, \dots, n$. And for a linear fit of $f(a, b) = a + bx$,

$$R^2(a, b) \equiv \sum_{i=1}^n [y_i - a - bx_i]^2 \quad (3.35)$$

The sum of squares are then defined as SS_{xx} , SS_{yy} and SS_{xy} :

$$SS_{xx} = \sum_{i=1}^n (x_i - \bar{x})^2 \quad (3.36)$$

$$SS_{yy} = \sum_{i=1}^n (y_i - \bar{y})^2 \quad (3.37)$$

$$SS_{xy} = \sum_{i=1}^n (x_i - \bar{x})(y_i - \bar{y}) \quad (3.38)$$

The overall quality of the fit parameterized in terms of a quantity known as the correlation coefficient, is defined as:

$$r^2 = \frac{SS_{xy}^2}{SS_{xx}SS_{yy}} \quad (3.39)$$

The *standard errors* for a and b are then defined as:

$$SE(a) = s \sqrt{\frac{1}{n} + \frac{\bar{x}^2}{SS_{xx}}} \quad (3.40)$$

$$SE(b) = \frac{s}{\sqrt{SS_{xx}}} \quad (3.41)$$

The uncertainties of the set of 26 thermocouples used for flow boiling tests are shown in 3.2.

	T1	T2	T3	T4	T5	T6	T7	T8	T9	T10	T11	T12	T13
$\delta T(K)$	0.07	0.04	0.04	0.04	0.06	0.05	0.07	0.07	0.05	0.06	0.05	0.04	0.06
	T14	T15	T16	T17	T18	T19	T20	T21	T22	T23	T24	T25	T26
$\delta T(K)$	0.06	0.06	0.05	0.07	0.07	0.07	0.07	0.07	0.04	0.03	0.06	0.02	0.05

Table 3.2: Regression error of the thermocouples used in the current experiments.

For reasons of consistency, the highest uncertainty of $\pm 0.07 K$ is used for all the thermocouples when evaluating the wall temperature measurement uncertainties. Thus, the total systematic uncertainty for wall temperature measurements is $\pm 0.08 K$ by taking into consideration of the $\pm 0.01 K$ uncertainty of the reference probes used during the calibration.

3.6.2 Data Acquisition System Uncertainty

The voltage drop through the evaporator electrodes is directly measured with the *NI-SCXI 1102* module to an accuracy of 0.035% of the reading. Thus,

$$\delta(\Delta V) = 0.00035\Delta V \quad (3.42)$$

and the current is measured directly with a non-intrusive current probe with an accuracy of

$$\delta(I) = 0.01I + 0.03 \quad (3.43)$$

3.6.3 Mass Flow Meter Uncertainty

The *Micromotion* Coriolis Mass Flow Meter (CMF010) specifies an instrument calibration accuracy of $\pm 0.044\%$ of reading as the base accuracy and a zero stability value of 5.56×10^{-7} . Thus, the measured uncertainty of the mass flow rate is defined as:

$$\frac{\delta\dot{m}}{\dot{m}} = 0.00044 + \frac{5.56 \times 10^{-7}}{\dot{m}} \quad (3.44)$$

3.6.4 Absolute and Differential Pressure Transducers

As mentioned, two absolute and one differential pressure transducer are used for pressure drop measurements. The test section inlet and outlet pressure is measured with 0-10 *bar* absolute piezoelectric pressure transducers, positioned at the test section inlet and outlet. The pressure taps are calibrated up to an accuracy of $\delta(P) = 5 \times 10^{-3}$ *bar* while the 0 - 5 *bar* differential pressure transducer used for independent pressure drop measurement presents an uncertainty of $\delta(P_{diff}) = 10 \times 10^{-3}$ *bar* obtained from the manufacturer's calibration certificate.

3.6.5 Channel Diameter and Heated Length

The stainless steel AISI 304 channels used in the tests are cold drawn and were acquired from an ISO 9001/13485 certified manufacturer with precise dimensional accuracy. They present superior concentricity on the channel *OD* and *ID*. The internal diameters of the preheater and evaporator were measured with micrometer needle probes while a micrometric caliper was used to measure the external diameter. Both the measuring needle and the caliper has an uncertainty of $\pm 10 \mu\text{m}$. The channels were cut into 2 sections and measurements were taken at all four ends. The exact heated length of the evaporator for the three channel sizes was measured with a vernier caliper with an uncertainty of $\pm 100 \mu\text{m}$.

D_{int} (mm)	D_{ext} (mm)	L_{ph} (mm)	L_{ev} (mm)
$1.030 \pm 10 \mu\text{m}$	$1.200 \pm 10 \mu\text{m}$	$50.00 \pm 100 \mu\text{m}$	$180.00 \pm 100 \mu\text{m}$
$2.200 \pm 10 \mu\text{m}$	$2.400 \pm 10 \mu\text{m}$	$110.00 \pm 100 \mu\text{m}$	$396.00 \pm 100 \mu\text{m}$
$3.040 \pm 10 \mu\text{m}$	$3.190 \pm 10 \mu\text{m}$	$150.00 \pm 100 \mu\text{m}$	$540.00 \pm 100 \mu\text{m}$

Table 3.3: The uncertainties of the channel diameter and heated length

3.6.6 Surface Roughness

The surface roughness profile measurements for the $D_{in}=1.03$, 2.20 and 3.04 mm channels were carried out using the non-contact, optical phase shifting and white light vertical scanning interferometry technique. The *WykoNT1100* optical profiling system with a *RMS* repeatability of 0.1 nm was used for the high resolution 3-dimensional surface profile measurements. For illustration purposes, in Fig. (3.5) a magnified image of the open section of the $D_{in}=1.03$ mm channel is shown on the left and the 3-dimensional surface roughness profile is depicted on the right.

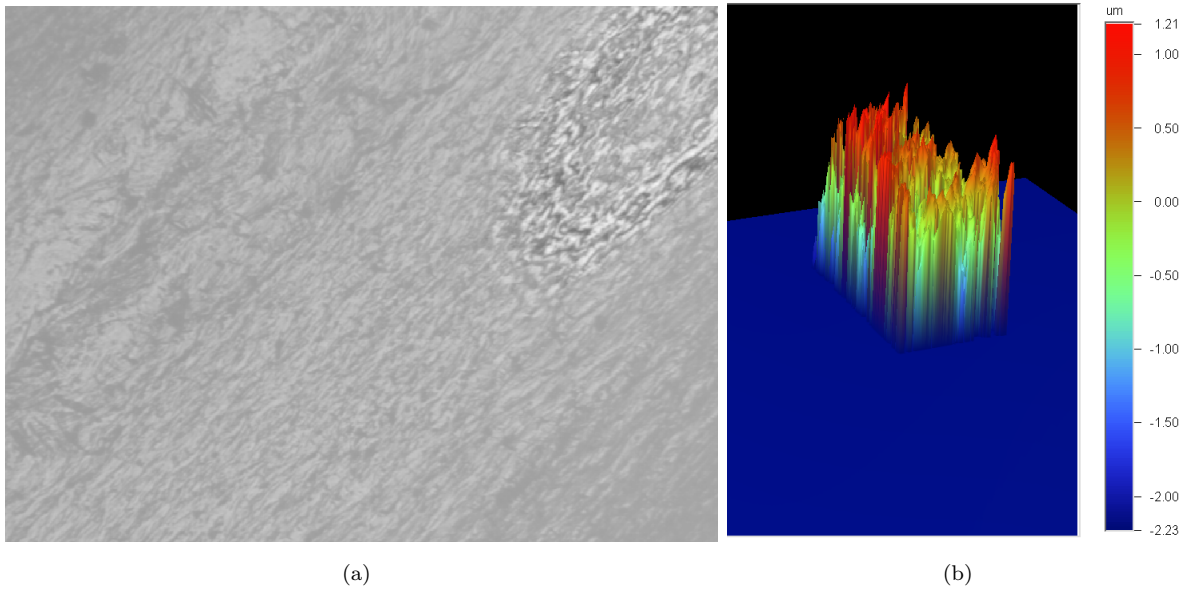


Figure 3.5: A magnified image of the surface roughness for the $D_{in}=1.03$ mm channel.

The surface roughness for the three channels corresponding to the root mean square (*RMS*) values are illustrated in Table 3.4.

D_{int} (mm)	Surface roughness (nm)
1.03	595.85
2.20	826.99
3.04	796.81

Table 3.4: The root mean square values of the surface roughness.

3.6.7 Fluid Property Regression

The refrigerant physical properties are calculated by applying a linear regression to the third order polynomial of the temperature referenced to the NIST Reference Fluid Thermodynamic and Transport Properties Database (REFPROP): Version 8. The general equation is:

$$\phi = a_0 + a_1T + a_2T^2 + a_3T^3 \quad (3.45)$$

while the corresponding error is taken as in Eq. (3.46)

$$\delta\phi = [a_1 + 2a_2T + 3a_3T^2]\delta T \quad (3.46)$$

3.6.8 Random Uncertainties

The random uncertainty is introduced by the scatter and variation in repeated measurements of the parameter. The experimental data are acquired with the use of National Instruments DAQs at an acquisition rate of 5000 *Hz*. The values of one hundred measured samples, corresponding to 0.02 *s* are averaged to yield a mean value. The appropriate standard deviation of the mean, $S_{\bar{x}}$, for the current measurement is written as:

$$S_{\bar{x}} = \frac{S_x}{\sqrt{N}} \quad (3.47)$$

while the random uncertainty sources of $N = 60$ finite sets of mean sample measurements corresponding to 1.20 *s* are estimated as $2S_{\bar{x}}$, which is a 95% confidence estimate of the effect on the average particular random uncertainty source. All the experimental data are carefully acquired in steady state conditions with no notable temperature or pressure oscillations or drifts being present. The uncertainty sources are grouped and then root-sum-squared to obtain a 95% confidence uncertainty in harmony with the ISO Guide from:

$$U = [B^2 + (2S_{\bar{x}})^2]^{1/2} \quad (3.48)$$

3.6.9 Total Measurement Uncertainties

The total uncertainty in the measurements is thus the combination of uncertainties due to systematic and random error, propagated to the result through the functional relationship between the results and the parameters. The effect of the measured quantities on the uncertainties for the mass velocity, heating efficiency, heat flux, local saturation pressure, vapor quality, pressure drop and the heat transfer coefficient have been evaluated accordingly by standard error propagation as shown below. The corresponding fluid parameter uncertainties, i.e. liquid enthalpy, latent heat and viscosity are evaluated from the general form using Eq. (3.46). Thus,

Mass Flux

$$\delta G = G \sqrt{\left(\frac{\delta \dot{m}}{m}\right)^2 + \left(2\frac{\delta D_{in}}{D_{in}}\right)^2} \quad (3.49)$$

Heat Flux

$$\delta q = q \sqrt{\left(\frac{\delta I}{I}\right)^2 + \left(\frac{\delta(\Delta V)}{\Delta V}\right)^2 + \left(\frac{\delta D_{in}}{D_{in}}\right)^2 + \left(\frac{\delta L_{ev}}{L_{ev}}\right)^2} \quad (3.50)$$

Saturation Length

$$\delta L_{sat} = \frac{\partial L_{sat}}{\partial G} \delta G + \frac{\partial L_{sat}}{\partial D_{in}} \delta D_{in} + \frac{\partial L_{sat}}{\partial q} \delta q + \frac{\partial L_{sat}}{\partial T_{inlet}} \delta T_{inlet} + \frac{\partial L_{sat}}{\partial T_{sat}} \frac{dT_{sat}}{dP_{sat}} \delta P_{sat} \quad (3.51)$$

Saturation Pressure

$$\delta P_{sat} = \frac{\partial P_{sat}}{\partial P_{TS,inlet}} \delta P_{TS,inlet} + \frac{\partial P_{sat}}{\partial G} \delta G + \frac{\partial P_{sat}}{\partial D_{in}} \delta D_{in} + \frac{\partial P_{sat}}{\partial L_{sat}} \delta L_{sat} + \frac{\partial P_{sat}}{\partial \rho_l} \delta \rho_l + \frac{\partial L_{sat}}{\partial \mu_l} \delta \mu_l \quad (3.52)$$

Local Pressure

$$\delta P = \sqrt{\left(\frac{\partial P}{\partial P_{sat}} \delta P_{sat}\right)^2 + \left(\frac{\partial P}{\partial L_{sat}} \delta L_{sat}\right)^2 + \left(\frac{\partial P}{\partial P_{TS,outlet}} \delta P_{TS,outlet}\right)^2 + \left(\frac{\partial P}{\partial L} \delta L\right)^2 + \left(\frac{\partial P}{\partial L_{ev}} \delta L_{ev}\right)^2} \quad (3.53)$$

Local Enthalpy

$$\delta H = \sqrt{\left(\frac{\partial H}{\partial q} \delta q\right)^2 + \left(\frac{\partial H}{\partial G} \delta G\right)^2 + \left(\frac{\partial H}{\partial D_{in}} \delta D_{in}\right)^2 + \left(\frac{\partial H}{\partial L} \delta L\right)^2 + \left(\frac{\partial H}{\partial H_{inlet}} \delta H_{inlet}\right)^2} \quad (3.54)$$

Vapor Quality

$$\delta x = \sqrt{\left(\frac{\partial x}{\partial H}\delta H\right)^2 + \left(\frac{\partial x}{\partial H_l}\delta H_l\right)^2 + \left(\frac{\partial x}{\partial H_{lv}}\delta H_{lv}\right)^2} \quad (3.55)$$

Finally, the uncertainty on the local heat transfer coefficient, h is evaluated as:

$$\delta h = h\sqrt{\left(\frac{\delta q}{q}\right)^2 + \left(\frac{\delta(T_w - T_f)}{T_w - T_f}\right)^2} \quad (3.56)$$

The range of uncertainties on the mass velocity, heat flux, saturation temperature, vapor quality and heat transfer coefficients for the $D_{in}=1.03, 2.20$ and 3.04 mm channels have been evaluated through propagation of error and is presented in Table 3.5.

$D_{int} = 1.03$ mm	R134a	R236fa	R245fa
G (kg/m ² s)	± 1 – 2 %	± 1 – 2 %	± 1 – 2 %
q (kW/m ²)	± 1.6 – 2.6 %	± 1.5 – 2.2 %	± 1.8 – 2.8 %
T_{sat} (K)	± 0.1 K	± 0.1 K	± 0.1 K
x (-)	± 3 %	± 2.8 %	± 2.7 %
D_{in} (mm)	± 1 %	± 1 %	± 1 %
h (kW/m ² K)	± 2.8 – 5.6 %	± 3.6 – 5.8 %	± 3.5 – 6.0 %

$D_{int} = 2.20$ mm	R134a	R236fa	R245fa
G (kg/m ² s)	± 1 – 2 %	± 1 – 2 %	± 1 – 2 %
q (kW/m ²)	± 1.3 – 2.4 %	± 1.4 – 2.1 %	± 1.5 – 2.6 %
T_{sat} (K)	± 0.1 K	± 0.1 K	± 0.1 K
x (-)	± 2.6 %	± 2.5 %	± 2.5 %
D_{in} (mm)	± 0.5 %	± 0.5 %	± 0.5 %
h (kW/m ² K)	± 2.2 – 4.8 %	± 2.8 – 4.9 %	± 2.8 – 5.1 %

$D_{int} = 3.04$ mm	R134a	R236fa	R245fa
G (kg/m ² s)	± 1 – 1.8 %	± 1 – 1.8 %	± 1 – 1.8 %
q (kW/m ²)	± 1.3 – 2.3 %	± 1.5 – 2.1 %	± 1.4 – 2.5 %
T_{sat} (K)	± 0.1 K	± 0.1 K	± 0.1 K
x (-)	± 2.6 %	± 2.3 %	± 2.2 %
D_{in} (mm)	± 0.4 %	± 0.4 %	± 0.4 %
h (kW/m ² K)	± 2.8 – 4.7 %	± 2.6 – 4.8 %	± 2.4 – 5.2 %

Table 3.5: Uncertainty range for the $D_{in}=1.03, 2.20$ and 3.04 mm channels.

Chapter 4

Two-Phase Flow Patterns

4.1 Experimental Procedure

The experimental two-phase flow patterns in this study have been objectively classified with the use of a photodiode laser signal system discussed earlier in Chapter 3, as opposed to the classification of flow patterns only on the basis of visual observation as often reported in literature. The laser photodiode signals were acquired at 10,000 Hz during steady state conditions and post-processed to determine the flow pattern present. Probability Density Function (PDF) analysis of the laser signals describe the density of the probability at each point in the signal sample space, thus enabling the respective classification of two-phase flow patterns. The PDF analysis of laser signals from Photodiode 1, located immediately at the inlet of the sight glass (near the exit of the evaporator test section) is used to identify and classify the two-phase flow patterns occurring in the channel. The flow regimes have been verified by flow visualizations using a high speed camera, acquired simultaneously with the laser signals. As an example, representative photodiode signals and PDF plots for the $D_{in}=1.03\text{ mm}$ are shown in Fig. (4.1).

4.2 Two-Phase Flow Patterns

In this experimental study, a wide range of test conditions have been performed to study the effects of confinement, fluid properties, mass flux and saturation temperature on two-phase flow patterns. In this section, a selection of flow pattern images from the study will be shown.

Four distinct flow patterns similar to experimental observations reported by Revellin et al. [24] have been observed for the $D_{in}=1.03\text{ mm}$ channel for all the three fluids tested, namely: a) Isolated bubble , b) Coalescing bubble, c) Wavy-annular and d) Smooth-annular flow. For simplicity reasons, the wavy-annular and smooth-annular flow have been classified together as one flow regime, annular flow. Fig. (4.2) illustrates in sequence the two-phase flow patterns observed as a function of heat flux and vapor quality for R236fa in the $D_{in}=1.03\text{ mm}$ channel for $Co=0.83$.

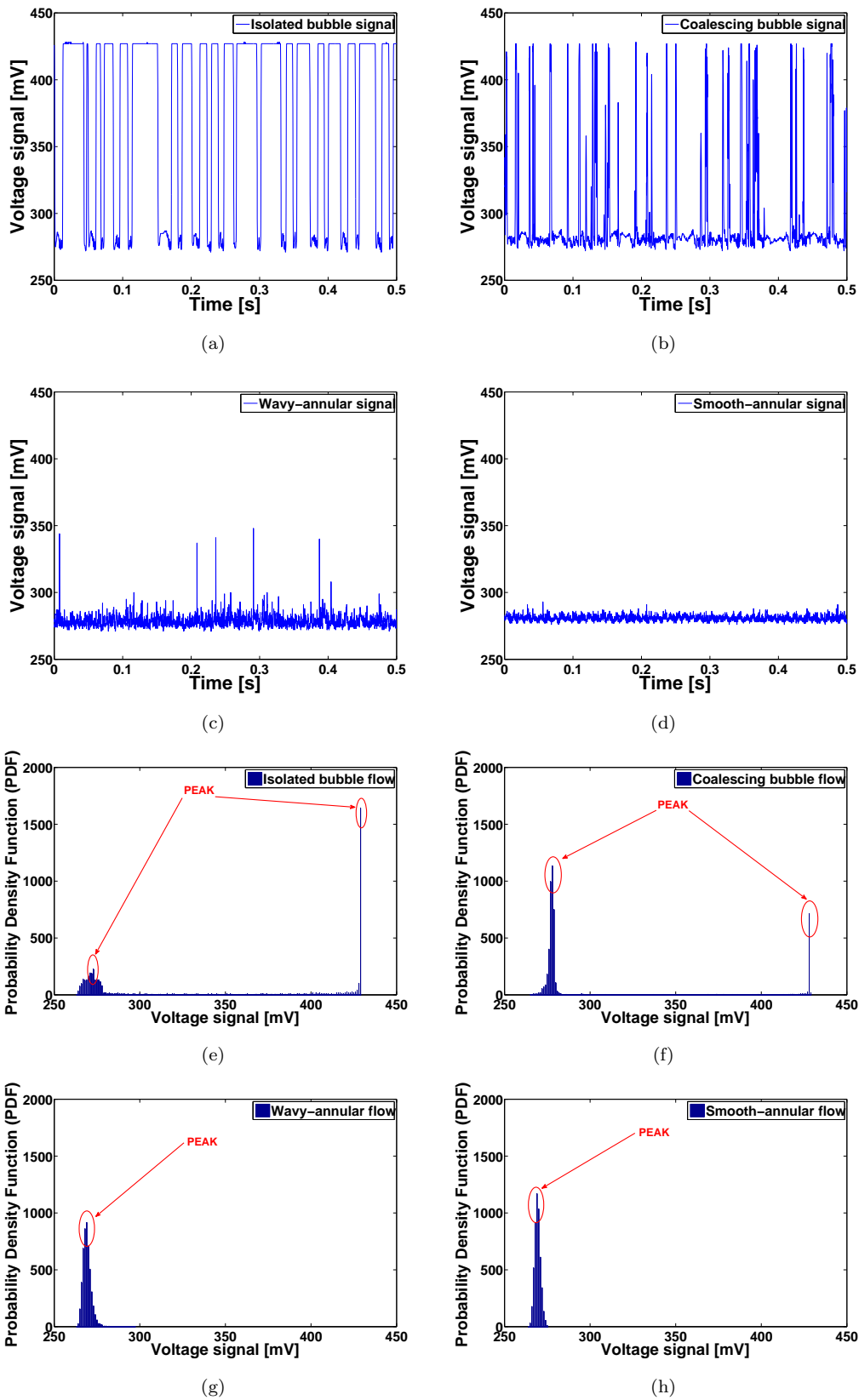


Figure 4.1: Probability Density Function for R236fa in the $D_{in}=1.03$ mm channel at $T_{sat}=31$ °C, $G=200$ kg/m²s and $T_{in}=27$ °C; (a) Isolate bubble, (b) Coalescing bubble, (c) Wavy-annular, (d) Smooth-annular flow, (e) Isolate bubble PDF, (f) Coalescing bubble PDF, (g) Wavy-annular PDF and (h) Smooth-annular flow PDF.

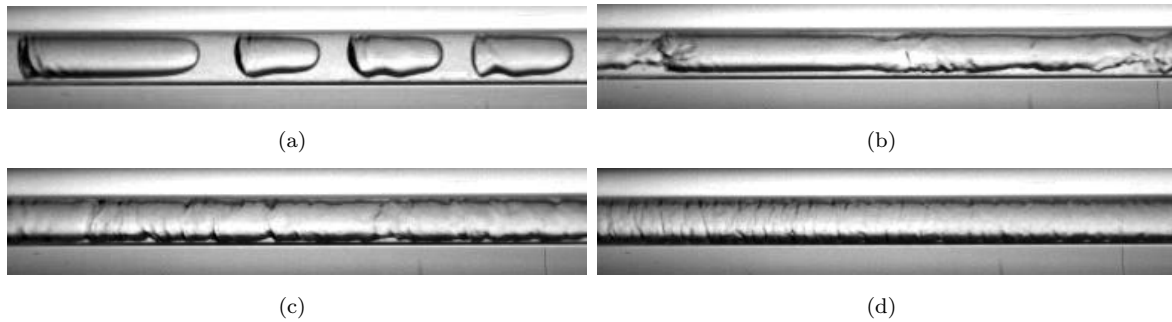


Figure 4.2: Flow patterns observed for R236fa in the $D_{in}=1.03$ mm channel at $T_{sat}=31$ °C, $G=201$ kg/m²s, $T_{in}=27$ °C and $Co=0.85$; (a) $q=2.95$ kW/m², $x=0.034$ (b) $q=9.6$ kW/m², $x=0.21$, (c) $q=20.1$ kW/m², $x=0.48$ and (d) $q=37.5$ kW/m², $x=0.92$.

For the $D_{in}=3.04$ mm channel, two distinct macroscale flow patterns, namely plug/slug and coalescing bubble (intermittent flow), have been observed for all the three fluids tested for confinement numbers ranging from $Co=0.27$ - 0.34. The flow patterns observed for this larger channel are classified as follows: a) Slug/Plug, b) Coalescing bubble, c) Wavy-annular and d) Smooth-annular flow as illustrated in Fig. (4.3). The plug/slug flow constitutes a long vapor bubble separated by liquid plugs that exhibit strong buoyancy effects and a thick stratified layer of liquid at the bottom. Increasing the vapor quality, the flow transitions to coalescing bubble flow (also termed intermittent flow) when the flow becomes more chaotic undergoing coalescence. Vapor bubbles were entrained in the liquid film surrounding the channel wall. The big and small vapor bubbles violently coalesce and no clear interface between the liquid and vapor can be seen. Upon full coalescence of the vapor bubbles, coalescing bubble flow transitions occur to wavy-annular and subsequently smooth annular flow. The wavy-annular flow is also called churn-annular flow in macroscale terms. As mentioned previously, the wavy-annular and smooth-annular flow regimes have been grouped together as annular flow.

Comparing the flow patterns shown in Fig. (4.2) and Fig. (4.3), it is evident that gravity dominance gradually decreased while surface tension forces gain dominance when channel confinement increases, as reflected in the confinement numbers. In the isolated bubble flow regime, the vapor bubble diameter is approximately the same size as the channel diameter. The vapor bubbles exhibit a characteristic hemispherical cap separated by liquid slugs between the head and tail while an equally thin layer of liquid film surrounds the periphery of the bubble. The plug/slug flow regime on the other hand showed strong buoyancy effects, with the large vapor bubble at the top portion of the channel and a thick layer of stratified liquid film at the bottom of the channel. The liquid-vapor interface can be smooth or wavy depending on the mass velocity and fluid properties of the fluid. As the surface tension forces increase, the liquid-vapor interface becomes smoother and flow becomes less turbulent. The flow structures are illustrated in Fig. (4.2)a and Fig. (4.2)b and Fig. (4.3)a and Fig. (4.3)b for R236fa in the $D_{in}=1.03$ and 3.04 mm channels, respectively. The onset of coalescence also tends to occur earlier for R245fa and R236fa due to the higher surface tension properties of the fluids in comparison with R134a.

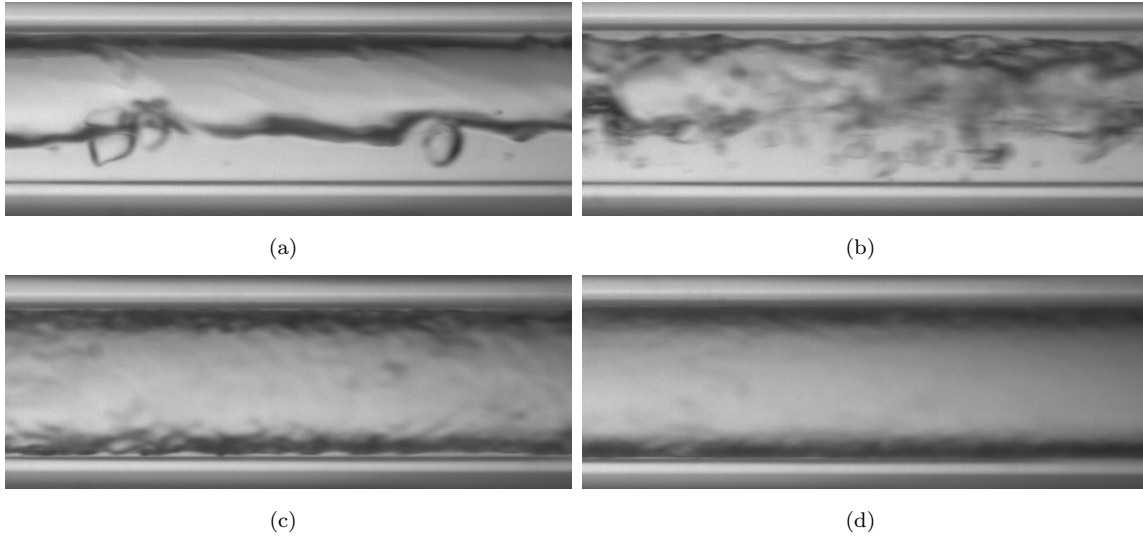


Figure 4.3: Flow patterns observed for R236fa in the $D_{in}=3.04$ mm channel at $T_{sat}=31$ °C, $G=405$ kg/m²s, $T_{in}=27$ °C and $Co=0.28$; (a) $q=7.9$ kW/m², $x=0.051$ (b) $q=12.1$ kW/m², $x=0.103$, (c) $q=29.1$ kW/m², $x=0.314$ and (d) $q=63.8$ kW/m², $x=0.74$

Fig. (4.4)a and Fig. (4.4)b depicts the isolated bubble (IB) regime for R134a in the $D_{in}=2.20$ mm channel and the slug/plug (S-P) regime for the $D_{in}=3.04$ mm channel is shown in Fig. (4.5)a and Fig. (4.5)b.

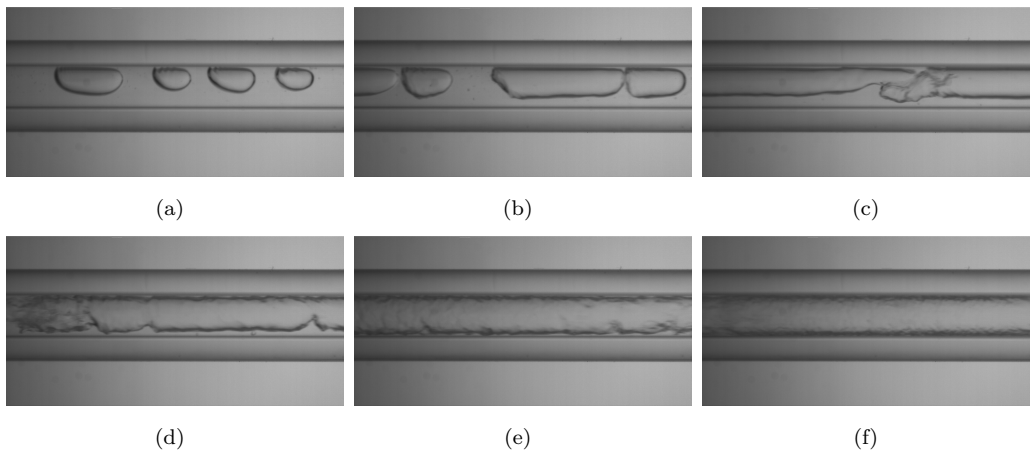


Figure 4.4: Flow patterns for R134a, $D_{in}=2.20$ mm channel at $T_{sat}=31$ °C, $G=307$ kg/m²s, $T_{in}=27$ °C and $Co=0.37$; (a) $q=3.5$ kW/m², $x=0.013$ (b) $q=5.2$ kW/m², $x=0.033$, (c) $q=9.4$ kW/m², $x=0.094$, (d) $q=19.0$ kW/m², $x=0.19$, (e) $q=36.0$ kW/m², $x=0.44$ and (f) $q=65.7$ kW/m², $x=0.81$.

Similar flow patterns are observed also for the two other fluids tested, and the flow patterns for R245fa is shown in Fig. (4.6)a and Fig. (4.6)b for isolated bubble (IB) and

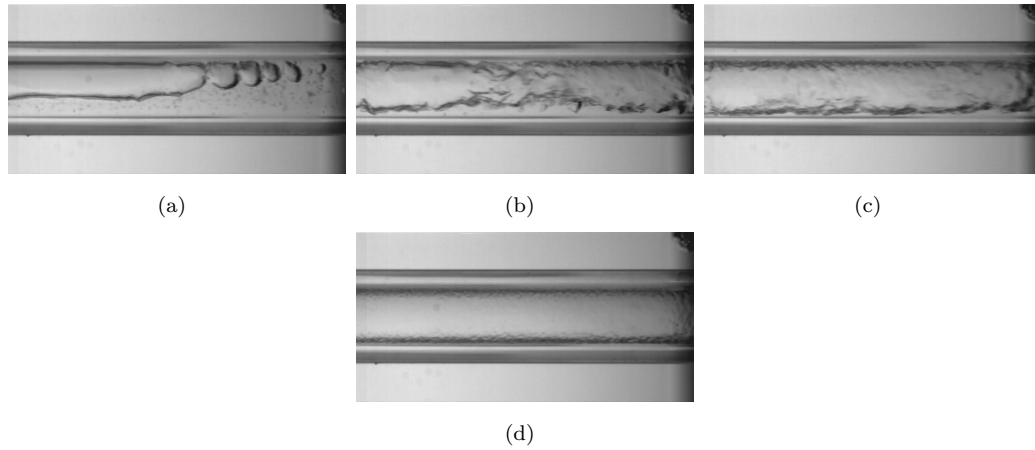


Figure 4.5: Flow patterns for R134a, $D_{in}=3.04$ mm channel at $T_{sat}=31$ °C, $G=299$ kg/m²s, $T_{in}=27$ °C and $Co=0.27$; (a) $q=6.6$ kW/m², $x=0.05$, (b) $q=21.4$ kW/m², $x=0.258$, (c) $q=34.7$ kW/m², $x=0.44$ and (d) $q=60.4$ kW/m², $x=0.80$.

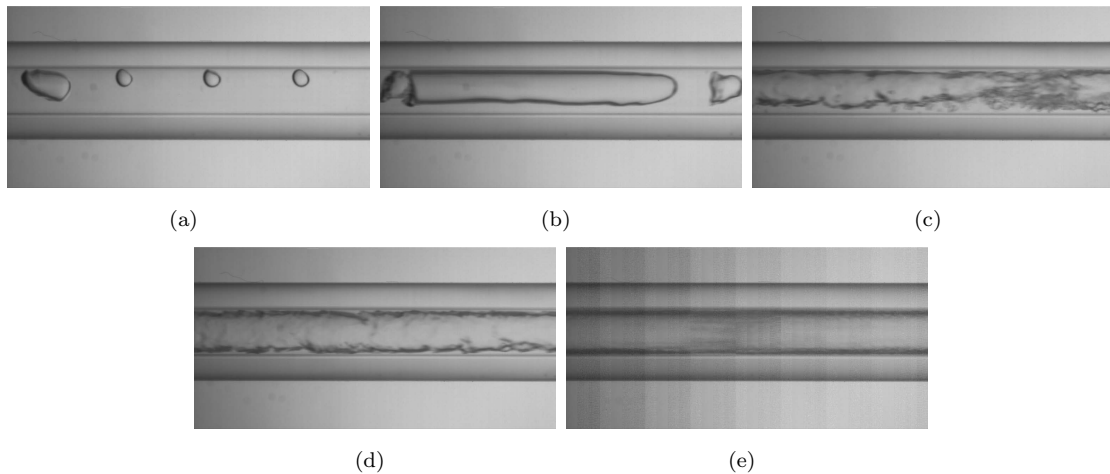


Figure 4.6: Flow patterns for R245fa, $D_{in}=2.20$ mm channel at $T_{sat}=31$ °C, $G=302$ kg/m²s, $T_{in}=27$ °C and $Co=0.46$; (a) $q=4.3$ kW/m², $x=0.014$ (b) $q=6.04$ kW/m², $x=0.03$, (c) $q=11.0$ kW/m², $x=0.09$, (d) $q=17.7$ kW/m², $x=0.18$ and (e) $q=56.7$ kW/m², $x=0.74$.

Fig. (4.7)a for slug/plug flow.

4.2.1 Effects of Mass Velocity

Fig. (4.7) and Fig. (4.8) illustrate the two-phase flow structure of R245fa in the $D_{in}=3.04$ mm channel for $G=298$ and 602 kg/m²s. From the images, it is observed that the transition from slug/plug(S-P) to coalescing bubble(CB) flow occurs earlier when increasing the mass velocity. The S-P/CB transition for R245fa at $G=298$ kg/m²s occurs at a vapor quality of $x=0.11$ while instead at $x=0.038$ for $G=602$ kg/m²s.

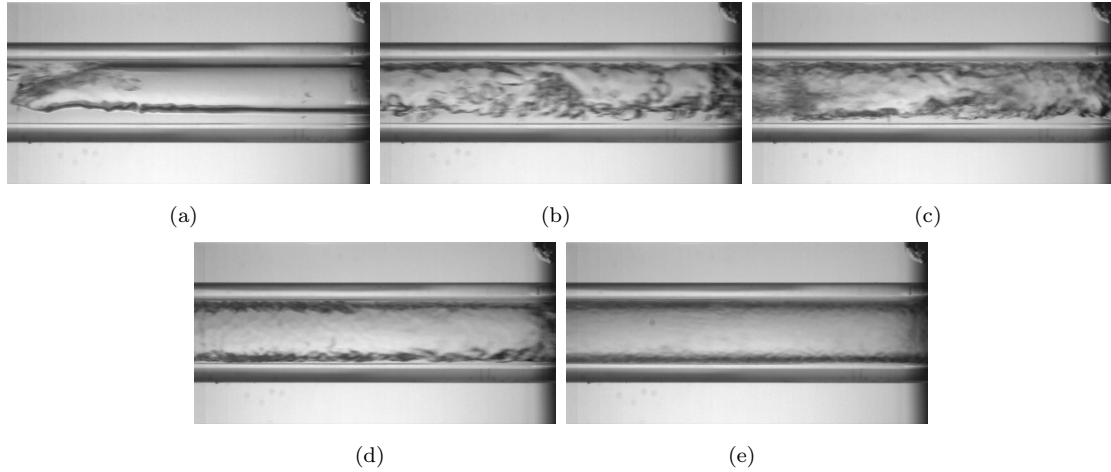


Figure 4.7: Flow patterns for R245fa, $D_{in}=3.04$ mm channel at $T_{sat}=31$ °C, $G=298$ kg/m²s, $T_{in}=27$ °C and $Co=0.34$; (a) $q=7.0$ kW/m², $x=0.058$ (b) $q=11.2$ kW/m², $x=0.11$, (c) $q=16.3$ kW/m², $x=0.17$, (d) $q=27.9$ kW/m², $x=0.314$ and (e) $q=62.3$ kW/m², $x=0.75$.

4.3 Experimental Flow Pattern Transitions

This section presents the experimental flow pattern data and '*experimental*' transition lines for the channels and fluids tested. From the experiments, the flow pattern transition lines have been found to be a function of mass flux, channel confinement, saturation temperature and fluid properties. The experimental flow patterns observed for R236fa in the $D_{in}=1.03$ channel and R134a in the $D_{in}=2.20$ and 3.04 mm channels are shown in Fig. (4.9), Fig. (4.10) and Fig. (4.11). Referring to the figures, the vapor quality corresponding to flow pattern transition tends to decrease as the mass velocity increases. This

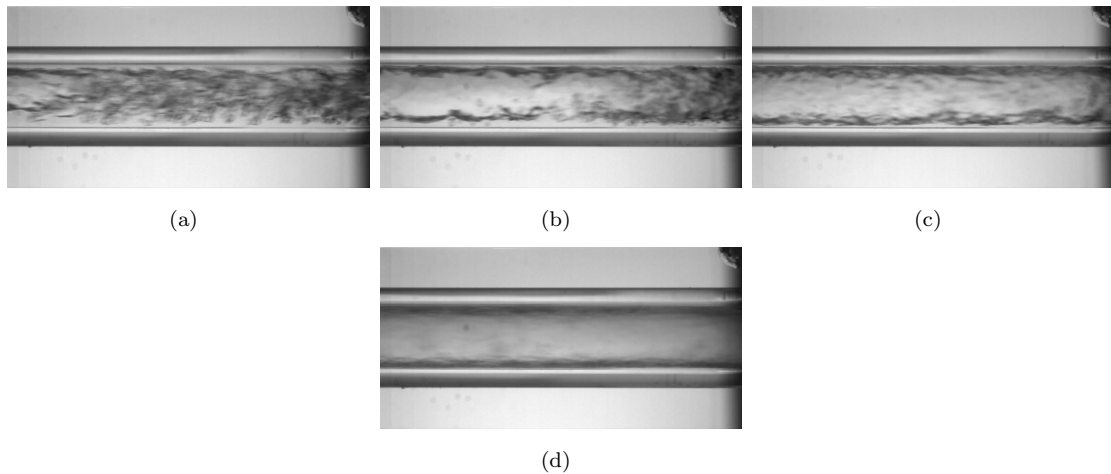


Figure 4.8: Flow patterns for R245fa, $D_{in}=3.04$ mm channel at $T_{sat}=31$ °C, $G=602$ kg/m²s, $T_{in}=27$ °C and $Co=0.34$; (a) $q=10.7$ kW/m², $x=0.038$ (b) $q=15.5$ kW/m², $x=0.06$, (c) $q=27.4$ kW/m², $x=0.13$ and (d) $q=82.3$ kW/m², $x=0.46$.

phenomenon was observed for all the channels and the fluids tested. Slug/plug flow was observed at low mass velocities in the $D_{in}=3.04\text{ mm}$ channel where a direct transition to annular flow is seen. Increasing the mass velocity, the slug/plug regime is gradually suppressed and the coalescing bubble flow dominates. It has been experimentally observed that one macroscale flow regime, i.e. the slug-plug flow being present in the $D_{in}=3.04\text{ mm}$ channel was completely suppressed for the smaller $D_{in}=1.03$ and 2.20 mm channel as channel confinement increases.

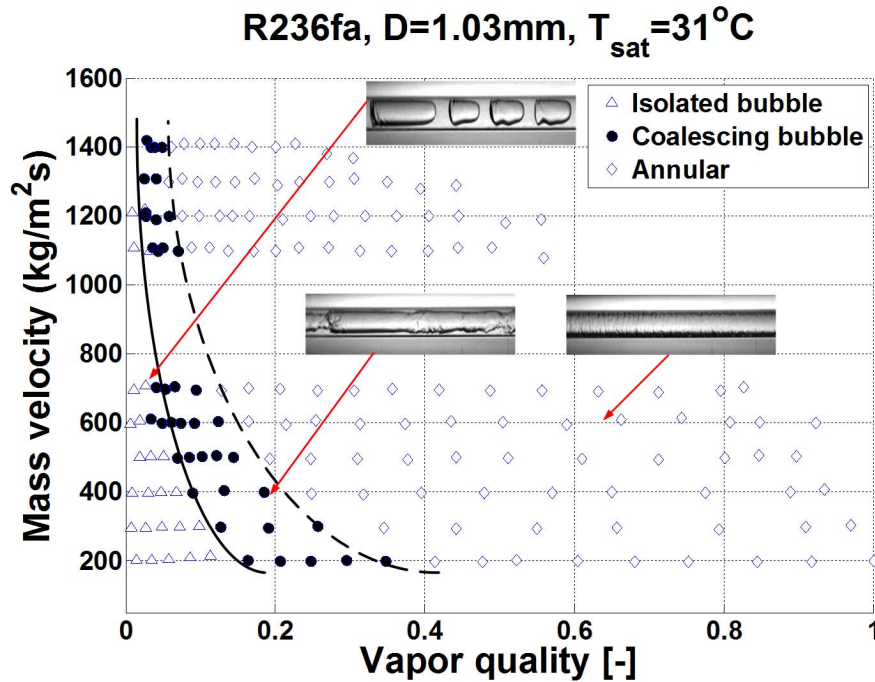


Figure 4.9: Experimental flow pattern transition lines for R236fa, $D_{in}=1.03\text{ mm}$ channel at $T_{\text{sat}}=31\text{ }^\circ\text{C}$, $T_{in}=27\text{ }^\circ\text{C}$ and $Co=0.83$.

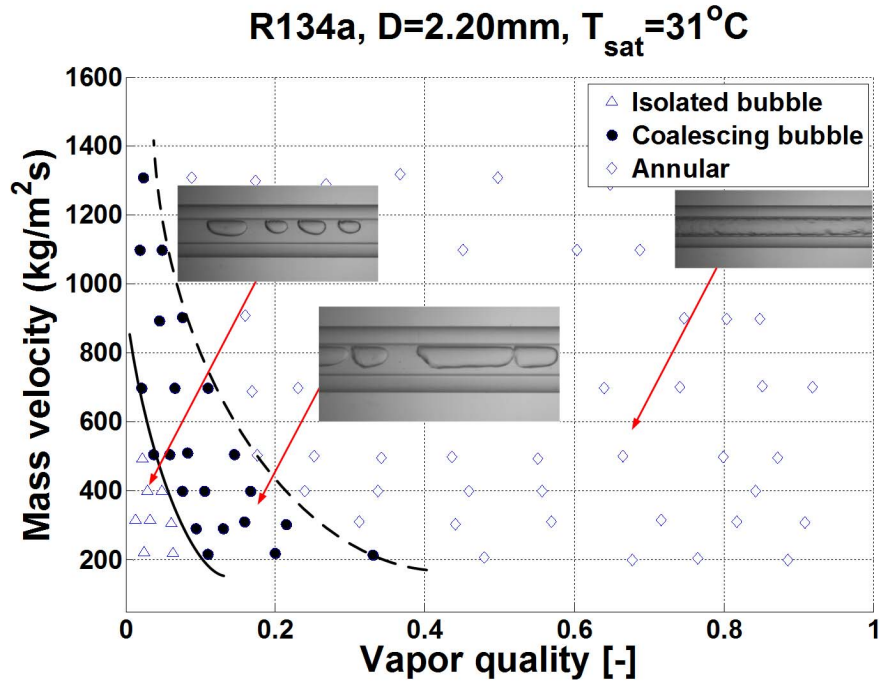


Figure 4.10: Experimental flow pattern transition lines for R134a, $D_{in}=2.20\text{ mm}$ channel at $T_{sat}=31\text{ }^\circ\text{C}$, $T_{in}=27\text{ }^\circ\text{C}$ and $Co=0.36$.

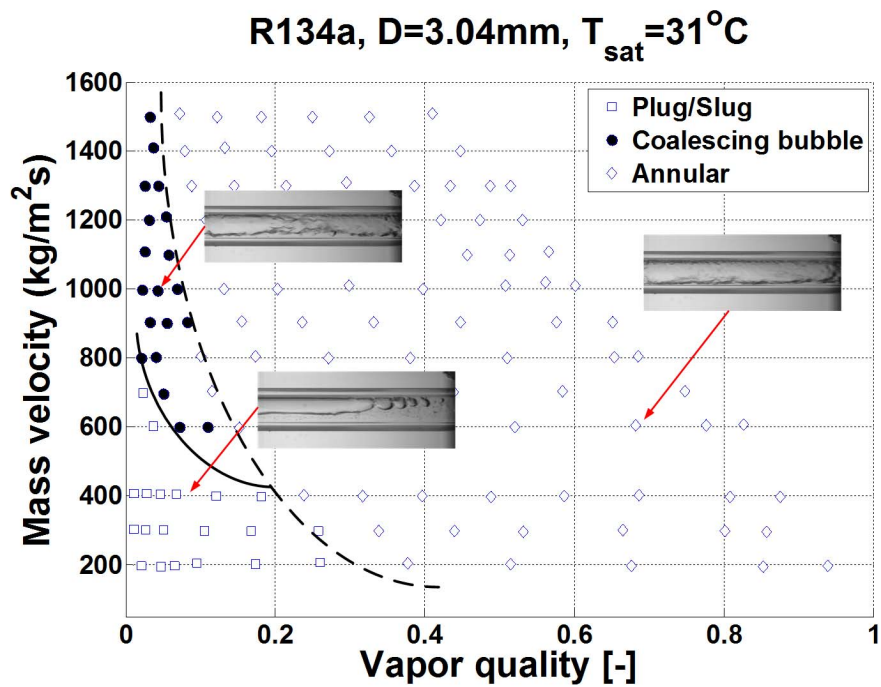


Figure 4.11: Experimental flow pattern transition lines for R134a, $D_{in}=3.04\text{ mm}$ channel at $T_{sat}=31\text{ }^\circ\text{C}$, $T_{in}=27\text{ }^\circ\text{C}$ and $Co=0.27$.

4.3.1 Effects of Channel Confinement

The effect of channel size on two-phase flow pattern transitions is presented in this section. Fig. (4.12)(a),(b) presents the flow pattern transition lines for R134a in the $D_{in}=0.50, 0.80, 1.03, 2.20$ and 3.04 mm channels corresponding to a confinement number range of $Co=0.27-1.61$ (the $D_{in}=0.50$ and 0.80 mm data are taken from Revellin [24]). Referring to Fig. (4.12)(a), the CB/A transition for R134a in the $D_{in}=0.50$ mm ($Co=1.61$) channel occurs earlier than the $D_{in}=0.80$ mm channel ($Co=1.01$) and similar to the $D_{in}=1.03$ mm channel ($Co=0.78$). When channel size decreases, the vapor bubbles quickly grow and coalesce to fill the channel cross section, expanding downstream as compared to larger channels, resulting in the expansion of the regimes. The CB/A transition is reached when inertia force dominate over the surface tension force, promoting coalescence to form a continuous vapor core and liquid film around the periphery of the channel. However, an opposite trend was observed when comparing the CB/A transition for the $D_{in}=1.03$ mm ($Co=0.78$) and $D_{in}=2.20$ mm channel ($Co=0.36$), with earlier transition to annular flow occurring for the larger $D_{in}=2.20$ mm channel ($Co=0.36$). This earlier CB/A transition trend was also observed for the $D_{in}=3.04$ mm channel ($Co=0.27$). Similar trends were observed for R236fa and R245fa as shown in Fig. (4.13). The horizontal red line in the flow pattern map for the $D_{in}=3.04$ mm channel refers to the threshold for flow pattern transition from Slug-Plug flow to annular flow. Above this horizontal red line, the flow pattern transits from slug-plug flow to coalescing bubble flow before the transition to the annular flow regime at higher vapor qualities.

The earlier CB/A transition for the $D_{in}=2.20$ mm ($Co=0.36$) and 3.04 mm channels ($Co=0.27$) is associated to the less dominant surface tension forces and the presence of small bubbles in the larger channels. In this case, the lower surface tension dominance compared to inertia reduces the ability of the flow to keep the liquid slug holdup between the vapor bubbles and thus promotes an earlier transition from CB/A. This CB/A transition boundary separates the surface tension dominated regime (IB and S-P) and the shear dominated regimes (A) when shear forces gain dominance. Increasing the mass velocity, the annular flow gradually expands and spans over a wider range of vapor qualities, at the expense of the gradually diminishing sizes of IB and CB regimes.

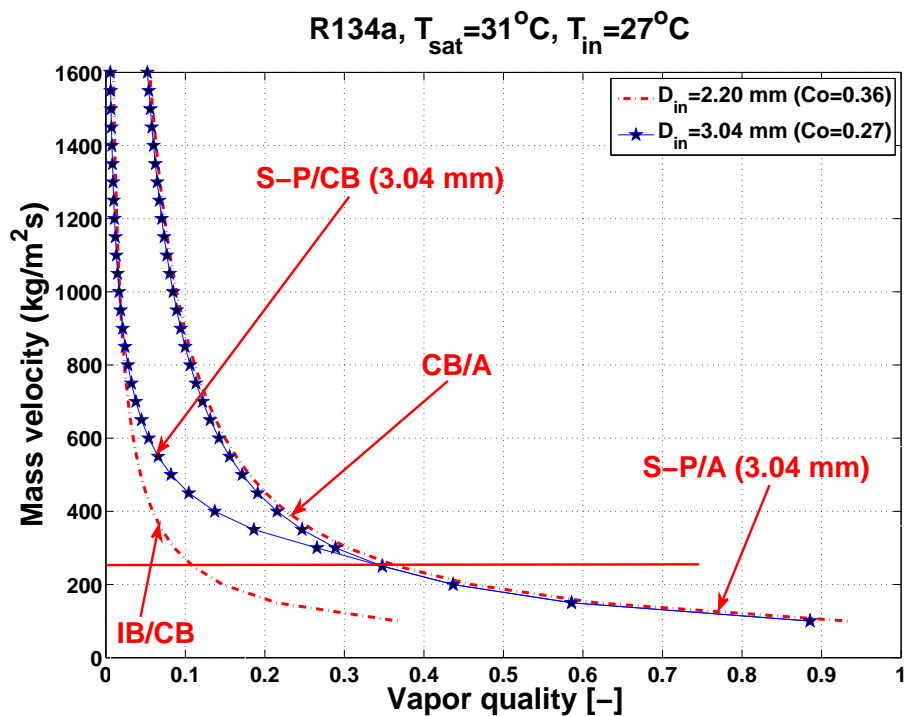
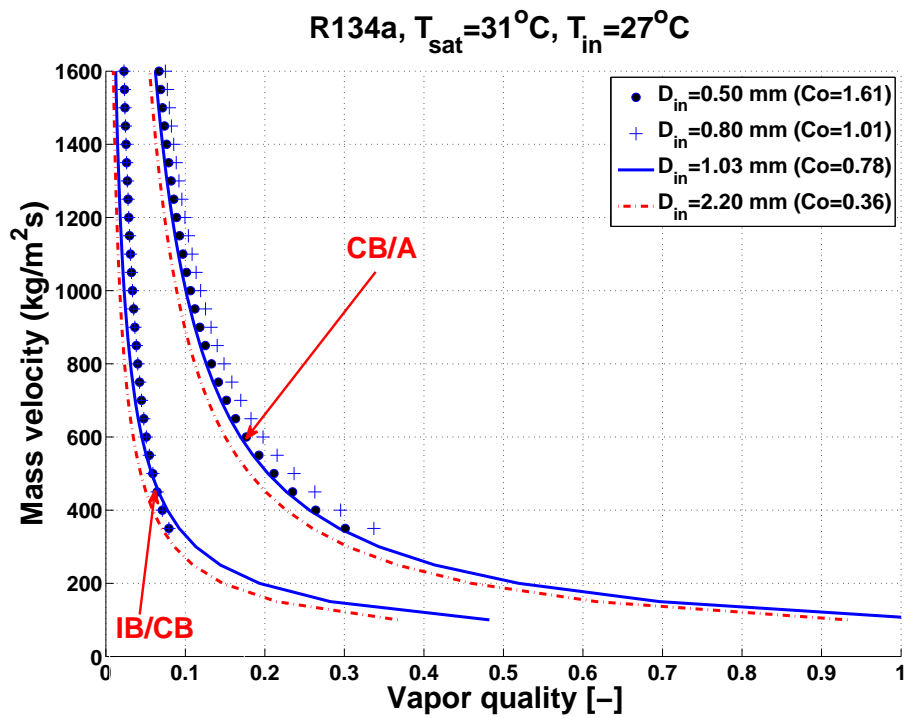


Figure 4.12: Flow pattern transition lines for R134a, $T_{sat}=31^{\circ}\text{C}$ and $T_{in}=27^{\circ}\text{C}$; (a) $D_{in}=0.50$, 0.80 , 1.03 and 2.20 mm and (b) $D_{in}=2.20$ and 3.04 mm. (The symbols represent the transition lines observed in the database and not the data points)

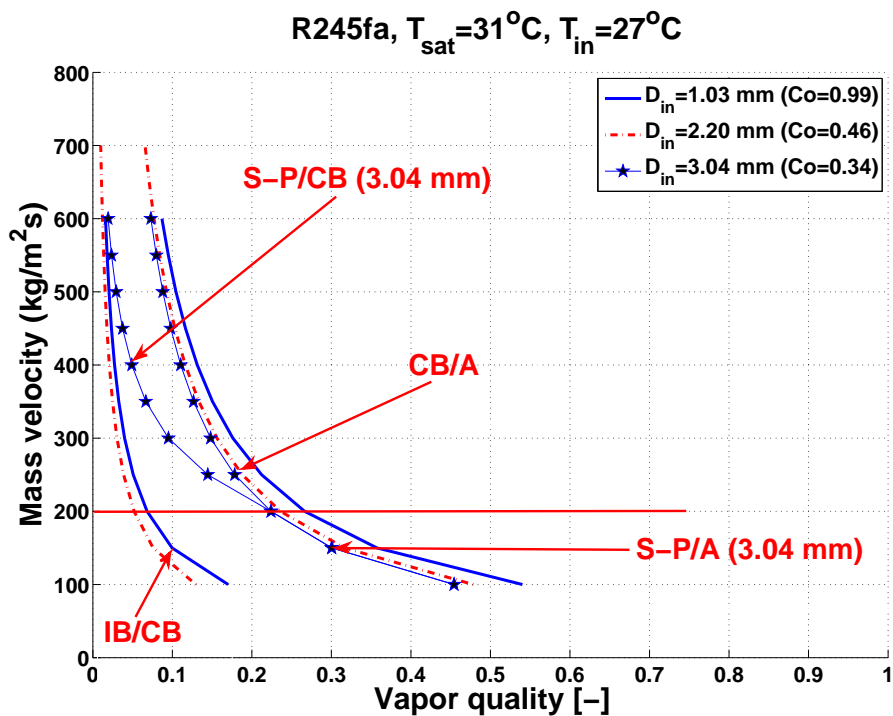
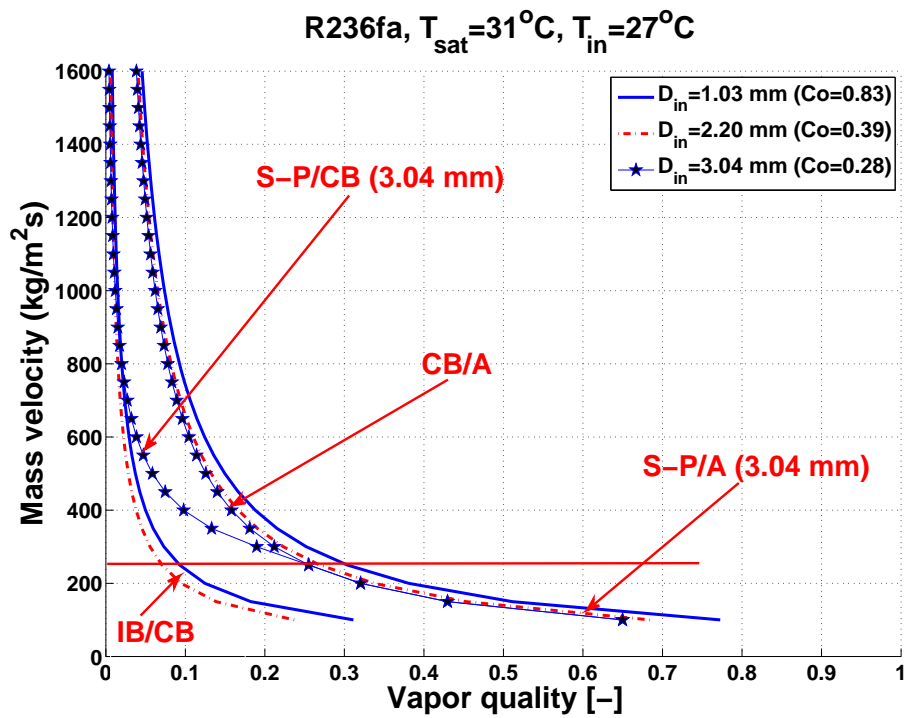
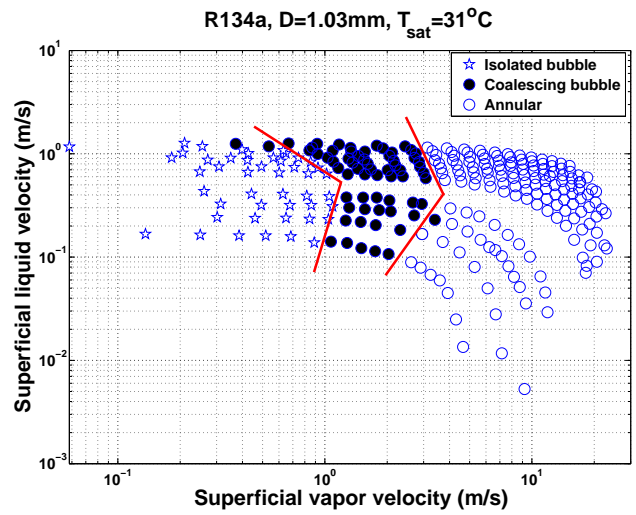


Figure 4.13: Flow pattern transition lines for R236fa and R245fa at $T_{sat}=31^{\circ}\text{C}$ and $T_{in}=27^{\circ}\text{C}$; (a) R236fa and (b) R245fa. (The symbols represent the transition lines observed in the database and not the data points)

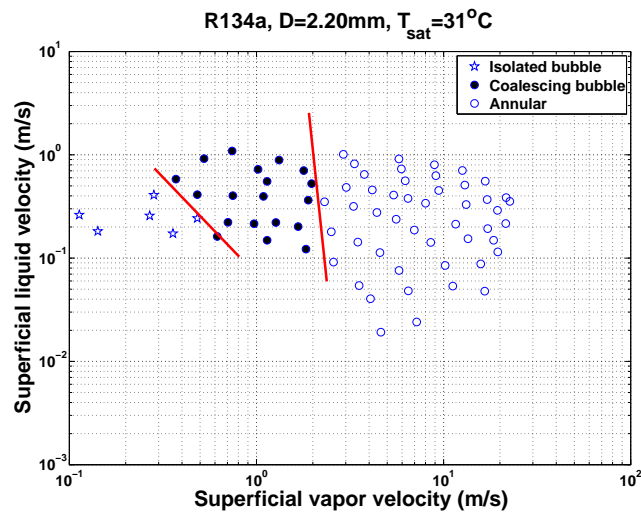
Fig. (4.14) to Fig. (4.16) illustrate the comparison of superficial velocities (often used in other older maps) of our current work for the three channels and working fluids. The superficial velocity plots all illustrate an increasing superficial vapor velocity for the CB/A transition when channel size decreases. This trend also agrees with those by Yang et al. [25], Damianides [71] and Bousman [107]. Yang [25] observed a shift in the slug to annular transition to a lower value of gas velocity when changing the working fluid from the high surface tension air-water to the lower surface tension R134a. This is also consistent with the observations by Diamianides [71], who concluded that smaller tubes require a larger gas flow to transit from intermittent to annular flow. The IB/CB transition lines also indicate similar trends, with decreasing superficial vapor velocity for larger channels. The IB/CB transition however is due to the bubble coalescence process where the surface tension and inertia forces plays a very important role. The same trend was also observed for the IB/CB flow pattern transition line for the $D_{in}=2.20$ mm ($Co=0.36$) and 3.04 mm ($Co=0.27$) channels but was not clearly visible for the $D_{in}=0.50$ mm ($Co=1.61$) and $D_{in}=0.80$ mm ($Co=1.01$) channel at high mass velocities. As explained by Taitel et al. [69], the shear force at higher mass velocities will cause a wavy liquid-vapor interface. The inertia forces will eventually dominate and the transition to annular flow will be independent of channel confinement, as observed in the experimental flow pattern results.

In general, for a given value of superficial liquid velocity, the flow pattern transition from IB/CB and CB/A shifts to higher superficial vapor velocity when channel confinement increases. As for the $D_{in}=3.04$ mm channel, the S-P/A transition line is also observed to shift to higher superficial vapor velocities when channel confinement increases, as shown in Fig. (4.14)c, Fig. (4.15)c and Fig. (4.16)c.

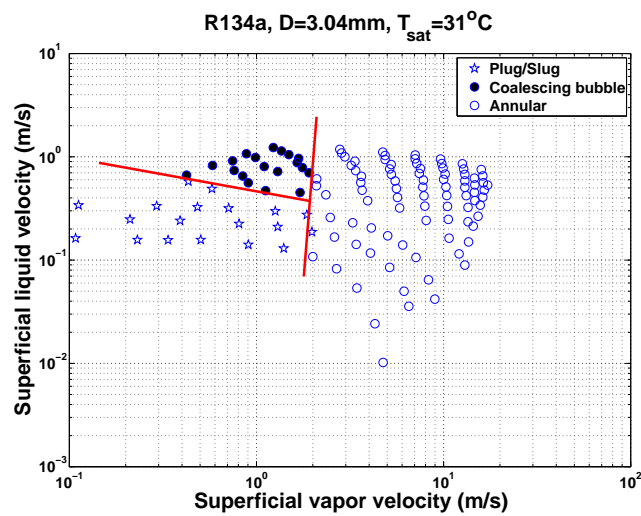
While not shown here, the superficial velocity type of map proposed by Tripplet [50, 79] for air-water flows does not work well for these refrigerants in channels of $D_{in}=1.0$ to 3.0 mm, as was already stated by Revellin [24] for his $D_{in}=0.5$ to 0.8 mm data.



(a)

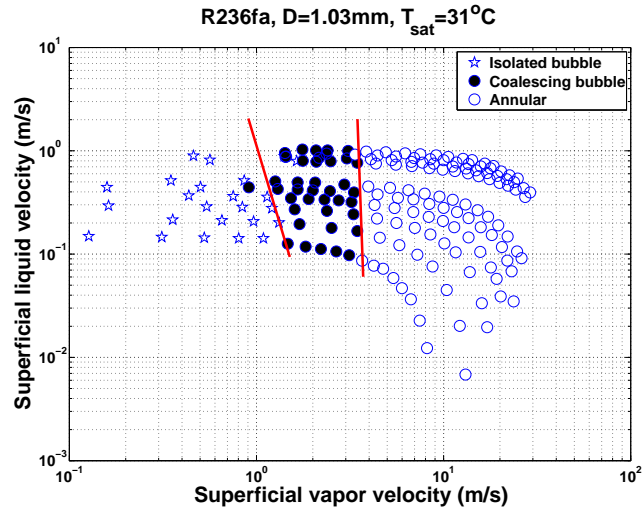


(b)

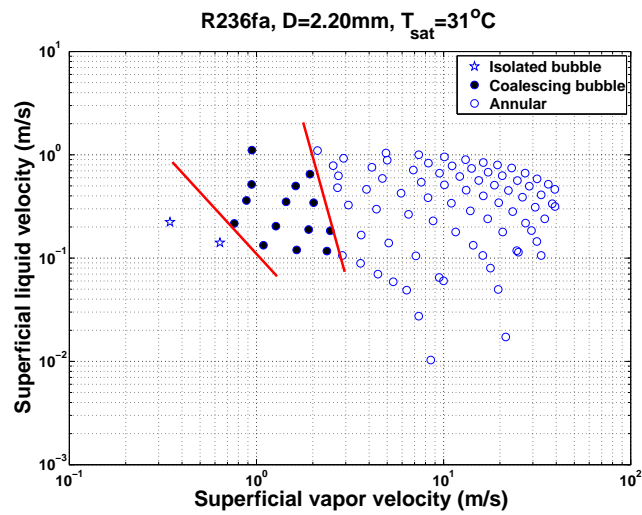


(c)

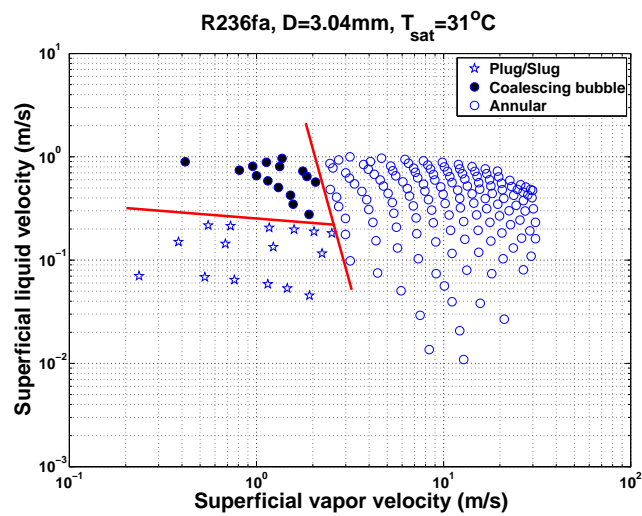
Figure 4.14: R134a flow patterns and transition lines with superficial phase velocities as coordinates for $T_{\text{sat}}=31^\circ\text{C}$ and $T_{\text{in}}=27^\circ\text{C}$; (a) $D_{\text{in}}=1.03\text{ mm}$, $Co=0.78$, (b) $D_{\text{in}}=2.20\text{ mm}$, $Co=0.36$ and (c) $D_{\text{in}}=3.04\text{ mm}$, $Co=0.27$.



(a)

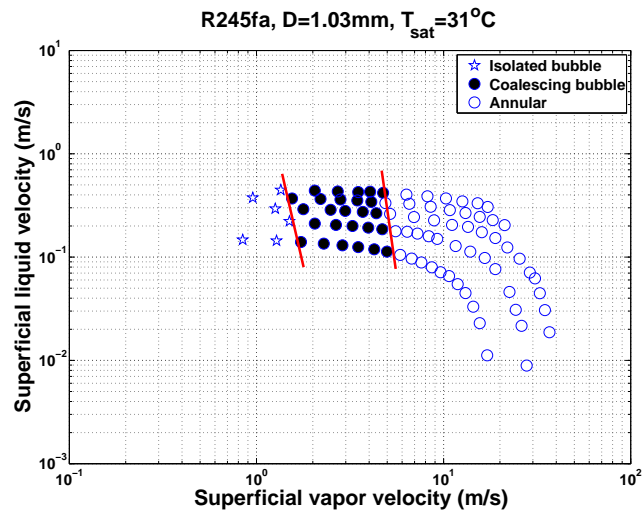


(b)

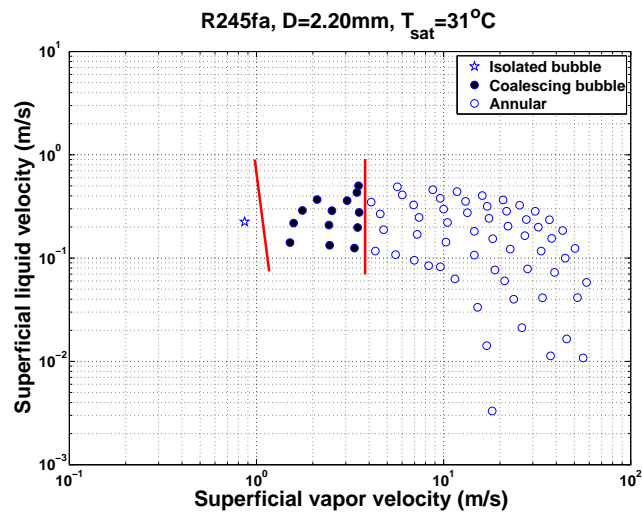


(c)

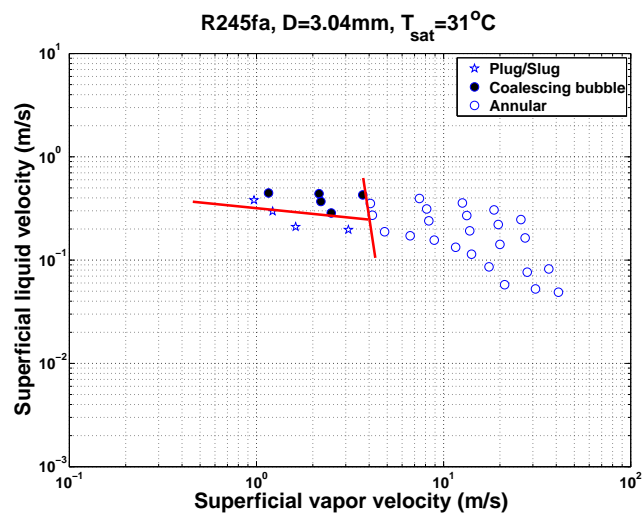
Figure 4.15: R236fa flow patterns and transition lines with superficial phase velocities as coordinates for $T_{\text{sat}}=31^{\circ}\text{C}$ and $T_{\text{in}}=27^{\circ}\text{C}$; (a) $D_{\text{in}}=1.03\text{ mm}$, $Co=0.83$, (b) $D_{\text{in}}=2.20\text{ mm}$, $Co=0.39$ and (c) $D_{\text{in}}=3.04\text{ mm}$, $Co=0.28$.



(a)



(b)



(c)

Figure 4.16: R245fa flow patterns and transition lines with superficial phase velocities as coordinates for $T_{\text{sat}}=31^\circ\text{C}$ and $T_{\text{in}}=27^\circ\text{C}$; (a) $D_{\text{in}}=1.03\text{ mm}$, $Co=0.99$, (b) $D_{\text{in}}=2.20\text{ mm}$, $Co=0.46$ and (c) $D_{\text{in}}=3.04\text{ mm}$, $Co=0.34$.

4.3.2 Effects of Fluid Properties

The effects of the working fluid on two-phase flow pattern transitions are shown in Fig. (4.17). It is observed that R245fa yields the lowest IB/CB and CB/A vapor quality transition, followed by R236fa and then R134a. At saturation temperature $T_{sat}=31^{\circ}C$, the surface tension of R245fa exceeds the value of R134a by over 80% while R236fa yields a surface tension value at an intermediate level with respect to the two other fluids. R245fa is also the most viscous fluid, by over +100% when compared to R134a. The vapor density of R245fa is also lower than that of R134a by over 70%, resulting in increased degree of expansion of the vapor phase during phase change.

Comparing Fig. (4.18)a and Fig. (4.18)b, the superficial Weber number for CB/A transition appears to be the highest for R134a, followed by R236fa and the lowest R245fa. The same trend is also observed for the larger channel, as depicted in Fig. (4.19) for the larger $D_{in}=2.20\text{ mm}$ channel. According to Tabatabai et al. [108], the transition criterion between surface tension/shear dominated regime can be expressed in terms of force per unit length of the flow regime for the surface tension, shear and buoyancy forces. For surface tension dominant flows:

$$|F_{\sigma}| > |F_{shear}| + |F_{buoyancy}| \quad (4.1)$$

The surface tension force is a function of the void fraction and gradually decreases with increasing void fraction. The surface tension per unit length is defined as:

$$|F_{\sigma}/L_{bubble}| = 2\sigma(1 - \alpha)^{0.5} \quad (4.2)$$

while

$$|F_{shear}/L_{bubble}| = (\pi D_{bubble}\alpha)(f_l)\left(\frac{\rho_l u_l^2}{4}\right) \quad (4.3)$$

where f_l is the liquid phase Reynolds number as a function of liquid fraction. The buoyancy force per unit length is defined as:

$$|F_{buoyancy}/L_{bubble}| = g(\rho_l - \rho_v)A_v \quad (4.4)$$

and A_v represents the vapor phase area.

As void fraction increases during evaporation, the surface tension force is gradually suppressed while the shear force gradually increases. The high relative liquid-vapor phase density difference of R245fa together with the combined effect of this fluids high viscosity explains flow pattern transitions occurring at lower Weber numbers and superficial velocities in these miniscale channels.

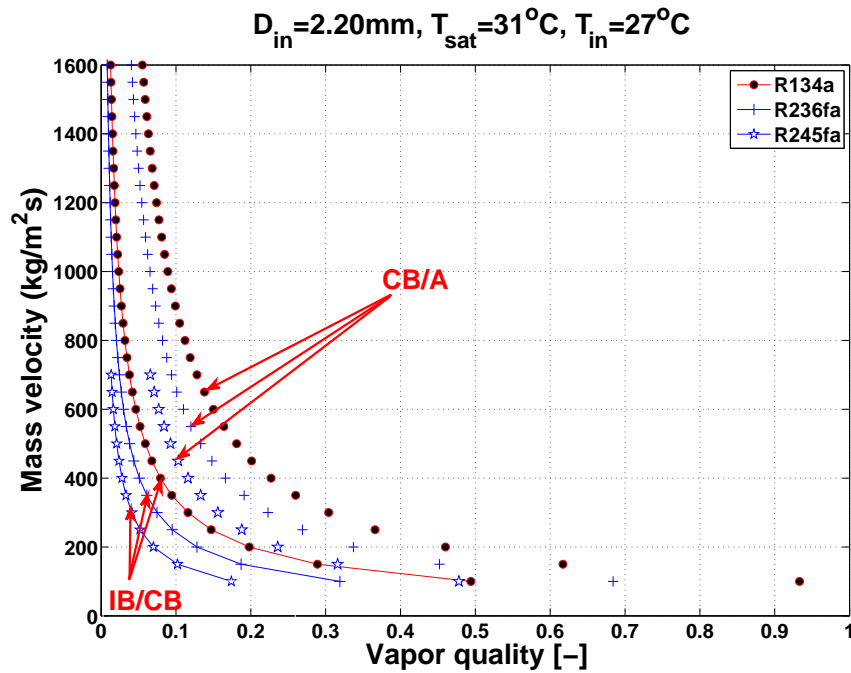
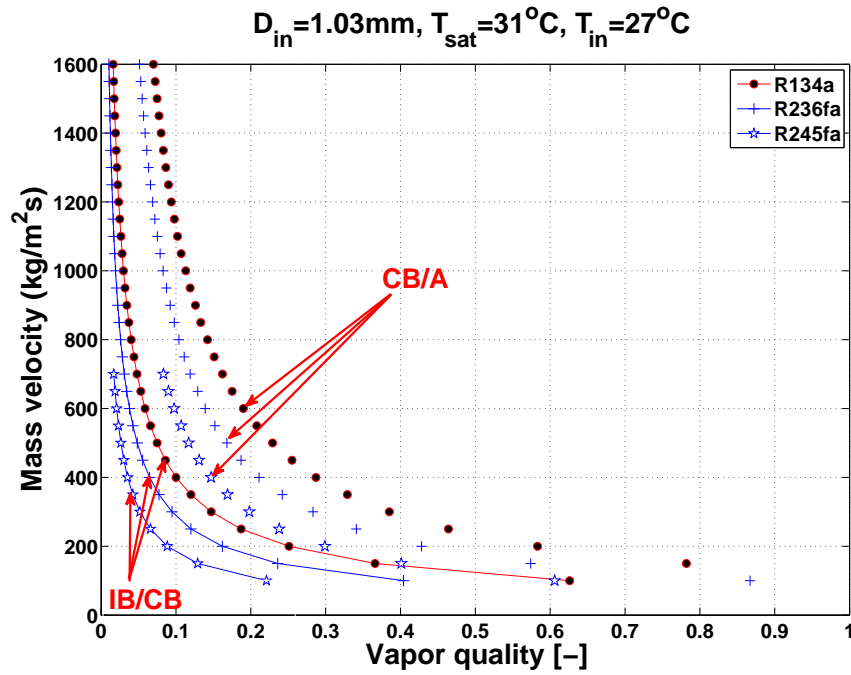


Figure 4.17: Flow patterns and transition lines for R134a, R236fa and R245fa at $T_{sat}=31^{\circ}\text{C}$ and $T_{in}=27^{\circ}\text{C}$; (a) $D_{in}=1.03\text{ mm}$ and (b) $D_{in}=2.20\text{ mm}$. (The symbols represent the transition lines observed in the database and not the data points)

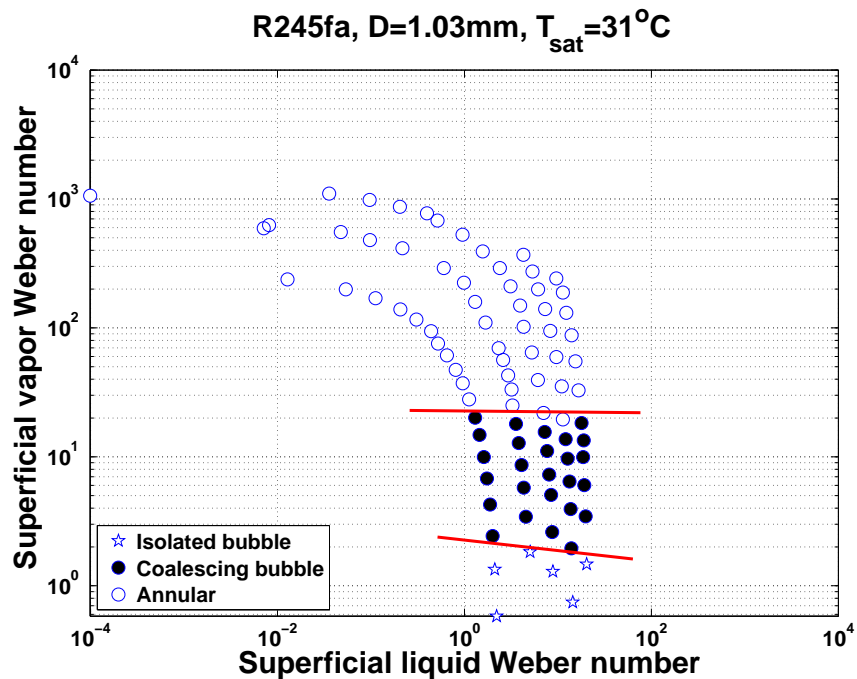
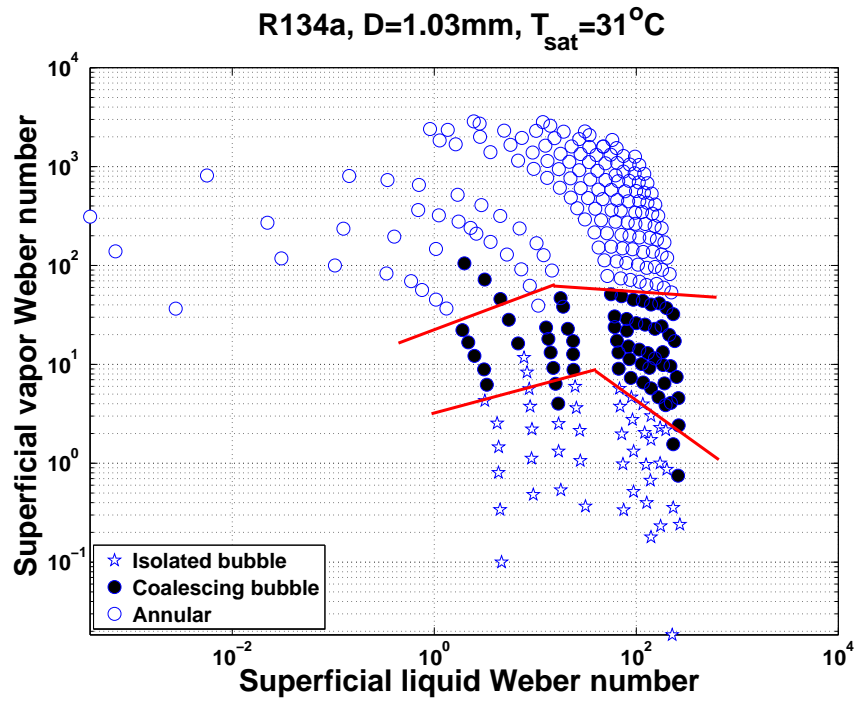


Figure 4.18: Flow patterns transition lines based on superficial Weber numbers in the $D_{in}=1.03\text{ mm}$, $T_{sat}=31\text{ }^\circ\text{C}$; (a) R134a, (b) R245fa.

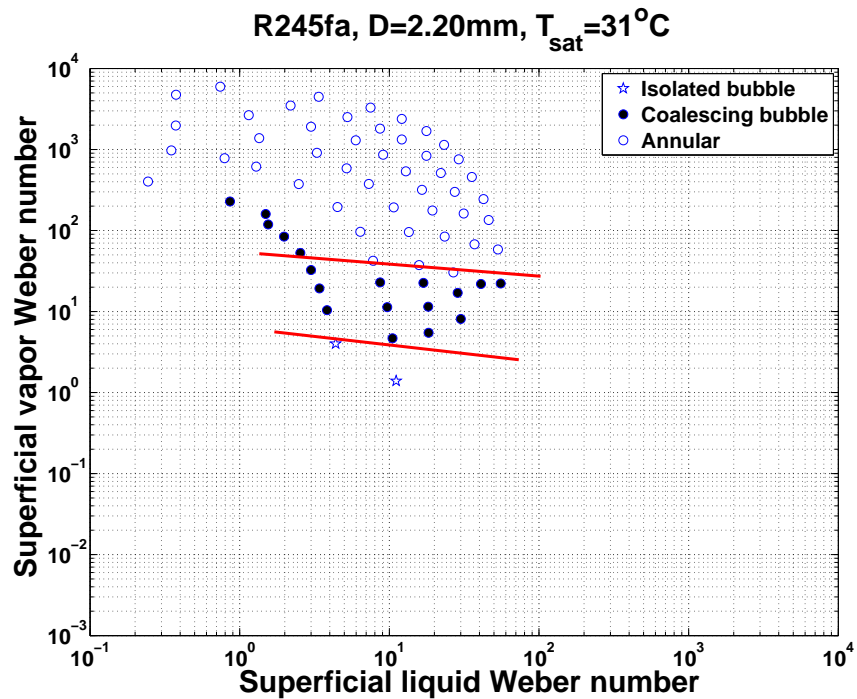
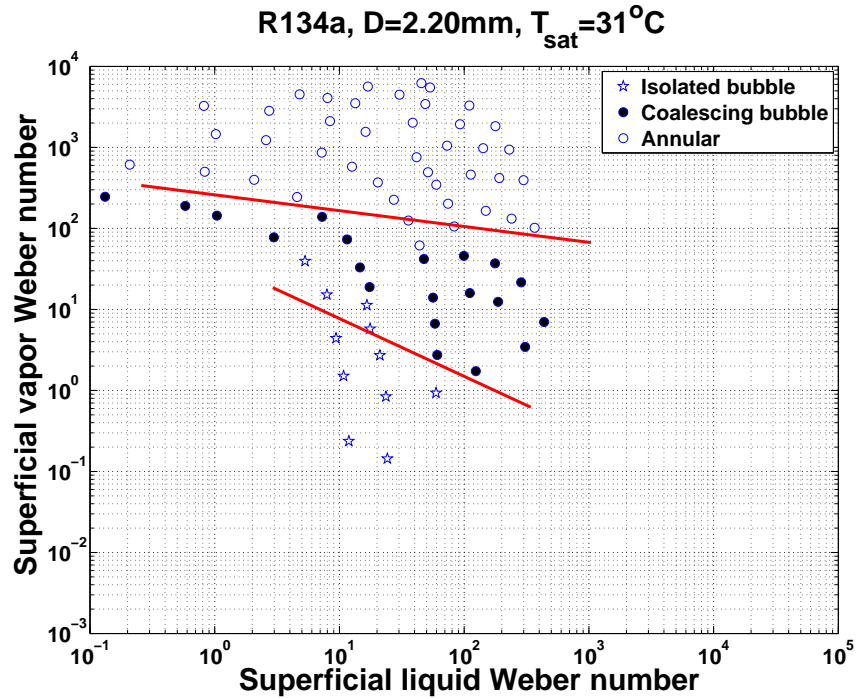


Figure 4.19: Flow patterns transition lines based on superficial Weber numbers in the $D_{in}=2.20\text{ mm}$, $T_{\text{sat}}=31\text{ }^\circ\text{C}$; (a) R134a, (b) R245fa.

4.3.3 Effects of Saturation Temperature

The effects of saturation temperature on flow pattern transitions is illustrated in Fig. (4.20). Comparing the figures, a mild shift in both the IB/CB and CB/A transition lines to lower vapor qualities for lower saturation temperatures was observed. This is visible for all the three refrigerants tested. At lower saturation temperatures, the surface tension, density and fluid viscosity increase, thus explaining the leftward expansion of the annular flow regime with increasing channel confinement.

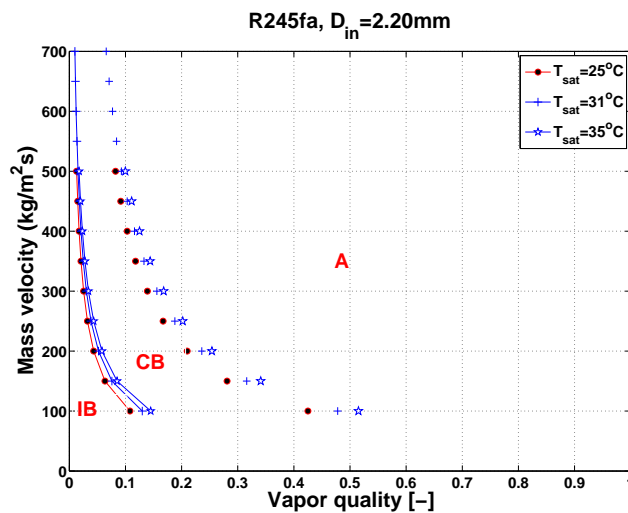
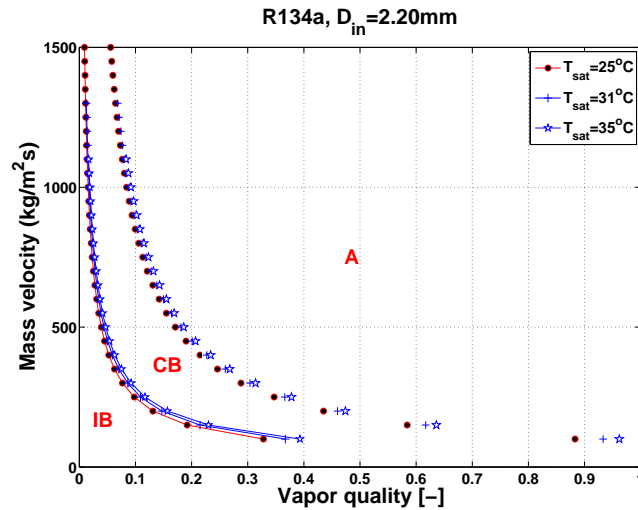
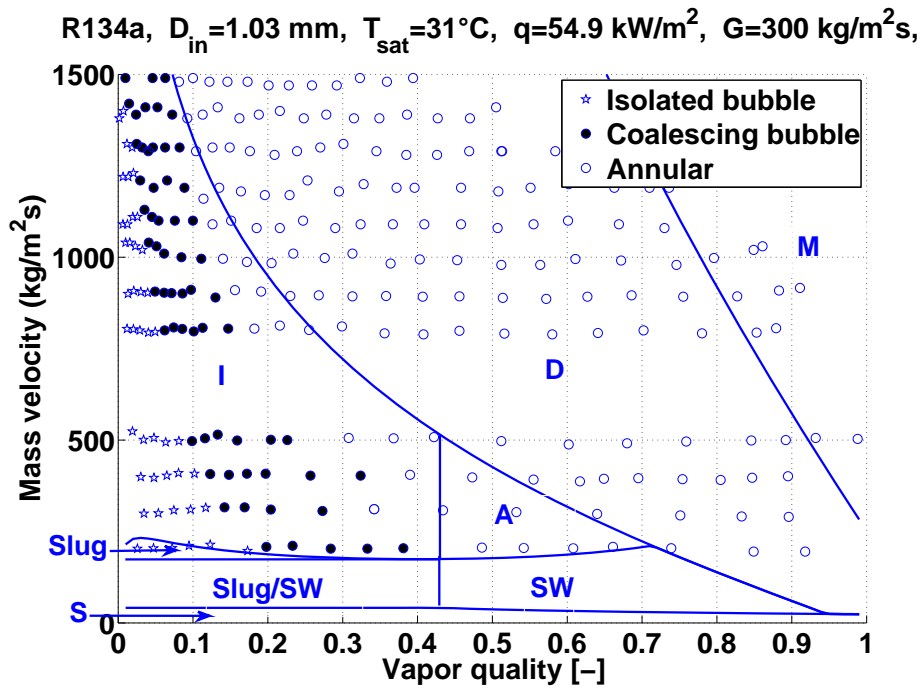


Figure 4.20: Flow patterns and transition lines for R134a, R236fa and R245fa for $T_{sat}=25, 31$ and $35\text{ }^{\circ}\text{C}$; (a) R134a and (b) R245fa. (The symbols represent the transition lines observed in the database and not the data points)

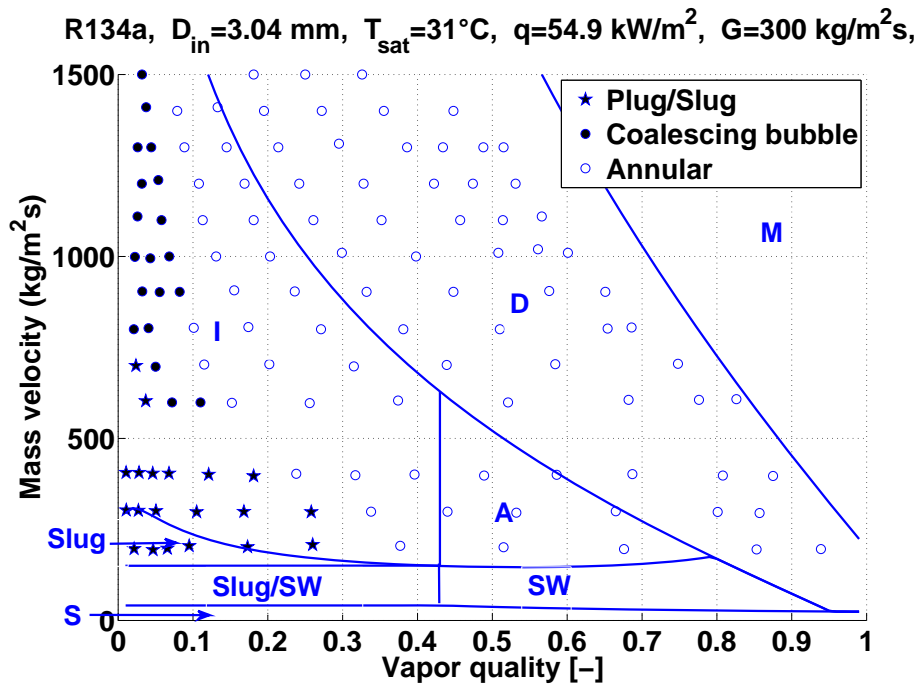
4.4 Flow Pattern Maps Comparisons

This section presents the current experimental flow pattern observations compared with the macroscale flow pattern map of Kattan et al. [4]. Fig. (4.21) illustrates the flow patterns prediction of Kattan extrapolated from $D_{in}=8 - 14 \text{ mm}$ to the $D_{in}=1.03$ and 3.04 mm channels tested here. The flow pattern predictions did not compare well with the current experimental data, in particular the annular flow and dryout zones. The flow pattern map of Kattan also predicted the IB/CB flow regime in their intermittent flow zone classified as plug and slug flows but with significant buoyancy effects. The stratified and stratified-wavy zone is not comparable as no flow regime data are available here at low enough mass velocities to reach these regimes. In conclusion, this macroscale flow pattern map was developed for macroscale sized tubes where buoyancy forces are dominant. However, one general trend can be observed when surface tension forces dominate is the gradual suppression of the macroscale intermittent flow regimes to IB(Taylor bubble) and CB flows while the annular flow regime expands when channel size decreases.

The microscale flow pattern map of Revellin et al. [24] extrapolated to the $D_{in}=1.03 \text{ mm}$ channel is shown in Fig. (4.22). The Revellin flow pattern map predicted well the CB/A flow pattern transition for R134a and R236fa but not for R245fa. The map predicts the IB/CB regime transition well at high mass velocities for all the fluids but less satisfactory for lower mass velocities.



(a)



(b)

Figure 4.21: Extrapolation of the macroscale flow pattern map of Wojtan [13] for R134a, $T_{sat}=31\text{ }^\circ\text{C}$; (a) $D_{in}=1.03\text{ mm}$ and (b) $D_{in}=3.04\text{ mm}$.

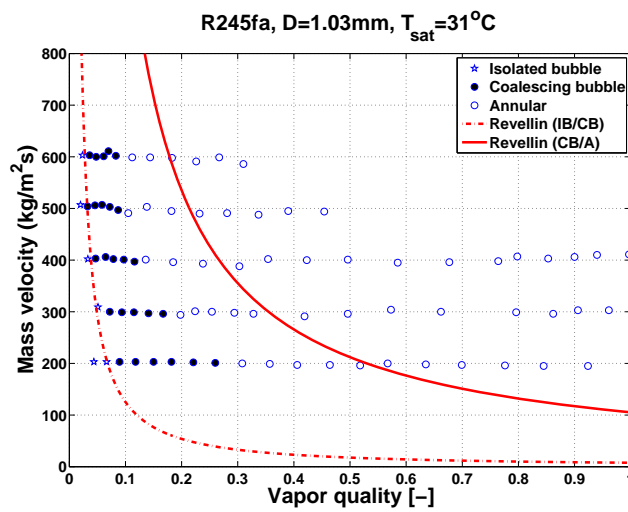
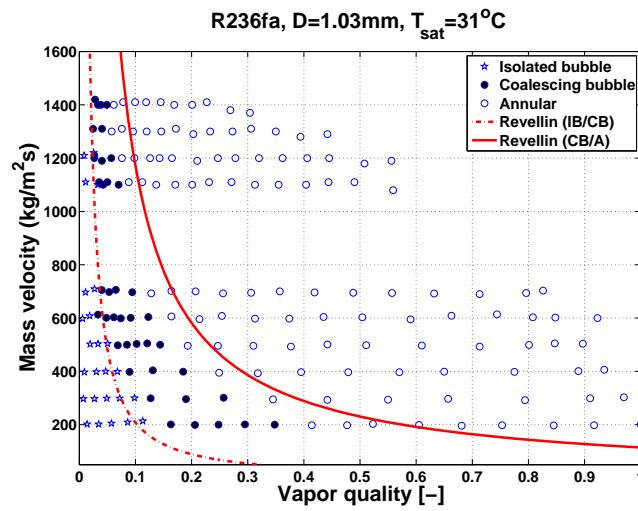
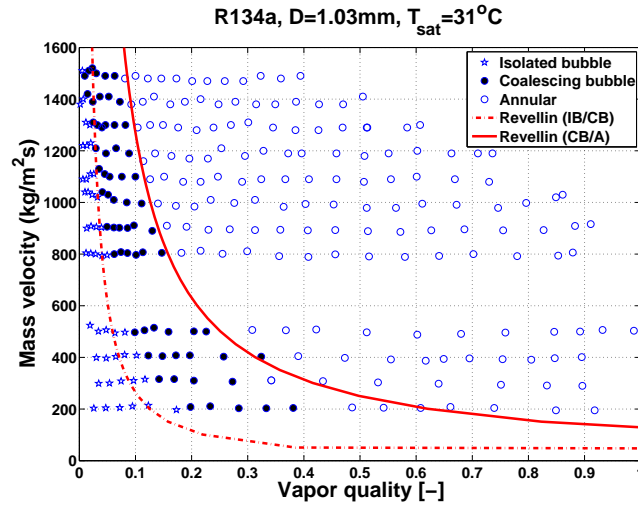


Figure 4.22: Extrapolation of the microscale flow pattern map of Revellin [24] for the $D_{in}=1.03$ mm channel; (a) R134a, (b) R236fa and (c) R245fa.

The comparison of Yang et al. [25] experimental flow pattern transition lines for R134a with the current experimental data are depicted in Fig. (4.23). However, it is to be noted the different classifications of the flow regimes by segregation into bubble, plug and slug flows as opposed to IB and CB flow definitions used in this manuscript. The bubble and plug flows are classified as IB bubble flow while the slug flow is termed CB flow in this manuscript. The slug to annular transition line of Yang compared well with the current experimental CB/A for the $D_{in}=2.20\text{ mm}$ channel and is also satisfactory for the $D_{in}=3.04\text{ mm}$ channel. The slug and plug flow regime compared very well for both the channels.

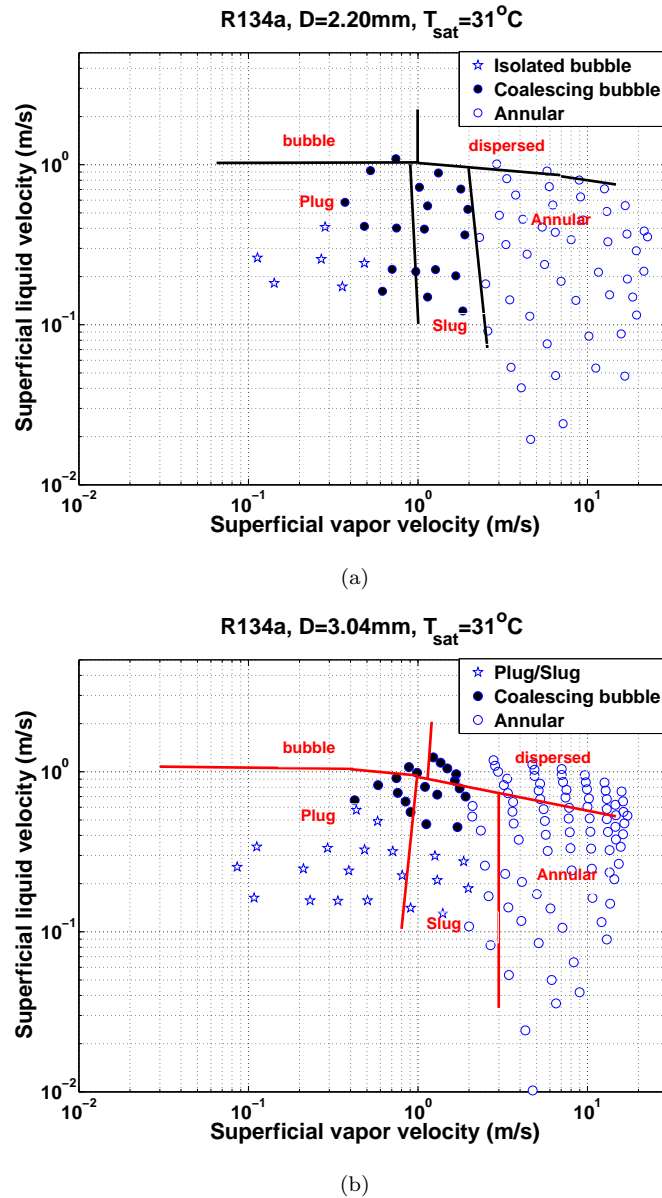


Figure 4.23: Flow pattern transition lines of Yang [25] for R134a; (a) $D_{in}=2.20\text{ mm}$ and (b) $D_{in}=3.04\text{ mm}$.

4.5 New Macro-Micro Flow Pattern Map

A new two-phase flow pattern map has been proposed here which is an improved version of the Revellin et al. [24] flow pattern map. The new flow pattern map was developed using the present current flows pattern data and the data of Revellin [24]. The proposed flow pattern map includes new dimensionless numbers accounting for the gravity, inertia and surface tension effects. The map also accounts for the heat flux effects for the prediction of the onset of coalescence. The proposed new flow pattern transition lines are as follows:

1. Isolated Bubble/Coalescing Bubble (IB/CB)

$$X_{IB/CB} = 0.36(Co^{0.20})(\mu_{VO}/\mu_{LO})^{0.65}(\rho_{VO}/\rho_{LO})^{0.9}Re_{VO}^{0.75}BO^{0.25}We_{LO}^{-0.91} \quad (4.5)$$

2. Coalescing bubble/Annular (CB/A)

$$X_{CB/A} = 0.047(Co^{0.05})(\mu_{VO}/\mu_{LO})^{0.7}(\rho_{VO}/\rho_{LO})^{0.6}Re_{VO}^{0.8}We_{LO}^{-0.91} \quad (4.6)$$

3. Plug–Slug/Coalescing bubble (S–P/CB) if $(X_{S-P/CB} < X_{CB/A})$

$$X_{S-P/CB} = 9(Co^{0.20})(\rho_{VO}/\rho_{LO})^{0.9}Fr_{LO}^{-1.2}Re_{LO}^{0.1} \quad (4.7)$$

The liquid Froude number is written as:

$$Fr_{LO} = \frac{G^2}{\rho_{LO}^2 g D_{in}} \quad (4.8)$$

4. Plug–Slug/Annular (S–P/A) if $(X_{S-P/CB} > X_{CB/A})$

$$X_{S-P/A} = X_{CB/A} \quad (4.9)$$

The subscripts VO and LO used in the terms above refer to vapor only and liquid only. The dimensionless numbers have been defined previously in the nomenclature section. The transition lines Eq. (4.7) and Eq. (4.9) are only used when the confinement number, $Co < 0.34$. This transition criterion was based on the current experimental conditions when transition from IB to Plug-Slug flow occurred at $T_{sat}=31$ °C in the $D_{in}=3.04$ mm channel.

	<i>R134a</i>	<i>R236fa</i>	<i>R245fa</i>
$Co, D_{in}=2.20$ (mm)	0.37	0.39	0.46
$Co, D_{in}=3.04$ (mm)	0.27	0.28	0.34

Table 4.1: A summary of the experimental confinements numbers at $T_{sat}=31$ °C for the $D_{in}=2.20$ and 3.04 mm channel.

Fig. (4.24) compares the new flow pattern transition lines with the transition lines of Revellin et al. [24] developed for the smaller $D_{in}=0.50$ and 0.80 mm channels.

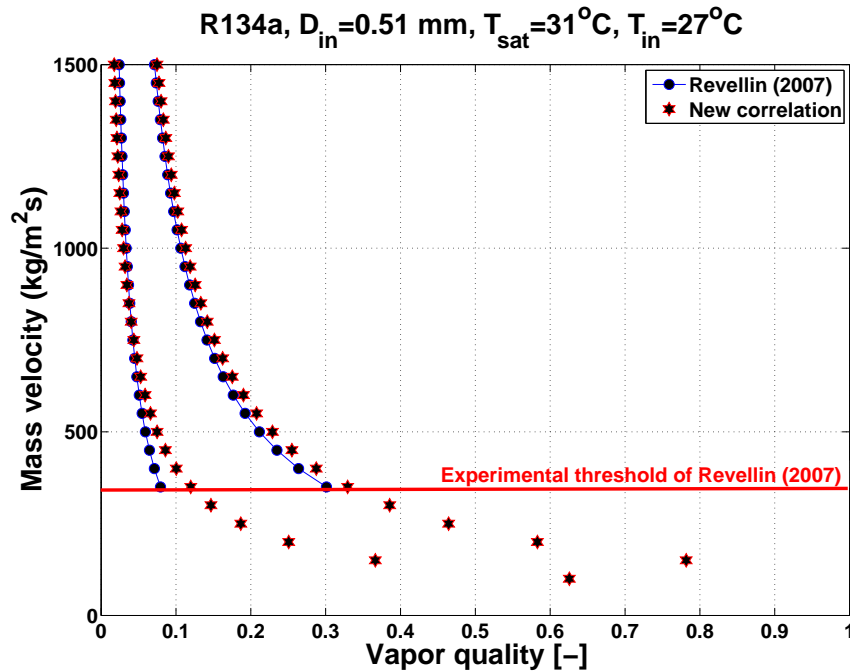


Figure 4.24: Comparison of the microscale flow pattern map of Revellin [24] and the new flow pattern map correlation for R134a, $D_{in}=0.51$ mm, $T_{sat}=31$ °C.

The newly proposed flow pattern map accurately predicts the experimental flow pattern transitions for channels with $D_{in}=0.50, 0.80, 1.03, 2.20$ and 3.04 mm channels for all the three fluids, R134a, R236fa and R245fa. For illustration purposes, Fig. (4.25)a and Fig. (4.25)b shows the comparison of the current experimental flow regime data with the new flow pattern map for the $D_{in}=2.20$ and 3.04 mm channels at $T_{sat}=31$ °C.

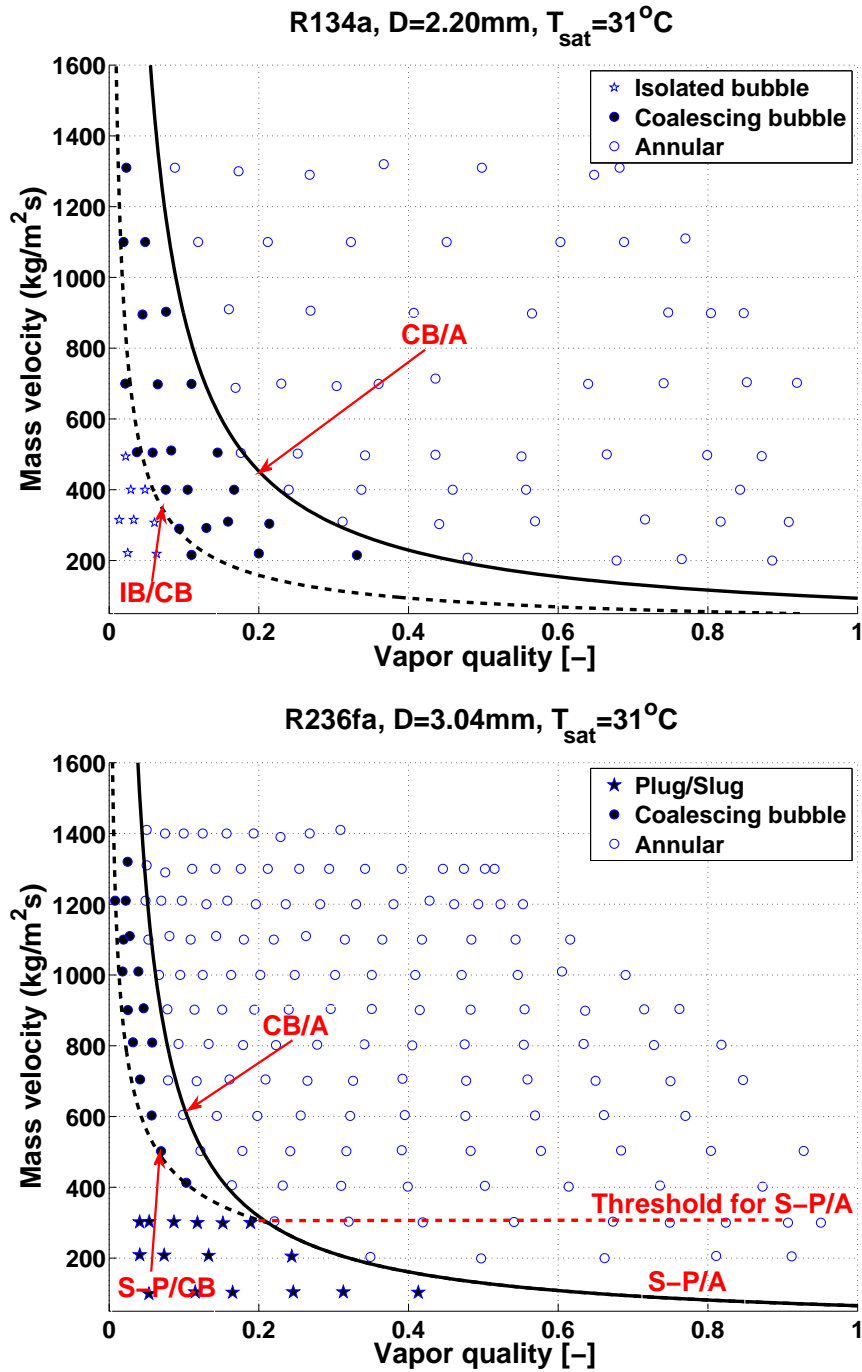


Figure 4.25: (a) R134a, $D_{in}=2.20\text{ mm}$ and (b) R236fa, $D_{in}=3.04\text{ mm}$.

4.6 Summary

In summary, the two-phase flow patterns and transitions have been observed to be a function of channel confinement, fluid property, mass velocity and saturation temperature. Three principal flow regimes (Isolated bubble, Coalescing bubble and Annular flow) were observed in the $D_{in}=1.03$ and 2.20 *mm* channels while another typical macroscale flow regime, namely the Slug-Plug flow pattern was present in the $D_{in}=3.04$ *mm* channel. As channel confinement increases, the respective IB/CB flow pattern transitions occur earlier and an expansion of the annular flow regime can be seen. For confinement number of $Co < 0.34$, it was found that the gravity force becomes more dominant. The fluid property such as the phase densities, surface tension and viscosity was also found to affect the transition between the flow regimes, namely the transition from surface tension dominated flows to inertia dominated flows. In conclusion, a new flow pattern map has been proposed to predict both microscale and miniscale flows.

Chapter 5

Flow Boiling Heat Transfer

This chapter presents the current experimental flow boiling heat transfer data acquired during this experimental campaign. The heat transfer data have been acquired for R134a, R236fa and R245fa in the $D_{in}=1.03, 2.20$ and 3.04 *mm* channels for a range of experimental conditions. This serves to investigate the effects of channel confinement, heat flux, mass velocity, saturation temperatures, sub-cooling and the effects of the working fluid properties on two-phase heat transfer as discussed in the following subsections.

For heat transfer measurements, 250 μm type *K* thermocouples were attached to the external wall of the channel to measure the external wall temperatures. The saturation pressures were measured with two absolute pressure transducers position at the inlet and the outlet of the test section. The data reduction procedure was discussed and presented earlier in Chapter 3.

5.1 Single-Phase Validation

The single-phase experimental heat losses obtained from sub-cooled fluid inlet–outlet temperature measurements across the evaporator for R134a and R245fa are compared to heat loss predictions, as shown in Fig. (5.1). The heat loss prediction method has been presented earlier in Chapter 3 to account for the heat losses to the ambient. Referring to Fig. (5.1), the heating efficiency is observed to increase with the heating power. This indicates that the lower values of $Q_{effective}$ are not relatively important as they are not indicative of the much larger heating power applied during the flow boiling tests, which were always above 9 *W*.

Fig. (5.2) and Fig. (5.3) illustrate the comparison of the experimental turbulent flow Nusselt numbers for R134a and R245fa versus the Gnielinski [26] and Dittus–Boelter [109] correlations. The experimental data showed very good agreement with the Gnielinski [26] correlation for both R134a and R245fa. The comparison yielded only a slight under prediction and was within $\pm 5\%$ for 84.6% of the R134a experimental data and $\pm 5\%$ for 96% of the R245fa data. Fig. (5.2) and Fig. (5.3) also illustrate the different sets of single-phase experimental tests being conducted on different days, with the data showing good reproducibility of the single-phase heat transfer results.

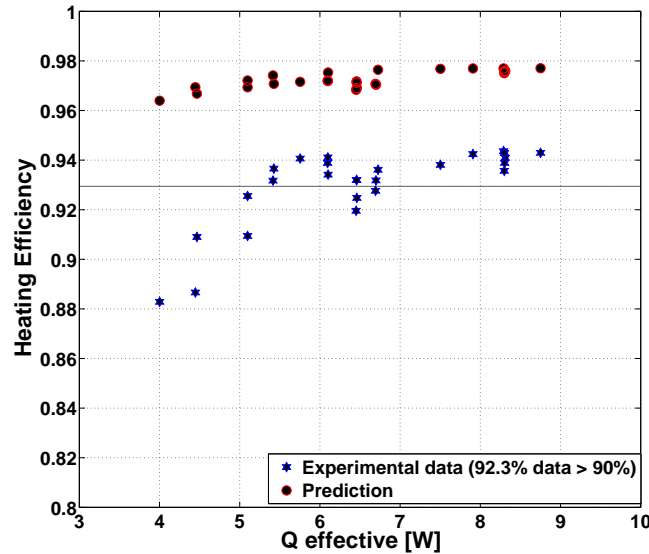


Figure 5.1: Single-phase experimental heat losses compared to predicted heating efficiency for R134a in the $D_{in}=1.03$ mm channel.

The single-phase heat transfer results for the $D_{in}=2.20$ and 3.04 mm channels (not shown here) also showed good comparison with the Gnielinski [26] correlation. In conclusion, the single-phase experiments serve as a good validation check for the $D_{in}=1.03$, 2.20 and 3.04 mm test sections before the initiation of flow boiling experiments.

5.2 Flow Boiling Heat Transfer

5.2.1 Flow Boiling Curves

Before the commencement of the flow boiling test campaign, a hysteresis analysis of the boiling heat transfer results was performed. The flow boiling map comparison for R134a and R245fa in the $D_{in}=1.03$ mm channel for the last thermocouple as an example is presented in Fig. (5.4). Comparing both these results, it was observed that the wall superheat for the onset of boiling differs significantly for R134a and R245fa, with R134a yielding the lowest wall superheat before the bubble nucleation onset in comparison with

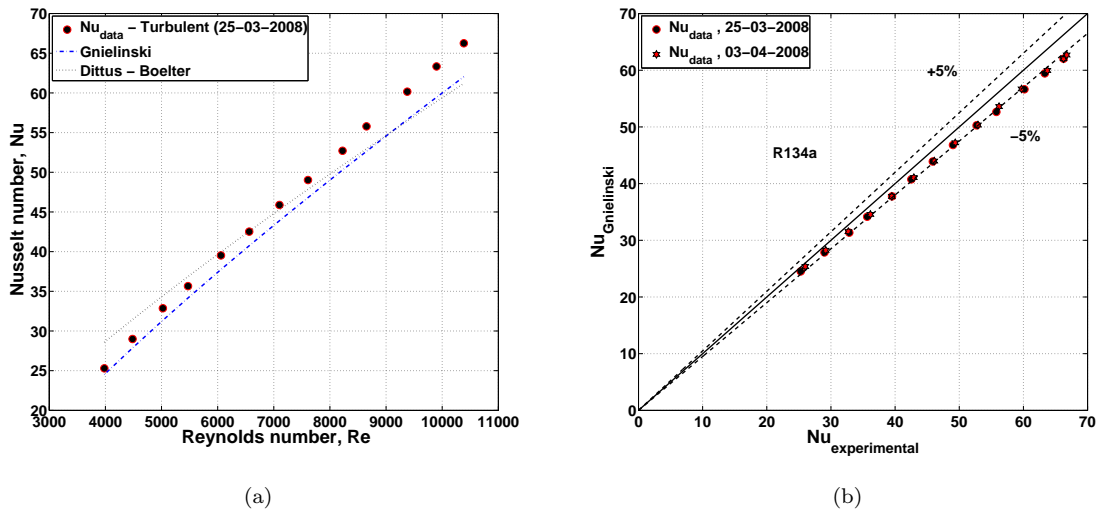


Figure 5.2: (a) Sub-cooled liquid heat transfer results for R134a in the $D_{in}=1.03\text{ mm}$ channel and (b) Experimental Nusselt numbers versus Gnielinski [26] correlation.

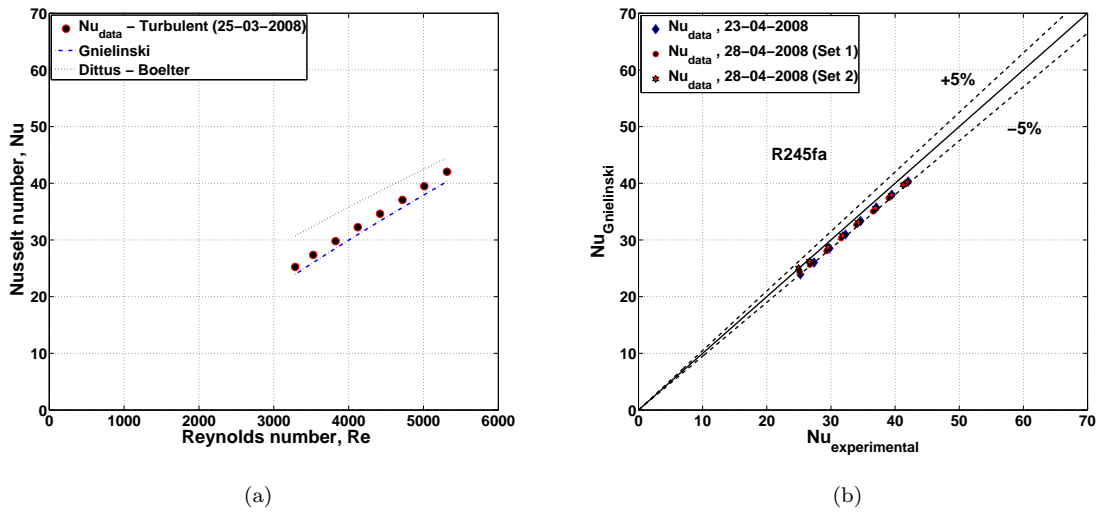


Figure 5.3: (a) Sub-cooled liquid heat transfer results for R245fa in the $D_{in}=1.03\text{ mm}$ channel and (b) Experimental Nusselt numbers versus Gnielinski [26] correlation.

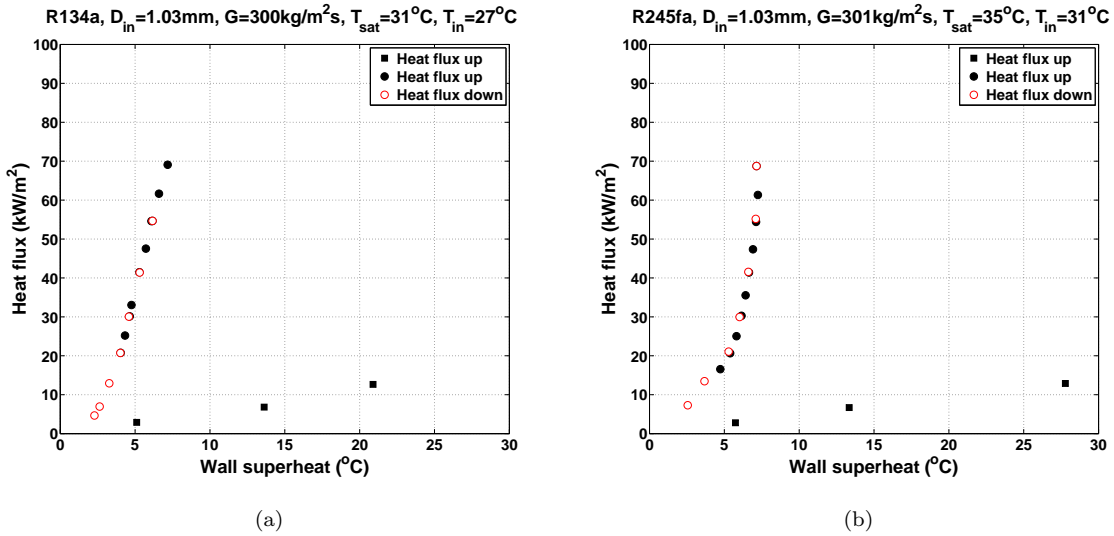


Figure 5.4: Boiling curve for the last thermocouple at heated length location of $Z=157$ mm in the $D_{in}=1.03$ mm channel; (a) R134a and (b) R245fa.

R245fa. As can be seen, the wall superheat increases with increasing heat flux until reaching a wall superheat of $T_{wall,sp} \approx 21$ K for R134a and $T_{wall,sp} \approx 26$ K for R245fa. After the onset of boiling, the wall superheat falls dramatically and increases with heat flux, reaching a value of $T_{wall,sp} \approx 7$ K for R134a and $T_{wall,sp} \approx 6.5$ K for R245fa. Decreasing the heat flux, it is clearly observed that there is no hysteresis on the wall superheat with increasing and decreasing heat flux, except for the onset of boiling.

For a given cavity size, the minimum radius of curvature of the bubble will occur when the bubble forms a hemisphere at the cavity mouth. The radius of curvature is then considered equal to the radius, (R) of the cavity opening. The pressure inside the bubble, P_{bub} is set to reach a maximum when $r=R$, which is the cavity radius. The pressure inside the bubble, P_{bub} is defined as:

$$P_{bub} = p + \frac{2\sigma}{r} \quad (5.1)$$

Before the onset of nucleation, the wall temperature required to trigger the onset of bubble growth is defined as in Eq. (5.6).

$$T_{wall} > T_{sat} + \frac{dT}{dp}(P_{bub} - P_V) \quad (5.2)$$

where P_V refers to the vapor pressure.

Referring to the pressure-temperature (P-T) diagram, the slope of the vapor pressure curve can be described by the *Clausius – Clapeyron* equation as defined in Eq. (5.3).

$$\frac{dP}{dT} = \frac{h_{lv}}{(\vartheta_V - \vartheta_L)T_{sat}} \quad (5.3)$$

where ϑ_V and ϑ_L refers to the specific volumes of the vapor and liquid. For $\vartheta_V \gg \vartheta_L$, Eq. (5.3) becomes

$$\frac{dP}{dT} = \frac{T_{sat}}{h_{lv}\rho_V} \quad (5.4)$$

The inequality as defined in Eq. (5.2) can be rewritten as:

$$T_{wall} > T_{sat} + \frac{2\sigma T_{sat}}{Rh_{lv}\rho_V} \quad (5.5)$$

Rearranging Eq. (5.5), the wall superheat, $T_{wall,sp}$ required for the onset of bubble growth becomes

$$T_{wall,sp} = \frac{2\sigma T_{sat}}{Rh_{lv}\rho_V} \quad (5.6)$$

The wall superheat, $T_{wall,sp}$ is shown to be a function of surface tension, vapor density and latent heat of vaporization. The higher surface tension characteristics of R245fa, with the combined effect of a lower vapor density explains the higher wall superheat reached to achieve the onset of nucleate boiling as depicted in Fig. (5.4).

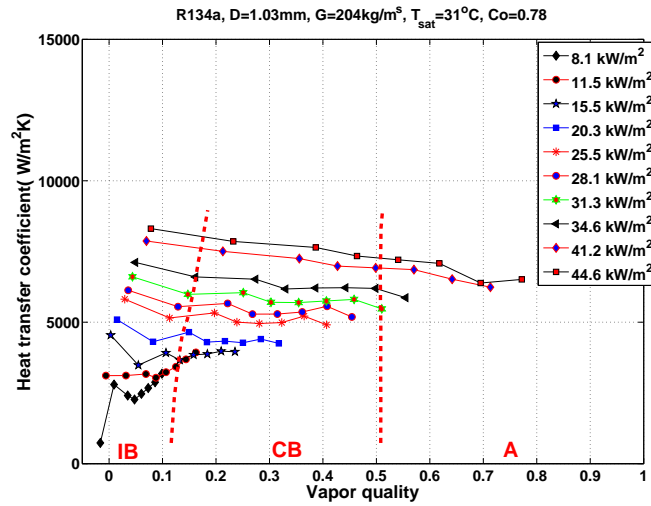
5.2.2 Effects of Channel Confinement

The effect of channel confinement on flow boiling heat transfer has been investigated in this experimental study. This section presents the flow boiling heat transfer data acquired during the experimental campaign for the three channels tested. As discussed in Chapter 4, the two-phase flow patterns and their transitions were significantly affected by channel confinement, resulting in the gradual expansion of the annular flow regime and the gradual suppression of the isolated bubble regime for confinement numbers $Co > 1.0$ as observed in Fig. (4.12)(a). A typical macroscale flow regime, the slug–plug was observed for confinement numbers $Co < 0.34$ at the lower range of mass velocities.

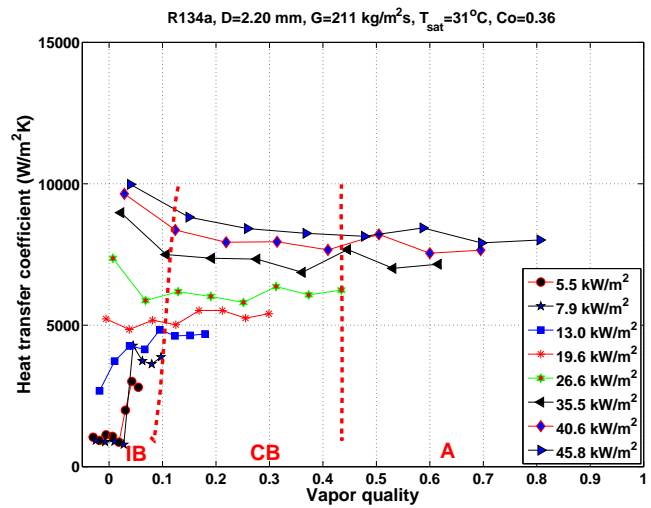
Fig. (5.5) illustrates the heat transfer coefficients for R134a at $T_{sat}=31\text{ }^\circ\text{C}$. The heat transfer results have been segregated into their respective flow regimes using the new flow pattern map proposed in Chapter 4. The classification of the heat transfer data into their respective flow regimes allows the identification of the dominant heat transfer mechanism affecting these small channels at the lower range of vapor quality, i.e. nucleate boiling in macro-channels or thin film evaporation in micro-channels. The individual vertical lines in the heat transfer figures represent the experimental flow regime transitions. The flow regimes are segregated into the isolated bubble (IB), the coalescing bubble (CB), the annular (A) and slug–plug (S-P) regimes for the three fluids. Comparing the figures in Fig. (5.5), the $D_{in}=3.04\text{ mm}$ channel with the lowest number of $Co=0.27$ has the highest heat transfer coefficient at lower vapor qualities corresponding to the slug–plug flow regime. In the slug–plug flow regime, small vapor bubbles were entrained in the liquid film surrounding the channel wall and the vapor bubbles violently coalesced with increasing vapor quality before the transition to the annular flow regime. As for the $D_{in}=2.20\text{ mm}$ channel with $Co=0.36$, the heat transfer coefficient in this surface tension dominated IB flow regime is also much higher in comparison with the heat transfer coefficients in the IB flow regime for the $D_{in}=1.03\text{ mm}$ channel with $Co=0.78$. The surface tension forces are much more dominant at lower vapor qualities when isolated bubbles are often encountered. Increasing the vapor quality, the surface tension forces becomes less important and the shear forces becomes dominant, corresponding to the transition from coalescing bubble to the annular flow regime.

The higher heat transfer trend in the IB flow regime can thus be attributed to higher nucleate boiling dominance for the larger channels with lower confinement numbers. The nucleate boiling mechanism described here is similar to nucleate boiling occurring in macro-scale channels. Then, a decreasing heat transfer trend was observed for the CB flow regime for $D_{in}=1.03$ and 2.20 mm channels and slug–plug flow regime for the $D_{in}=3.04$ mm channel. At higher vapor qualities, the heat transfer coefficients appear to converge at higher vapor qualities corresponding to convective boiling characterized by annular flow. The R134a data shown in Fig. (5.5)a conform to this explanation at the lower heat flux only. The heat transfer comparison for R236fa and R245fa at similar conditions, $G \approx 200$ kg/m²s, is shown in Fig. (5.6) and Fig. (5.7). In the IB flow regime, the heat transfer coefficients are higher for the larger channels with lower confinement numbers. A similar decreasing trend was also observed in the CB and S–P flow regime for both the fluids tested, conforming with the observations for R134a.

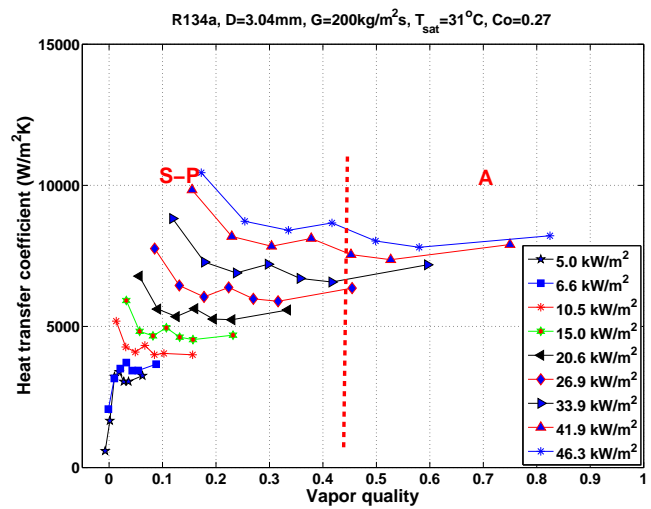
Comparing the results in Fig. (5.6), the heat transfer coefficients in the IB regime at similar heat fluxes for the $D_{in}=1.03$ mm channel with $Co=0.83$ are much lower than those in the $D_{in}=3.04$ mm channel, $Co=0.28$, while the data for $D_{in}=2.20$ mm channel, $Co=0.39$ fall in between. The results indicate a lower dependency of the heat transfer coefficient on heat flux when channel confinement increases. After the transition to annular flow, the heat transfer coefficient increased and converged for all the heat fluxes. This indicates a strong dominance of forced convection as the dominant flow boiling mechanism in this shear dominated regime. This trend is even more pronounced with R245fa as shown in Fig. (5.7). For the $D_{in}=1.03$ mm channel, $Co=1.02$, the results indicated a low heat flux effect on the heat transfer coefficient when compared to the $D_{in}=2.20$ mm channel. At higher vapor qualities, i.e. $x=0.70$, the heat transfer coefficient for the $D_{in}=1.03$ mm channel is on the order of 30 % higher than for the $D_{in}=3.04$ mm channel. Comparing the heat transfer coefficients in the IB flow regime for the three fluids in the $D_{in}=1.03$ mm channel, as illustrated in Fig. (5.5)a, Fig. (5.6)a, Fig. (5.7)a, R134a showed the highest heat flux dependency and yields the highest heat transfer coefficients, followed by R236fa and R245fa. In the annular flow regime, a reversed trend was observed where R245fa yields the highest heat transfer coefficients in comparison with R134a for $x=0.70$. From the heat transfer results, it was observed that effects of heat flux are gradually suppressed with increasing channel confinement, as illustrated in this case for R245fa $D_{in}=1.03$ mm channel with $Co=0.99$.



(a)

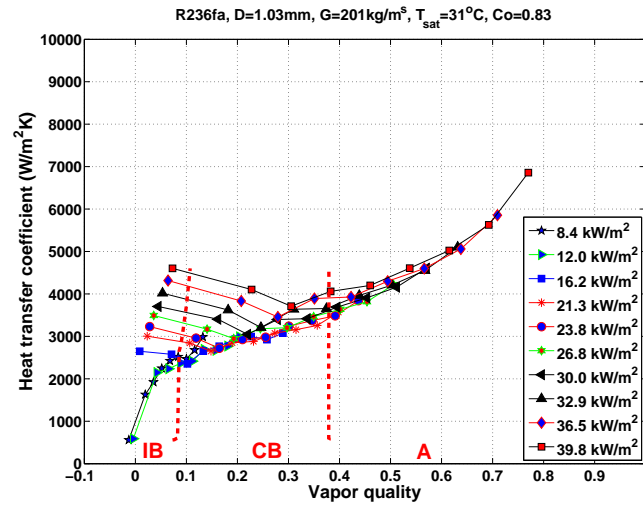


(b)

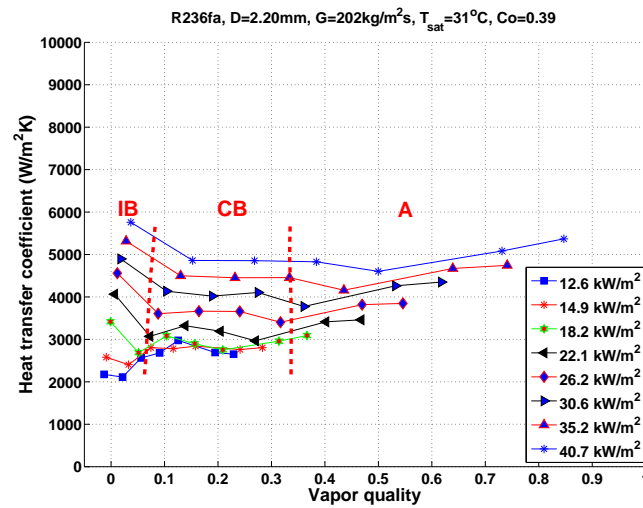


(c)

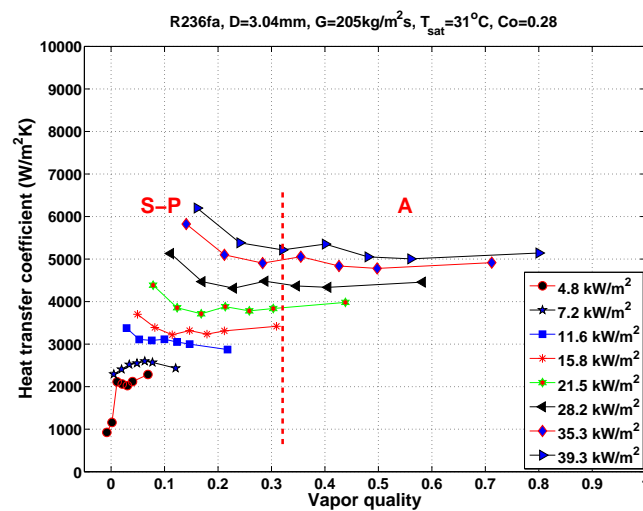
Figure 5.5: Heat transfer coefficients for R134a at $T_{\text{sat}}=31^\circ\text{C}$; (a) $D_{\text{in}}=1.03\text{mm}$ channel, $Co=0.78$, (b) $D_{\text{in}}=2.20\text{mm}$ channel, $Co=0.36$ (c) $D_{\text{in}}=3.04\text{mm}$ channel, $Co=0.27$.



(a)



(b)



(c)

Figure 5.6: Heat transfer coefficients for R236fa at $T_{\text{sat}}=31^\circ\text{C}$; (a) $D_{\text{in}}=1.03\text{ mm}$ channel, $Co=0.83$, (b) $D_{\text{in}}=2.20\text{ mm}$ channel, $Co=0.39$ (c) $D_{\text{in}}=3.04\text{ mm}$ channel, $Co=0.28$.

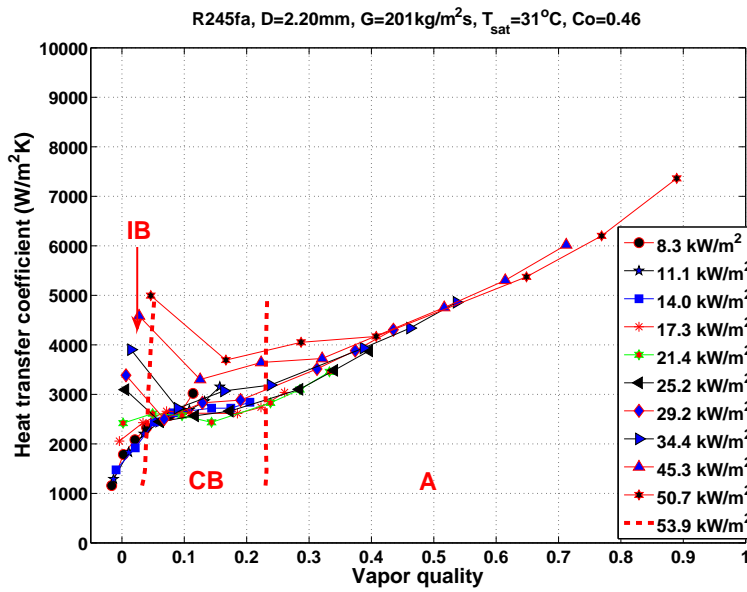
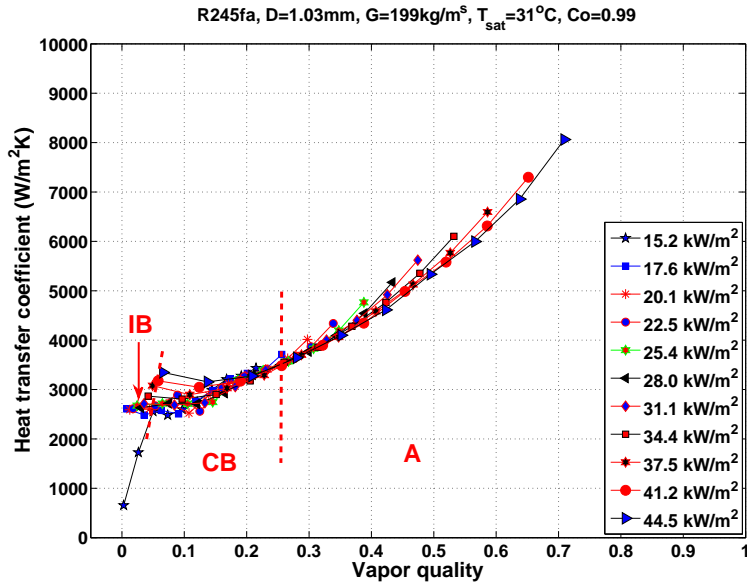
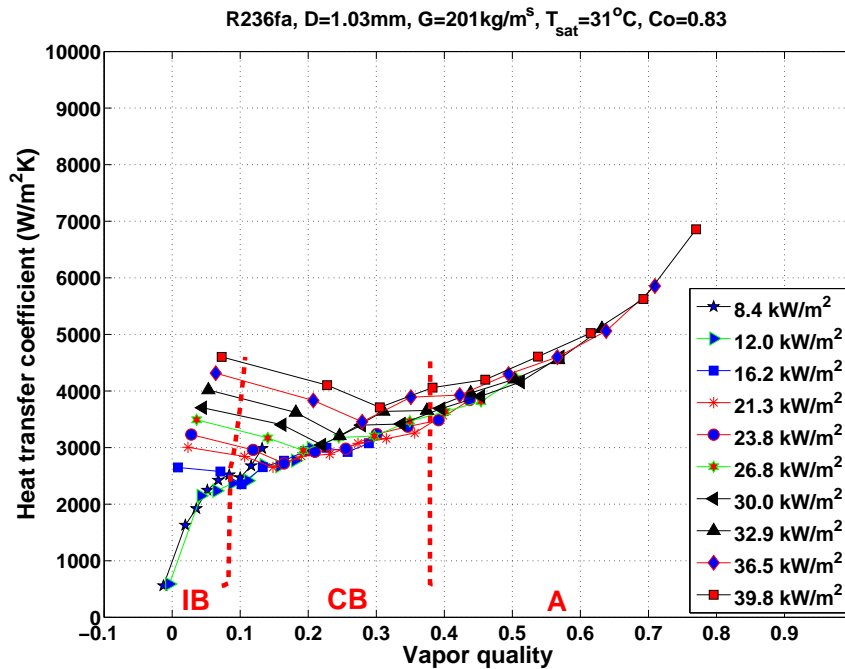


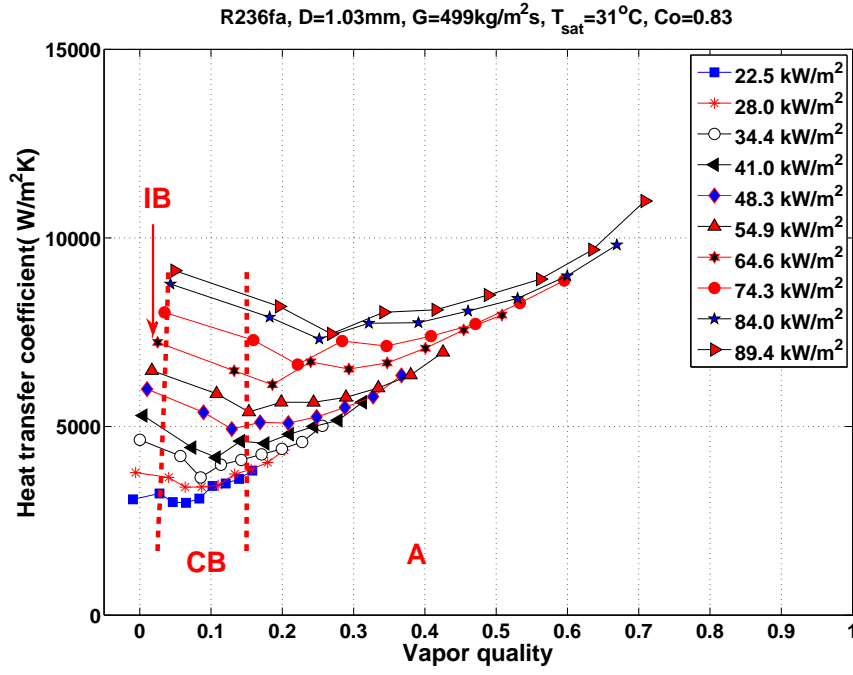
Figure 5.7: Heat transfer coefficients for R245fa at $T_{\text{sat}}=31^\circ\text{C}$; (a) $D_{in}=1.03\text{ mm}$ channel, $Co=0.99$ and (b) $D_{in}=2.20\text{ mm}$ channel, $Co=0.46$.

Fig. (5.8) depicts the heat transfer coefficients for R236fa in the $D_{in}=1.03\text{ mm}$ channel, $Co=0.83$ at $G \approx 200$ and $G \approx 500\text{ kg/m}^2\text{s}$. It can be seen that the flow pattern transition is a function of mass velocity, with the IB flow regime spanning a smaller range of vapor qualities and the expansion of the annular flow regime with increasing mass velocities. Comparing the two graphs, the heat transfer coefficients are similar in magnitude for a similar range of heat fluxes in the IB regime. This is not the case for the heat transfer coefficients in the annular flow regime, which is observed to be mass velocity dependent. The heat transfer coefficients for $G \approx 500\text{ kg/m}^2\text{s}$ is 80% higher than that of $G \approx 200\text{ kg/m}^2\text{s}$ at $x=0.60$. This indicates an increasing dominance of forced convection at higher mass velocities, justified by the rise of shear force dominance. With increasing interfacial shear forces, the rate of entrainment of small liquid bubbles into the vapor core will increase. As a consequence, the liquid film around the wall periphery becomes thinner thus explaining the higher heat transfer coefficients in the annular flow regime. Chapter 7 presents the results of the relative top-bottom film thickness measurements through image processing of the high speed videos acquired during this research campaign.

Fig. (5.9) on the other hand shows the heat transfer coefficients for R245fa in the $D_{in}=1.03\text{ mm}$ channel, $Co=0.99$ at $G \approx 200$ and $G \approx 500\text{ kg/m}^2\text{s}$. As expected, the heat transfer trends observations conform to the observations for R236fa. It is also seen that the heat transfer coefficients for $G \approx 500\text{ kg/m}^2\text{s}$ at $x=0.35$ are on the order of +100% higher in comparison with $G \approx 200\text{ kg/m}^2\text{s}$ thus indicating thin film evaporation as the dominant mechanism for small mini-scale channels.

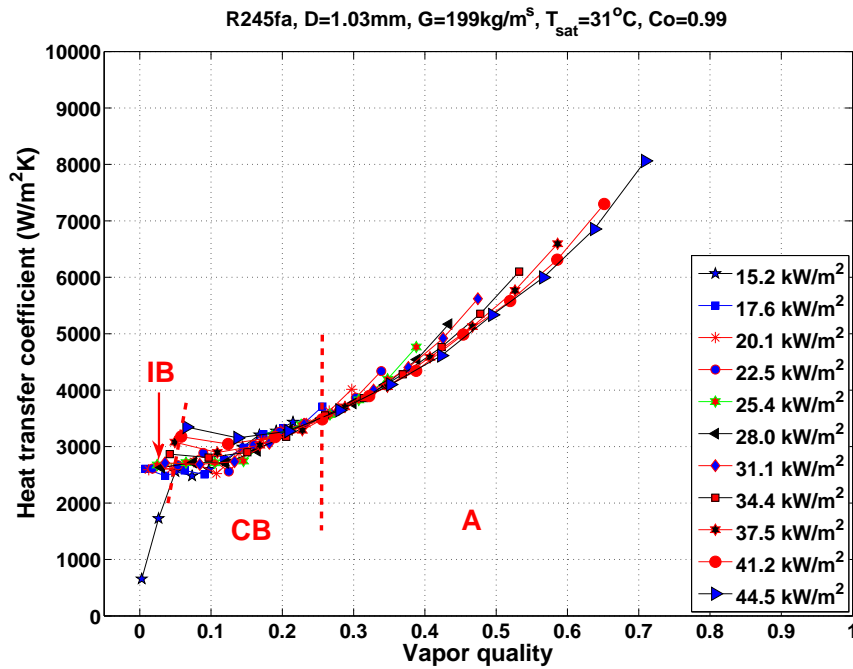


(a)

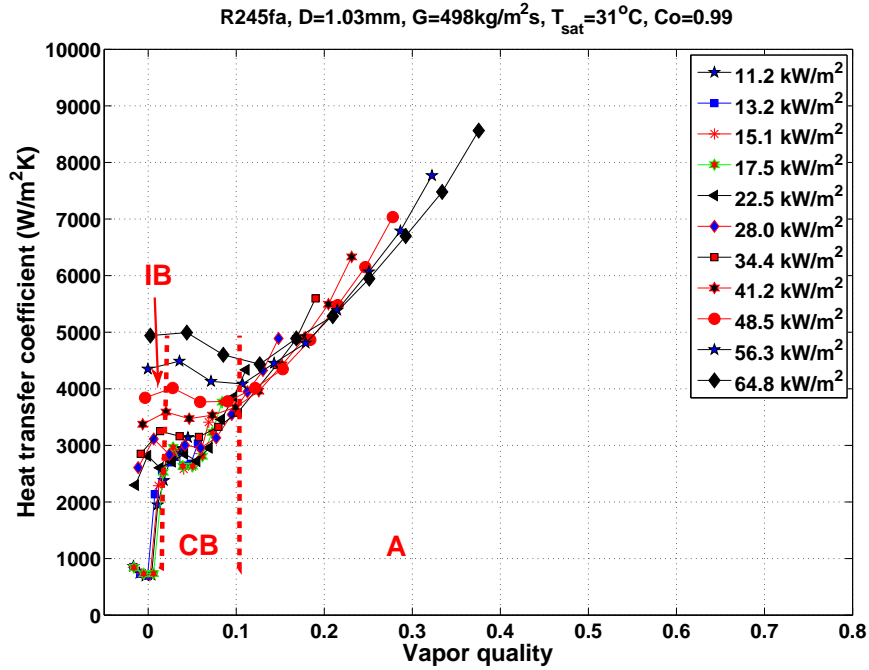


(b)

Figure 5.8: Heat transfer coefficients for R236fa in the $D_{in}=1.03\text{ mm}$ channel at $T_{sat}=31\text{ }^\circ\text{C}$, $Co=0.83$; (a) $G=201\text{ kg/m}^2\text{s}$ and (b) $G=499\text{ kg/m}^2\text{s}$.



(a)



(b)

Figure 5.9: Heat transfer coefficients for R245fa in the $D_{in}=1.03\text{ mm}$ channel at $T_{sat}=31\text{ }^\circ\text{C}$, $Co=0.99$; (a) $G=199\text{ kg/m}^2\text{s}$ and (b) $G=498\text{ kg/m}^2\text{s}$.

5.2.3 Effects of Fluid Properties

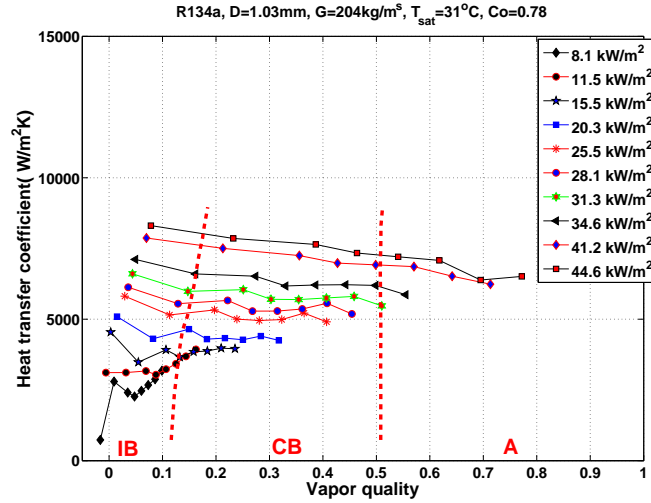
The effects of fluid properties on flow boiling heat transfer in these small channels were investigated during this experimental campaign. The comparison of the fluid properties for the refrigerants tested is shown in Fig. (5.10).

Properties	Refrigerants				
	R134a	R236fa	% variation with R134a	R245fa	% variation with R134a
Pressure (bar)	7.9257	3.3148	-58.2%	1.8421	-76.8%
Liquid Density (kg/m^3)	1183.5	1339.3	13.2%	1322.1	11.7%
Vapor Density (kg/m^3)	38.65	22.26	-42.4%	10.52	-72.8%
Liquid Enthalpy (kJ/kg)	243.17	238.56	-1.9%	240.44	-1.1%
Vapor Enthalpy (kJ/kg)	415.3	380.9	-8.3%	427.16	2.9%
Liquid Entropy (kJ/kg-K)	1.1482	1.1331	-1.3%	1.1398	-0.7%
Vapor Entropy (kJ/kg-K)	1.7142	1.6011	-6.6%	1.7538	2.3%
Liquid Cp	1.4511	1.2799	-11.8%	1.3355	-8.0%
Liquid Viscosity ($\mu\text{Pa}\cdot\text{s}$)	180.85	264.88	46.5%	377.5	108.7%
Liquid Prandtl	3.341	4.771	42.8%	5.848	75.1%
Surf. Tension (mN/m)	7.286	9.360	28.5%	13.275	82.2%

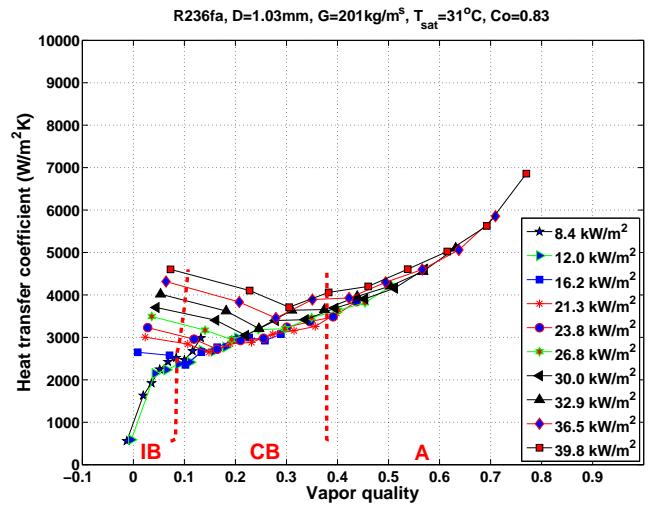
Figure 5.10: Comparison of refrigerant properties at $T_{sat}=31\text{ }^\circ\text{C}$.

Fig. (5.11) illustrates the flow boiling heat transfer coefficients for R134a, R236fa and R245fa at $T_{sat}=31\text{ }^{\circ}\text{C}$, $G \approx 200\text{ kg/m}^2\text{s}$ in the $D_{in}=1.03\text{ mm}$ channel, corresponding to confinement numbers $Co=0.78$, 0.83 and 0.99 respectively. Comparing the three fluids, R134a has the highest heat transfer coefficients at lower vapor qualities corresponding to the IB flow regimes, followed by R236fa and R245fa. This is probably due to the higher pressure characteristics of R134a as seen in increasing heat transfer coefficients with saturation temperature, in comparison with the two other fluids. On the other hand, surface tension effects are most dominant for R245fa among the three, thus representing the highest confinement for the $D_{in}=1.03\text{ mm}$ channel $T_{sat}=31\text{ }^{\circ}\text{C}$. The higher surface tension of R245fa also yields the lowest IB/CB and CB/A transition vapor quality flow. After the onset of boiling at $x \approx 0$, a drop in heat transfer can be observed for R134a and R236fa, but was not clearly observed for R245fa due to the small 'width' of the IB region. The heat transfer drop at these very small vapor qualities is probably related to the transition from pure bubbly flow to bubbly/elongated bubble through evaporation and the coalescence phenomena at higher vapor qualities. Similar heat transfer trends were also observed for the three fluids with the same saturation condition for $G \approx 300\text{ kg/m}^2\text{s}$ as published earlier in Ong et al. [81].

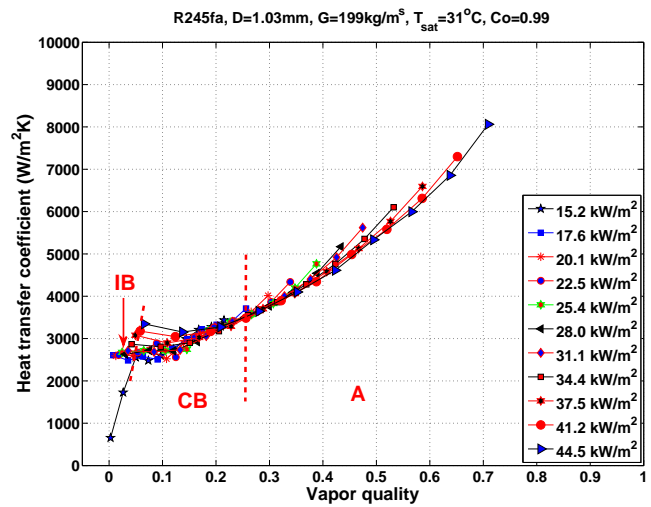
Another comparison of the heat transfer coefficients for the three different fluids at higher mass velocities, $G \approx 500\text{ kg/m}^2\text{s}$ is depicted in Fig. (5.12) in the $D_{in}=1.03\text{ mm}$ channel. The same decreasing trend was observed for R236fa and R245fa but was observed for R134a only at moderate heat fluxes. A mild converging heat transfer trend was observed for R134a at $G \approx 500\text{ kg/m}^2\text{s}$, corresponding to the annular flow regime. This justified the rising dominance of convective boiling, which is normally associated with a rising trend in heat transfer coefficient versus vapor quality as the dominant heat transfer mechanism. A monotonically converging trend was also observed for the other two fluids. Among the three fluids tested, the heat transfer coefficients for R245fa showed less dependence on heat flux when compared to R236fa and the highest for R134a at small vapor qualities. At higher vapor qualities, a steep converging heat transfer coefficient trend was more pronounced for R245fa as compared to R134a, indicating the dominance of film evaporation for this fluid. From the experimental observations, one can conclude that R134a illustrated a higher heat flux effect followed by R236fa and R245fa at low vapor qualities. The gradual suppression of heat flux effects and an increasing dominance of forced convection is due to higher channel confinement effects as shown in the confinement numbers for the three different fluids.



(a)

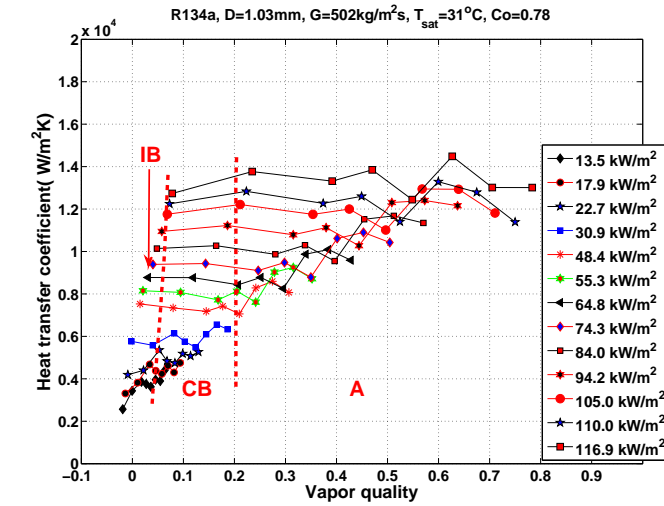


(b)

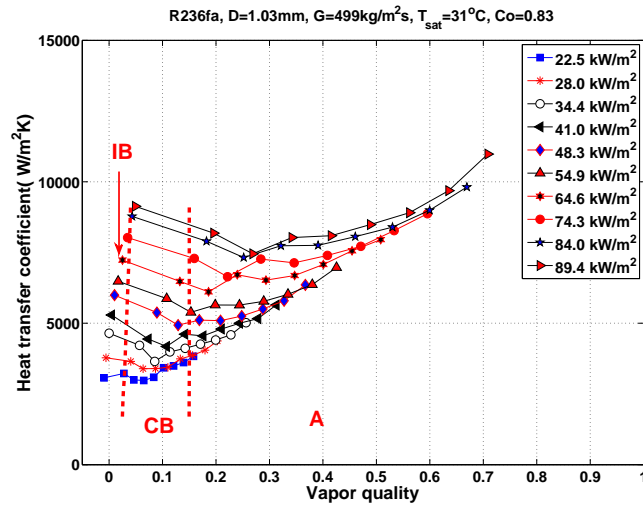


(c)

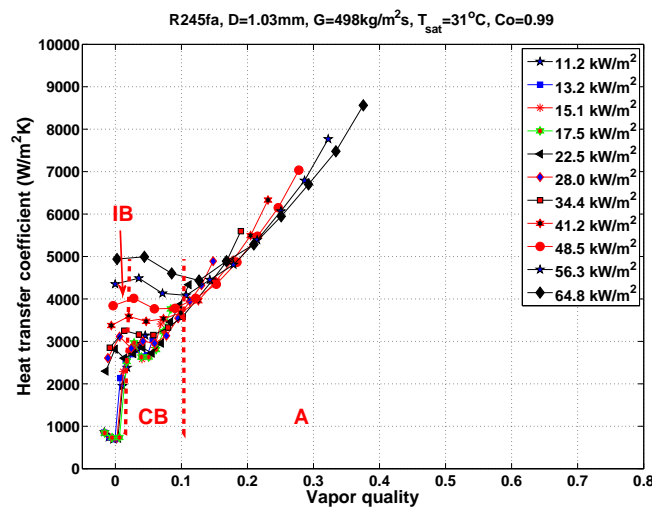
Figure 5.11: Heat transfer comparison for R134a, R236fa and R245fa in the $D_{in}=1.03\text{ mm}$ channel at $T_{\text{sat}}=31^\circ\text{C}$, $G \approx 200\text{ kg/m}^2\text{s}$; (a) $Co=0.78$, (b) $Co=0.83$ and (c) $Co=0.99$.



(a)



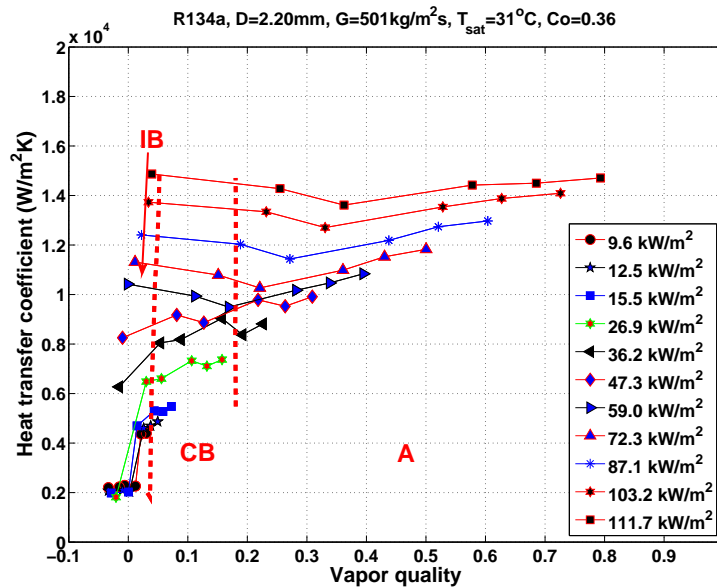
(b)



(c)

Figure 5.12: Heat transfer comparison for R134a, R236fa and R245fa in the $D_{in}=1.03\text{ mm}$ channel at $T_{\text{sat}}=31^\circ\text{C}$, $G \approx 500\text{ kg/m}^2\text{s}$; (a) $Co=0.78$, (b) $Co=0.83$ and (c) $Co=0.99$.

Fig. (5.13) and Fig. (5.14) present the heat transfer coefficients for $G \approx 500 \text{ kg/m}^2\text{s}$ at $T_{\text{sat}}=31 \text{ }^\circ\text{C}$ in the $D_{\text{in}}=2.20$ and 3.04 mm channels. With increasing channel size, a lower confinement number was encountered. At lower confinement numbers, the surface tension forces become less dominant in comparison with the buoyancy and shear forces. As shown in Fig. (5.12), Fig. (5.13) and Fig. (5.14), it was observed that the heat transfer coefficients in the IB flow regime increase with increasing channel size for all the three fluids. As explained before, the higher heat transfer coefficients for the $D_{\text{in}}=3.04 \text{ mm}$ channel are attributed to the higher nucleate boiling dominance similar to macro-scale channels. For the CB and annular flow regimes, R134a also poses the highest heat transfer coefficients among the three fluids except for R245fa in the $D_{\text{in}}=1.03$ channel due to insufficient data. In conclusion, the three fluids pose different heat transfer characteristics with R134a being the most heat flux dependent while R245fa being the most vapor quality dependent. It is sufficient to conclude that the confinement number only illustrates the effects of heat flux dependency at low vapor qualities when surface tension forces are dominant.



(a)

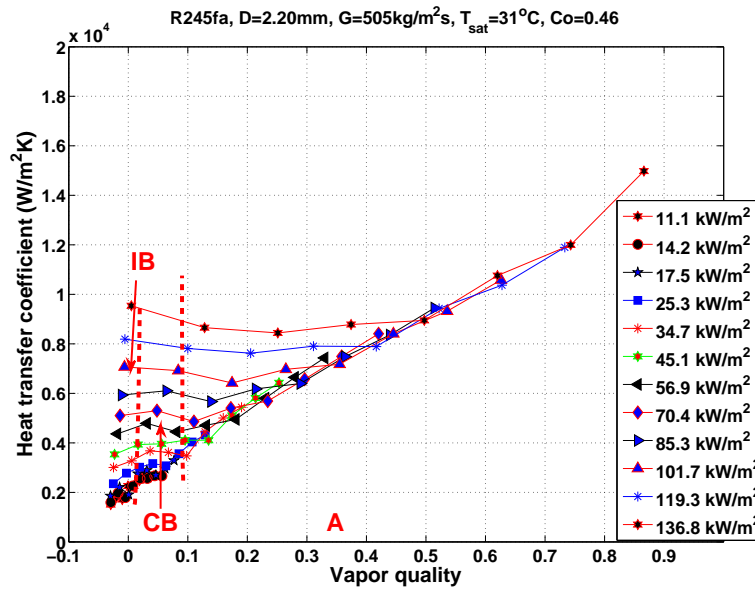
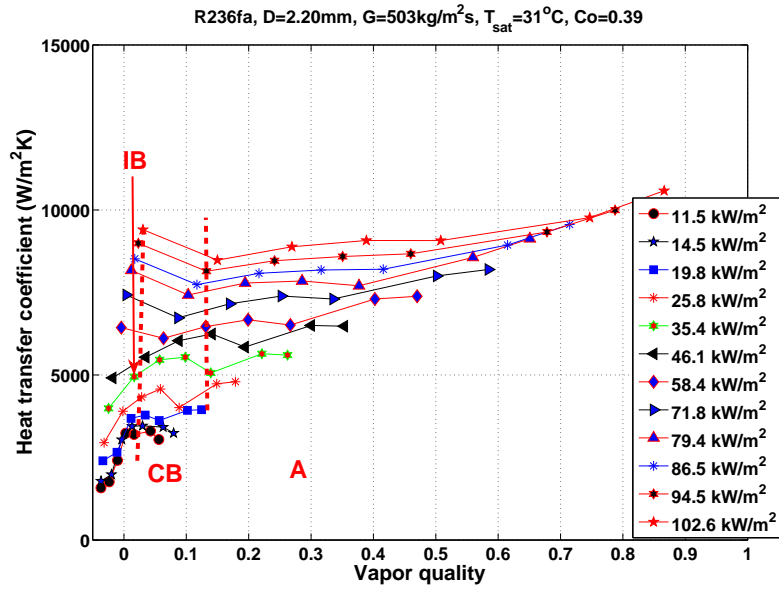
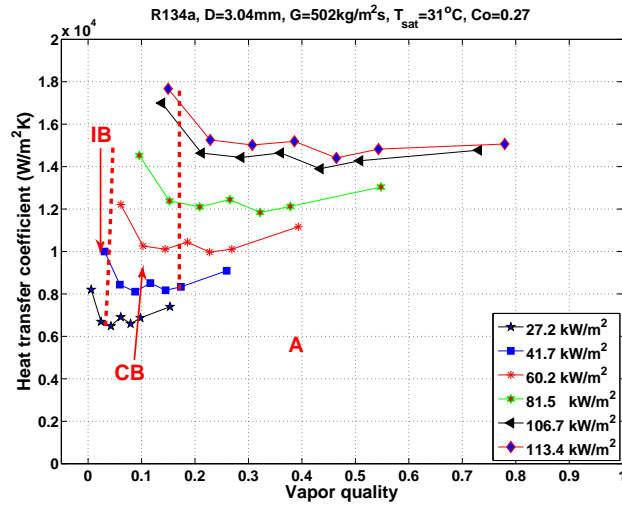
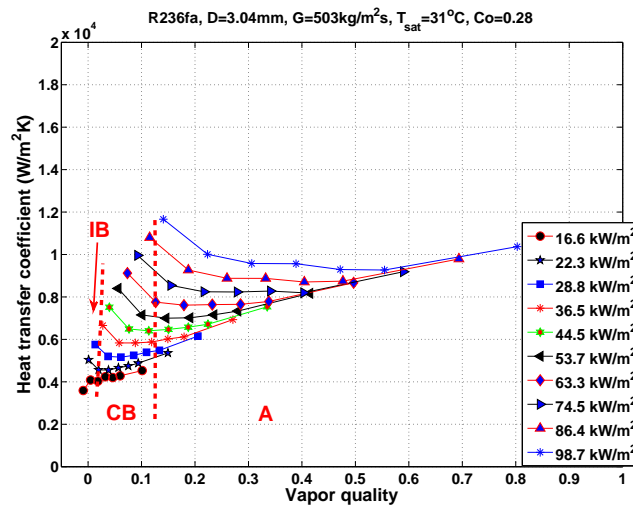


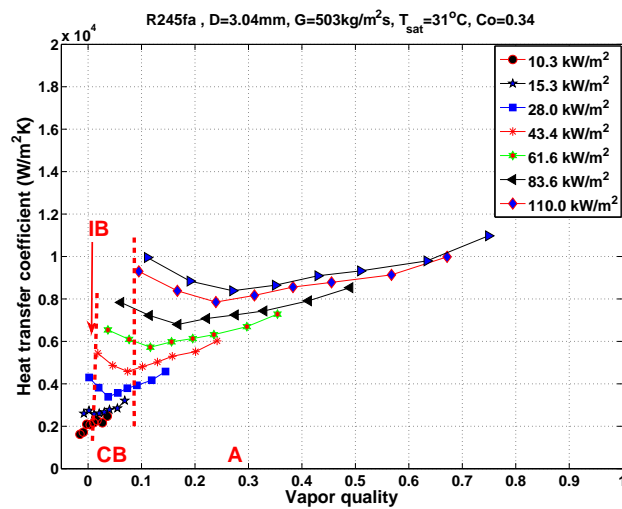
Figure 5.13: Heat transfer comparison for R134a, R236fa and R245fa in the $D_{in}=2.20\text{ mm}$ channel at $T_{sat}=31\text{ }^\circ\text{C}$, $G \approx 500\text{ kg/m}^2\text{s}$; (a) $Co=0.36$, (b) $Co=0.39$ and (c) $Co=0.46$.



(a)



(b)

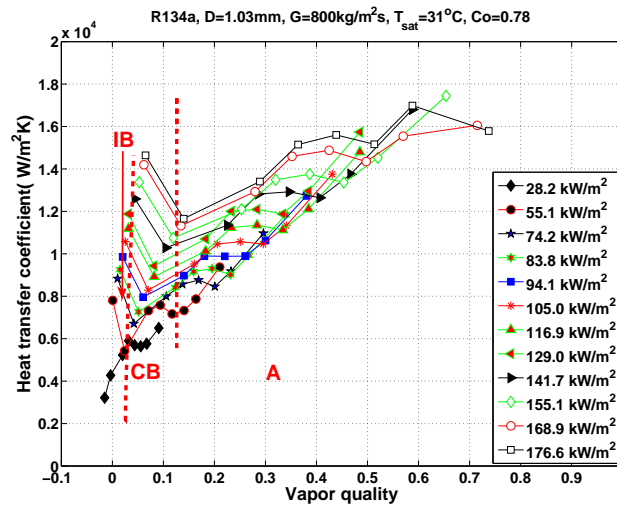


(c)

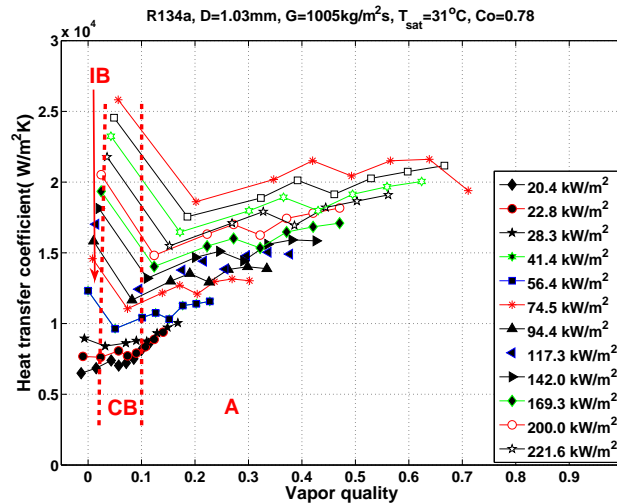
Figure 5.14: Heat transfer comparison for R134a, R236fa and R245fa in the $D_{in}=3.04\text{ mm}$ channel at $T_{\text{sat}}=31^\circ\text{C}$, $G \approx 500\text{ kg/m}^2\text{s}$; (a) $Co=0.27$, (b) $Co=0.28$ and (c) $Co=0.34$.

5.2.4 Effects of Mass Velocity

As discussed previously in Chapter 4, the flow pattern transitions are dependent on the mass velocity. At higher mass velocities, the flow pattern transitions occur earlier at lower vapor qualities and this results in the gradual suppression of the IB and CB flow regimes and the expansion of the annular flow regime. With the expansion of the annular flow regime, forced convection is expected to dominate earlier which is normally associated with a rising trend in heat transfer coefficient versus vapor quality, more easily seen at lower heat fluxes. Fig. (5.15) presents the heat transfer results for R134a in the $D_{in}=1.03$ mm channel for $G \approx 800$ kg/m²s and $G \approx 1200$ kg/m²s at $T_{sat}=31$ °C.



(a)

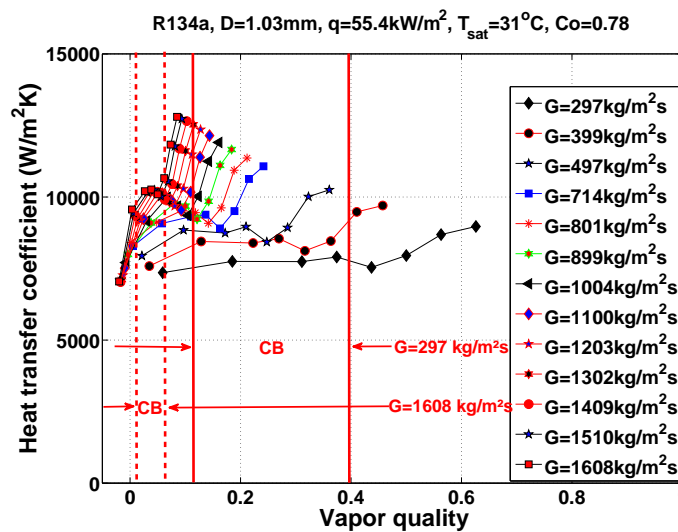


(b)

Figure 5.15: Mass velocity effects on heat transfer for R134a in the $D_{in}=1.03$ mm channel at $T_{sat}=31$ °C, $Co=0.78$; (a) $G \approx 800$ kg/m²s and (b) $G \approx 1000$ kg/m²s.

Comparing the results in Fig. (5.15), it is clear that the heat transfer coefficient increases with increasing mass velocity at similar heat fluxes. The IB flow regime spans over a very small range of vapor qualities, from $x \approx 0-0.02$ at $G \approx 1200 \text{ kg/m}^2\text{s}$. The distinctive sharp drop on the heat transfer coefficients in the CB flow regime occurs due to the bubble coalescence process with the increase in vapor quality. In the annular flow regime at $x \approx 0.50$, the heat transfer coefficients for $G \approx 1200 \text{ kg/m}^2\text{s}$ are on the order of $\approx 43\%$ higher in comparison with $G \approx 800 \text{ kg/m}^2\text{s}$ indicating the dominance of forced convection.

Fig. (5.16) refers to flow boiling experiments for R134a, R236fa and R245fa for a constant wall heat flux over a wide range of mass velocities with the classification of flow regimes indicated for the lowest and highest mass velocity. The IB and CB flow regimes have been observed to continuously shrink in size with increasing mass velocity, occupying a much smaller vapor quality range. The annular flow regime in particular covers the widest range of vapor quality range at the highest mass velocity, as illustrated in the results. The heat transfer coefficients indicate a significant mass flux influence for all the fluids in the annular flow regime, in contrast with earlier studies mentioned previously in Chapter 2. In the IB flow regime, the heat transfer coefficients registered approximately the same magnitude due to the onset of boiling but increased after the transition from CB to annular flow is complete. By relative comparison, the heat transfer coefficient for R134a at $G=1608 \text{ kg/m}^2\text{s}$ and $x=0.10$ is $\approx 67\%$ higher in comparison with $G=297 \text{ kg/m}^2\text{s}$ at $x=0.10$. As for R236fa, a similar comparison of the heat transfer coefficient at $G=1209 \text{ kg/m}^2\text{s}$, $x=0.10$ registered a $\approx 20\%$ higher magnitude in comparison with $G=297 \text{ kg/m}^2\text{s}$ for the same vapor quality. This is however not observed for R245fa with $Co=1.02$, since no significant difference in the magnitude can be seen in the CB flow regime due to a monotonically decreasing heat transfer trend.



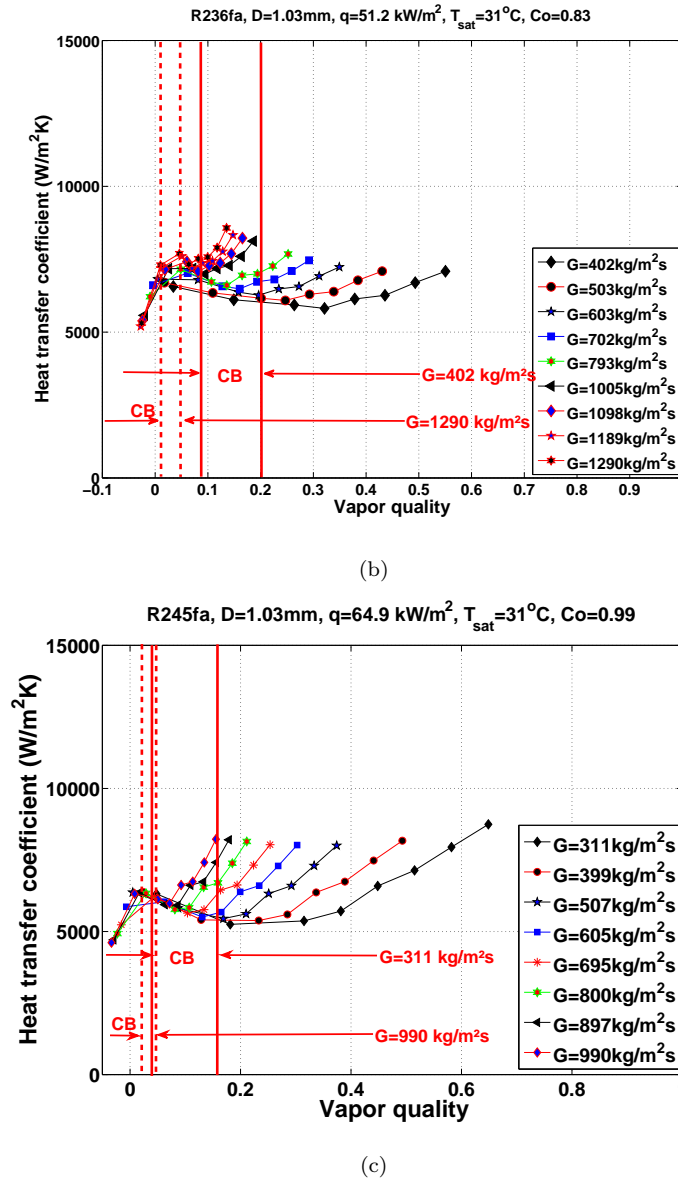


Figure 5.16: Mass velocity effects on heat transfer for R134a, R236fa and R245fa in the $D_{in}=1.03\text{ mm}$ channel at $T_{sat}=31\text{ }^\circ\text{C}$; (a) R134a, $Co=0.78$, (b) R236fa, $Co=0.83$ and (c) R245fa, $Co=0.99$.

Fig. (5.17) presents the heat transfer coefficients for R134a and R236fa at a similar wall heat flux for different mass velocities in the $D_{in}=2.20\text{ mm}$ channel. The experimental condition corresponds to $T_{sat}=25\text{ }^\circ\text{C}$, a confinement number of $Co=0.38$ for R134a and $Co=0.47$ for R245fa respectively. The heat transfer coefficients rise for R134a in the annular flow regime appears to be more subdued when compared to R236fa. It was also observed that the heat transfer coefficients in the IB and annular flow regimes for R134a at $G=1495\text{ kg/m}^2\text{s}$ are somewhat similar. This is not the case for R236fa, as the heat transfer coefficients were observed to increase after the onset of nucleation.

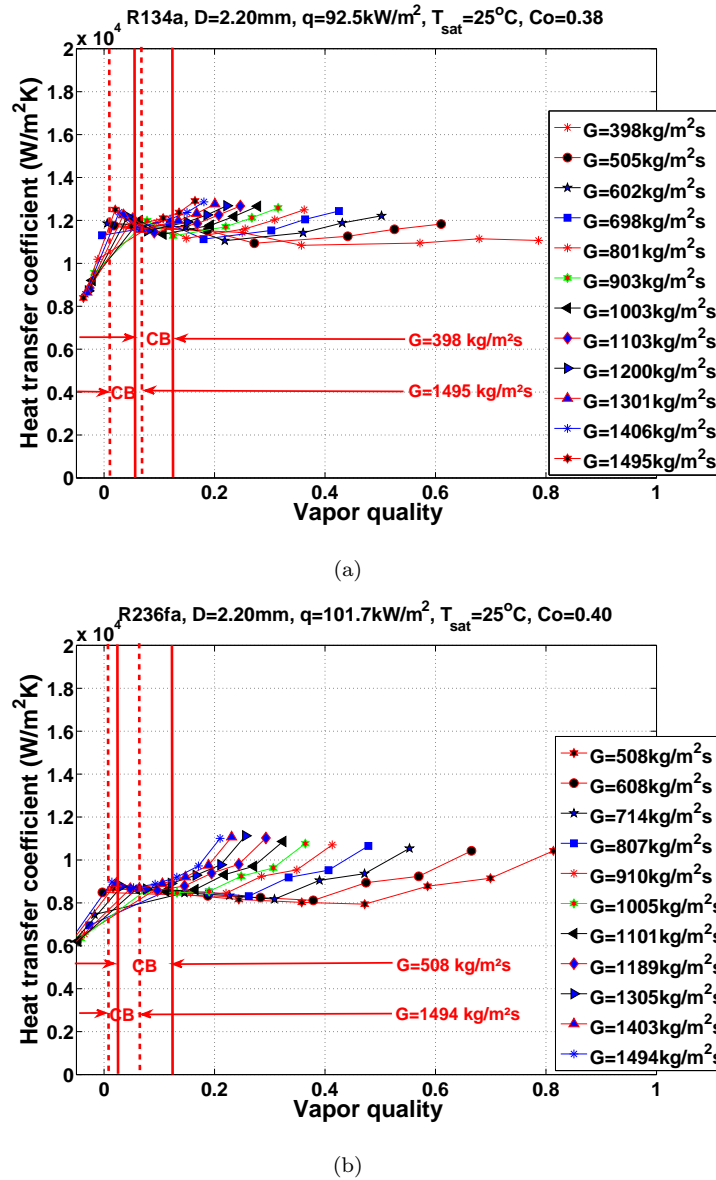
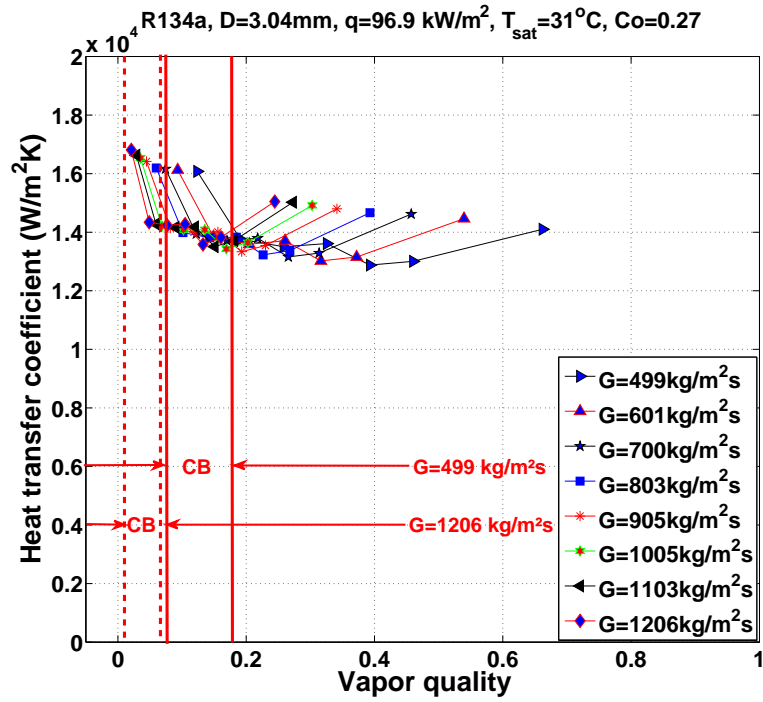
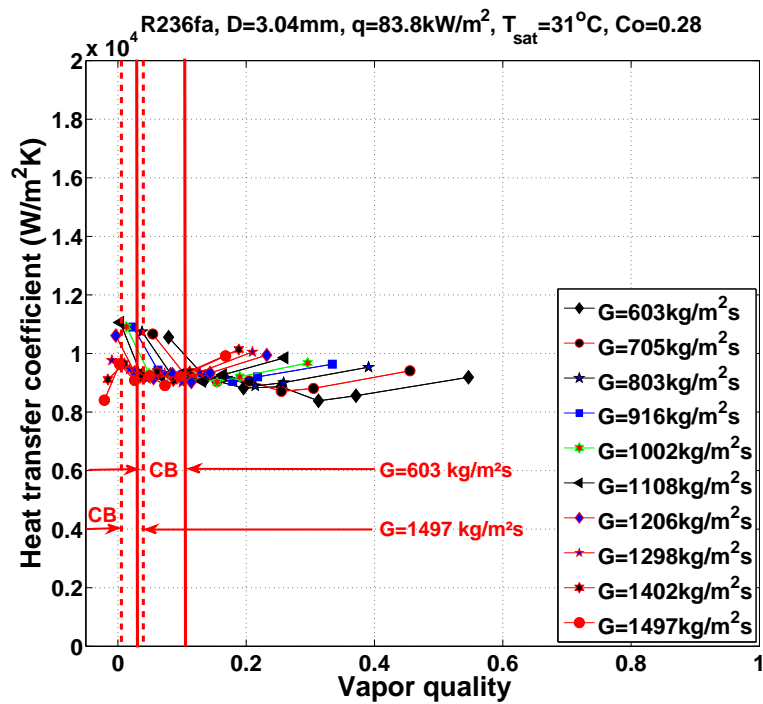


Figure 5.17: Mass velocity effects on heat transfer for R134a and R236fa in the $D_{in}=2.20$ mm channel at $T_{sat}=25$ °C; (a) R134a, $Co=0.38$ and (b) R236fa, $Co=0.40$.

The results shown in Fig. (5.18) depict the heat transfer results for all the three fluids in the larger $D_{in}=3.04$ mm channel corresponding to confinement numbers of $Co=0.27$ - 0.34. The heat transfer trends appear to show less convective boiling dominance, as reflected in the results. The heat transfer coefficients in the IB regime for R134a and R236fa registered the highest value, as opposed to a usually higher heat transfer trend seen in the $D_{in}=1.03$ mm channel. The rising heat transfer trends appears to be more subdued with increasing channel size. As for R245fa, the results were not conclusive due to the extremely small 'width' of the IB flow regime. However, a plateau shaped heat transfer trend was still observed for the smaller range of mass flux tested due to test facility limitations for this low pressure fluid.



(a)



(b)

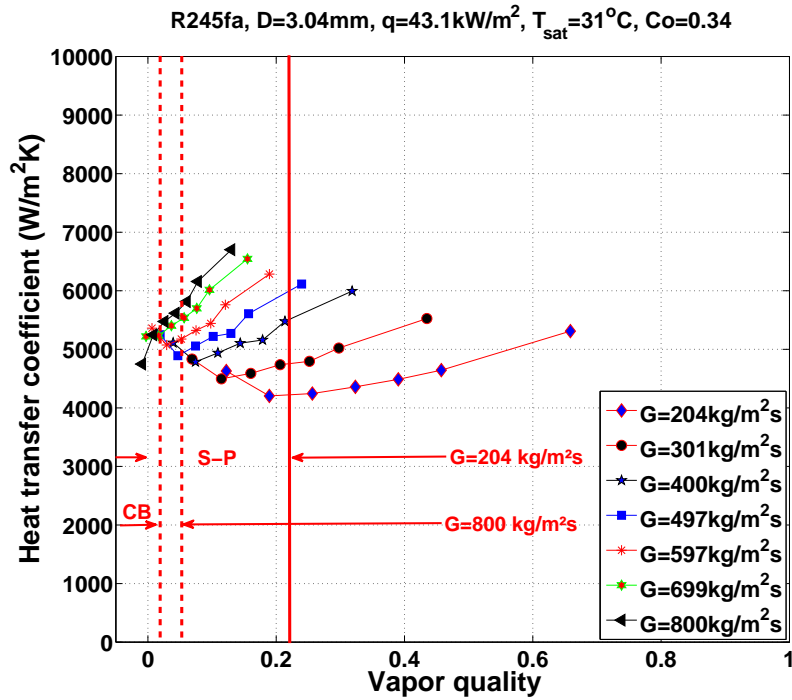


Figure 5.18: Mass velocity effects on heat transfer for R134a, R236fa and R245fa in the $D_{in}=3.04\text{ mm}$ channel at $T_{sat}=31\text{ }^\circ\text{C}$; (a) R134a, $Co=0.27$, (b) R236fa, $Co=0.28$ and (c) R245fa, $Co=0.34$.

5.2.5 Effects of Saturation Temperature

This section investigates the effects of saturation temperature on heat transfer. Fig. (5.19) and Fig. (5.20) present the R236fa and R245fa data at $T_{sat}=31$ and $35\text{ }^\circ\text{C}$ for a wide range of heat fluxes in the $D_{in}=1.03\text{ mm}$ channel. As observed, the heat transfer coefficients appear to be higher throughout the IB and CB flow regime for higher saturation temperature or pressures. In the annular flow regime, for example at $x=0.40$, the heat transfer coefficient for R236fa at $T_{sat}=35\text{ }^\circ\text{C}$, $q=60.3\text{ kW/m}^2$ is $\approx 5\%$ higher in comparison to $T_{sat}=31\text{ }^\circ\text{C}$ at $q=60.6\text{ kW/m}^2$. The same trend can be observed for R45fa at $T_{sat}=35\text{ }^\circ\text{C}$ for all the heat fluxes, with the heat transfer coefficients registering $\approx 7\%$ higher values in comparison to $T_{sat}=31\text{ }^\circ\text{C}$, as shown in Fig. (5.20).

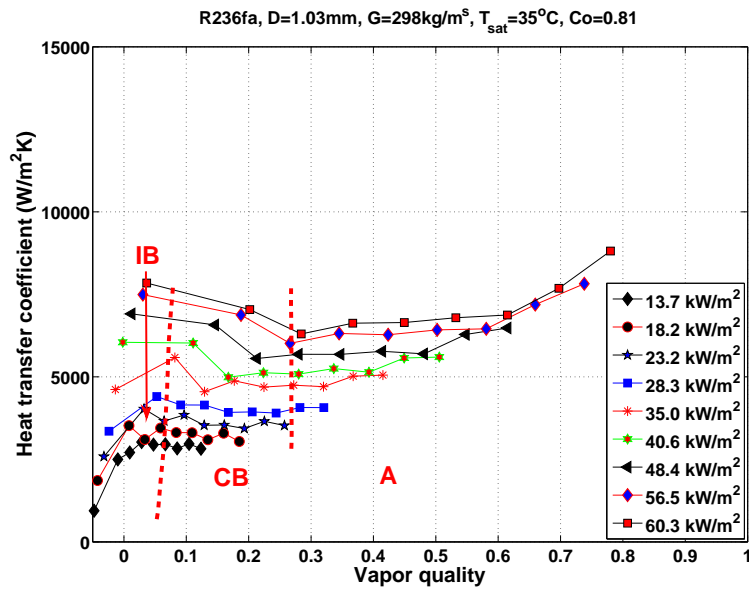
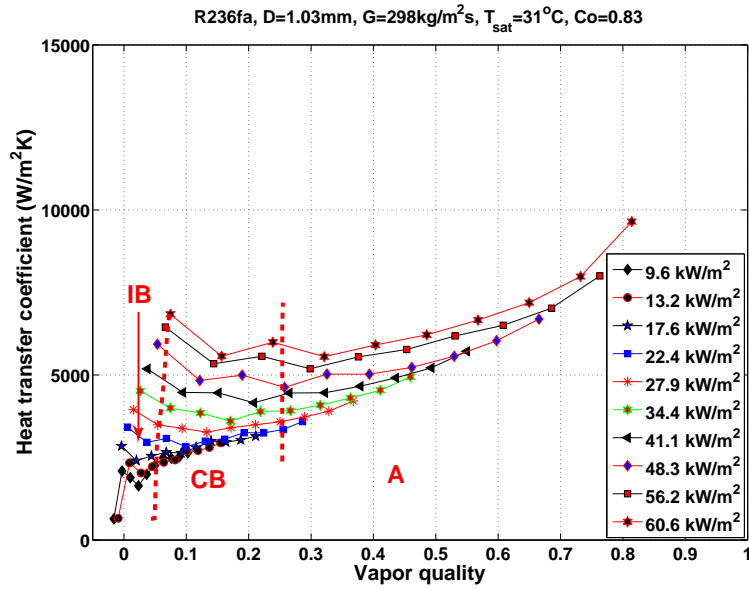


Figure 5.19: Heat transfer coefficients for R236fa at $G \approx 300 \text{ kg/m}^2\text{s}$; (a) $T_{sat}=31 \text{ }^\circ\text{C}$, $Co=0.83$ and (b) $T_{sat}=35 \text{ }^\circ\text{C}$, $Co=0.81$.

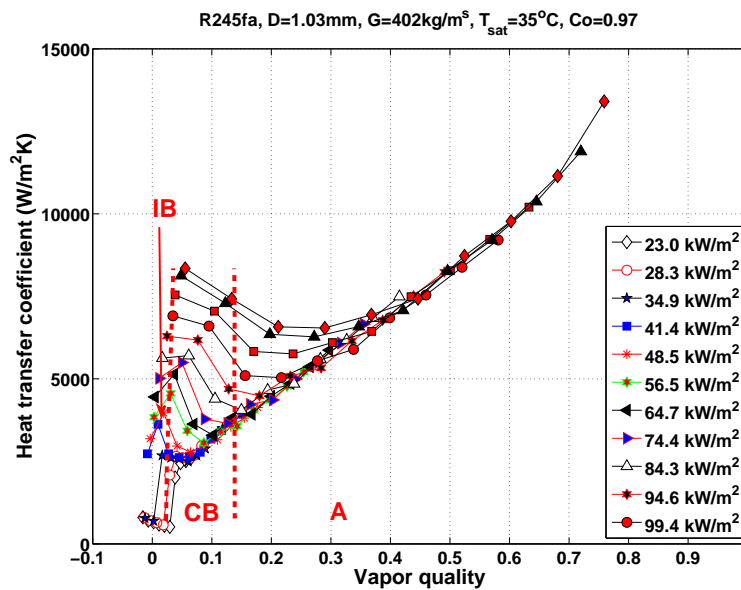
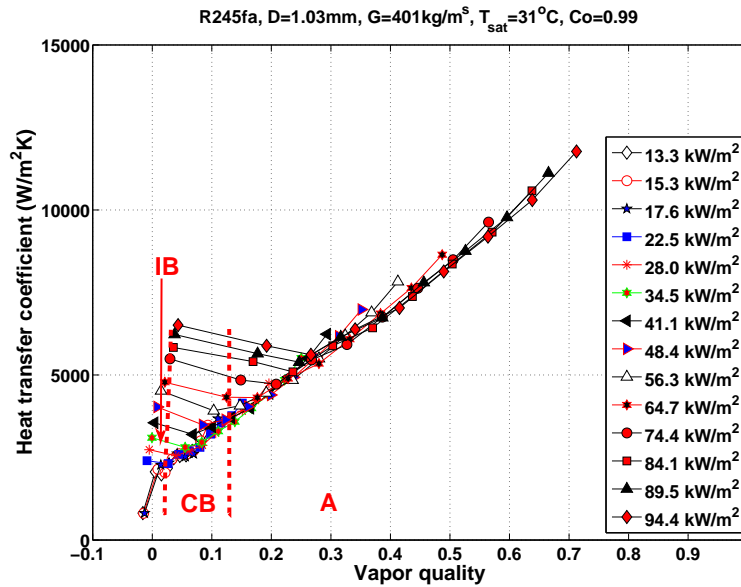
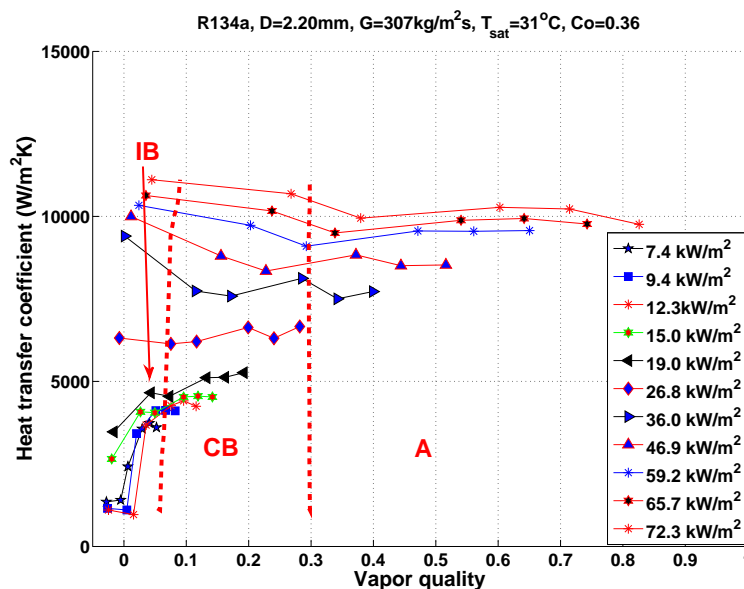
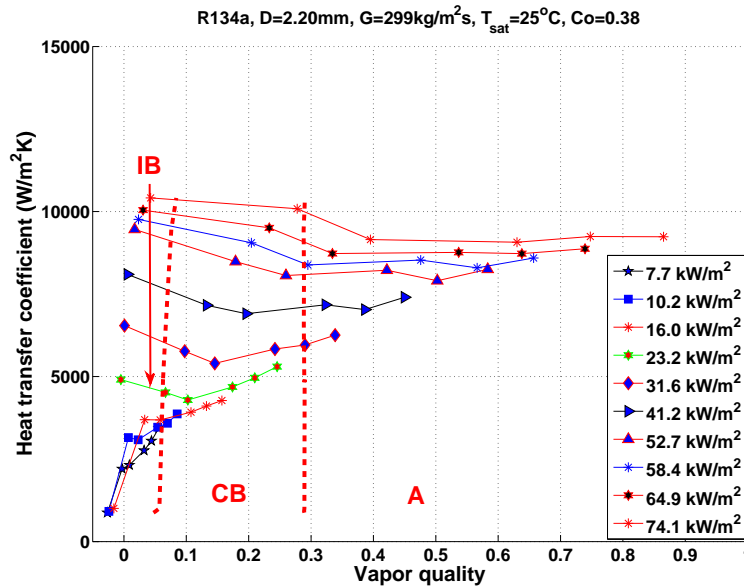
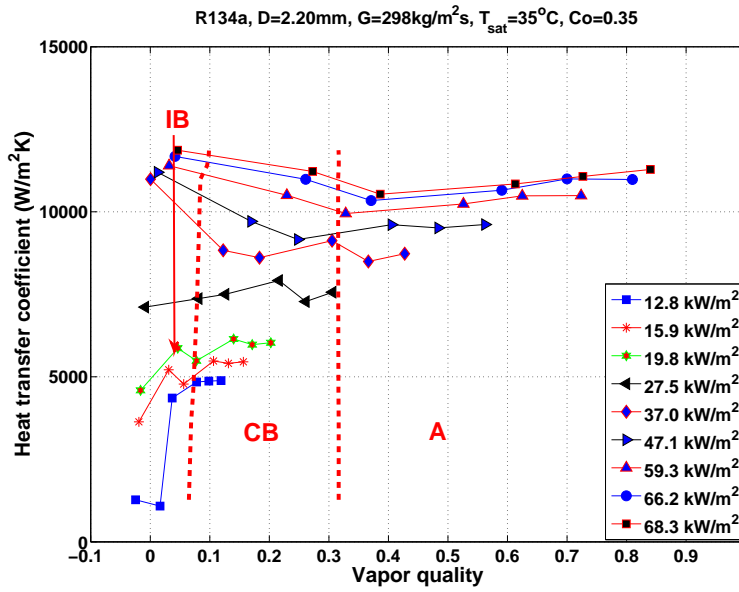


Figure 5.20: Heat transfer coefficients for R245fa at $G \approx 400 \text{ kg/m}^2\text{s}$; (a) $T_{\text{sat}}=31^\circ\text{C}$, $Co=0.99$ and (b) $T_{\text{sat}}=35^\circ\text{C}$, $Co=0.97$.

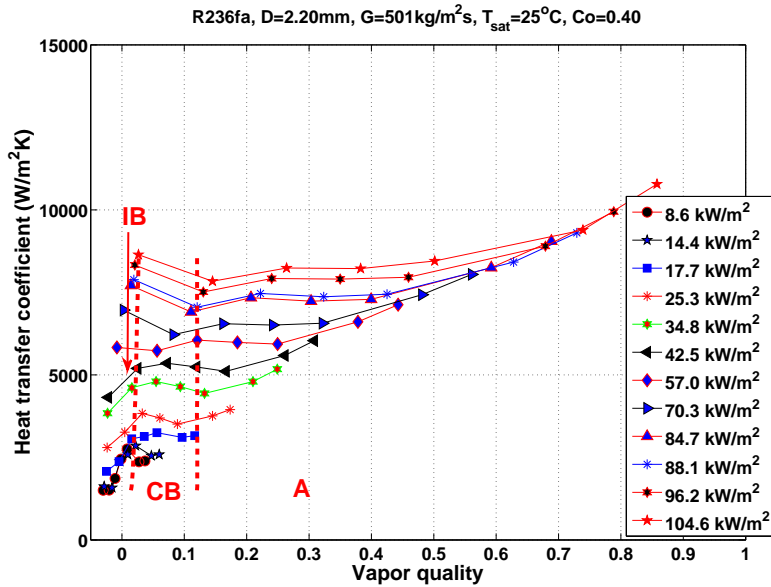
Similar heat transfer characteristics were observed for the $D_{in}=2.20\text{ mm}$ channel at low vapor qualities. The heat transfer coefficients are higher for higher saturation temperatures at similar heat fluxes, as illustrated in Fig. (5.21) and Fig. (5.22) in the IB/CB flow regime. At high vapor qualities of $x \approx 0.80$, higher heat transfer coefficients were also registered for the higher saturation experiments for R134a. This might be due to the lower latent heat at higher saturation temperatures, causing the higher evaporation and the rapid thinning of the liquid film layer around the wall as proposed by Jacobi et al. [52], Saitoh et al. [66] and Petterson [110]. Similar higher heat transfer coefficients at $x \approx 0.80$ can also be seen for R236fa but to a lower extent as compared to R134a.





(c)

Figure 5.21: Heat transfer coefficients for R134a in the $D_{in}=2.20\text{ mm}$ channel for $G \approx 300\text{ kg/m}^2\text{s}$; (a) $T_{\text{sat}}=25\text{ }^\circ\text{C}$, $Co=0.38$, (b) $T_{\text{sat}}=31\text{ }^\circ\text{C}$, $Co=0.36$ and (c) $T_{\text{sat}}=35\text{ }^\circ\text{C}$, $Co=0.35$.



(a)

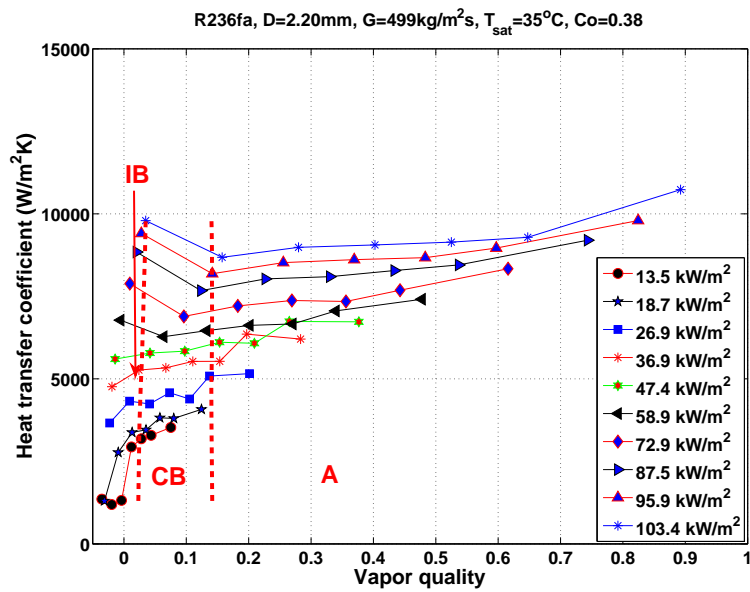
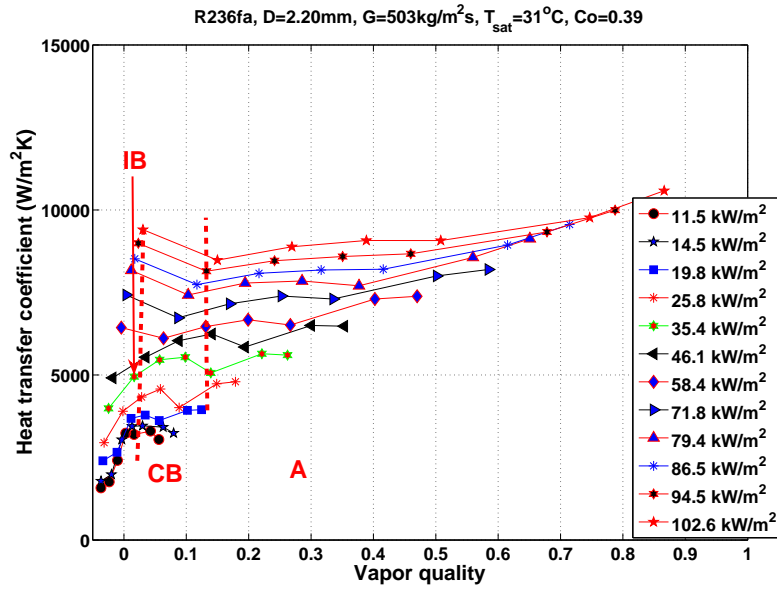


Figure 5.22: Heat transfer coefficients for R236fa in the $D_{in}=2.20\text{ mm}$ channel for $G \approx 500\text{ kg/m}^2\text{s}$; (a) $T_{\text{sat}}=25\text{ }^\circ\text{C}$, $Co=0.40$, (b) $T_{\text{sat}}=31\text{ }^\circ\text{C}$, $Co=0.39$ and (c) $T_{\text{sat}}=35\text{ }^\circ\text{C}$, $Co=0.38$.

5.2.6 Effects of Inlet Sub-cooling

Fig. (5.23)a shows the heat transfer for two different mass fluxes for R134a in the $D_{in}=1.03$ mm channel. The results suggest a little residue effect of inlet sub-cooling on the heat transfer coefficients in the saturated region up to the CB/A transition lines. The CB/A transition line is simulated using the newly proposed flow pattern map for the respective mass velocities at $T_{sat}=31$ °C with inlet temperature $T_{in}=27$ °C. Thus, in the IB and CB flow regimes, there seems to be some effect and this explains the various trends observed here and elsewhere at low vapor qualities. This is likely due to the influence of sub-cooling on the onset of boiling along the channel length. The same trend was observed here in the $D_{in}=3.04$ mm channel, as shown in Fig. (5.23)b.

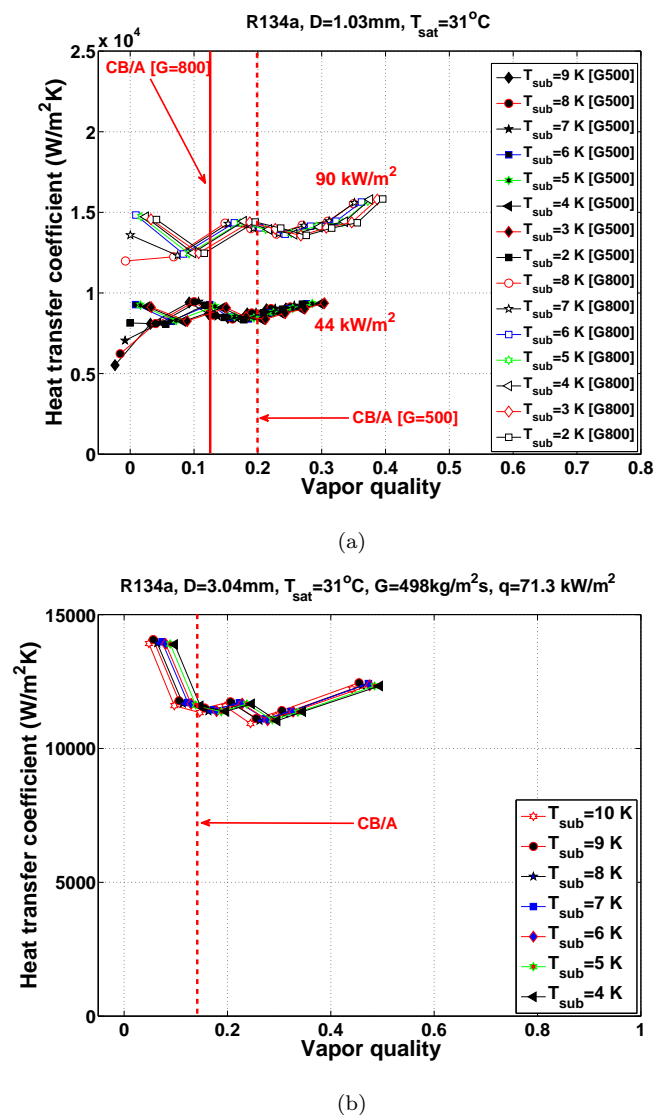
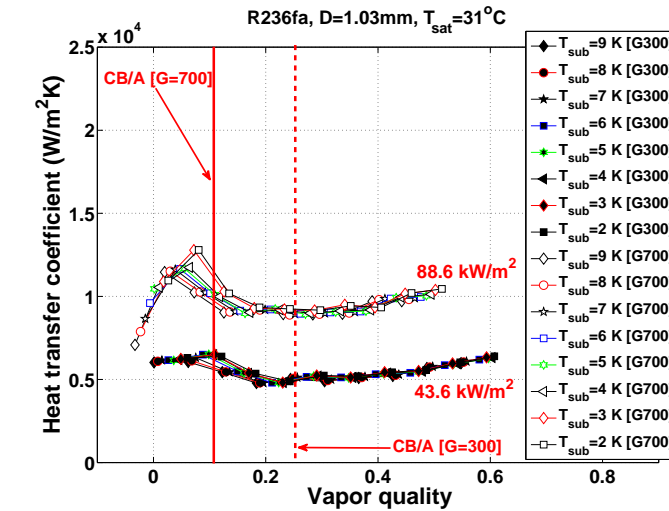
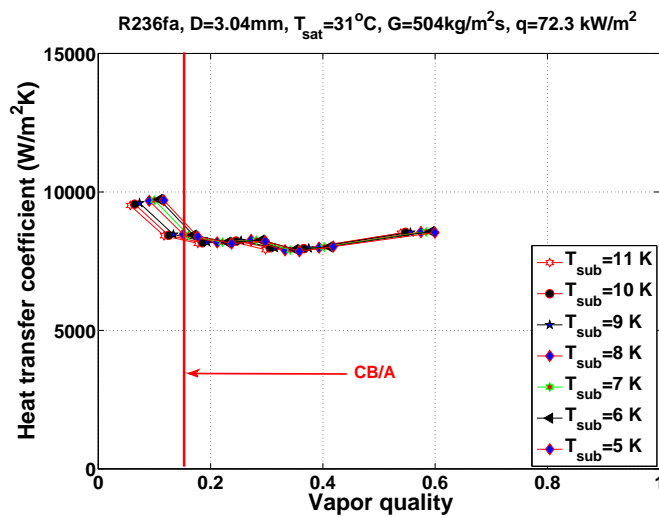


Figure 5.23: Sub-cooling effects the on heat transfer coefficient for R134a at $T_{sat}=31$ °C; (a) $D_{in}=1.03$ mm channel, $Co=0.78$ and (b) $D_{in}=3.04$ mm channel, $Co=0.27$.



(a)

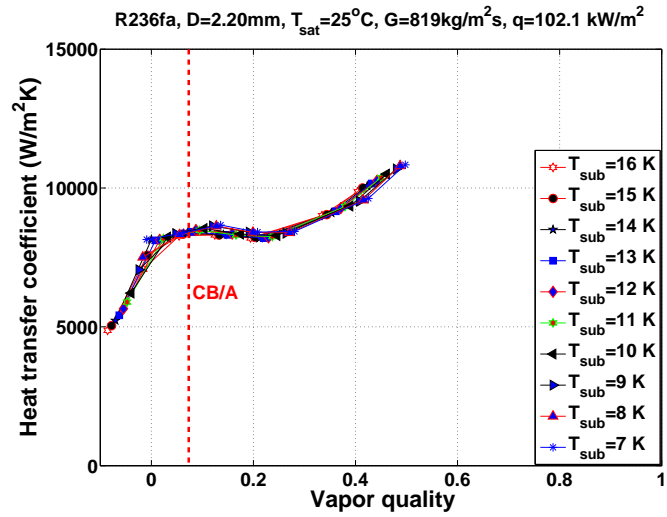


(b)

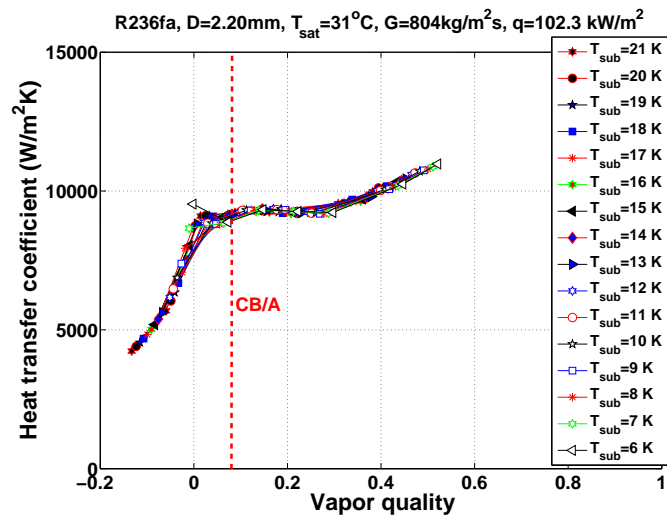
Figure 5.24: Sub-cooling effects on the heat transfer coefficient for R236fa at $T_{sat}=31\text{ }^{\circ}\text{C}$; (a) $D_{in}=1.03\text{ mm}$ channel, $Co=0.83$ and (b) $D_{in}=3.04\text{ mm}$ channel, $Co=0.28$.

Fig. (5.24) refers to the heat transfer results for R236fa for different inlet sub-coolings in the $D_{in}=1.03$ and 3.04 mm channel. The results indicate the same trends as observed earlier for R134a, which might be due to the influence of inlet sub-cooling on the location of onset of bubble nucleation.

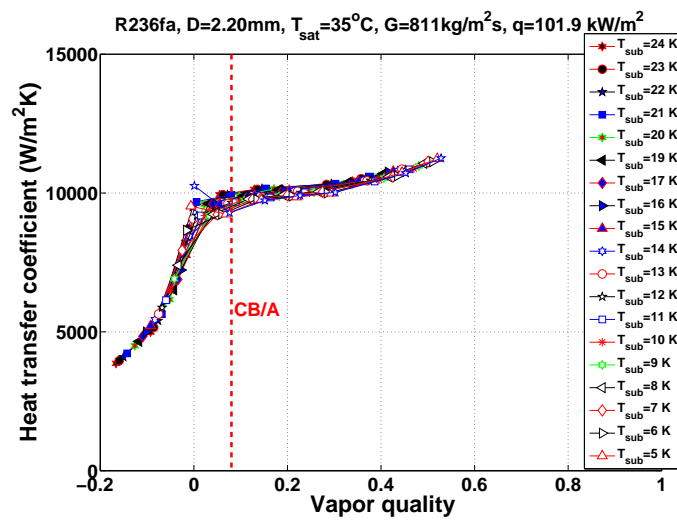
Fig. (5.25) illustrates the comparison of the effects of inlet sub-cooling for R236fa at $T_{sat}=25, 31$ and $35\text{ }^{\circ}\text{C}$ in the $D_{in}=2.20\text{ mm}$ channel. Here, there are no residue effects of sub-cooling. The heat transfer coefficients are higher saturation for higher saturation temperatures.



(a)



(b)



(c)

Figure 5.25: Sub-cooling effects on the heat transfer coefficient for R236fa in the $D_{in}=2.20\text{ mm}$ channel; (a) $T_{\text{sat}}=25^\circ\text{C}$, $Co=0.40$, (b) $T_{\text{sat}}=31^\circ\text{C}$, $Co=0.39$ and (c) $T_{\text{sat}}=35^\circ\text{C}$, $Co=0.38$.

5.2.7 Discussion of Heat Transfer Results

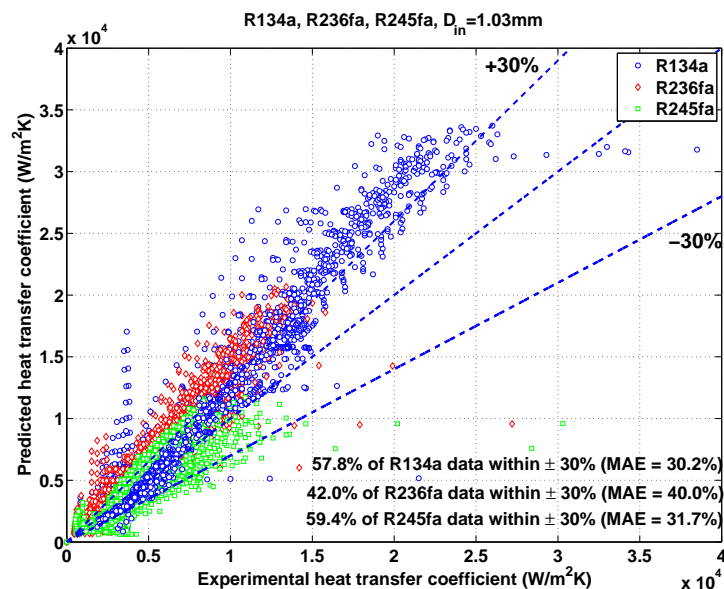
The heat transfer trends observed for the three refrigerants R134a, R236fa and R245fa displayed similar characteristics in comparison with the heat transfer experimental results of Lazarek et al. [5] for R-113 in a single-channel with $D_{in}=3.1\text{ mm}$, Kew et al. [49] for R141b for channels with internal diameters of $D_{in}=1.39 - 3.69\text{ mm}$, Lin et al. [6] for R141b in single channels with channel diameters $D_{in}=1.10, 1.80, 2.80, 3.60\text{ mm}$ and Saitoh et al. [66] for R134a in channels with $D_{in}=0.51, 1.12\text{ and }3.10\text{ mm}$.

The rising heat transfer coefficients with heat flux shown in the current experimental results in the sub-cooled and saturated region conforms with the results observed by Lazarek et al. [5] who concluded that the local heat transfer coefficient increases rapidly from a low value in the sub-cooled region to a larger value coinciding with the onset of saturated boiling. The minichannel heat experimental results of Kew et al. [49] also indicated a significant rise in the heat transfer values from the sub-cooled region to an increasing heat transfer trend with increasing vapor qualities. These authors observed a drop in heat transfer coefficients at low vapor qualities after the onset of boiling, before increasing monotonically at higher vapor qualities corresponding to convective boiling. However, these authors reported a decreasing heat transfer trend for the $D_{in}=1.39\text{ mm}$ with $Co=0.87$ for $G=1480\text{ kg/m}^2\text{s}$ which might be due to flow instabilities as described in Consolini [10]. On the other hand, Lin et al. [6] concluded from their experiments that the heat transfer coefficients were strongly dependent on heat flux and increased with vapor quality. The main conclusion from these authors is that the region corresponding on nucleate boiling region is seen in the larger tubes, but differs in that the reduction of heat transfer with quality is marked for the smaller tubes. Finally, Saitoh et al. [66] concluded from their results that the effects of heat flux were observed at lower vapor qualities and also saw a monotonically converging trend at higher vapor qualities. These authors result also corresponded well with the current heat transfer results, which indicates a higher heat transfer for higher saturation temperatures.

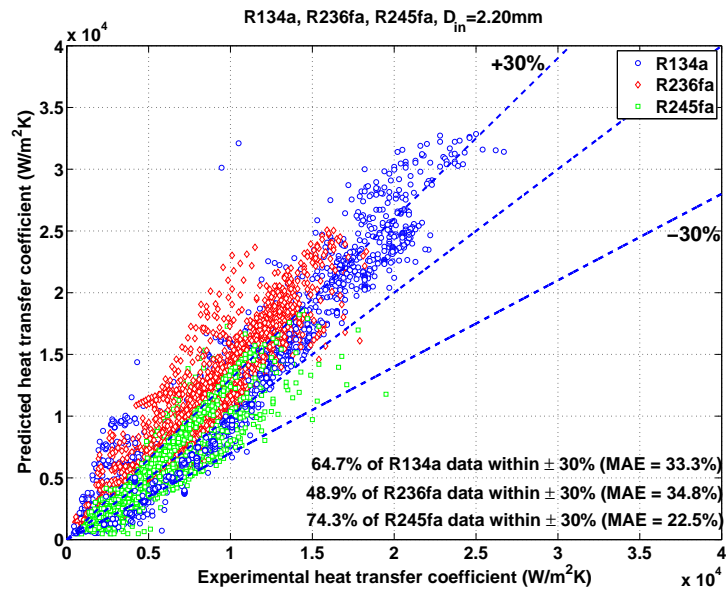
5.3 Heat Transfer Prediction Method Comparisons

This section compares the current experimental heat transfer results versus various heat transfer prediction methods from the literature.

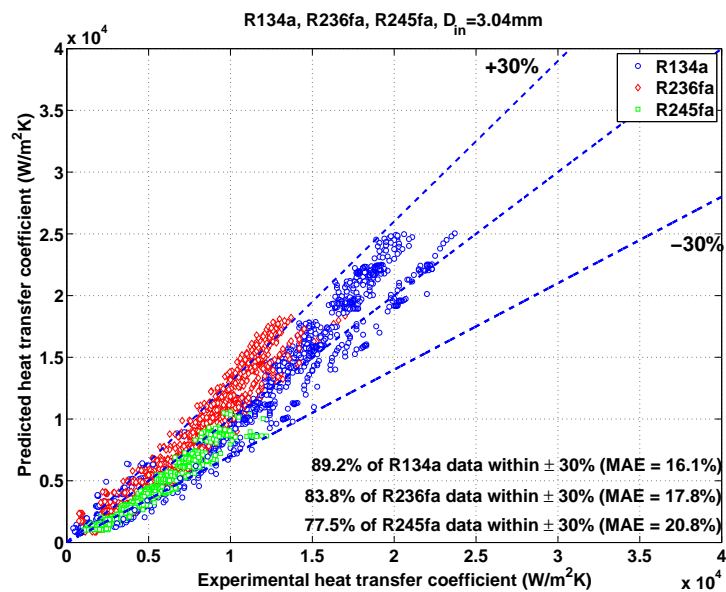
Fig. (5.26) compares the experimental heat transfer data for R134a, R236fa and R245fa in the $D_{in}=1.03, 2.20$ and 3.04 mm channels with the heat transfer correlation from Lazarek et al. [5]. The correlation predicted the heat transfer coefficients for the $D_{in}=1.03$ mm channel with rather poor accuracy, with 57.8% of the R134a data to within $\pm 30\%$ (MAE of 30.2%), 42.0% of the R236fa data to within $\pm 30\%$ (MAE of 40.0%) and 59.4% of the R245fa data to within $\pm 30\%$ (MAE of 31.7%). The prediction method's accuracy increased for the larger $D_{in}=2.20$ and 3.04 mm, as depicted in Fig. (5.26). For the $D_{in}=3.04$ mm channel, the correlation predicted 89.2% (MAE of 16.1%) data for R134a, 83.8% (MAE of 17.8%) data for R236fa and 77.5% (MAE of 20.8%) data for R245fa to within $\pm 30\%$ respectively. The better accuracy of this prediction for the larger channels is likely due to the fact that the correlation was developed based on heat transfer data for round channels with $D_{in}=3.10$ mm.



(a)



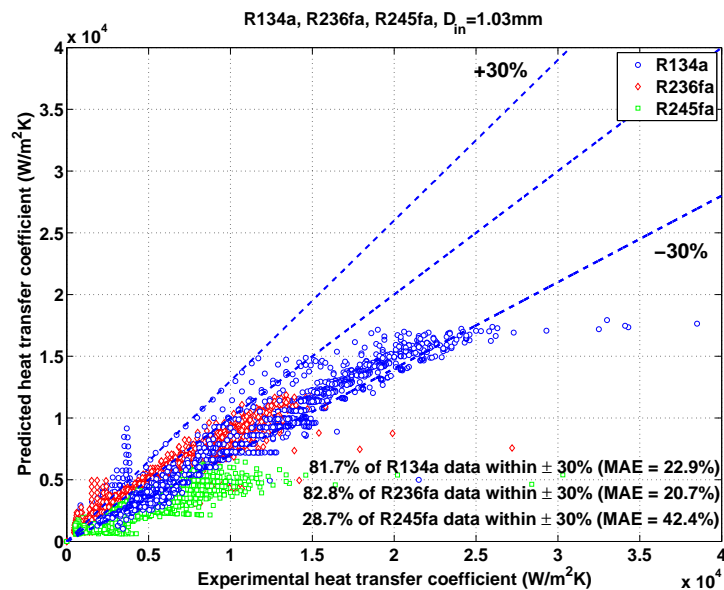
(b)



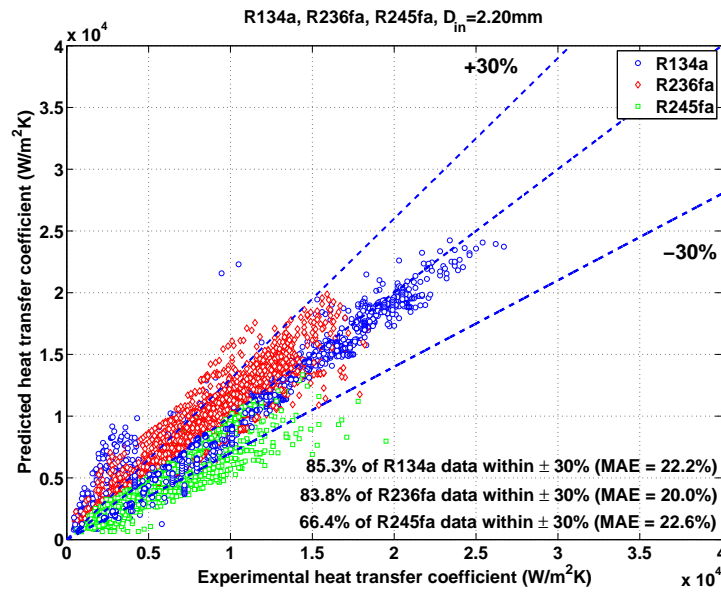
(c)

Figure 5.26: Experimental heat transfer coefficient comparison with Lazarek et al. [5] correlation for R134a, R236fa and R245fa; (a) $D_{in}=1.03\text{ mm}$ channel, (b) $D_{in}=2.20\text{ mm}$ and (c) $D_{in}=3.04\text{ mm}$ channel.

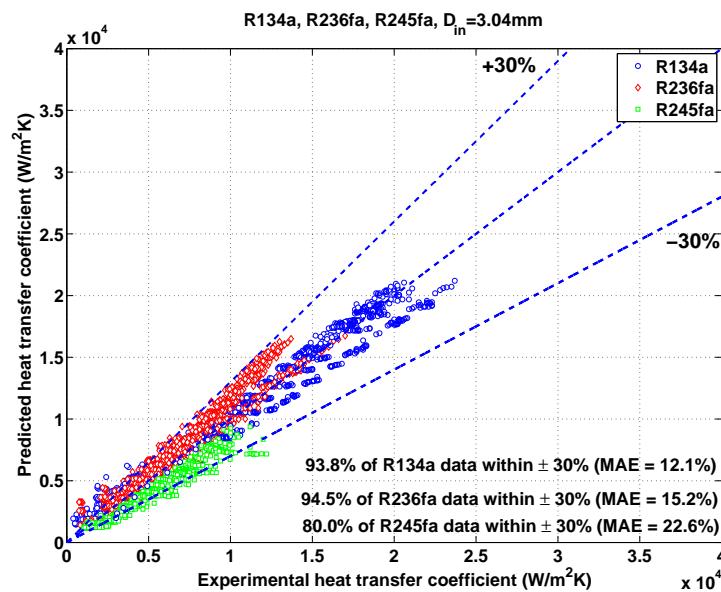
Fig. (5.27) on the other hand depicts the comparison of the Tran et al. [27] heat transfer correlation with the current experimental heat transfer data. The correlation was developed based on their experimental data for circular and square channels with internal diameters of $D_{in}=2.40 - 2.92 \text{ mm}$ for R12 and R113. The correlation from Tran et al. [27] incorporates the Weber number and considers the fluid property effects such as the liquid and vapor density ratio, surface tension and latent heat of vaporization for the heat transfer coefficient predictions. Referring to Fig. (5.27), the method compared very well for R134a and R236fa for the $D_{in}=1.03$ and 2.20 channels with over 80% of the data to within $\pm 30\%$ and over 90% of the data to within $\pm 30\%$ prediction for the $D_{in}=3.04 \text{ mm}$ channel. However, the correlation only managed to predict 28.7% of the R245fa data in the $D_{in}=1.03 \text{ mm}$ channel to within $\pm 30\%$, 66.4% of the data to within $\pm 30\%$ for the $D_{in}=2.20 \text{ mm}$ channel and 80% of the data to within $\pm 30\%$ for the $D_{in}=3.04 \text{ mm}$ channel. In conclusion, the correlation predicts the larger $D_{in}=2.20$ and 3.04 mm channels with higher accuracy than the smaller $D_{in}=1.03 \text{ mm}$ channel. The accuracy of the heat transfer coefficient predictions increased with increasing channel size, as observed in Fig. (5.27). The better prediction for the larger channels is probably attributed to the fact that the correlation was developed for mini-scale channels, similar to the larger two channel sizes tested here.



(a)



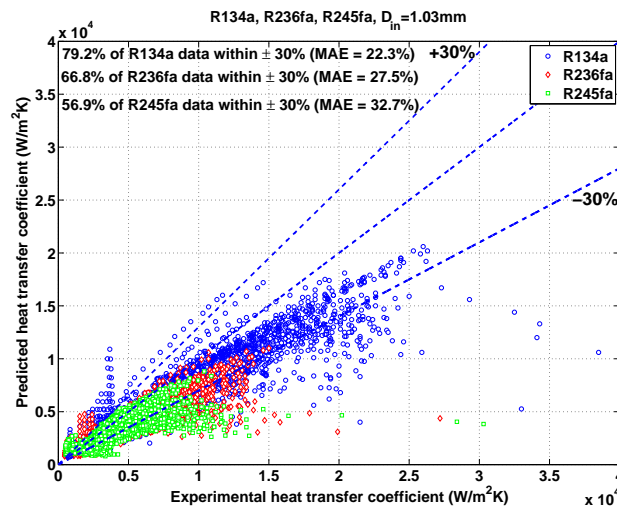
(b)



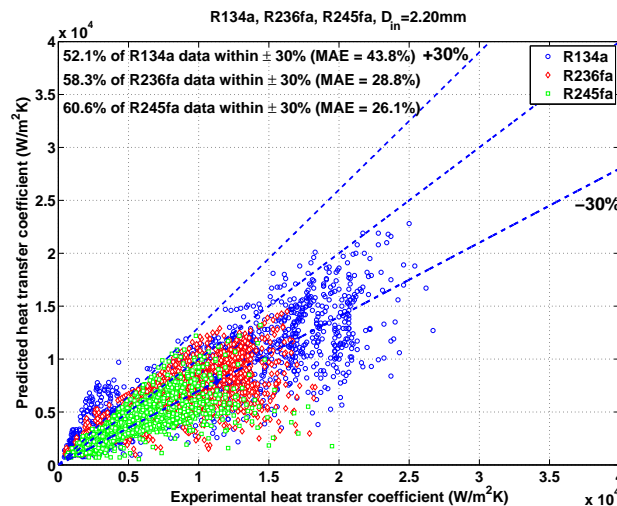
(c)

Figure 5.27: Experimental heat transfer coefficient comparison with Tran et al. [27] correlation for R134a, R236fa and R245fa; (a) $D_{in}=1.03\text{ mm}$ channel, (b) $D_{in}=2.20\text{ mm}$ and (c) $D_{in}=3.04\text{ mm}$ channel.

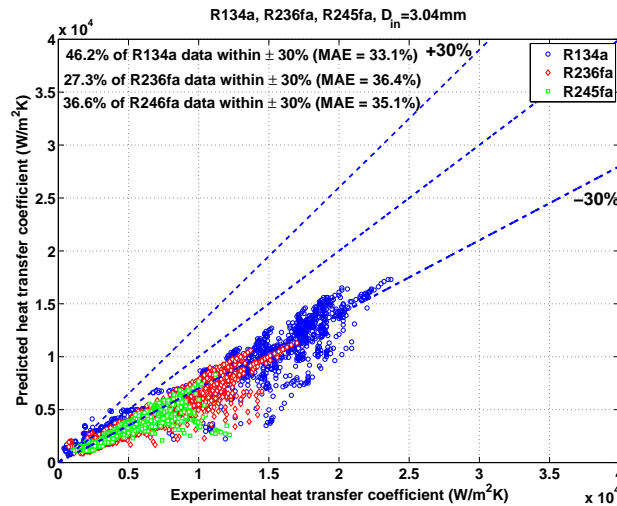
Fig. (5.28) illustrates the comparison of the current heat transfer data with the saturated flow boiling heat transfer correlation of Garimella et al. [28]. The correlation was developed from a database of 3899 data points covering 12 different wetting and non-wetting fluids, hydraulic diameters ranging from $D_h=0.16$ to 2.92 mm and confinement numbers from 0.3 to 4.0. The correlation includes both the nucleate boiling and convective heat transfer components. As shown in Fig. (5.28)a, the correlation predicted 79.2% of the R134a data to within $\pm 30\%$ and a MAE of 22.3% for the $D_{in}=1.03$ mm channel. The correlation only managed to predict 66.8% of the R236fa data to within $\pm 30\%$ (MAE of 27.5%) and 56.9% of the R245fa data to within $\pm 30\%$ (MAE of 32.7%) for the $D_{in}=1.03$ mm channel. The predictions for the $D_{in}=2.20$ and 3.04 mm channels are less satisfactory. From the current comparison, the accuracy of the correlation generally decreases with increasing channel size, with significant under prediction of the heat transfer coefficients for the $D_{in}=3.04$ mm channel as shown here in Fig. (5.28)c.



(a)



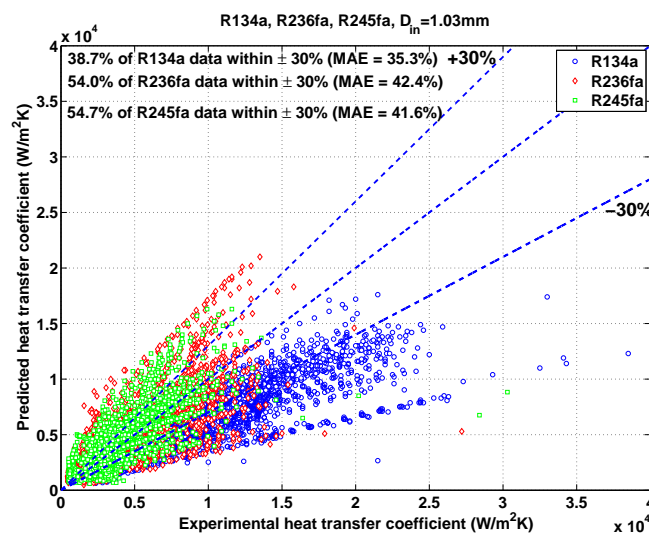
(b)



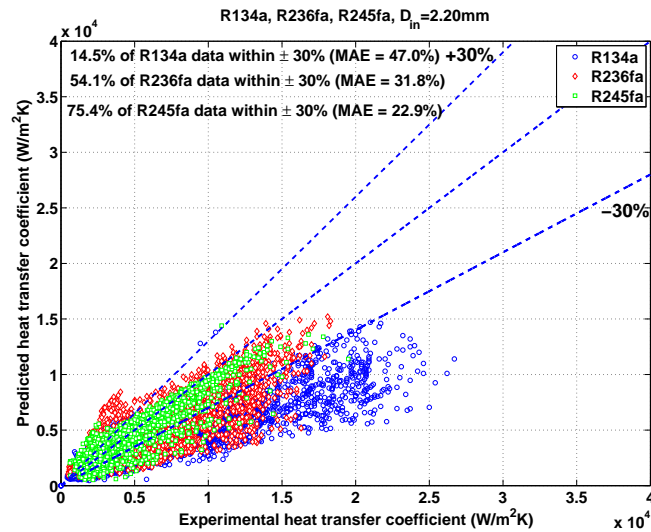
(c)

Figure 5.28: Experimental heat transfer coefficient comparison with Garimella et al. [28] correlation for R134a, R236fa and R245fa; (a) $D_{in}=1.03\text{ mm}$ channel, (b) $D_{in}=2.20\text{ mm}$ and (c) $D_{in}=3.04\text{ mm}$ channel.

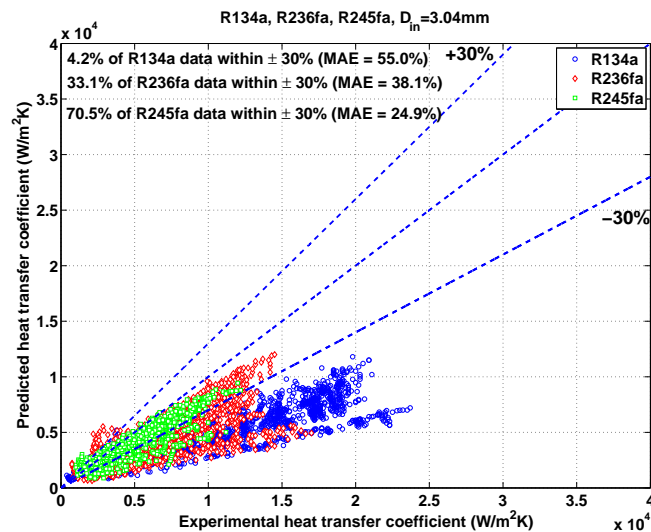
Fig. (5.29) illustrates the comparison of the Liu and Winterton [29] correlation with the current experimental heat transfer results. In general, the predictions are less satisfactory for R134a and R236fa in comparison with R245fa for the three channels tested. It was also observed that the prediction accuracy generally decreases for R134a and R236fa with increasing channel size. As for R245fa, an opposite trend was observed with better result predictions for the $D_{in}=2.20$ and 3.04 mm channels. In summary, the correlation predicted the R245fa results the best, followed by R236fa and the least accurate predictions for R134a.



(a)



(b)

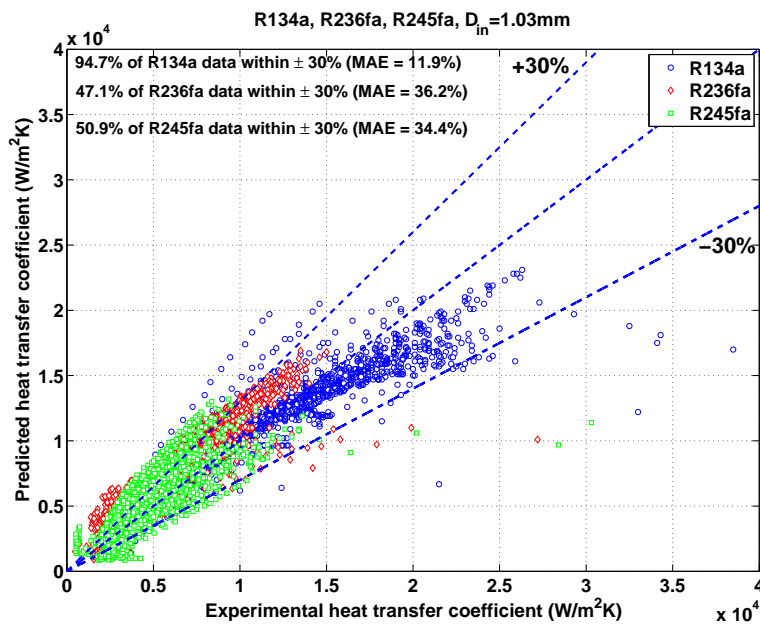


(c)

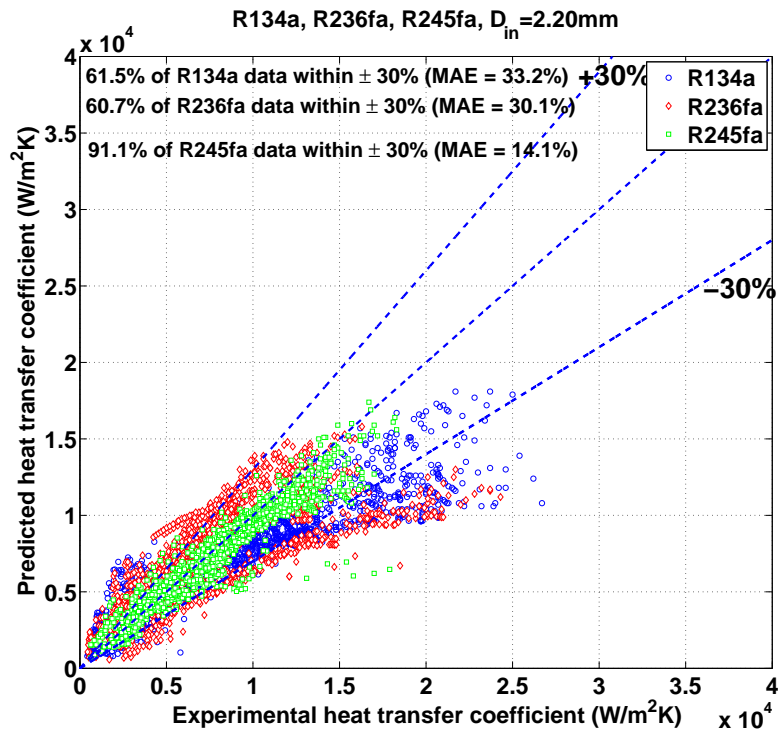
Figure 5.29: Experimental heat transfer coefficient comparison with Liu & Winterton [29] correlation for R134a, R236fa and R245fa; (a) $D_{in}=1.03\text{ mm}$ channel, (b) $D_{in}=2.20\text{ mm}$ and (c) $D_{in}=3.04\text{ mm}$ channel.

The comparison of the current experimental results with the Saitoh et al. [30] correlation is depicted in Fig. (5.30). This correlation was developed from a R134a heat transfer database obtained from a wide range of tube diameters, $D_{in}=0.51$ to 11.0 mm channels, and accounts for the effect of channel confinement in flow boiling heat transfer. The effects of tube diameter on flow boiling heat transfer coefficient was characterized by the introduction of the Weber number in the gas phase. Comparing the three fluids, the correlation predicted the heat transfer data for R134a in the $D_{in}=1.03\text{ mm}$ channel very well with 94.7% of the data to within $\pm 30\%$ and a MAE of 11.9%. However, the correlation significantly under predicted the heat transfer coefficient for R134a for

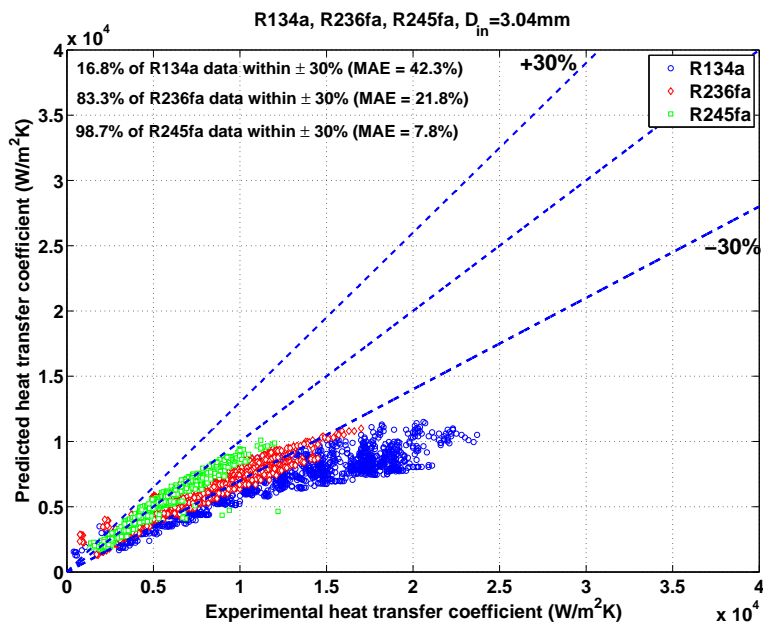
the larger $D_{in}=3.04 \text{ mm}$ channel, with only 16.8% of the data to within $\pm 30\%$ and a MAE of 42.3%. This reason for the loss of accuracy in the heat transfer prediction for the larger $D_{in}=2.20$ and 3.04 mm channels is due to the fact that the correlation was empirically correlated using a R134a heat transfer database acquired under lower saturation temperature/pressures conditions at $P_{sat} \approx 4 \text{ bar}$, as illustrated in work of Oh et al. [111] for the $D_{in}=2.0 \text{ mm}$ channel and Shin et al. [112] for the $D_{in}=7.70 \text{ mm}$ channel. An opposite trend however, was observed for R245fa in the $D_{in}=2.20$ and 3.04 mm channel, with the correlation successfully predicting 91.1% of the data to within $\pm 30\%$ and a MAE of only 14.1% for the $D_{in}=2.20$ channel and 98.7% of the data to within $\pm 30\%$ with a MAE of only 7.8% for the $D_{in}=3.04 \text{ mm}$ channel. On the other hand, the correlation predicted the heat transfer coefficients for R236fa in the $D_{in}=3.04 \text{ mm}$ channel with 83.3% of the data are to within $\pm 30\%$ with a MAE of 21.8% but for the $D_{in}=1.03 \text{ mm}$ channel, with only 50.9% of the data to within $\pm 30\%$ prediction. In summary, the correlation performed well for R134a but not very good for R245fa in the $D_{in}=1.03 \text{ mm}$ channel. As for the $D_{in}=3.04 \text{ mm}$ channel, the correlation predicted the R236fa and R245fa data with better accuracy. This might be due to the lower pressure nature of the two fluids, thus coinciding with the heat transfer database of Oh et al. [111] and Shin et al. [112] acquired at lower saturation pressures.



(a)



(b)

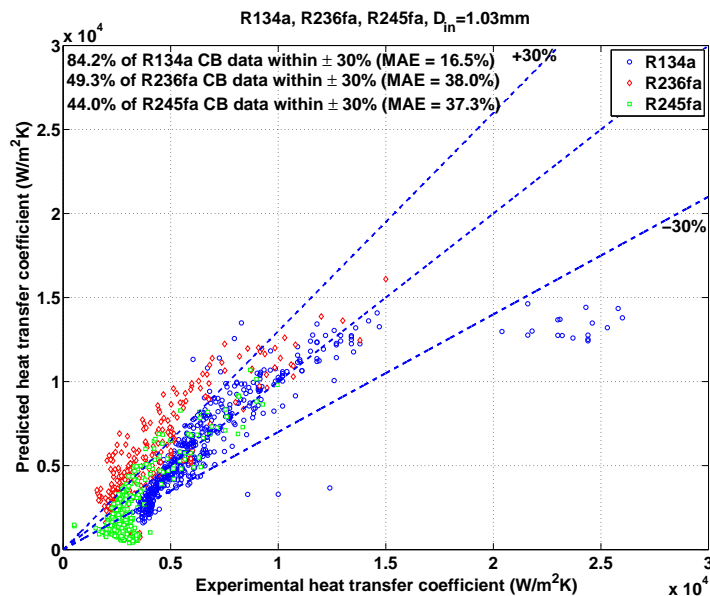


(c)

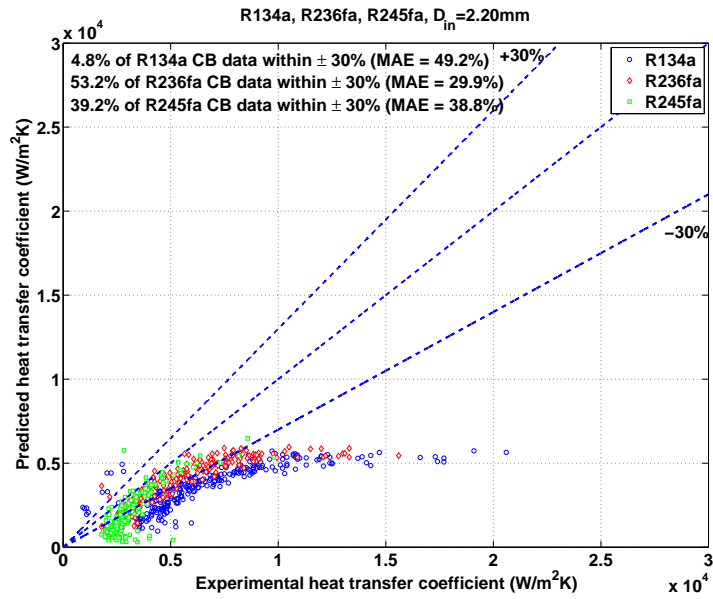
Figure 5.30: Experimental heat transfer coefficient comparison with Saitoh et al. [30] correlation for R134a, R236fa and R245fa; (a) $D_{in}=1.03\text{ mm}$ channel, (b) $D_{in}=2.20\text{ mm}$ and (c) $D_{in}=3.04\text{ mm}$ channel.

Consolini and Thome [32] recently proposed a one-dimensional heat transfer model of confined coalescing bubble flow for the prediction of micro-channel convective heat transfer during evaporation. The proposed model assumes the heat transfer to occur only by conduction through the thin evaporating liquid film trapped between the elongated bubble and the channel wall. The authors then included a simplified description of the dynamics of the formation and flow of the liquid film and the thin film evaporation process by taking into the account the added mass transfer by breakup of the bridging liquid slugs. The model performed very well with the heat transfer data for R134a, R236fa and R245fa in their original database for $D_{in}=0.51$ and 0.79 mm channels, with a successful prediction of 83% of their heat transfer database to within $\pm 30\%$ error band.

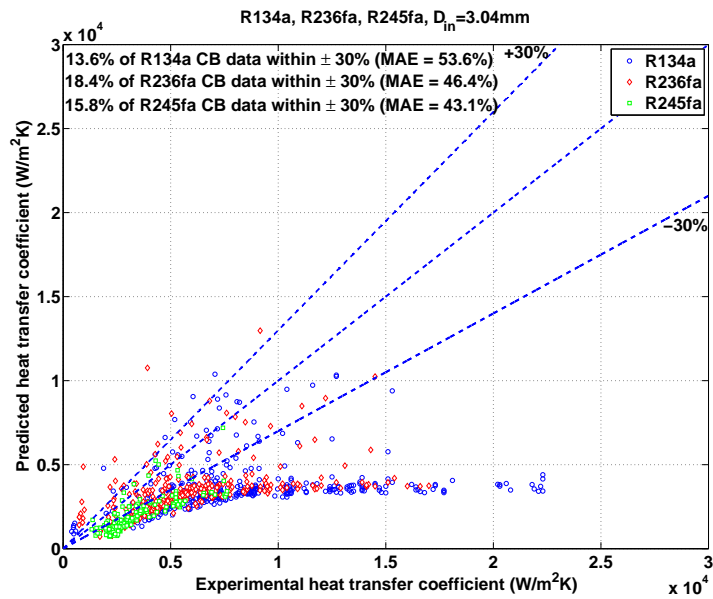
Fig. (5.31) illustrates the comparison of the current heat transfer database for R134a, R236fa and R245fa in the three channels with the model of Consolini and Thome [32]. The model predicted the R134a data in the $D_{in}=1.03$ mm channel with good accuracy, with 84.2% of the R134a data to within $\pm 30\%$ and a MAE of 16.5%. The comparison for R236fa and R245fa are 49.3% to within $\pm 30\%$ (MAE of 38.0%) and 44.0% to within $\pm 30\%$ (MAE of 37.3%). As a general rule, the model performed well for R134a but only satisfactorily for R236fa and R245fa. As for the $D_{in}=2.20$ and 3.04 mm channels, the prediction method failed to predict the heat transfer database accurately with significant under predictions observed. This is expected due to the effect of channel size on the two-phase flow structure, as reported earlier in Chapter 4. According to the their paper, the interfacial shear, τ_i presented in the model was empirically correlated with a heat transfer coefficients database for $D_{in}=0.51$ and 0.79 mm channels. As channel confinement increase, the interfacial shear is expected to increase as the flow becomes more laminar in small micro-scale channels. This justifies the lower accuracy of this prediction method when extrapolated to compare heat transfer results for larger channels.



(a)



(b)



(c)

Figure 5.31: Comparison of the current experimental heat transfer data for CB flow with the new Consolini et al. [31, 32] coalescing bubble heat transfer model for R134a, R236fa and R245fa; (a) $D_{in}=1.03\text{ mm}$ channel, (b) $D_{in}=2.20\text{ mm}$ and (c) $D_{in}=3.04\text{ mm}$ channel.

5.3.1 The Three-Zone Heat Transfer Model

This section describes and compares the three-zone flow boiling model for evaporation of elongated bubbles in microchannels proposed by Thome et al. [33, 34] with the current experimental heat transfer data for R134a, R236fa and R245fa in the $D_{in}=1.03, 2.20$ and 3.04 mm channels. The heat transfer model of Thome et al. [33,34] describes the transient variation in the local heat transfer coefficient during the sequential and cyclic passage of (i) a liquid slug, (ii) an evaporating elongated bubble and (iii) a vapor slug. The model illustrates the importance of the strong cyclic variation in the heat transfer coefficient and the strong dependency of heat transfer on the bubble frequency, the minimum liquid film thickness at dry-out and the liquid film formation thickness. The authors concluded that the heat transfer in the thin film evaporation region is typically on the order of several times that of the liquid slug while that for the vapor slug is considered to be nearly negligible. The time-averaged local heat transfer coefficient of a pair (liquid slug and elongated bubble) or triplet (liquid slug, elongated bubble and vapor slug) passing by a specific location, z is defined as :

$$h(z) = \frac{t_{liquid}}{\tau} h_{liquid}(z) + \frac{t_{film}}{\tau} h_{film}(z) + \frac{t_{dry}}{\tau} h_{vapor}(z) \quad (5.7)$$

where t_{liquid} , t_{film} and t_{dry} refer to the residence times for the liquid slug, liquid film between the elongated bubble while the wall and the dry-out zone and τ refers to the pair period. The heat transfer model identified the optimum value of the pair frequency, f_{opt} to be strongly dependent on the heat flux and a power law was applied to provide the best fit to the experimental database included in the development of the model:

$$f_{opt} = \left(\frac{q}{q_{ref}}\right)^{n_f} \quad (5.8)$$

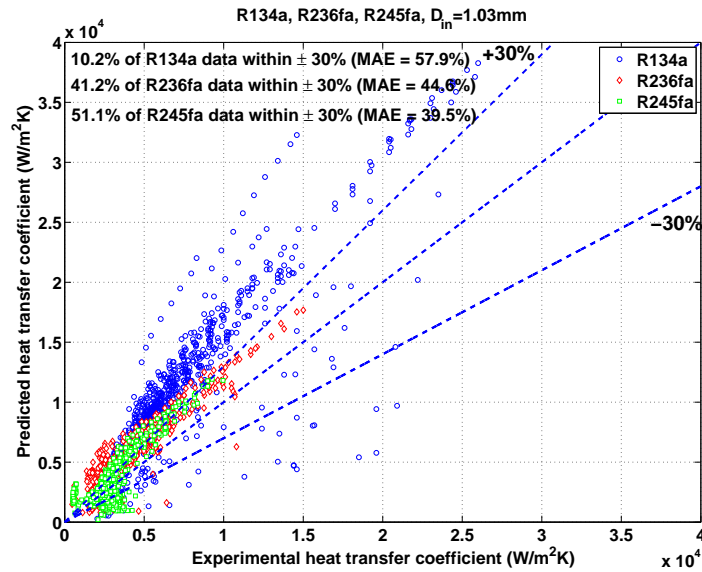
where q refers to the heat flux, q_{ref} is the reference heat flux expressed as a function of the reduced pressure of the fluid and the dimensionless exponent $n_f=1.74$. The authors also proposed the correcting factor on the initial film thickness, $C_{\delta_0}=0.29$ and the minimum film thickness, $\delta_{min}=300$ nm. The minimum film thickness, δ_{min} is assumed to be on the same order of magnitude as the surface roughness.

The comparison of the isolated bubble and coalescing bubble heat transfer data for R134a, R236fa and R245fa in the $D_{in}=1.03, 2.20$ and 3.04 mm channels is shown in Fig. (5.32). The local heat transfer coefficients corresponding to the isolated bubble and coalescing bubble flow regime have been segregated using the new proposed flow pattern map presented earlier in Chapter 4.

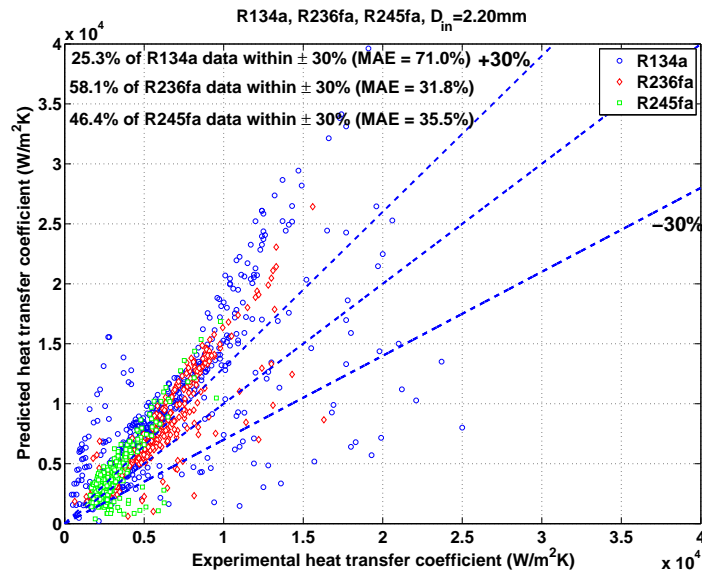
Fig. (5.33) illustrates another comparison of only the coalescing bubble heat transfer data for the $D_{in}=1.03$ and 2.20 mm channels with the Thome et al. [33, 34] three-zone model, i.e. those most appropriate for the models application. The comparison of the coalescing bubble heat transfer data is similar to the the results presented in Fig. (5.33), with marginal over prediction of the current experimental data.

Using the original surface roughness of 300 nm from their paper, the corresponding successful predictions for R134a, R236fa and R245fa to within $\pm 30\%$ in the $D_{in}=1.03$ mm channel are 10.2% (MAE of 57.9%), 41.2% (MAE of 44.6%) and 51.1% (MAE of 39.5%).

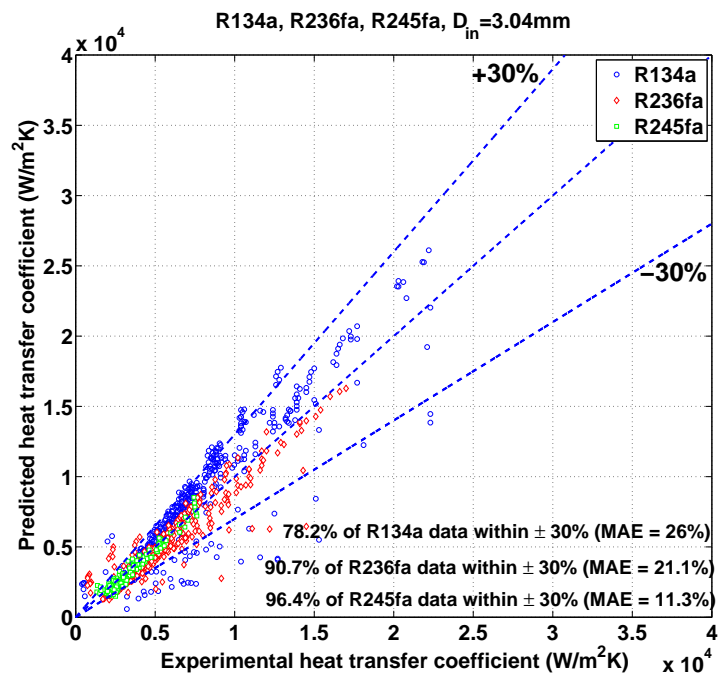
For the $D_{in}=2.20\text{ mm}$ channel, the values are 25.3% (MAE of 71.0%) for R134a, 58.1% (MAE of 31.8%) for R236fa and 46.4% (MAE of 35.5%) for R245fa. As for the $D_{in}=3.04\text{ mm}$ channel, the model of Thome managed to predict the R236fa and R245fa heat transfer data with good accuracy, where 80.6% of the R236fa data are to within $\pm 30\%$ with a MAE of 24.4% and 91.5% of the R245fa data to within $\pm 30\%$ and a MAE of 16.1%. In general, the model better predicted the heat transfer results for R236fa and R245fa, but did not accurately predict the heat transfer data of R134a for all the channels tested.



(a)

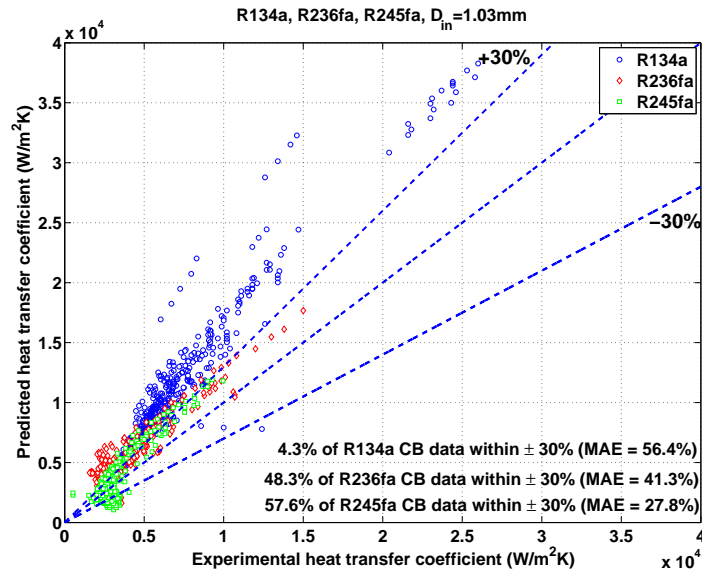


(b)

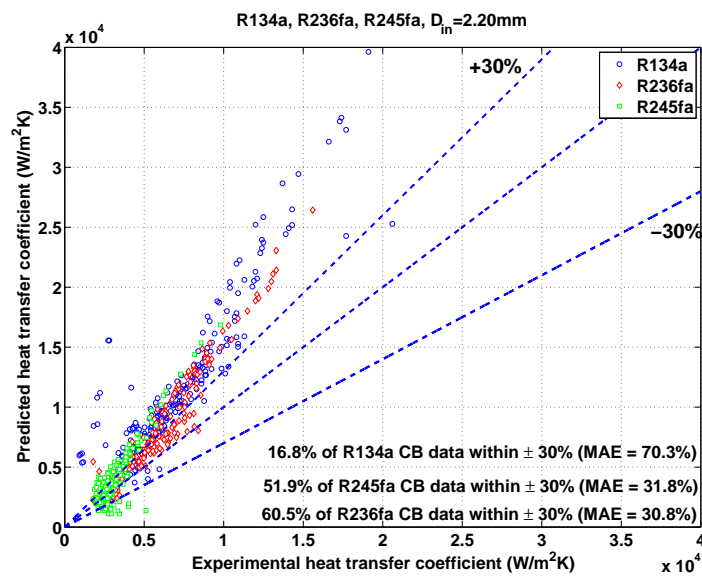


(c)

Figure 5.32: Comparison of the current experimental heat transfer data with the Thome et al. three-zone model for R134a, R236fa and R245fa; (a) $D_{in}=1.03\text{ mm}$ (IB and CB flow), (b) $D_{in}=2.20\text{ mm}$ (IB and CB flow) and (c) $D_{in}=3.04\text{ mm}$ channel (S-P and CB flow) .



(a)



(b)

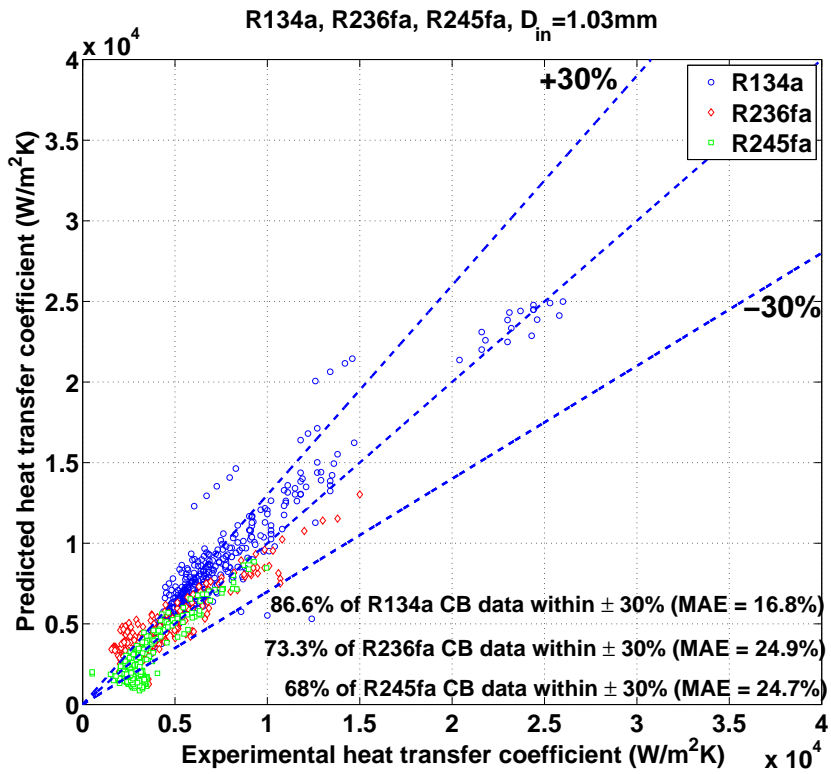
Figure 5.33: Comparison of the current experimental heat transfer data for CB flow with the Thome et al. [33,34] heat transfer model for R134a, R236fa and R245fa; (a) $D_{in}=1.03\text{ mm}$ and (b) $D_{in}=2.20\text{ mm}$ channel.

As presented earlier in Table 3.4, the root mean square (*rms*) surface roughness for the $D_{in}=1.03$, 2.20 and the 3.04 *mm* channels are on the order of $\approx 100\%$ higher than the original film thickness of 300 *nm* proposed in the Thome et al. three zone model. Thus, the original minimum film thickness, δ_{min} values have been replaced with the actual surface roughnesses measured for the three channels, as shown here in Table 5.1.

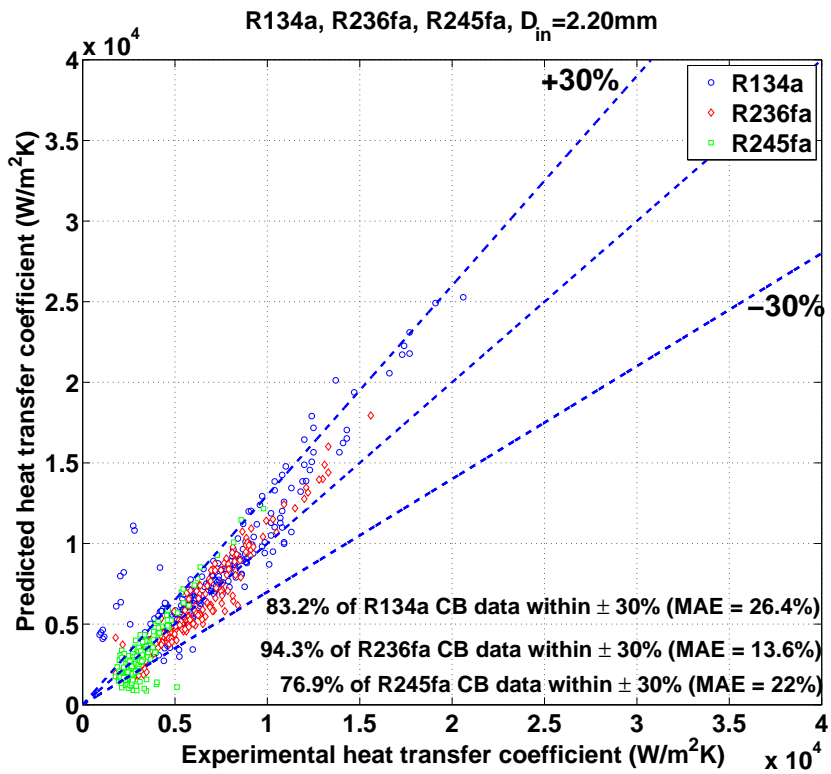
D_{int} (<i>mm</i>)	δ_{min} (<i>nm</i>)
1.03	595.8
2.20	826.9
3.04	796.8

Table 5.1: Minimum film thickness, δ_{min} for the $D_{in}=1.03$, 2.20 and 3.04 *mm* channels.

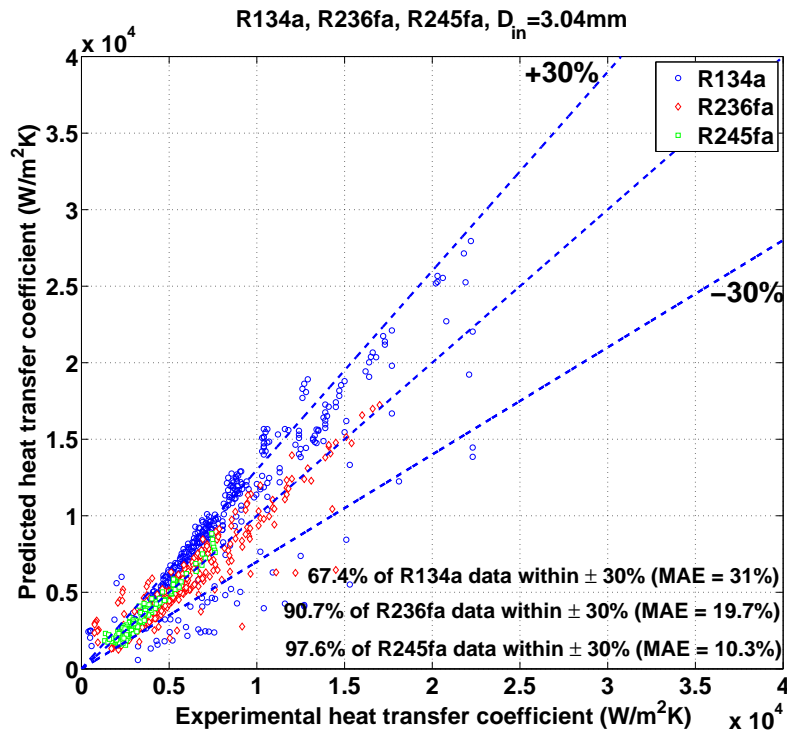
Fig. (5.34) illustrates the new comparisons of the present experimental database using the modified values of δ_{min} . For instance, the Thome et al. three-zone model now predicts 86.6% of the R134a data to within $\pm 30\%$ (MAE of 31.8%), 73.3% of the R236fa data to within $\pm 30\%$ (MAE of 24.9%) and 68.0% of the R245fa data to within $\pm 30\%$ (MAE of 24.7%) for the $D_{in}=1.03$ *mm* channel, as shown in Fig. (5.34)a. As for the $D_{in}=2.20$ *mm* channel, the model predicted 83.2% of the R134a data to within $\pm 30\%$ (MAE of 26.4%), 94.3% of the R236fa data to within $\pm 30\%$ (MAE of 13.6%) and 76.9% of the R245fa data to within $\pm 30\%$ (MAE of 22.0%). The comparison of the S-P and CB flow heat transfer results for the $D_{in}=3.04$ *mm* channel is shown in Fig. (5.34)c. In general, the model predicted 78.2% of the R134a S-P and CB flow heat transfer data in the $D_{in}=3.04$ *mm* channel to within $\pm 30\%$ (MAE of 26.0%). As for R236fa and R245fa, the model predicted 90.7% of the R236fa data to within $\pm 30\%$ (MAE of 21.1%) and 96.4% of the R245fa data to within $\pm 30\%$ (MAE of 11.3%).



(a)



(b)



(c)

Figure 5.34: Comparison of the current CB flow experimental heat transfer data with the Thome et al. three-zone model for R134a, R236fa and R245fa; (a) $D_{in}=1.03\text{ mm}$ (CB flow), (b) $D_{in}=2.20\text{ mm}$ (CB flow) and (c) $D_{in}=3.04\text{ mm}$ channel (S-P and CB flow).

Summary

The three-zone model performed well in the prediction of CB flow heat transfer coefficients in the $D_{in}=1.03$ and 2.20 mm channels and the S-P and CB flow in the $D_{in}=3.04\text{ mm}$ channel with the modified δ_{min} parameter. As illustrated in the results, the accuracy of the heat transfer prediction by the three-zone model is highly dependent on the defined surface roughness value of the individual channels. The same conclusion was arrived by Agostini et al. [39], who managed to predict their experimental data for silicon multi-microchannels with 90% predicted to within $\pm 30\%$ for R245fa by incorporating the actual surface roughness of the multi-microchannels tested. In many existing micro-scale channel evaporation experimental studies, the surface roughness value of the channels are often not specified and the original δ_{min} value was assumed. This justifies the lower accuracy of the three-zone model, as reported by some researchers when comparing the method's prediction against their own heat transfer data. It should also be noted that the three-zone model was developed for slug flows and thus, should only be compared against heat transfer coefficients corresponding to coalescing bubble flows and not for the annular flow regime. In conclusion, the present analysis demonstrates the importance to report the surface roughness in microchannel flow boiling papers, and also it can be concluded the difference in the published results from one study to another is probably due to the surface roughness effect.

Chapter 6

Two-Phase Pressure Drop

This chapter presents the current experimental adiabatic two-phase pressure drop data acquired during this experimental campaign. The pressure drop data shown here in this chapter correspond to refrigerants R134a, R236fa and R245fa in the $D_{in}=1.03, 2.20$ and 3.04 mm channels. As mentioned previously in Chapter 5, the main purpose of this investigation is to study the effects of channel confinement, heat flux, mass velocity, saturation temperatures, sub-cooling and the effects of the working fluid properties on adiabatic two-phase pressure drops through the sight glass installed adjacent to the outlet of the evaporator.

First, a single phase pressure drop validation was performed using the two absolute pressure transducers installed at the test section inlet and outlet. As for the adiabatic two-phase pressure drop measurements through the sight glass, the test section outlet absolute pressure transducer and a 2 mm type K thermocouple was used to measure the exit pressure. The 250 μm type K thermocouple located at the evaporator exit (inlet of the sight glass) is used to directly measure the fluid saturation temperature at the evaporator outlet. The measuring technique and the data reduction process is presented in detail in Chapter 3.

6.1 Single-Phase Validation

This section presents the single-phase pressure drop measurements performed to validate the pressure drop measurements across the test section. The single-phase pressure drop measurements have been conducted under sub-cooled liquid inlet-outlet conditions without sub-cooled boiling in the test section. Fig. (6.1)a and Fig. (6.2)a illustrates the experimental single-phase frictional pressure loss for R134a and R245fa compared to conventional pressure drop correlations from literature. The laminar flow data was compared to the well known Hagen-Poiseuille number, $64/Re$ for fully developed laminar flow and the Shah and London correlation [113] for developing flow. The Fanning friction factor did not compare well with the Hagen-Poiseuille number but is well predicted by the Shah and London correlation for developing flow.

The friction factor for turbulent flow compared well with the correlation by Philips [114]

and the well known Blasius equation, with 100% of the data to within $\pm 10\%$ prediction. For illustration purposes, the results comparison for the $D_{in}=1.03\text{ mm}$ channel is shown in Fig. (6.1)b and Fig. (6.2)b. Not shown here in the manuscript, similar results were also found for the $D_{in}=2.20$ and 3.04 mm channels with good predictions with the Shah and London correlation for developing flow.

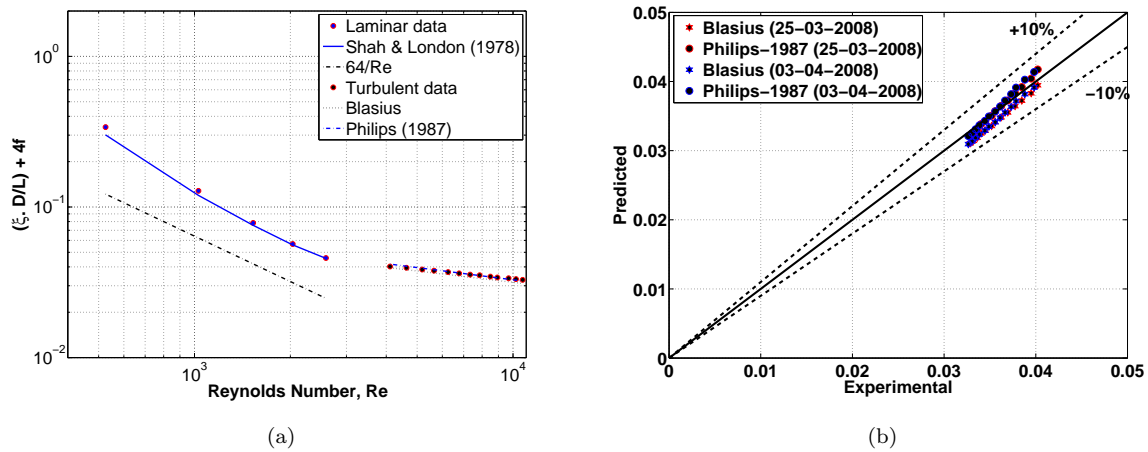


Figure 6.1: (a) Single-phase friction factor for R134a in the $D_{in}=1.03\text{ mm}$ channel and (b) Experimental versus Prediction.

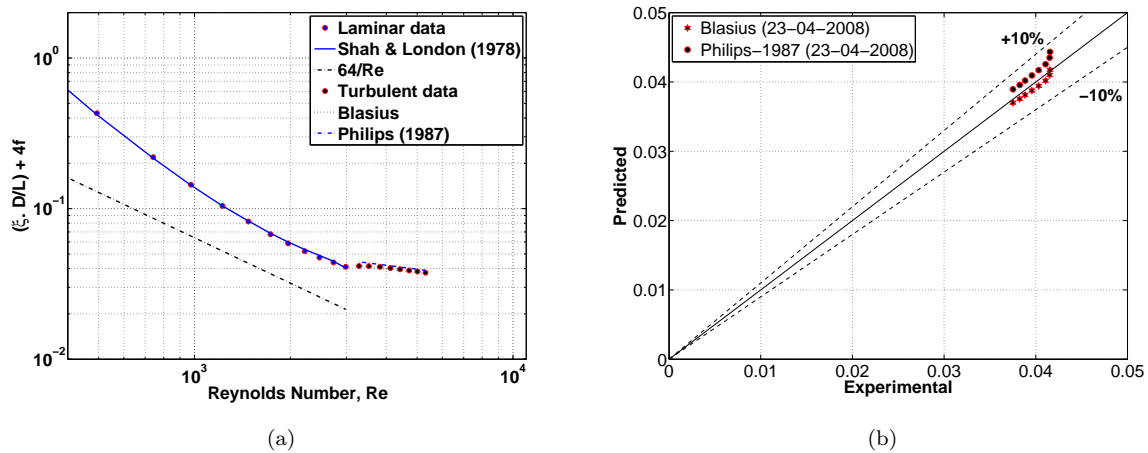
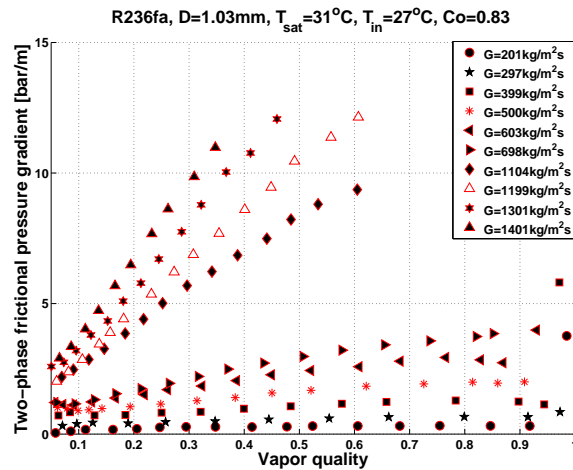


Figure 6.2: (a) Single-phase friction factor for R245fa in the $D_{in}=1.03\text{ mm}$ channel and (b) Experimental versus Prediction.

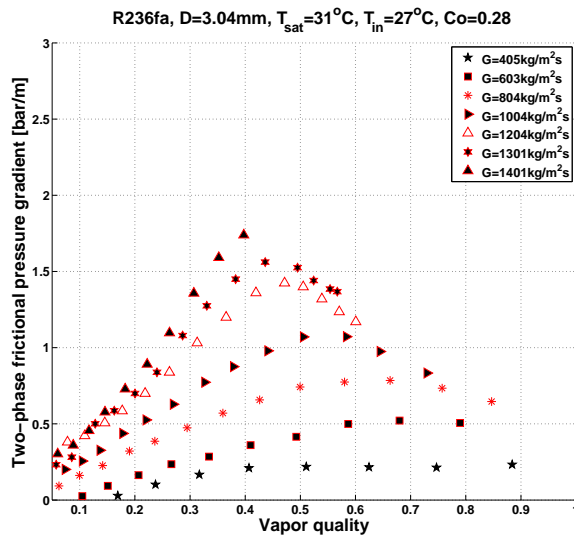
6.2 Adiabatic Two-Phase Pressure Drops

6.2.1 Effects of Channel Confinement

Fig. (6.3) and Fig. (6.4) depicts the comparison of the two-phase pressure gradient data for R236fa and R245fa in the $D_{in}=1.03$ and 3.04 mm channels corresponding to different confinement numbers. The results indicate that the two-phase pressure drop gradient is higher for higher channel confinement, as shown here for both R236fa and R245fa. The same trend was also observed for R134a and the results are not shown here.



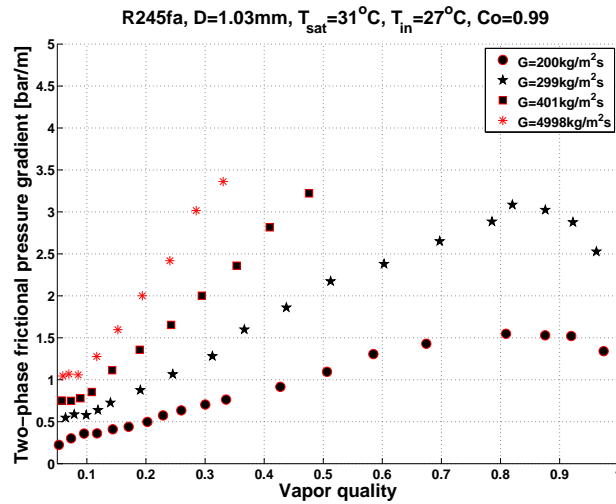
(a)



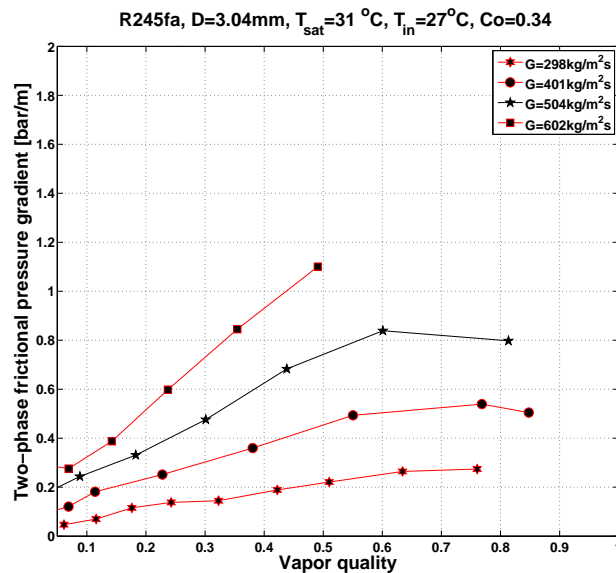
(b)

Figure 6.3: Two-phase pressure drops for R236fa in the $D_{in}=1.03$ and 3.04 mm channels at $T_{sat}=31$ °C; (a) $D_{in}=1.03$ mm, $Co=0.83$ and (b) $D_{in}=3.04$ mm, $Co=0.28$.

Referring to Fig. (6.3) and Fig. (6.4), it can be seen that the pressure gradient increases



(a)



(b)

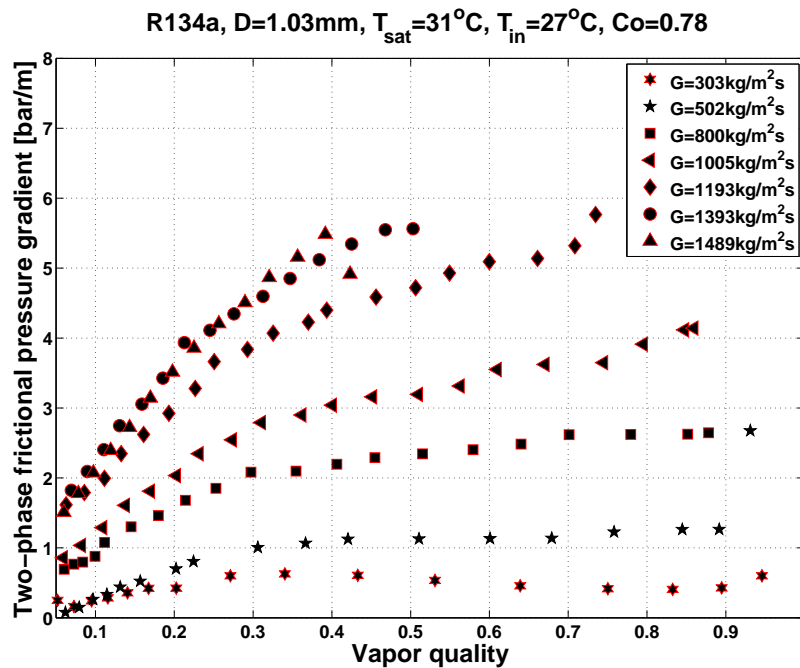
Figure 6.4: Two-phase pressure drops for R236fa in the $D_{in}=1.03$ and 3.04 mm channels at $T_{\text{sat}}=31^\circ\text{C}$; (a) $D_{in}=1.03$ mm, $Co=0.99$ and (b) $D_{in}=3.04$ mm, $Co=0.34$.

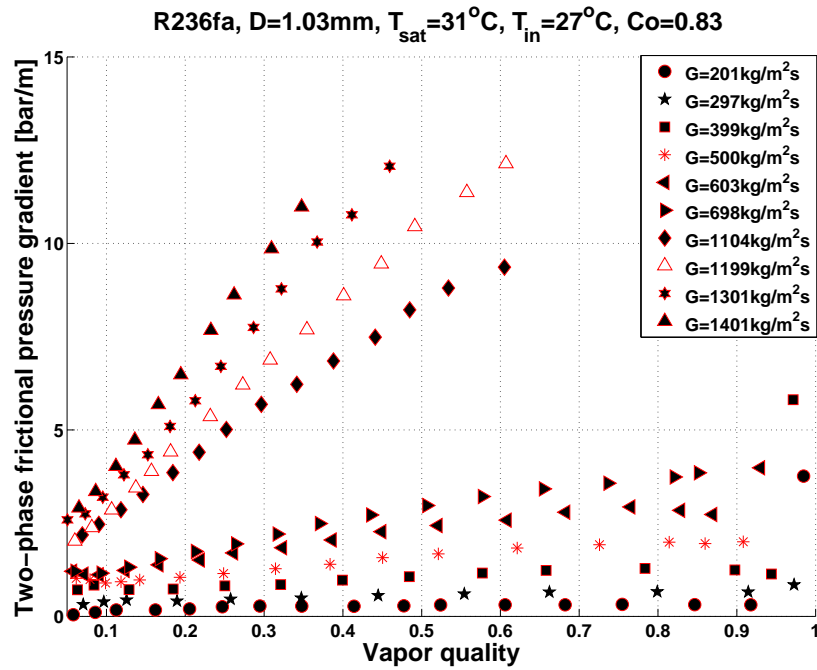
with vapor quality until it reaches a peak before a decreasing trend is observed at higher vapor qualities. This is evident for both R236fa and R245fa in the $D_{in}=3.04$ mm channel. With increasing channel confinement, the peak shifts to higher vapor qualities as can be seen in the $D_{in}=1.03$ mm channel.

6.2.2 Effects of Fluid Properties

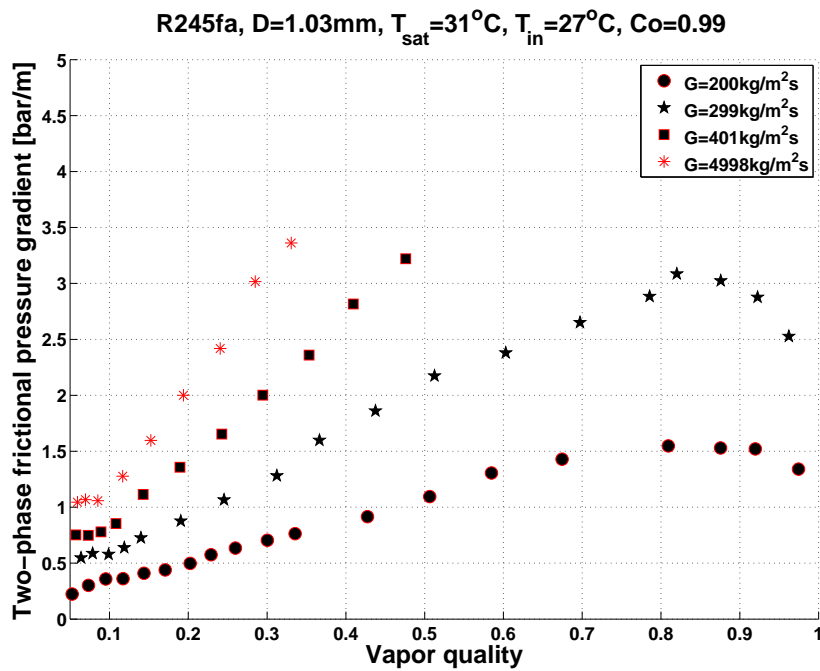
This section presents the experimental two-phase frictional pressure drop for R134a, R236fa and R245fa in the $D_{in}=1.03, 2.20$ and 3.04 mm channels to study the effects of the different fluid properties on the two-phase frictional pressure drop. The comparison of the experimental two-phase pressure drops for the three refrigerants in the $D_{in}=1.03$ channel are shown in Fig. (6.5), where the two-phase pressure gradient is the highest for R245fa, followed by R236fa and then R134a. This is as expected as the liquid viscosity of R236fa is on the order of $\approx 46.5\%$ higher than that of R134a and is $\approx 108.7\%$ higher than that of R134a for R245fa as shown in Fig. (5.10).

On the other hand, the vapor density for R245fa and R236fa at the same saturation temperature is $\approx 72.8\%$ and $\approx 42.4\%$ lower than that of R134a respectively. The liquid density of R245fa and R236fa is also marginally higher than that of R134a, which is on the order of $\approx +11.7\%$ and $\approx +13.2\%$. The lower vapor density and a higher liquid phase density for both R236fa and R245fa thus contributes to the higher pressure drop observed in the experiments. This explains the higher pressure drop for R236fa and R245fa observed for the $D_{in}=1.03, 2.20$ and 3.04 mm channels, the latter data shown in Fig. (6.6).



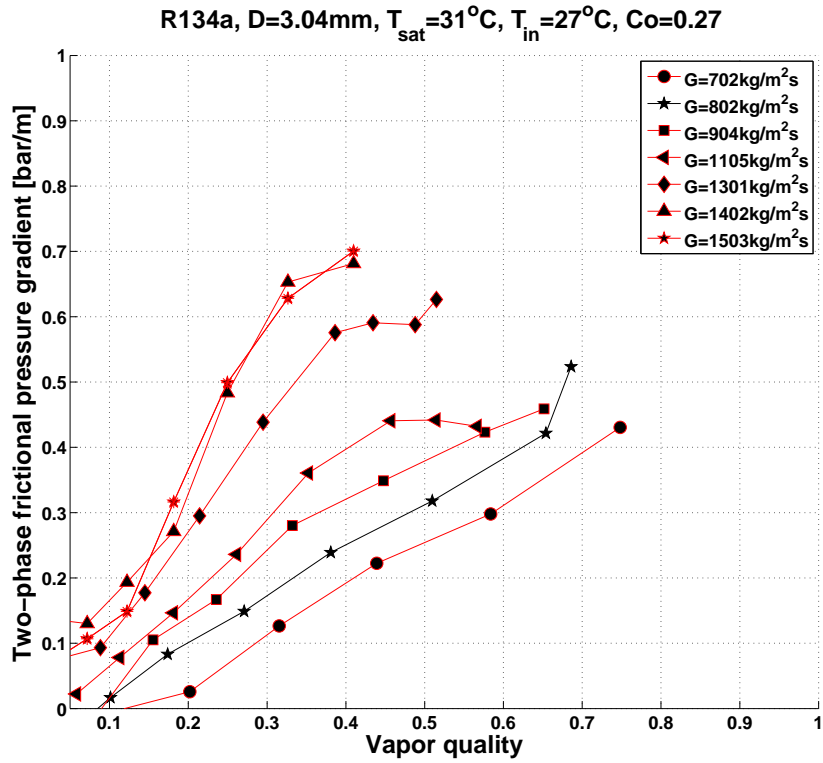


(b)

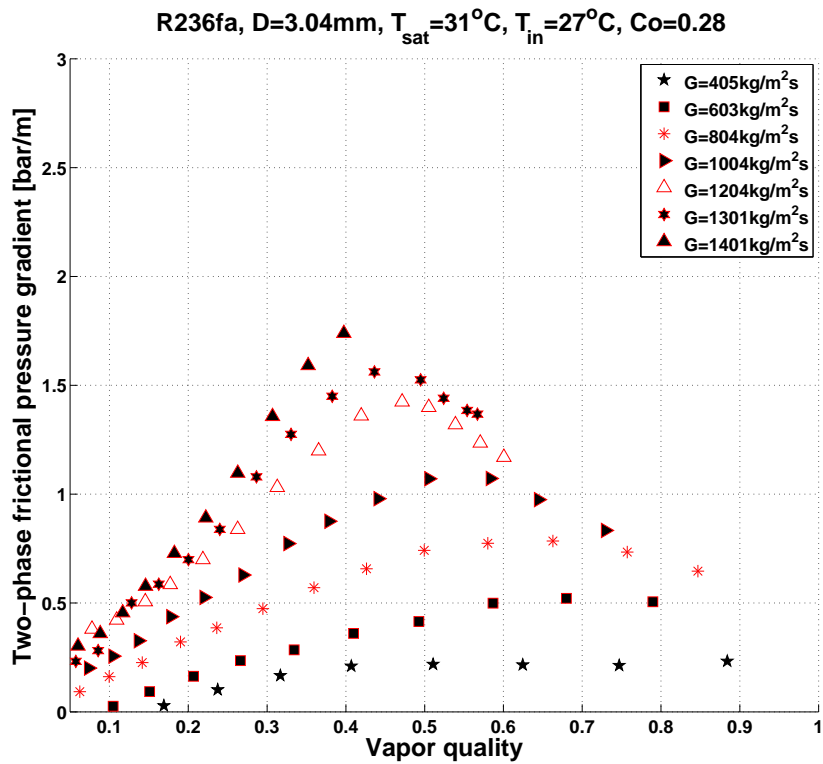


(c)

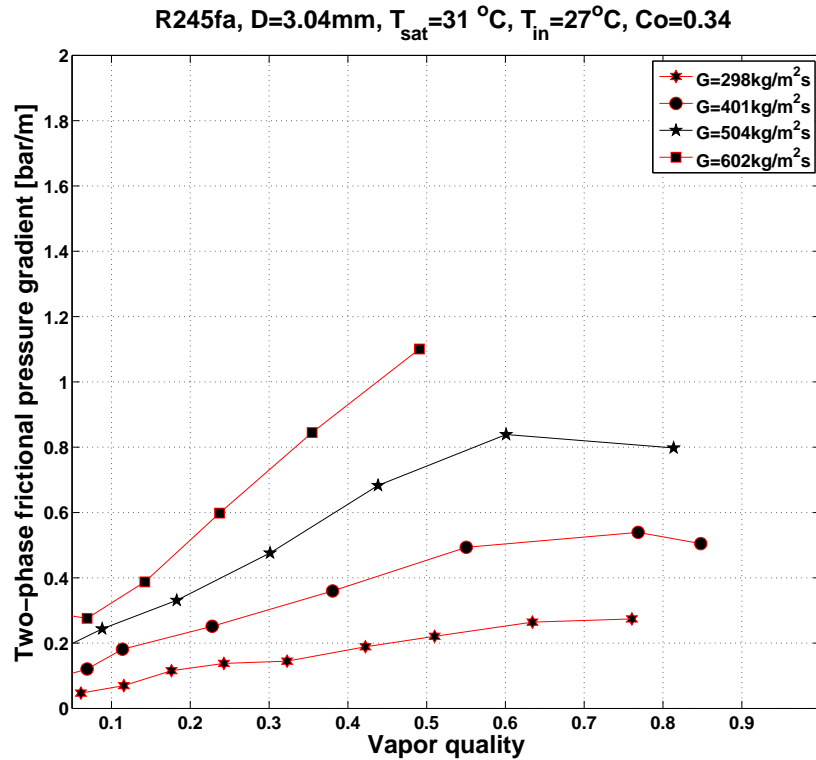
Figure 6.5: Two-phase pressure drops for R134a, R236fa and R245fa in the $D_{in}=1.03\text{ mm}$ channel at $T_{\text{sat}}=31^\circ\text{C}$; (a) R134a, (b) R236fa and (c) R245fa.



(a)



(b)



(d)

Figure 6.6: Two-phase pressure drops for R134a, R236fa and R245fa in the $D_{in}=3.04\text{ mm}$ channel at $T_{\text{sat}}=31\text{ }^\circ\text{C}$; (a) R134a, (b) R236fa and (c) R245fa.

6.2.3 Effects of Saturation Temperature

The effect of saturation temperature on the two-phase pressure was investigated during the course of this research campaign. It was widely reported that the two-phase pressure drop decreases with increasing saturation temperature or pressure, which also corresponds to a lower confinement numbers. This trend is justified when viscosity decreases with increasing saturation temperature, thus reducing the frictional pressure drop. In other words, the liquid-vapor density ratio decreases with increasing pressure or saturation temperature. The current experimental pressure drop results for all the three fluids tested conforms well with the smaller pressure drop trend reported in literature for higher saturation temperatures. The comparison of the two-phase pressure drop results for R236fa at $T_{\text{sat}}=25$ and $31\text{ }^\circ\text{C}$ in the $D_{in}=2.20\text{ mm}$ channel is shown in Fig. (6.7).

6.2.4 Effects of Mass Mass Velocity

As shown previously in Fig. (6.5) and Fig. (6.6), the two-phase pressure drop uniformly increased with mass velocity. This behavior was observed for all three fluids, in all the three channels tested. In summary, the increase in the frictional two-phase pressure drop

seems to agree with the trends observed in conventional macroscale channels.

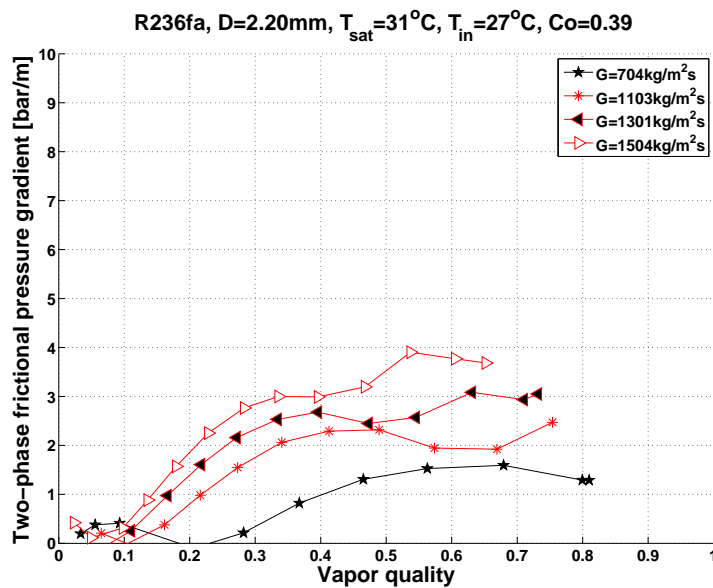
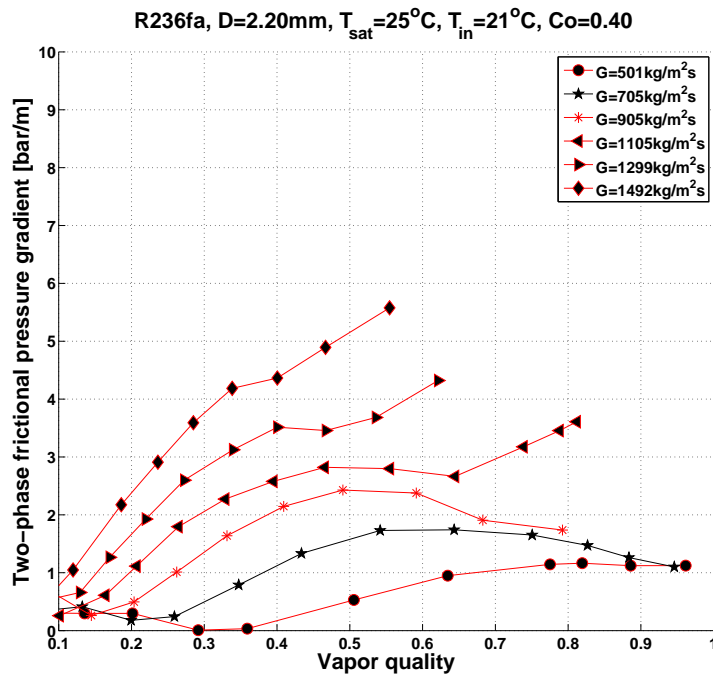


Figure 6.7: Two-phase pressure drops for R236fa in the $D_{in}=2.20\text{ mm}$ channel; (a) $T_{\text{sat}}=25^\circ\text{C}$ and (b) $T_{\text{sat}}=31^\circ\text{C}$.

6.3 Two-Phase Pressure Drops Comparison

This section compares the current experimental data with various existing macro-scale and micro-scale pressure drop models and correlations from literature. The two-phase pressure gradient comparisons include 8 conventional macroscale pressure drop prediction methods, namely the homogeneous and separated flow models as illustrated in Fig. (6.10)-Fig. (6.13) and 4 microscale pressure drop prediction methods, as shown in Fig. (6.16)-Fig. (6.19).

Fig. (6.10)-Fig. (6.9) depicts the comparison of the current experimental two-phase pressure data with the homogeneous model. The homogeneous viscosity definition, μ_h used in the comparison includes the homogeneous viscosity definition proposed by McAdams(1942), Cicchitti(1960), Dukler(1964) and Owens(1961). The homogeneous two-phase viscosity definitions proposed by McAdams(1942), Cicchitti(1960), Dukler(1964) and Owens(1961) are shown respectively in Eq. (6.1)-Eq. (6.4):

McAdams definition

$$\mu_H = \left(\frac{1-x}{\mu_L} + \frac{x}{\mu_V} \right) \quad (6.1)$$

Cicchitti definition

$$\mu_H = (1-x)\mu_L + x\mu_V \quad (6.2)$$

Dukler definition

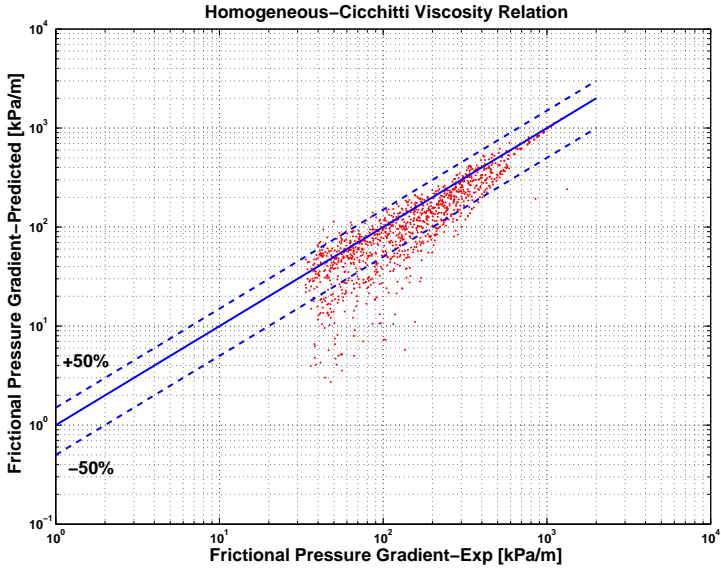
$$\mu_H = \rho_H((1-x)\mu_L + x\mu_V) \quad (6.3)$$

Owens definition

$$\mu_H = \mu_L \quad (6.4)$$

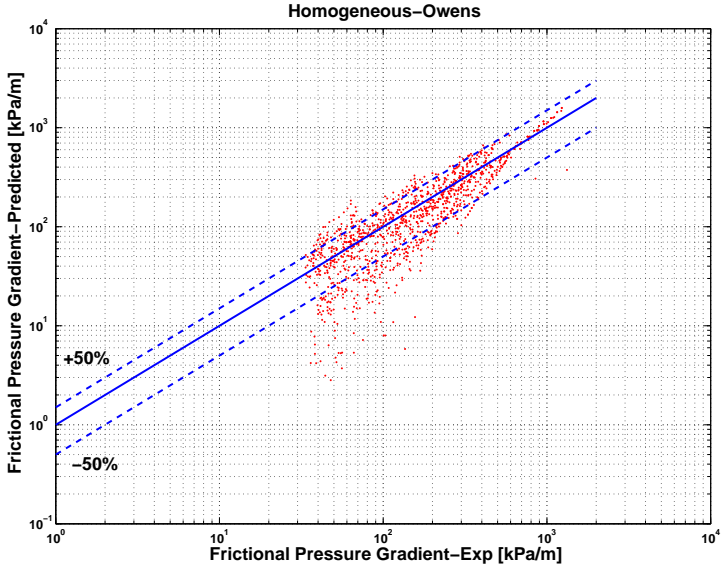
Comparing the four viscosity definitions, the homogeneous viscosity proposed by Cicchitti(1960) yields the best prediction with 76.9% data within $\pm 50\%$ prediction (MAE of 31.4%), followed by Owens(1961) with 70.1% data within $\pm 50\%$ prediction (MAE of 35.2%). The homogeneous viscosity definition proposed by McAdams(1942) managed to predict only 57.4% data within $\pm 50\%$ prediction (MAE of 46.8%) and Dukler(1964) with only 46.8% data within $\pm 50\%$ prediction (MAE of 50.5%).

Fig. (6.12) depicts the experimental pressure drop comparison with the Lockhart-Martinelli [115] separated flow model for macroscale flows. The prediction method compared fairly well with the current experimental data with 75.6% data within $\pm 50\%$ prediction (MAE of 40.5%). On the other hand, Fig. (6.13) illustrates the comparison of the current experimental data with the macroscale correlation of Baroczy [116] and Chisholm [117]. This prediction method managed to predict 83.3% of the data to within $\pm 50\%$ with a MAE of 29.6%. The Baroczy-Chisholm correlation is by far the best macroscale prediction method with the highest accuracy with the lowest mean absolute error.



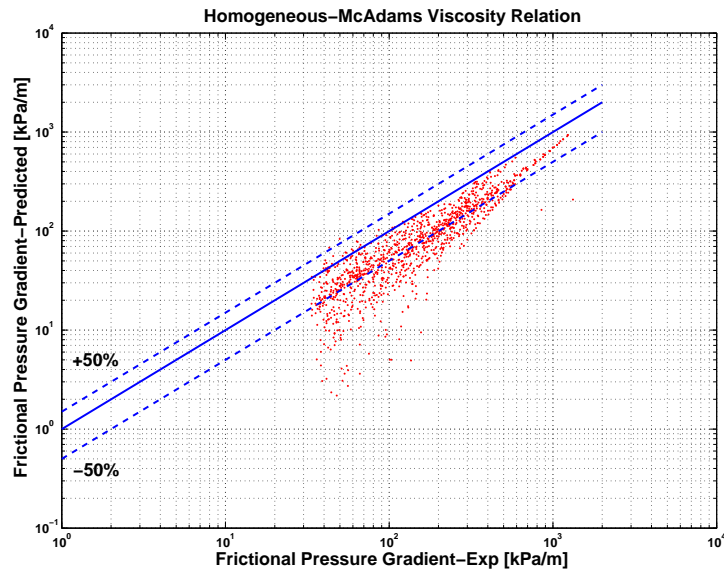
(a)

Figure 6.8: Homogeneous Cicchitti prediction: 76.9% data within $\pm 50\%$ prediction (MAE of 31.4%).



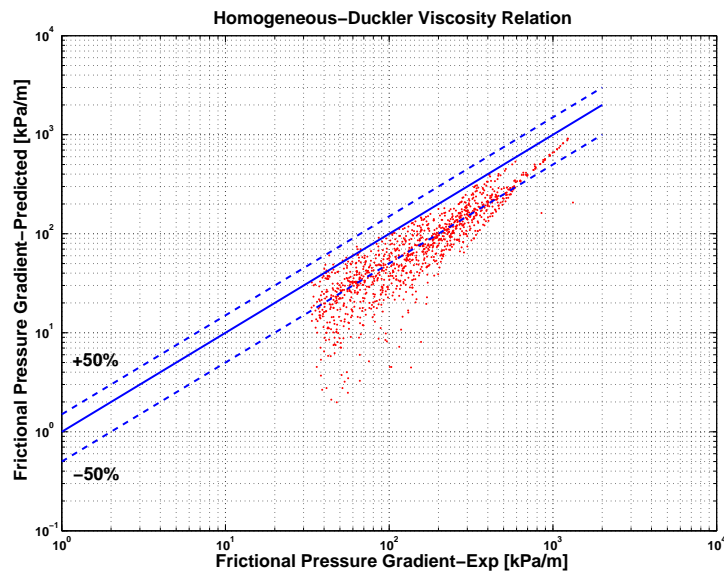
(a)

Figure 6.9: Homogeneous Owens prediction: 70.1% data within $\pm 50\%$ prediction (MAE of 35.2%).



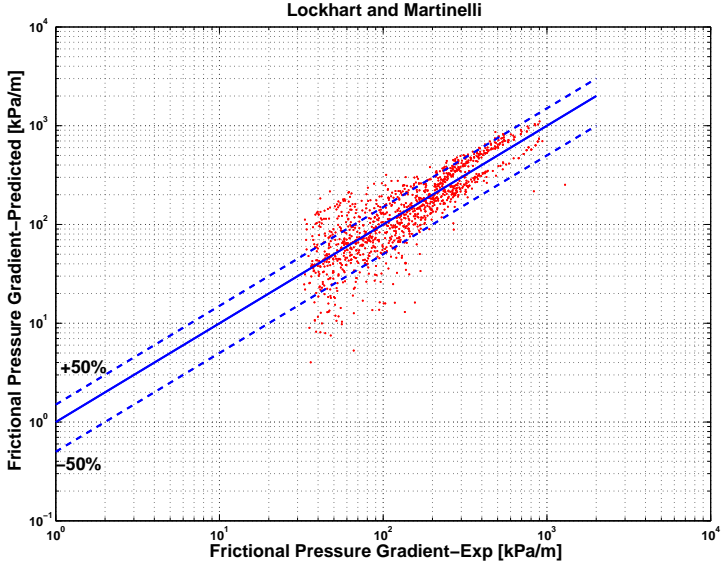
(a)

Figure 6.10: Homogeneous McAdams prediction: 57.4% data within $\pm 50\%$ prediction (MAE of 46.8%).



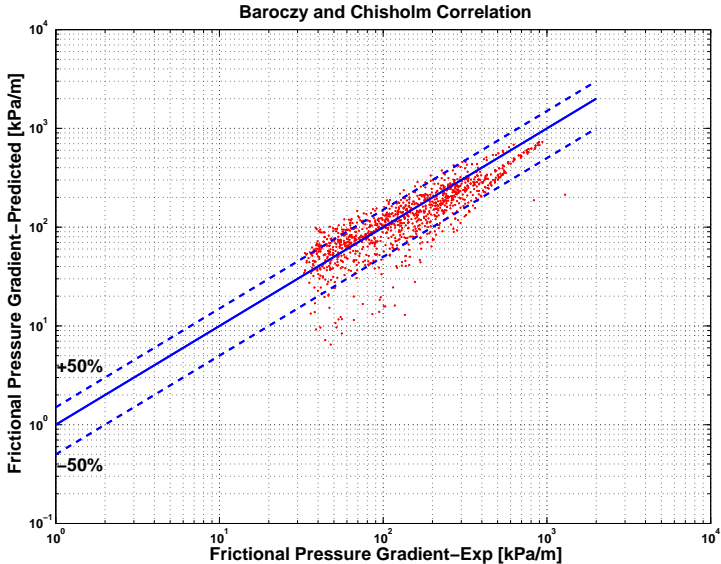
(a)

Figure 6.11: Homogeneous Duckler prediction: 46.8% data within $\pm 50\%$ prediction (MAE of 50.5%).



(a)

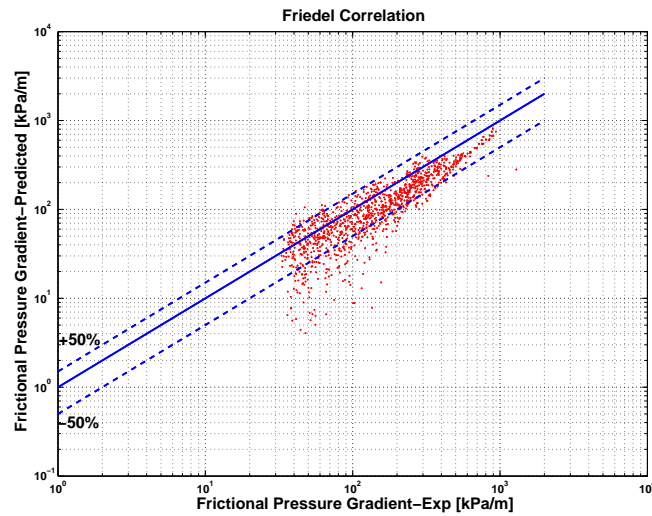
Figure 6.12: Lockhart-Martinelli prediction: 75.6% data within $\pm 50\%$ prediction (MAE of 40.5%).



(a)

Figure 6.13: Baroczy-Chisholm prediction: 83.3% data within $\pm 50\%$ prediction (MAE of 29.6%).

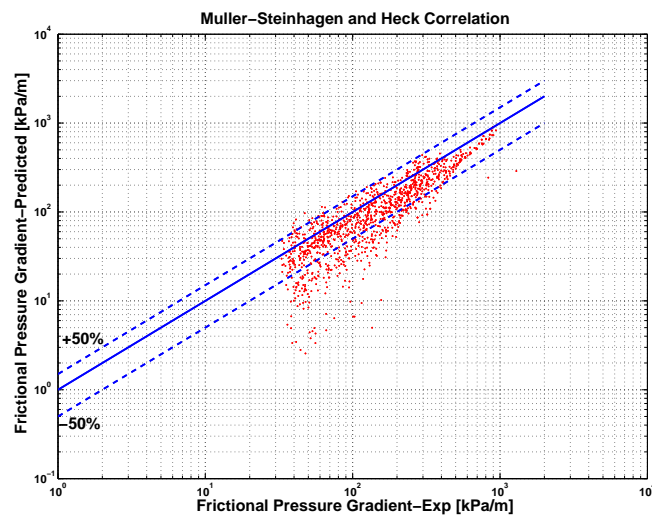
Fig. (6.14) shows the comparison of the two-phase pressure gradient with the macro-scale Friedel [118] correlation. The correlation managed to predict 78.1% of the current experimental data within $\pm 50\%$ prediction with a MAE of 34.2%. The comparison



(a)

Figure 6.14: Friedel prediction: 78.1% data within $\pm 50\%$ prediction (MAE of 34.2%).

with the macro-scale Muller-Steinhagen and Heck et al. [91] correlation is illustrated in Fig. (6.15). This correlation predicted 74.2% data within $\pm 50\%$ prediction with a MAE of 35.6%.



(a)

Figure 6.15: Muller-Steinhagen and Heck prediction: 74.2% data within $\pm 50\%$ prediction (MAE of 35.6%).

The following section compares the current experimental two-phase pressure gradients with 4 microscale pressure drop prediction methods by Mishima-Hibiki [92], Tran et al. [86], Zhang-Mishima [119] and Sun-Mishima [120]. The correlation of Mishima et al. [92] was based on the modification of the Lockhart-Martinelli correlation to better fit the microscale data. The authors proposed a method to calculate the constant C , which they correlated as:

$$C = 21[1 - \exp(-0.319D_{in})] \quad (6.5)$$

In a later version, Zhang-Mishima [119] proposed a version to evaluate the constant, C based on the Laplace constant, La .

$$C = 21[1 - \exp(\frac{-0.358}{La})] \quad (6.6)$$

$$La = \frac{1}{D_{in}} [\frac{\sigma}{g(\rho_L - \rho_V)}]^{0.5} \quad (6.7)$$

Another version by Sun-Mishima [120] correlates the C parameter as:

$$C = 1.79X^{-1.19}(\frac{Re_{VO}}{Re_{LO}})^{0.4}(\frac{1-x}{x})^{0.5} \quad (6.8)$$

The comparisons of the current experimental data with the correlations of Mishima-Hibiki [92], Zhang-Mishima [119] and Sun-Mishima [120] are shown in Fig. (6.16), Fig. (6.17) and Fig. (6.18), respectively. Among the three correlations, the C parameter by Sun-Mishima Eq. (6.8) yielded the best prediction with 72.6% of the data within ± 50 % prediction (MAE of 39.3%), followed by Zhang-Mishima Eq. (6.6) predicting 70.3% of the data within ± 50 % prediction (MAE of 42.7%). The correlation by Mishima-Hibiki Eq. (6.5) is the least accurate among the three and managed to predict only 61.4% data within ± 50 % prediction with a MAE of 44.4%.

Fig. (6.19) depicts the current experimental data comparison with the correlation of Tran et al. [86], which is a modification of of the Baroczy-Chisholm [116] correlation adapted for microscale pressure drop predictions. The correlation only managed to predict 42.8% of the current experimental data to within ± 50 % prediction with a relatively high MAE of 71.6%. The comparison is shown in Fig. (6.19).

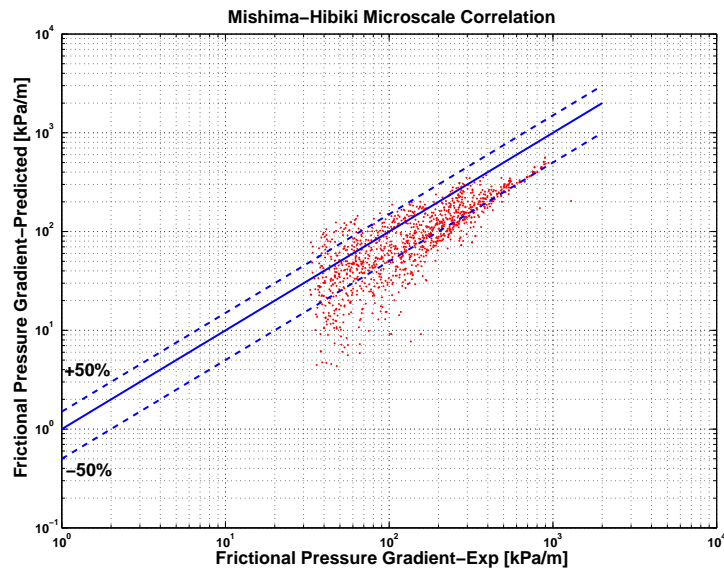


Figure 6.16: Mishima Hibiki prediction: 61.4% data within $\pm 50\%$ (MAE of 44.4%).

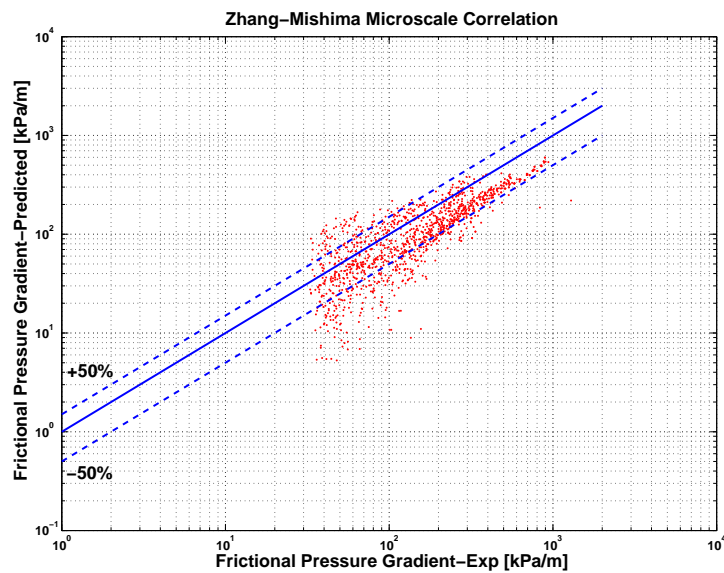
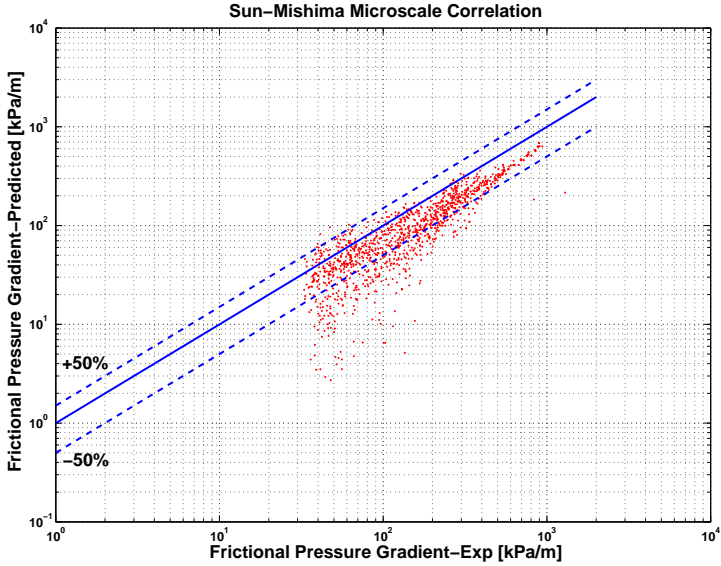
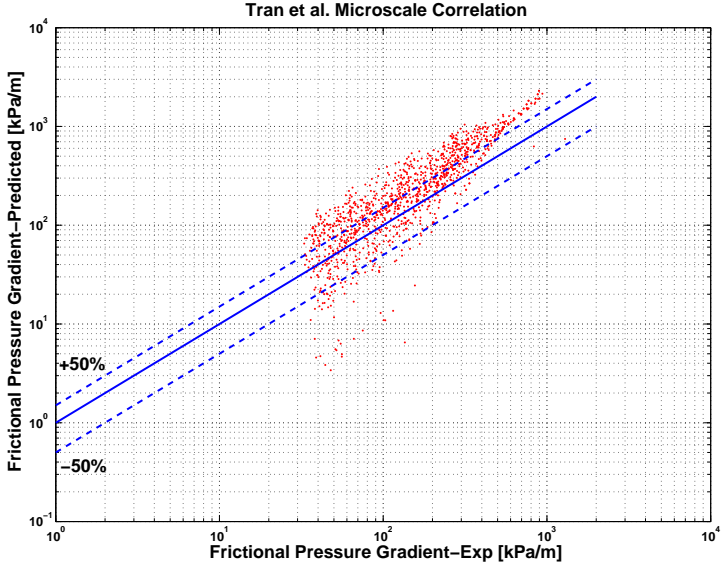


Figure 6.17: Zhang Mishima prediction: 70.3% data within $\pm 50\%$ (MAE of 42.7%).



(a)

Figure 6.18: Sun-Mishima prediction: 72.6% data within $\pm 50\%$ (MAE of 39.3%).



(a)

Figure 6.19: Tran et al. prediction: 42.8% data within $\pm 50\%$ (MAE of 71.6%).

6.4 Summary

Summarizing in brief, the Baroczy-Chisholm [116] method yields the best prediction of the current experimental data, followed by the Friedel [118] method. The homogeneous model using the Cicchitti two-phase viscosity definition ranks third among the macroscale prediction methods presented in this chapter. The separated flow model of Lockhart-Martinelli [115] and Muller Steinhagen-Heck prediction methods are also fairly accurate in predicting these miniscale pressure drop data. As for the microscale pressure drop prediction methods, the Sun-Mishima [120] and Zhang-Mishima [119] methods yield the best predictions of our current pressure drop data.

Chapter 7

Film Thickness Measurement

As described earlier in Section 3.4.6, the high speed flow visualization videos acquired during the experimental campaign were processed to obtain a 'qualitative' comparison of the film thicknesses at the top and bottom of the channel. The work is reported in the chapter. The image processing toolbox of MATLAB was used to directly process the images, in order to determine the liquid-vapor interface at the top and bottom part of the channel.

7.1 Objective

The main objective for this analysis is to study the effect of channel confinement on the film stratification by comparing the film thickness at the top to the bottom of the channel. The aim is thus to define the lower threshold of the macro-to-microscale transition by investigating the dominance of surface tension forces against gravity forces according to the confinement number, Co , e.g. by determining when gravity no longer affects the film thickness. As for the two larger channels, it was clearly observed that film stratification effects are present and the bottom liquid film thickness is much thicker in comparison to the top liquid film as shown previously in Chapter 4. Thus, only the high speed images corresponding to the highest confinement numbers; i.e. $Co=0.83$ for R236fa and $Co=0.99$ for R245fa in the $D_{in}=1.03\text{ mm}$ channel are processed for liquid film thickness comparisons here.

7.2 Experimental Setup

The high speed images of the flow visualization videos have been acquired through the use of a PHOTRON Ultima APX high speed, high resolution camera positioned at the inlet of the sight glass. To provide sufficient background lighting for the high speed video acquisition, a continuous halogen light source was positioned at the rear side of the sight glass at mid-plane. A diffusive filter paper is positioned between the light source and sight glass to diffuse the light source and to obtain a soft lighting effect. The high speed videos were acquired at a rate of 4,000 *fps*. The images were then post processed with a

MATLAB image processing code to detect the liquid-vapor bubble interface and compute the top and bottom liquid layer film thickness in terms of the number of image pixels.

7.3 Image Processing Algorithm

Central to the determination of the top and bottom liquid layer film thickness is the edge detection of the liquid-vapor bubble interface and the liquid-wall boundary. Thus, the core of the image processing algorithm is to detect the liquid-vapor interface by locating the pixel which has the peak gradient in light intensity in the vertical direction. In the preprocessing stage, the raw images are converted into gray scale (intensity images) that contains intensity values in the range of 0 to 255. A two-dimensional Gaussian low-pass filter is applied to the image to smoothen the image and reduce the image noise. Due to the linearity of the convolution sum, the convolution was performed as two one-dimensional sums instead of one two-dimensional sum. The filtering was achieved by the averaging operation where the values are normalized by dividing each term in the kernel by the sum of all terms in the kernel. In the current analysis, two 1×3 filters, one applied horizontally and one vertically and a standard deviation, $S_{\bar{x}}=2$ pixels was applied to smoothen the images. The images were then processed to determine the intensity gradient in the vertical Y-direction corresponding to a given pixel coordinate, X to detect the liquid-wall boundaries and liquid-vapor interfaces by locating the peak in the maximum and minimum values from the image gradient data.

7.4 Calibration

The most critical parameter needed for the evaluation of the liquid film thickness (in pixels) is to accurately calibrate and determine the wall boundaries in full single-phase flow. The purpose of the image calibration procedure is to exactly determine the pixel position corresponding to the internal and external boundaries of the channel wall without the presence of vapor bubbles. In this study, 100 images of the channel corresponding to full liquid flow were processed to detect the wall boundaries. Fig. (7.1) illustrates the intensity gradient plot along the solid red line, as shown in the wall image for R236fa in the $D_{in}=1.03 \text{ mm}$ channel. The relative pixel positions corresponding to the internal and external wall boundaries are then evaluated from the image calibration process. The vertical pixel positions corresponding to the internal top and bottom wall boundary are defined as $Y_{wall,top}$ and $Y_{wall,bottom}$. The top and bottom liquid-vapor interface is then determined by evaluating the intensity gradients vertically (from the top to bottom) between the inner wall boundaries of the real-time flow visualization images. The top liquid-vapor interface is determined by locating the pixel with a minimum intensity gradient while a maximum gradient corresponds to the bottom liquid-vapor interface. The curvature of the vapor bubble interface causes a slightly darker pixel with lower intensity, a light refraction and reflection phenomena due to the dissimilar liquid and vapor phase densities. With the identification of the liquid-vapor interface, it is then possible to evaluate the liquid film thickness (in pixels) by subtracting the top and bottom liquid-vapor interface pixel posi-

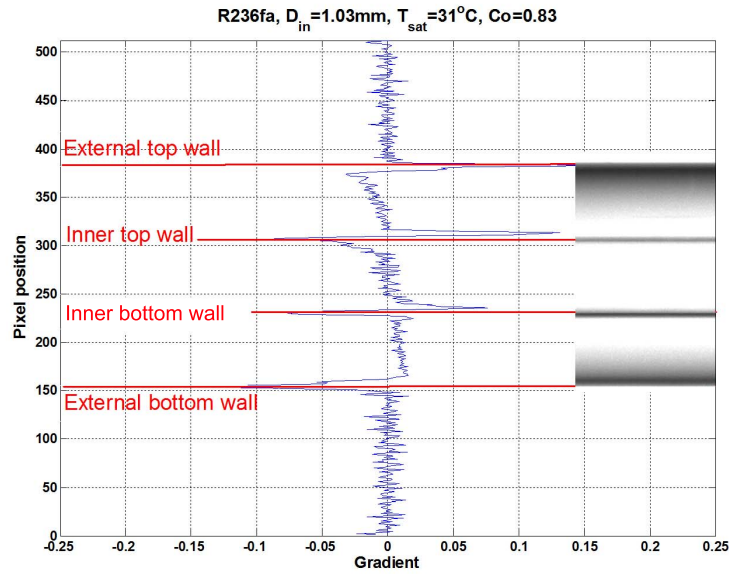


Figure 7.1: Full liquid image calibration for the $D_{in}=1.03 \text{ mm}$ channel.

tions with the wall pixel boundaries. The results allows only a 'qualitative' comparison of the film thicknesses at the top and bottom, since the magnification effect of the glass is not accounted for and because of the limited number of pixels representing the liquid film thickness.

7.5 Effect of Mass Velocity

This section presents the effects of mass velocity on the liquid film thickness for R236fa and R245fa at $G \approx 600 \text{ kg/m}^2\text{s}$. Fig. (7.2) shows the film thickness results for R236fa at $T_{sat}=31 \text{ }^\circ\text{C}$. From the results, it is clear that liquid film stratification effects are still present and significant even at higher mass velocities as illustrated in Fig. (7.2).

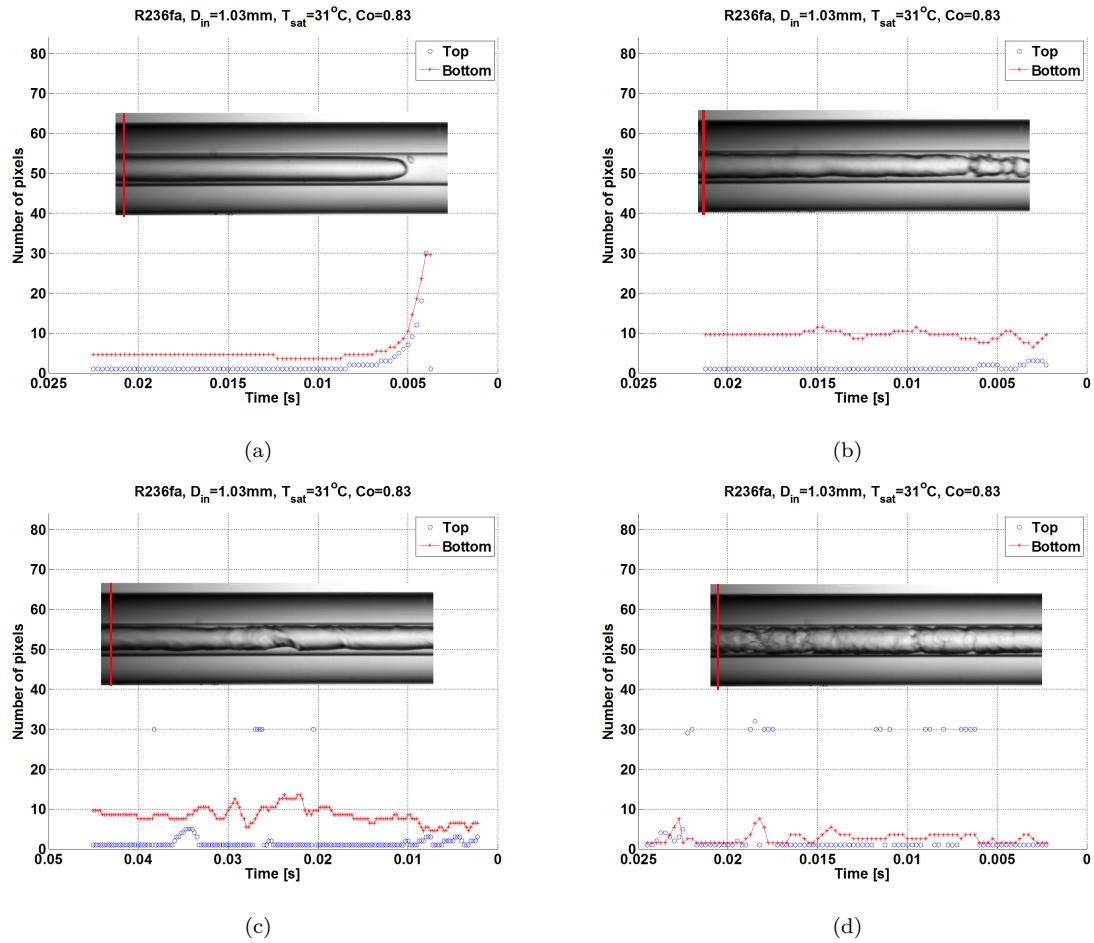


Figure 7.2: Top and bottom liquid film thickness for R236fa in the $D_{in}=1.03\text{ mm}$ channel at $T_{sat}=31\text{ }^\circ\text{C}$, $G=603\text{ kg/m}^2\text{ s}$; a) $q=7.1\text{ kW/m}^2$, $x=0.03$, (b) $q=10.3\text{ kW/m}^2$, $x=0.06$, (c) $q=13.9\text{ kW/m}^2$, $x=0.09$ and (d) $q=23.2\text{ kW/m}^2$, $x=0.16$.

The liquid film thickness comparison for R245fa at the same approximate conditions is shown in Fig. (7.3). Here, instead, the top and bottom liquid film thickness are similar in magnitude, except for some wavy interfacial structure caused by the bubble coalescence process. In general, it is sufficient to conclude that the microscale threshold is reached when confinement number, $Co \approx 1$ as shown in the results.

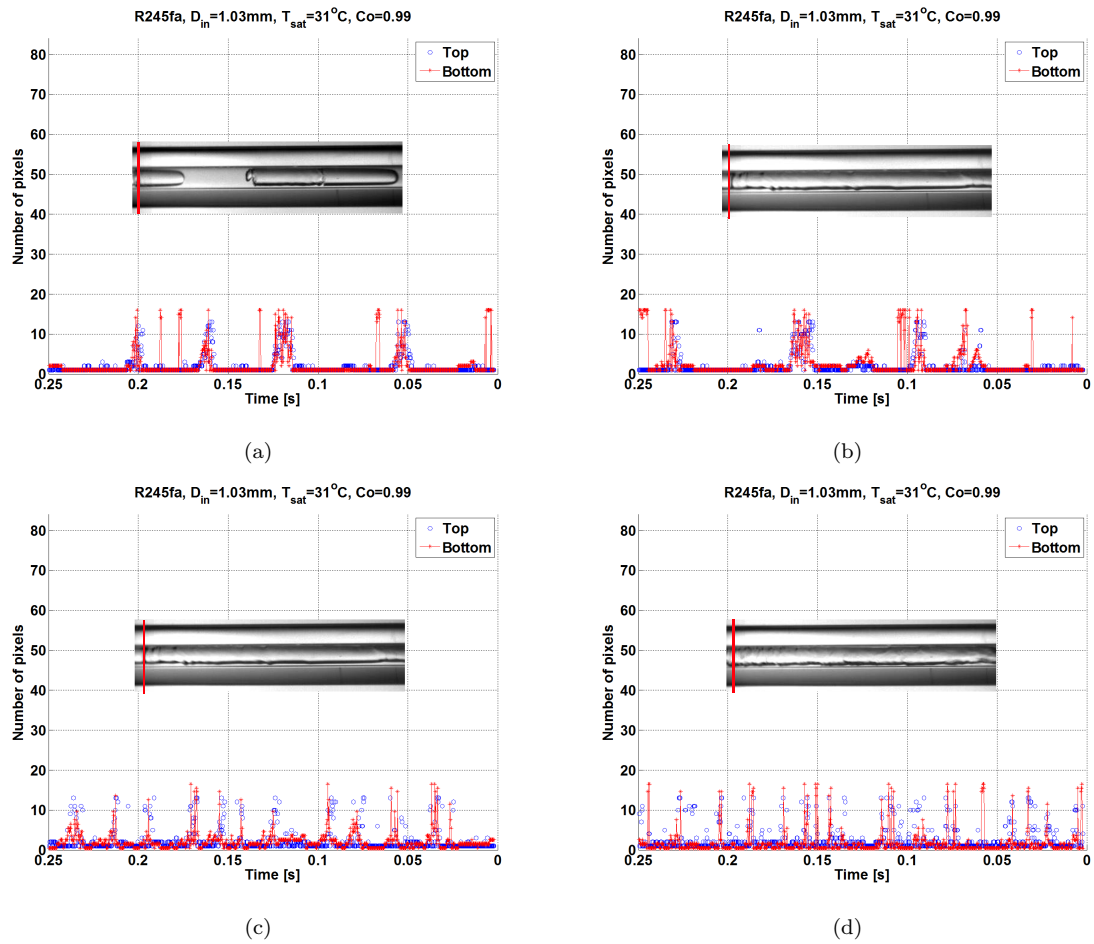
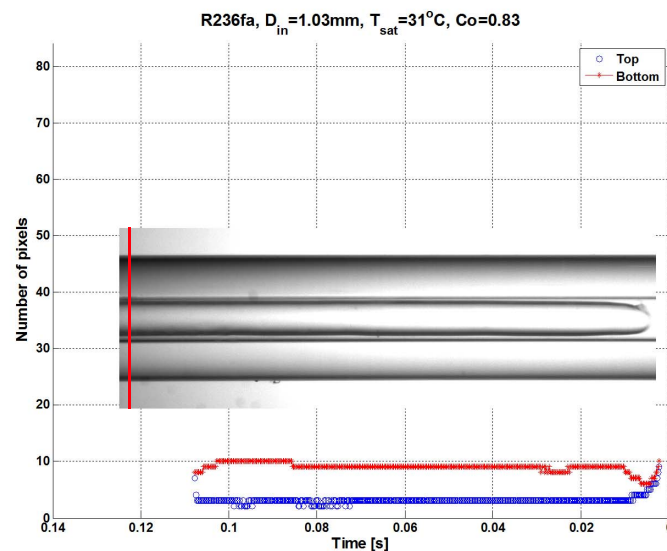


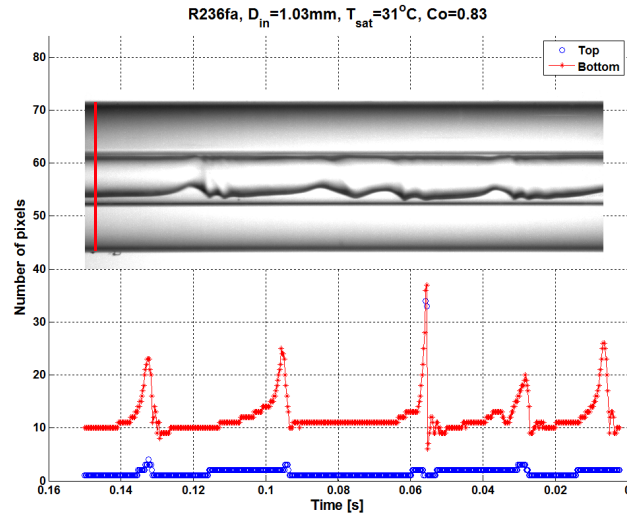
Figure 7.3: Top and bottom liquid film thickness for R245fa in the $D_{in}=1.03$ mm channel at $T_{sat}=31^{\circ}\text{C}$, $G=599$ kg/m²s; a) $q=9.9$ kW/m², $x=0.04$, (b) $q=11.5$ kW/m², $x=0.05$, (c) $q=17.8$ kW/m², $x=0.08$ and (d) $q=22.6$ kW/m², $x=0.11$.

7.6 Film Thickness Comparison

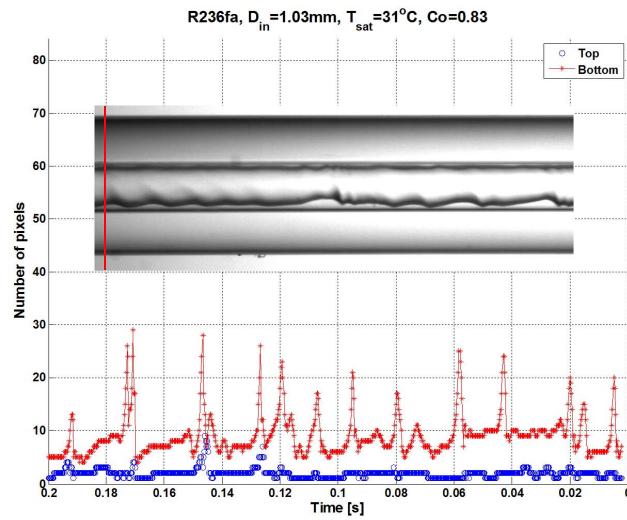
Fig. (7.4) depicts the comparison of the top and bottom liquid film thickness (in pixels) of an elongated slug bubble for R236fa in the $D_{in}=1.03\text{ mm}$ channel at $T_{sat}=31\text{ }^{\circ}\text{C}$. The liquid film thickness is evaluated along the X-pixel position illustrated by the solid red line during the passage of the bubble. Processing the image, the liquid film thickness at the bottom of the channel is thicker than the liquid film observed for the top portion of the channel. The confinement number for R236fa at $G=100\text{ kg/m}^2\text{s}$ and $T_{sat}=31\text{ }^{\circ}\text{C}$ corresponds to $Co=0.83$. Fig. (7.4)a, corresponds to the IB flow regime while Fig. (7.4)b and Fig. (7.4)c correspond to the CB flow regime. In all three cases, mild liquid film stratification to the bottom of the channel is observed. In Fig. (7.4)a, the liquid film is about 3 times thicker at the bottom than the top, illustrating a significant stratification effect. Fig. (7.4)b and Fig. (7.4)c illustrate again significant stratification and showed that the image processing technique is able to pick up the frequency of the interfacial waves and an approximate idea of their relative magnitudes. At higher vapor qualities, where Fig. (7.4)d corresponds to the annular flow regime, the mean liquid film thickness at the bottom of the channel is still on the order of 2 times thicker in comparison to the liquid film at the top portion of the channel. From the results illustrated in Fig. (7.4), it is conclusive that the effect of gravity is still dominant compared to the surface tension forces.



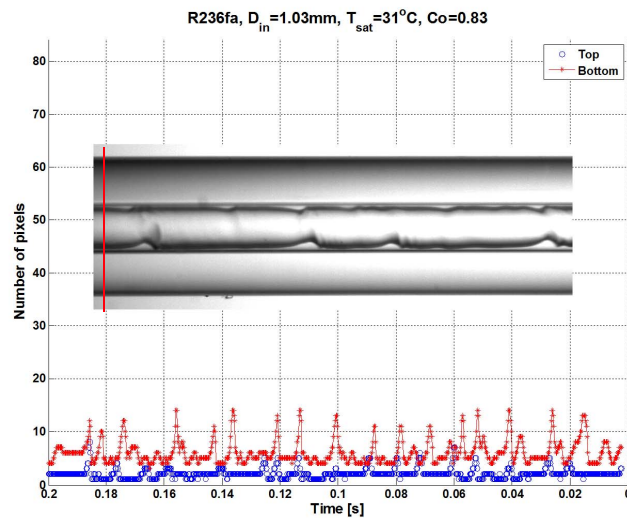
(a)



(b)



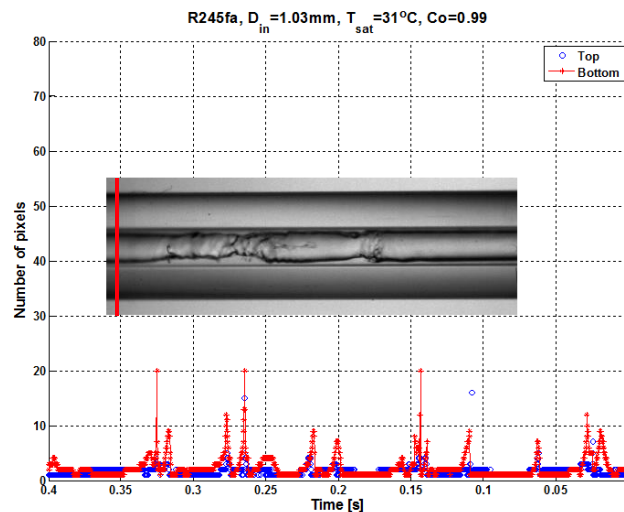
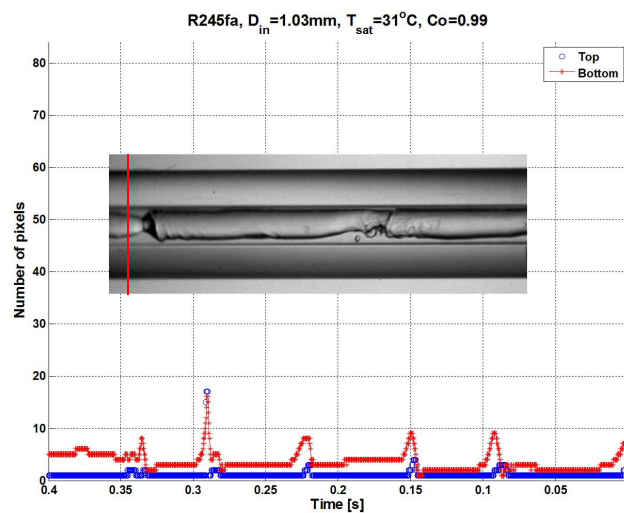
(c)

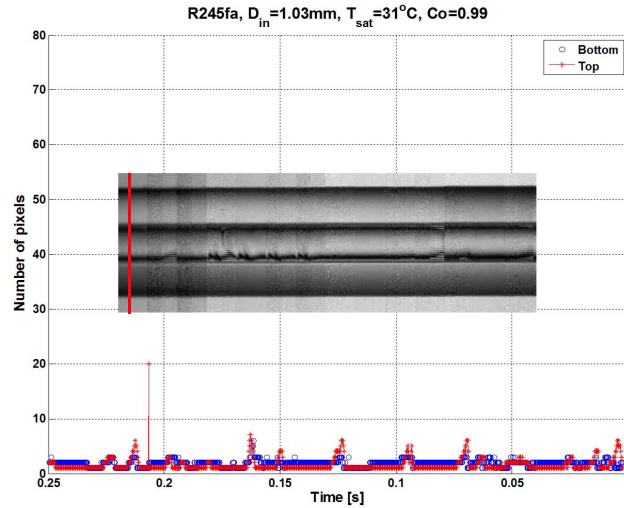


(d)

Figure 7.4: Top and bottom liquid film thickness for R236fa in the $D_{in}=1.03\text{ mm}$ channel at $T_{sat}=31\text{ }^\circ\text{C}$, $G=100\text{ kg/m}^2\text{s}$; a) $q=5.1\text{ kW/m}^2$, $x=0.208$, (b) $q=7.9\text{ kW/m}^2$, $x=0.33$, (c) $q=11.3\text{ kW/m}^2$, $x=0.49$ and (d) $q=15.2\text{ kW/m}^2$, $x=0.69$.

Fig. (7.5) depicts the results of the liquid film thickness for R245fa at $G=100 \text{ kg/m}^2\text{s}$ and $T_{sat}=31 \text{ }^\circ\text{C}$ corresponding to $Co=0.99$. Fig. (7.5)a corresponds to the IB flow regime while Fig. (7.5)b illustrates the film thickness in the CB flow regime and Fig. (7.5)c shows the annular flow regime. In the IB regime, the top liquid film thickness is observed to be thinner than the liquid film at the bottom. In the CB and annular flow regime for higher vapor qualities, the liquid film thickness at the top and bottom are instead comparable in magnitude. This indicates the dominance of the surface tension forces over gravity when $Co \approx 1.0$ in the latter two regimes but not yet in the first regime. Hence, if one wished to define the lower threshold of the macro-to-microscale transition as the point where buoyancy effects disappear, then this threshold is shown here to be a function of flow regime, and not only the value of Co .

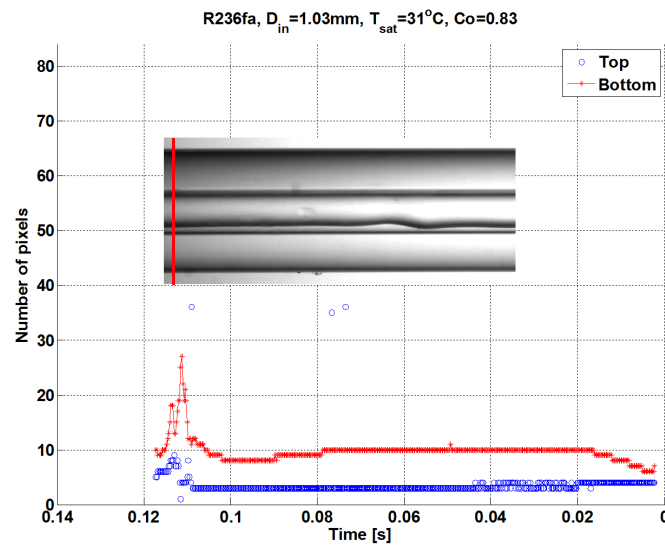




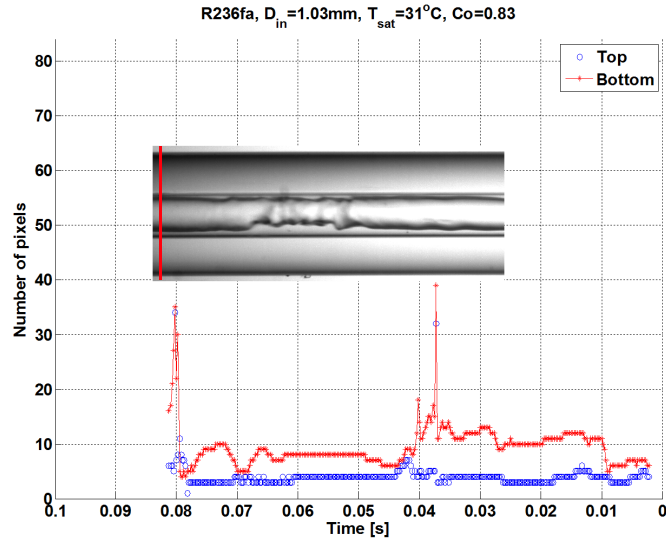
(c)

Figure 7.5: Top and bottom liquid film thickness for R245fa in the $D_{in}=1.03\text{ mm}$ channel at $T_{sat}=31\text{ }^\circ\text{C}$, $G=100\text{ kg/m}^2\text{s}$; a) $q=5.4\text{ kW/m}^2$, $x=0.16$, (b) $q=12.1\text{ kW/m}^2$, $x=0.41$ and (c) $q=15.9\text{ kW/m}^2$, $x=0.57$.

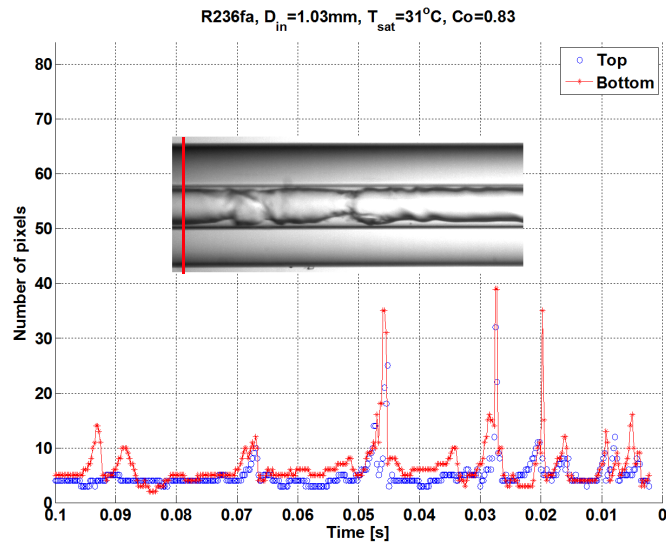
Fig. (7.6) on the other hand illustrates the film thickness results for R236fa at $G=199\text{ kg/m}^2\text{s}$ and $T_{sat}=31\text{ }^\circ\text{C}$. As expected, the top liquid film thickness is much thinner in comparison with the bottom liquid film thickness, as illustrates in Fig. (7.7)a,b and c. At higher vapor qualities, the top and bottom film thicknesses appear to be similar in magnitude but wavier at the bottom. Again, the flow pattern effect on the uniformity of the flow is still very evident, showing that the macro-microscale transition is a function of flow pattern, and not just the value of Co .



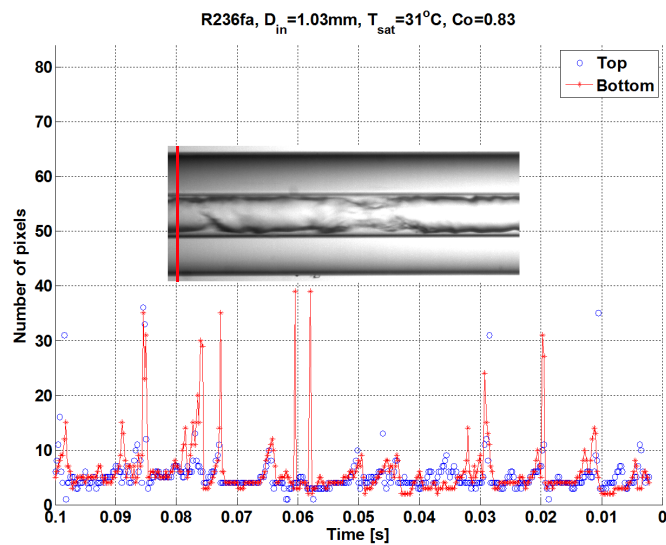
(a)



(b)



(c)



(d)

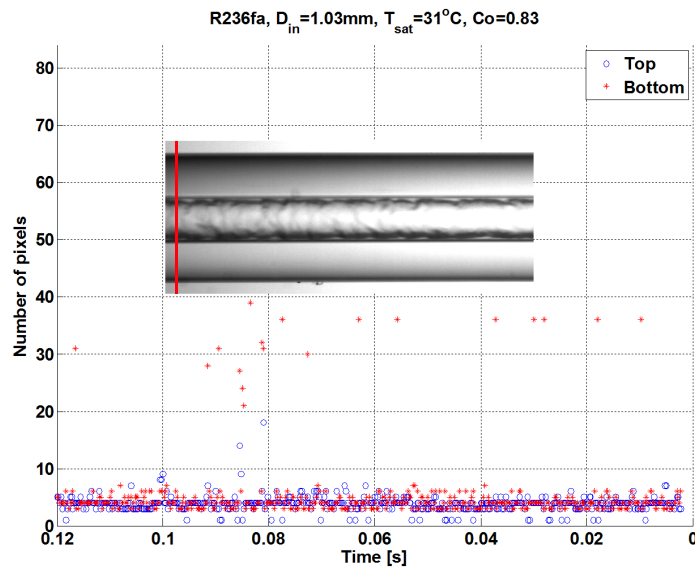
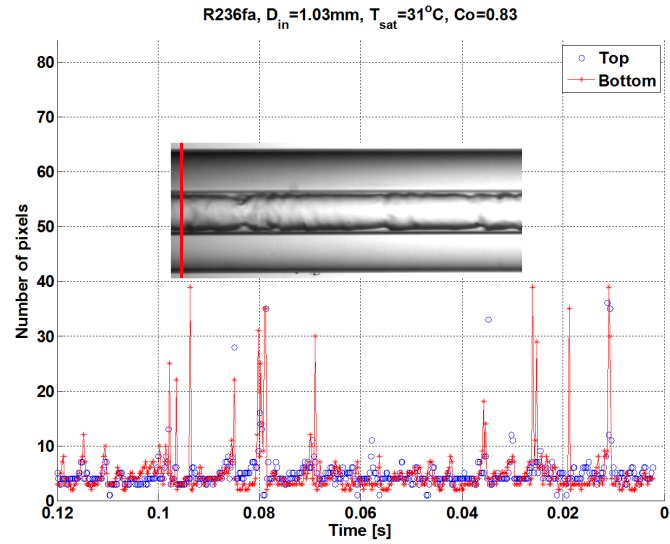
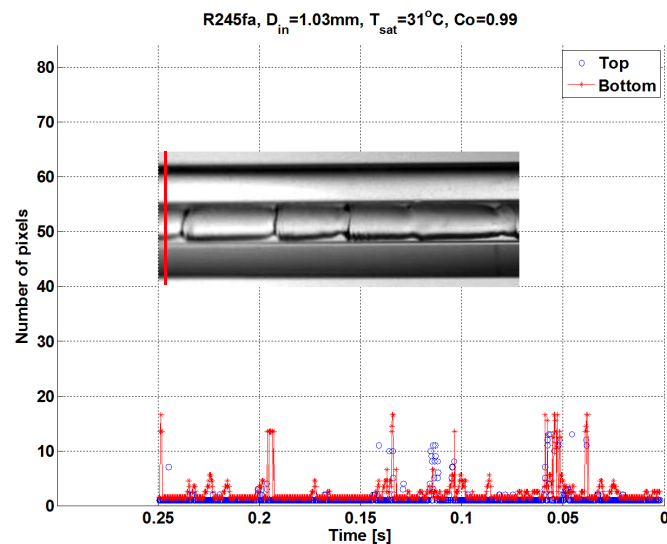
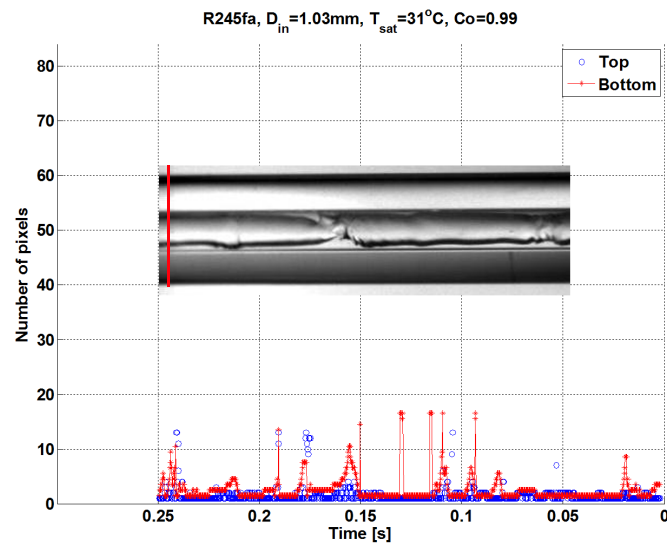
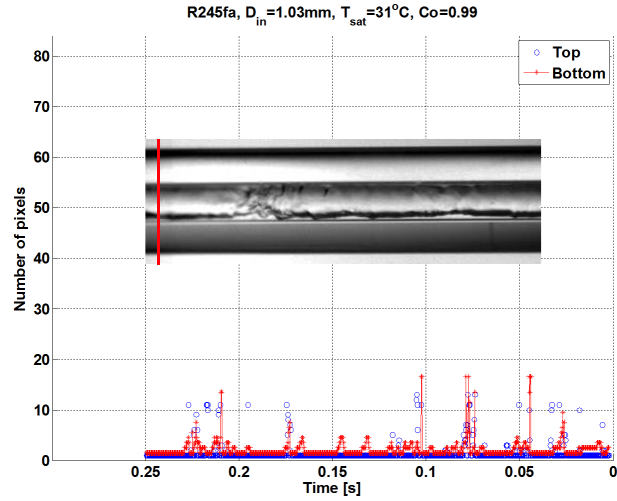


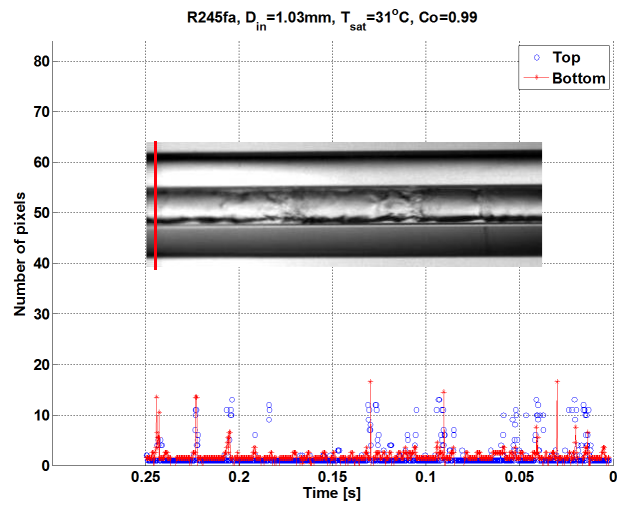
Figure 7.6: Top and bottom liquid film thickness for R236fa in the $D_{in}=1.03\text{ mm}$ channel at $T_{sat}=31\text{ }^\circ\text{C}$, $G=200\text{ kg/m}^2\text{s}$; a) $q=7.9\text{ kW/m}^2$, $x=0.16$, (b) $q=11.2\text{ kW/m}^2$, $x=0.25$, (c) $q=13.2\text{ kW/m}^2$, $x=0.29$, (d) $q=15.2\text{ kW/m}^2$, $x=0.35$, (e) $q=20.1\text{ kW/m}^2$, $x=0.48$ and (f) $q=31.1\text{ kW/m}^2$, $x=0.68$.

The liquid film thickness comparison for R245fa for the same condition is shown in Fig. (7.7). Referring to the results shown here, it is clearly observed that the magnitude of the liquid film thickness corresponding to the top and bottom side is similar in magnitude with the mean difference ≈ 1 pixel. Thus, this indicates no influence of gravity on the two-phase distribution but rather the dominance of surface tension forces acting on two-phase flow at the value of $Co=0.99$, as opposed to that of the conditions in ???. Hence, again the lower value of Co does not appear to be able to define the lower threshold of the macro-to-microscale transition.

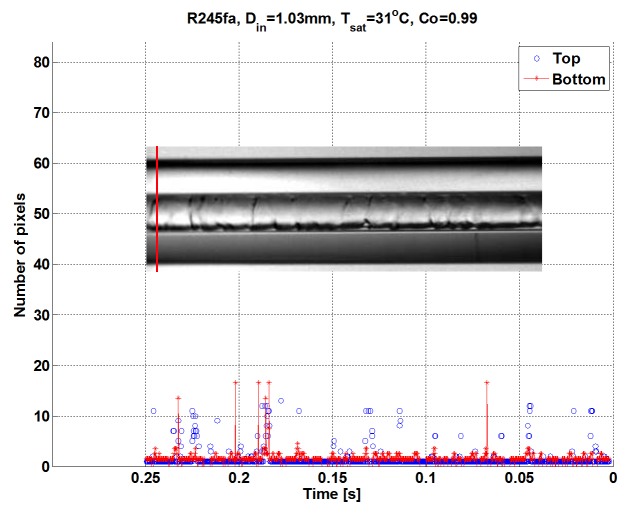




(c)



(d)



(e)

Figure 7.7: Top and bottom liquid film thickness for R245fa in the $D_{in}=1.03\text{ mm}$ channel at $T_{sat}=31\text{ }^\circ\text{C}$, $G=199\text{ kg/m}^2\text{s}$; a) $q=9.6\text{ kW/m}^2$, $x=0.15$, (b) $q=15.0\text{ kW/m}^2$, $x=0.26$, (c) $q=17.6\text{ kW/m}^2$, $x=0.31$, (d) $q=22.5\text{ kW/m}^2$, $x=0.41$ and (e) $q=25.4\text{ kW/m}^2$, $x=0.46$.

7.7 Summary of Macro-to-Microscale Transition

In summary, it was observed that the gravity forces are fully suppressed and overcome by the surface tension forces when confinement number approaches 1, $Co \approx 1$, where the top and bottom liquid film thicknesses are similar in magnitude. This can be interpreted as the lower threshold of the macro-to-microscale transition. However, there still seems to be some flow pattern effects on this threshold, with elongated bubbles still more buoyant than annular flows. Hence, as an approximate rule, one could assume that the lower threshold of macroscale flow is $Co=0.3 - 0.4$ whilst the upper threshold of microscale flow is $Co \approx 1$, with a transition region in between, i.e. $0.3 - 0.4 \leq Co \leq 1.0$. In Chapter 2, the recommended range for macro-to-microscale transition by Li et al. [41] for flow condensation is $0.57 < Co < 4.5$, with the lower threshold of macroscale flow being similar to the value proposed here.

Chapter 8

Critical Heat Flux

The objective of this part of the study is to investigate the macro-microscale evaporative two-phase flow transition on critical heat flux, CHF. Our current experimental CHF campaign covers a wide range of test conditions involving three fluids, primarily to study the effects of channel size, saturation temperature, mass flux, fluid properties and inlet sub-cooling on CHF (note: all CHF tests occur in the saturated zone of the channel). After presenting the new experimental results, the comparison of the new CHF database with various CHF prediction methods is presented in the following sub-sections of this chapter. Then, an improved CHF correlation is proposed with the inclusion of the threshold diameter D_{th} and the viscosity ratio term. The threshold diameter, D_{th} is evaluated based on the Confinement number, $Co=0.5$ proposed by Kew et al. [49]. The confinement number is related to the Bond number, $Bo=\frac{1}{Co^2}=4$ which represents the force balance between gravitational and surface tension forces. The new method is shown to cover heated hydraulic diameters in the range from 0.35 *mm* to 3.04 *mm* in circular and non-circular channels.

8.1 Experimental CHF Results

As described earlier in Chapter 3, the CHF was determined with the last thermocouple located just 1 *mm* from the evaporator outlet electrode. Upon reaching the onset of dryout, significant wall temperature fluctuations were observed at the last thermocouple location. For consistency reasons, the CHF criteria is reached when wall temperature fluctuations were observed and the wall superheat exceeds 40 *K* during small increments in heat flux. The supplied power to the electrodes is automatically cut once the CHF criteria is reached to avoid test section burnout. This criteria has been adopted for all the CHF experiments performed during this experimental campaign for all the three refrigerants and channels tested. For illustration purposes, Fig. (8.1) shows the evolution of the wall superheat as a function of heat flux for R134a in the $D_{in}=1.03$ *mm* channel.

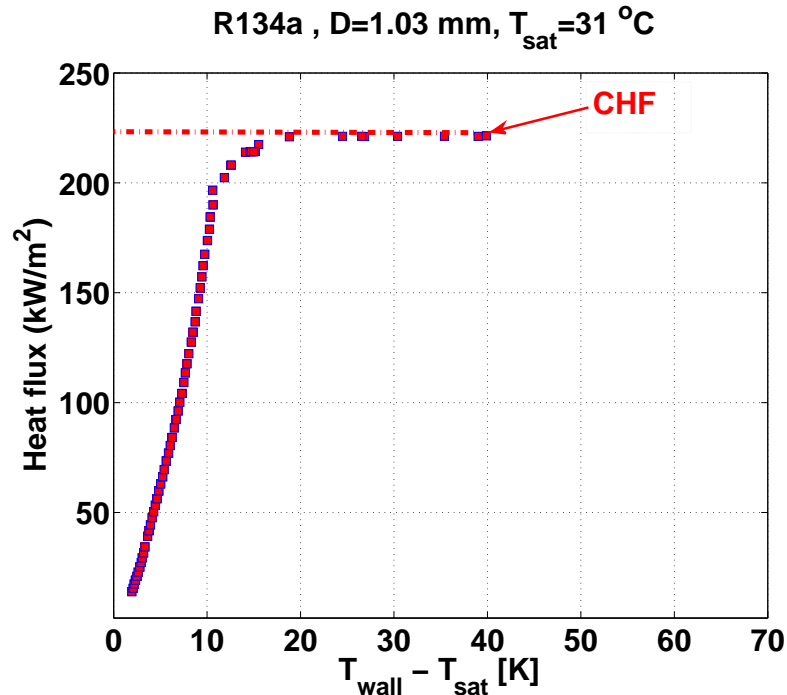


Figure 8.1: CHF criteria for R134a in the $D_{in}=1.03$ mm channel at $T_{sat}=31$ °C and $G=928$ kg/m²s.

Referring to Fig. (8.1), the onset of dryout was reached when the wall superheat increased to $T_{wall,sp} \approx 18.8$ K for $q=220.9$ kW/m² and that the CHF is reached when the heat flux increased to $q=221.2$ kW/m² with the wall superheat reaching $T_{wall,sp} \approx 40.1$ K. This indicate that the current CHF criteria defined when $T_{wall,sp} \approx 40$ K is appropriate and that increasing the CHF criteria for higher wall superheats will not have any significant effect on the measured absolute CHF values.

8.1.1 Effects of Mass Velocity and Channel Diameter

This section presents the CHF results for refrigerants R134a, R236fa and R245fa in the $D_{in}=1.03, 2.20, 3.04$ mm channels, as shown in Fig. (8.2). From the experimental CHF results, the CHF increased with increasing mass velocity for all the three fluids in all the three channels tested. This increasing CHF trend with mass velocity was also observed and reported by the following researchers [19, 21, 39, 43, 121–123]. Referring to Fig. (8.2)a and b, an increasing and diverging CHF trend can be observed as the channel size decreases. It was observed that there is no channel size effects on the CHF for the range of mass velocity of up to $G=500$ kg/m²s. Above $G=500$ kg/m²s, the CHF values diverge and a higher CHF value is observed for the smaller $D_{in}=1.03$ mm channel for R134a and R236fa, but was not observed for R245fa for the range of mass velocity tested.

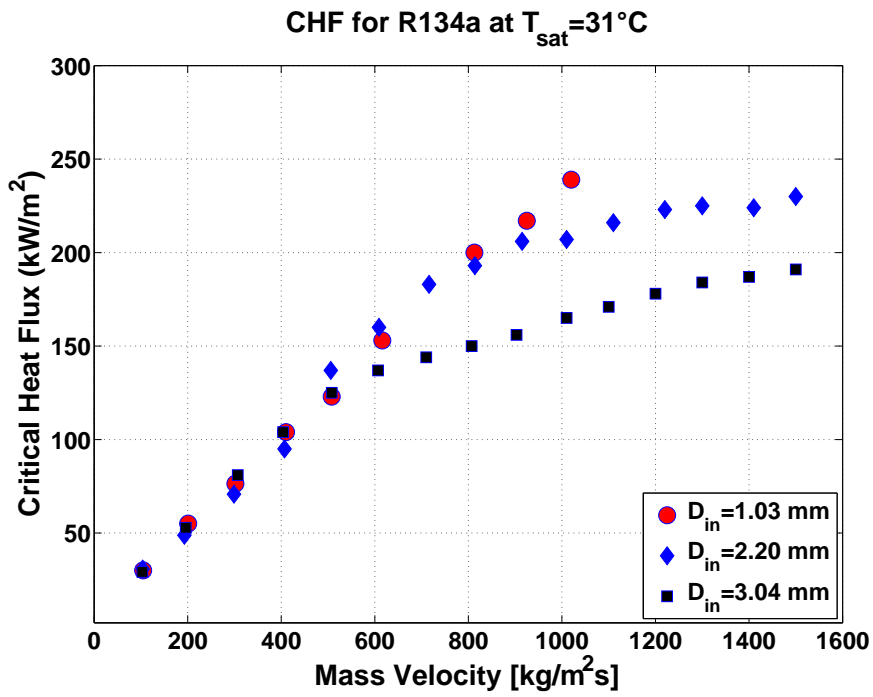
The increasing CHF trend is consistent with the findings of Celata and coworkers [94], who studied geometrical effects on CHF in subcooled flow boiling conditions with water as the working fluid. Bergles et al. [19, 21, 95] observed in their experimental study that

CHF increases in a non-linear fashion as the channel diameter decreases. Nariai et al. [22] concluded from their experiments that CHF increases at high mass flux with a decrease in the tube diameter. At low mass fluxes however, the effects of diameter on the CHF disappear. The rise on the magnitude of CHF is attributed to the dependency of CHF on channel confinement and the dominance of surface tension and viscosity over gravitational and inertia forces in microscale tubes.

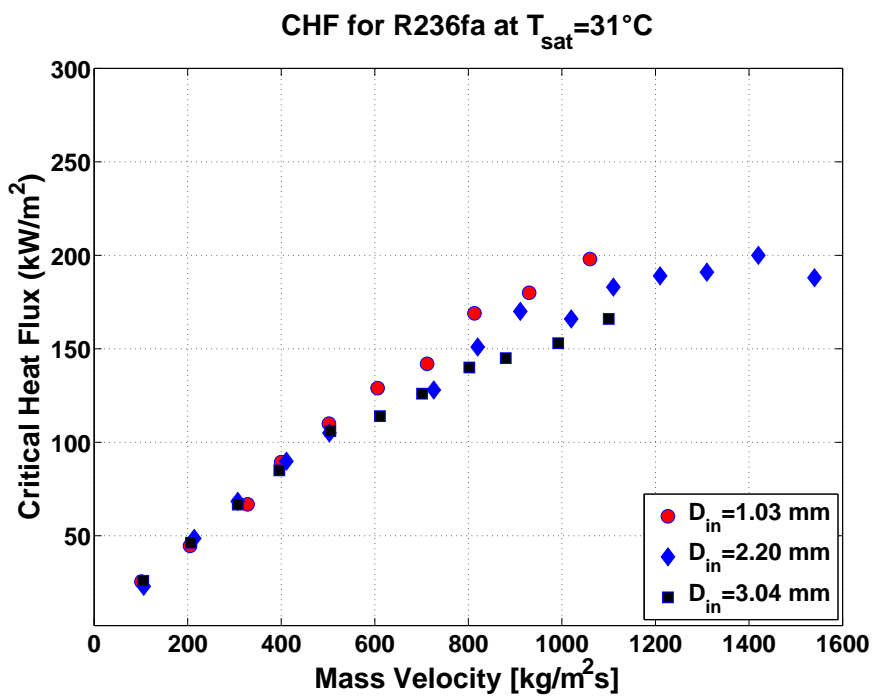
The comparison of the current CHF data with the CHF database of Wojtan et al. [23] for R134a in the $D_{in}=0.51, 0.79, 1.03, 2.20, 3.04 \text{ mm}$ is illustrated in Fig. (8.3). By universally comparing the CHF values for the five channels, the results show an increase in CHF with decreasing channel size. The CHF trend was also observed to have reached a 'peak', for the $D_{in}=0.79$ and 1.03 mm channels. Among the channels, the CHF values for the $D_{in}=0.79$ and 1.03 mm channels were the highest CHF values, followed by the $D_{in}=2.20 \text{ mm}$ and the lowest being the $D_{in}=0.51$ and 3.04 mm channels. From the results, CHF increases when the channel size decreases before reaching a threshold diameter (on the order of the value of D_{th} , followed by a decreasing CHF trend for further decrease in channel size. This behavior is explained again by Bergles et al. [96] that CHF increased with decreasing diameter according to the hydrodynamic theory but also claimed that CHF cannot increase indefinitely as the diameter is decreased from macro-microscale. The authors hypothesized that the breakdown in increasing CHF would be expected at some very small channel diameter when the liquid film around the wall ruptures due to the departure from thermal-hydraulic equilibrium. Instead, here it seems to be related to 'confinement' of the flow.

8.1.2 Effects of Saturation Temperature

A series of experiments were performed in order to identify the effects of saturation temperature on CHF. Fig. (8.4) presents the CHF results for the three fluids tested in the $D_{in}=2.20 \text{ mm}$ channel under various saturation temperatures. Based on the results in Fig. (8.4)a and b, CHF for R134a and R236fa is observed to be mildly affected by the saturation temperature, registering a lower CHF with increasing saturation temperature for a given mass velocity. This is due to a smaller latent heat at higher saturation temperatures. However, the trend was not clearly observed for R245fa for the mass velocity conditions tested as the temperature variation is small and the low pressure characteristics of this fluid. The CHF results for R134a and R236fa in the larger $D_{in}=3.04 \text{ mm}$ channel are depicted in Fig. (8.5). The results indicated no effect of saturation temperature/pressure at the lower range of mass velocities for both R134a and R236fa. However, the CHF trend for R134a diverged when $G > 800 \text{ kg/m}^2\text{s}$ and a slight increase in CHF was observed for $T_{sat}=31 \text{ }^\circ\text{C}$, as shown in Fig. (8.5)a. This trend was also observed by Vandervort and Bergles [19] and Ornatkii et al. [124], who reported a decrease in CHF with increasing pressure for a given fluid.



(a)



(b)

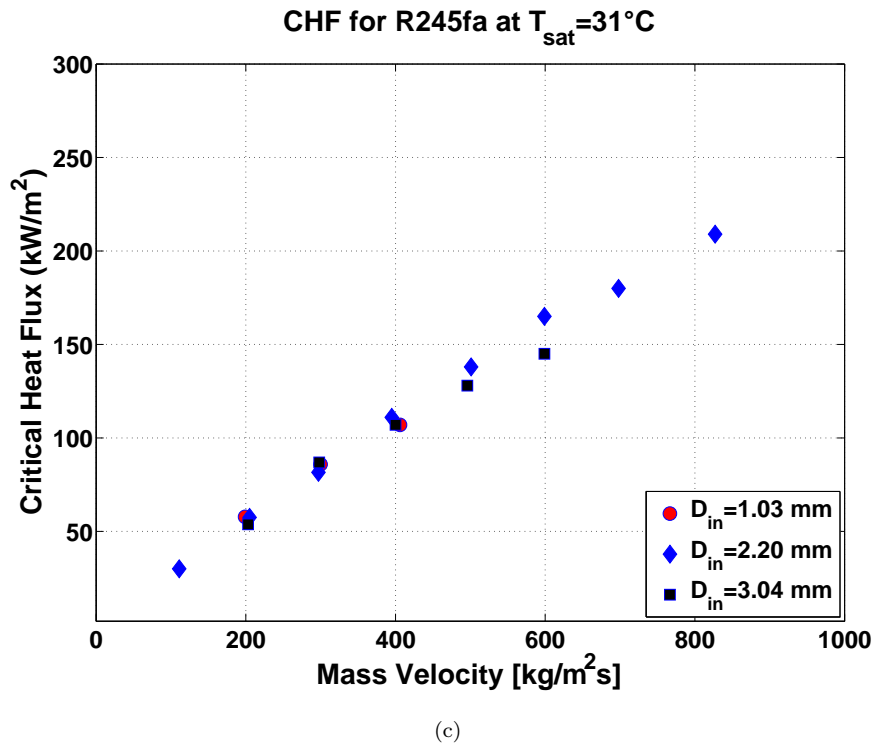


Figure 8.2: CHF comparison for R134a, R236fa and R245fa in the $D_{in}=1.03, 2.20, 3.04$ mm channels at $T_{sat}=31^{\circ}\text{C}$; (a) R134a, (b) R236fa and (c) R245fa.

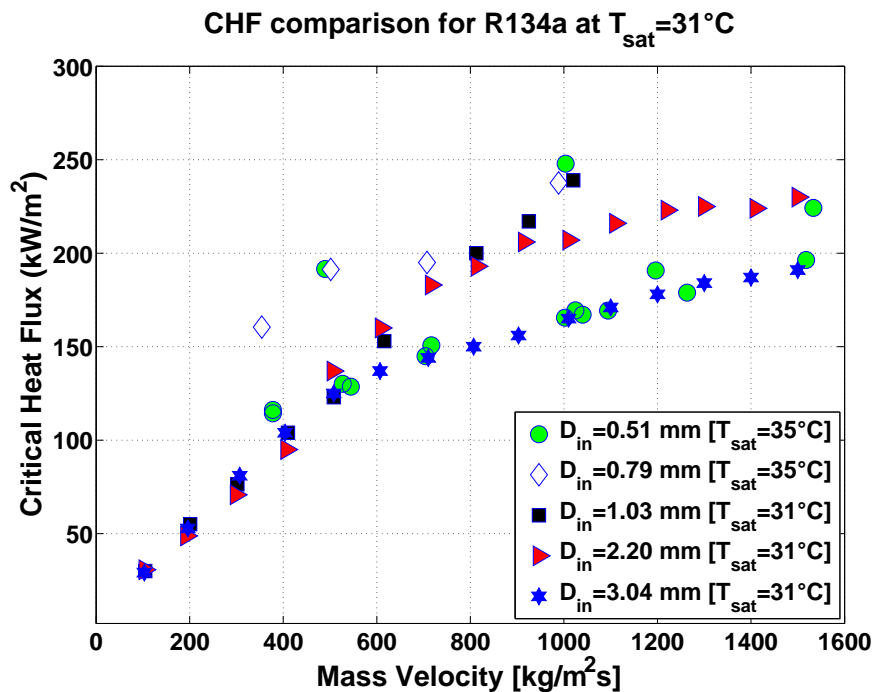
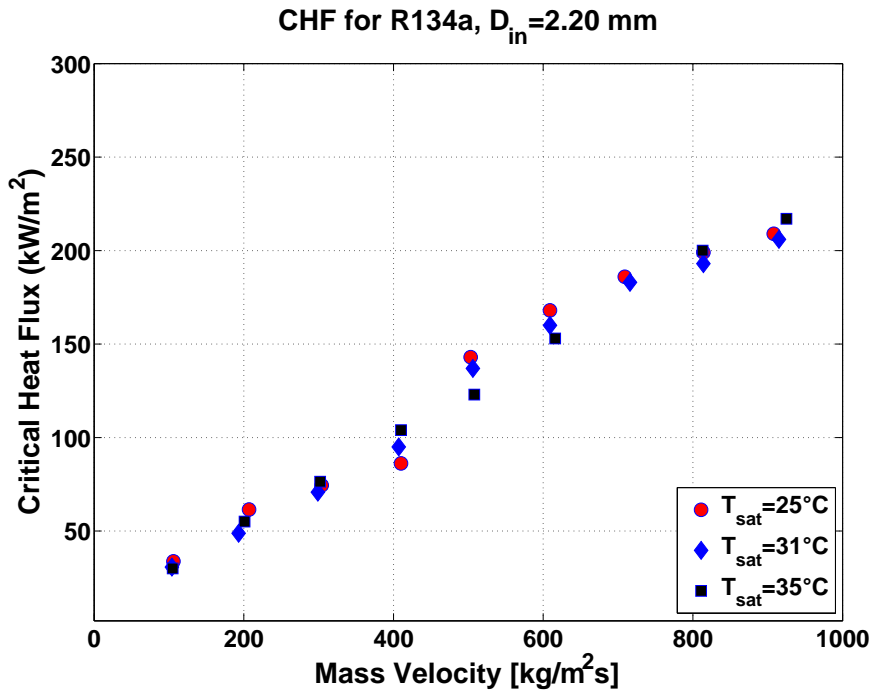
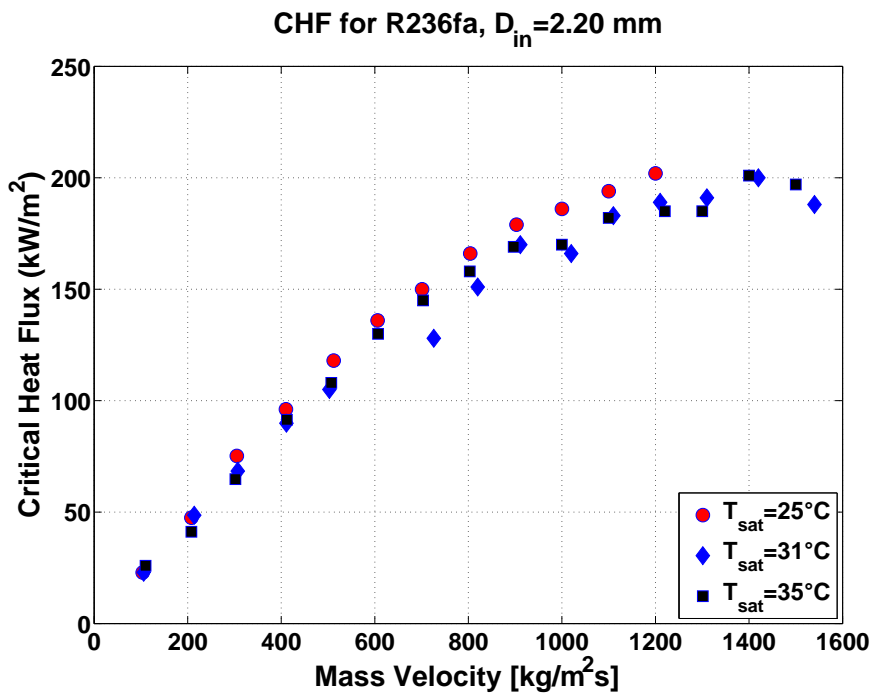


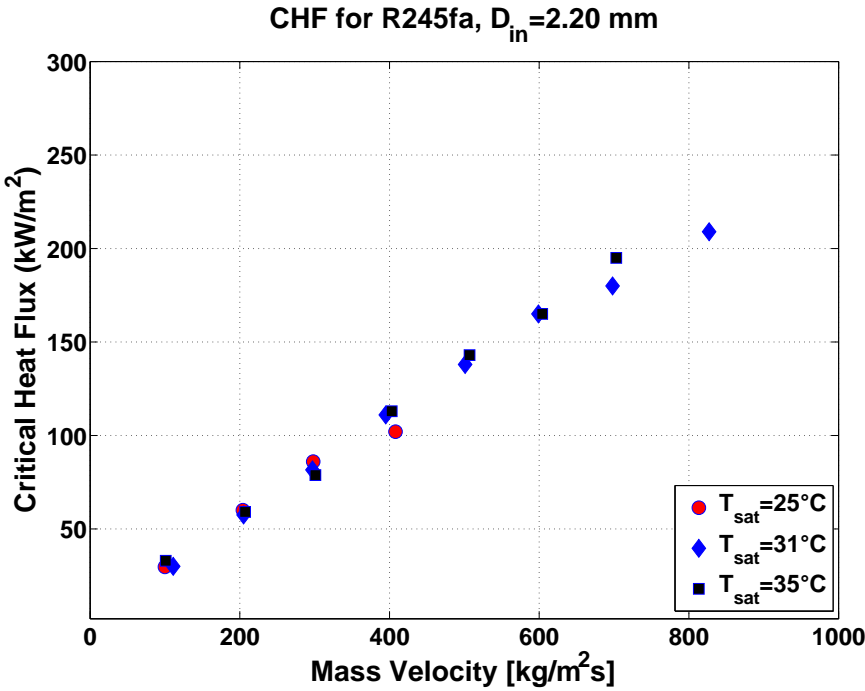
Figure 8.3: CHF comparison for R134a in the $D_{in}=0.51, 0.79, 1.03, 2.20, 3.04$ mm channels at $T_{sat}=31^{\circ}\text{C}$.



(a)

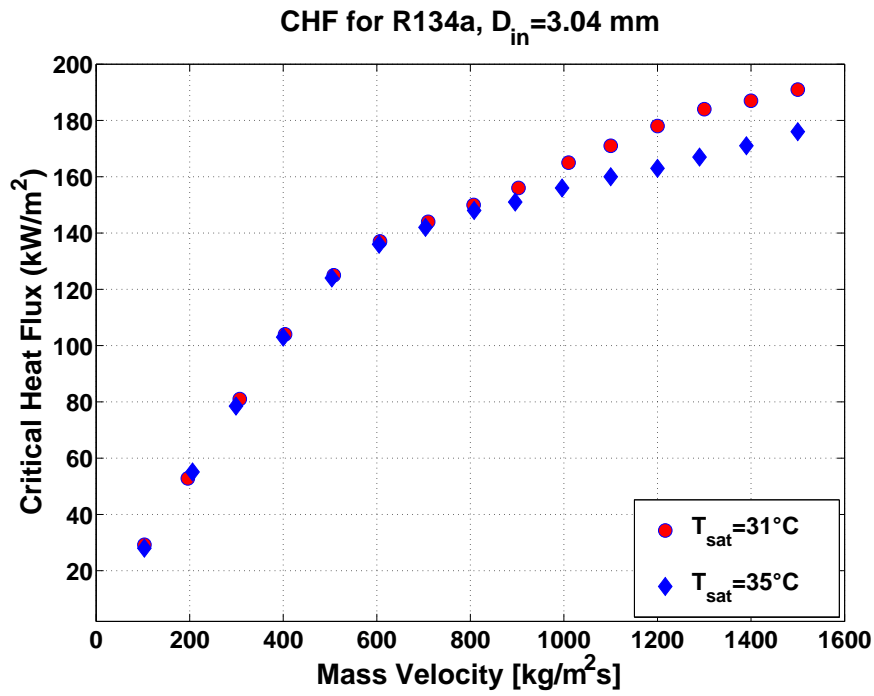


(b)

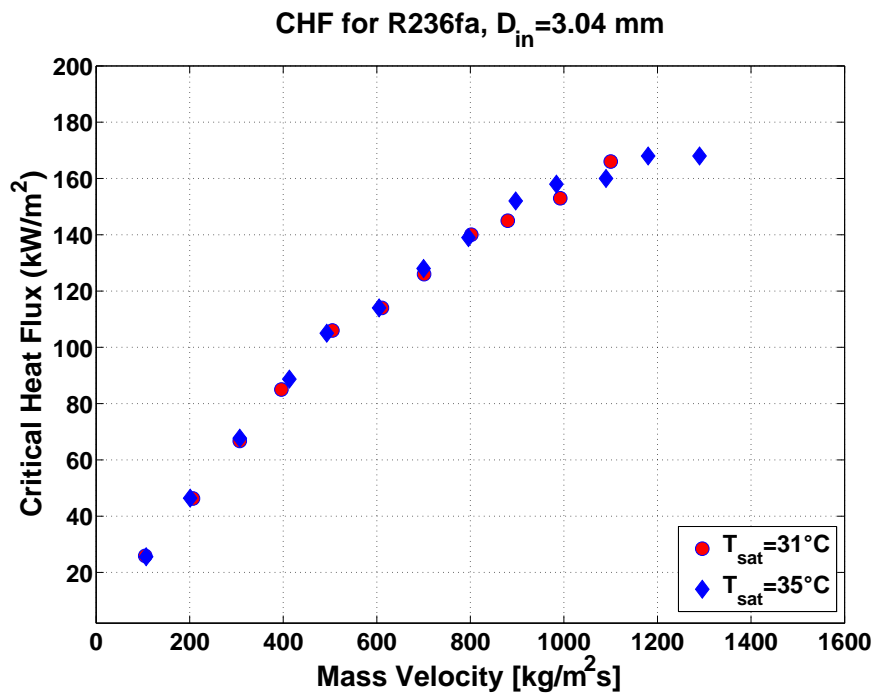


(c)

Figure 8.4: Effects of saturation temperature for R134a, R236fa and R245fa in the $D_{in}=2.20$ mm channel at $T_{sat}=25, 31, 35$ °C; (a) R134a, (b) R236fa and (c) R245fa.



(a)

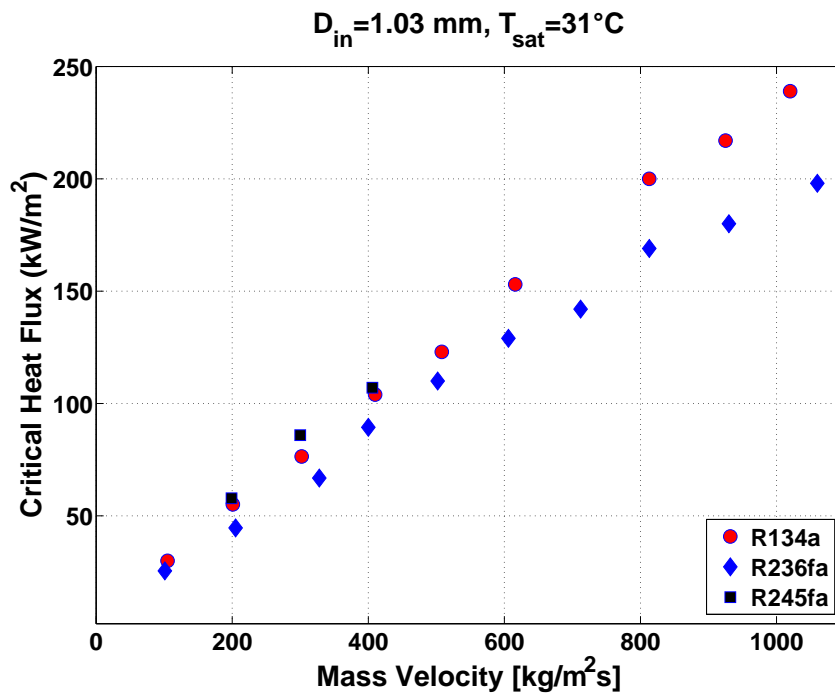


(b)

Figure 8.5: CHF comparison for R134a and R236fa in the $D_{in}=3.04$ mm channel at $T_{sat}=31, 35$ °C; (a) R134a and (b) R236fa.

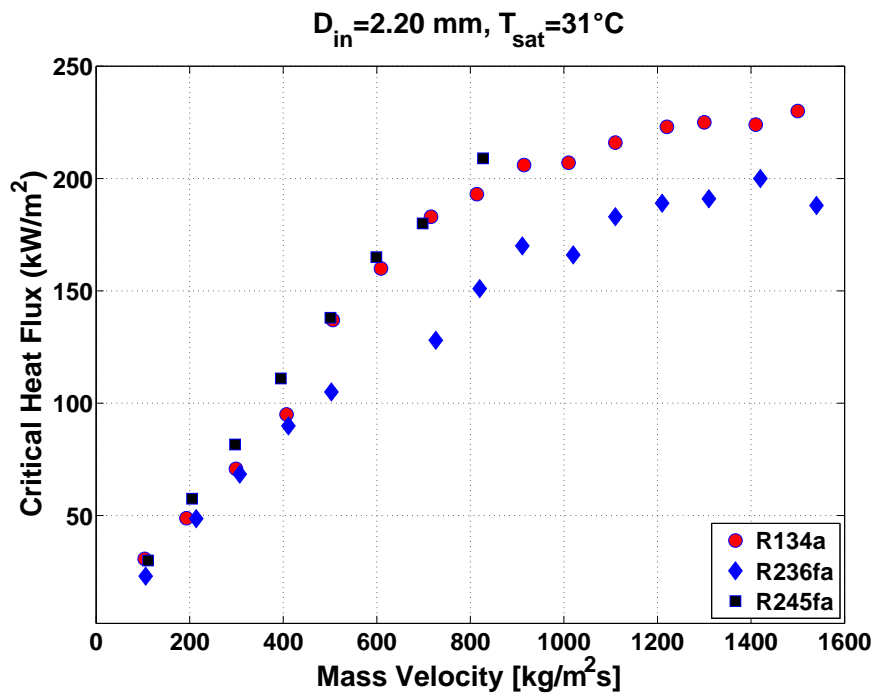
8.1.3 Effects of Fluid Properties

The CHF results for the three refrigerants R134a, R236fa and R245fa at $T_{sat}=31\text{ }^{\circ}\text{C}$ are shown in Fig. (8.6). From the results, R245fa registered the highest CHF value compared to R134a for a given mass velocity while R236fa registered the lowest CHF in comparison with the two other fluids. This was expected as the latent heat of R236fa is lower than that of R134a by -17.3% at $T_{sat}=31\text{ }^{\circ}\text{C}$, while the latent heat of R245fa exceeds the value of R134a by 8.5%. The latent heat difference corresponds very well to the CHF trends observed, with R245fa distinguishing itself as the best fluid due to its higher latent heat, followed by R134a and R236fa.

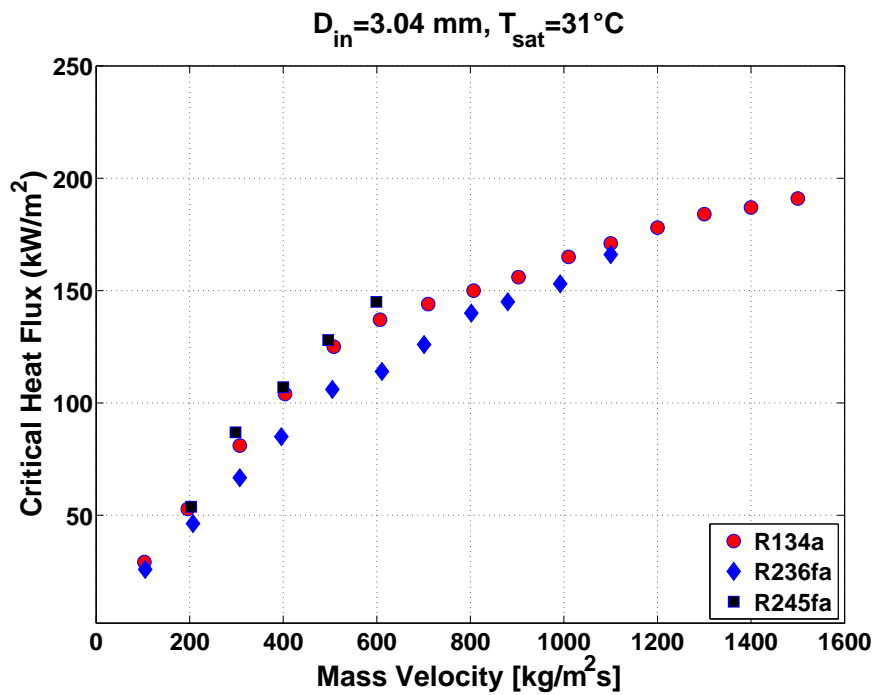


(a)

Fig. (8.7) illustrates another CHF comparison for the three fluids in the $D_{in}=2.20$ and 3.04 mm channels for various saturation temperatures. The same trends were observed here for both cases, with R245fa yielding the highest CHF value followed by R134a and R236fa.

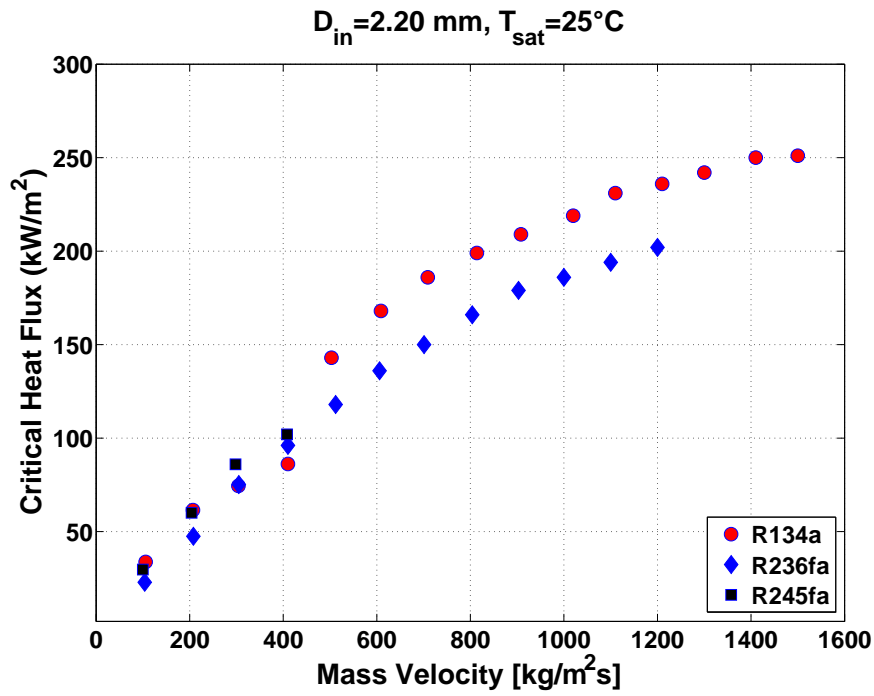


(b)

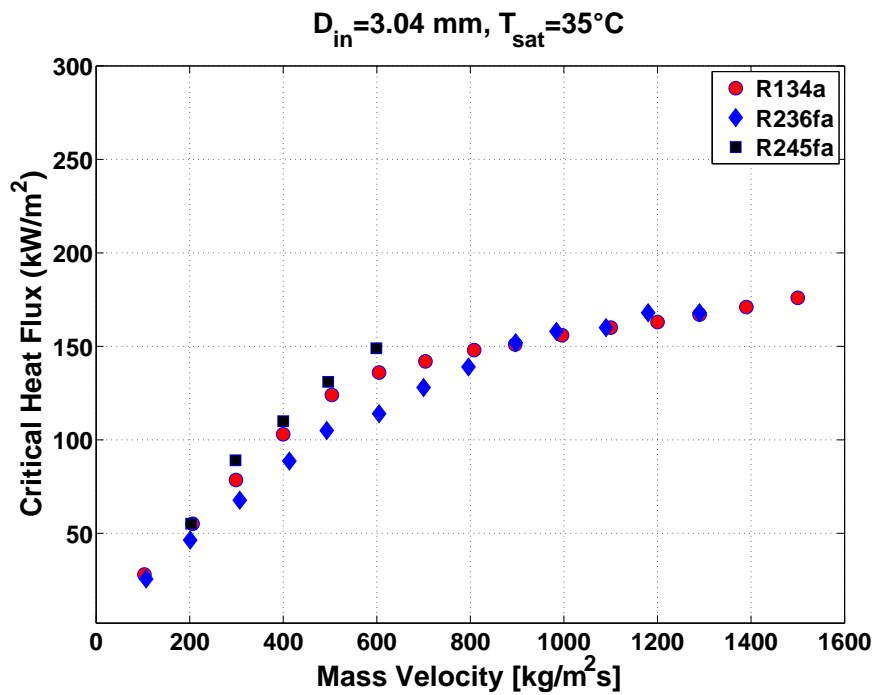


(c)

Figure 8.6: CHF comparison for R134a, R236fa and R245fa at $T_{sat} = 31^\circ\text{C}$; (a) $D_{in} = 1.03 \text{ mm}$, (b) $D_{in} = 2.20 \text{ mm}$ and (c) $D_{in} = 3.04 \text{ mm}$.



(a)



(b)

Figure 8.7: CHF comparison for R134a, R236fa and R245fa in the $D_{in} = 2.20$ and 3.04 mm channels; (a) $D_{in} = 2.20 \text{ mm}, T_{sat} = 25^\circ\text{C}$ and (b) $D_{in} = 3.04 \text{ mm}, T_{sat} = 35^\circ\text{C}$.

8.1.4 Effects of Sub-cooling

The effects of inlet sub-cooling on saturated CHF was investigated in this experimental campaign, with the results illustrated in Fig. (8.8). From the results, it was observed that there is no effect of inlet sub-cooling on CHF for the range of conditions tested. This agrees to the fact that sub-cooling effects on heat transfer diminishes when channel diameter decreases. From the literature, it is known that a higher level of sub-cooling in the incoming liquid requires a higher heat flux to initiate and to sustain bubble activity. As the bubbles grow in macroscale channels, the bubbles are in contact with the sub-cooled liquid core causing condensation at the liquid-vapor interface. The departing bubbles then condense rapidly depending on the level of liquid sub-cooling in the core. However, this phenomenon diminishes in the microscale as the bubbles quickly grow and occupy most of the channel. However, the effects of sub-cooling on CHF might be visible at higher levels of sub-cooling, when the bubbles experience an increased condensation rate while they are still attached to the heater surface resulting in small bubble departure diameters. All the CHF results here have CHF occurring in the saturated zone of the heated test section and it appears that CHF initiates at or near the exit like in macroscale tests.

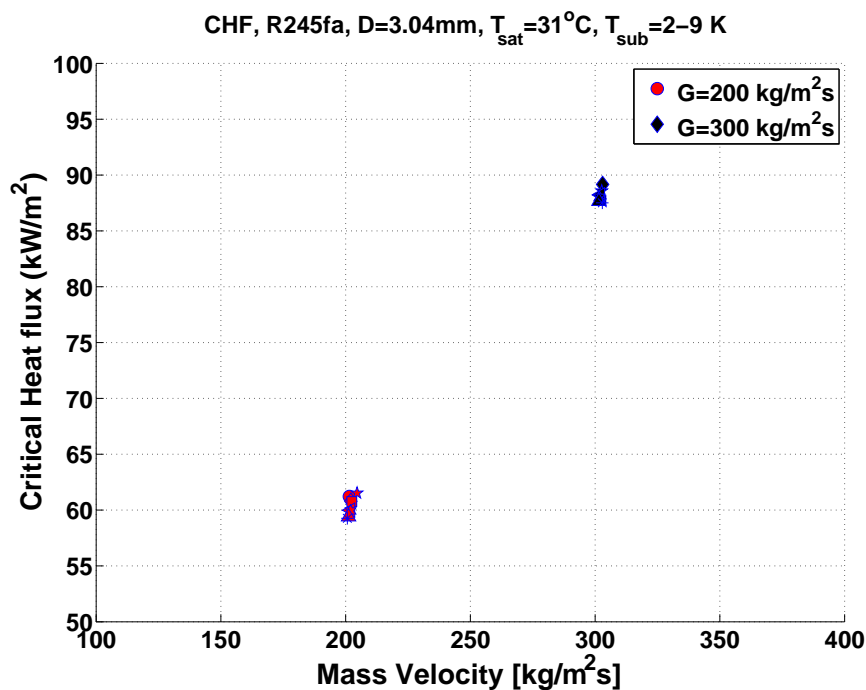


Figure 8.8: Effects of sub-cooling on CHF in the $D_{in}=3.04\text{ mm}$ channel.

8.1.5 Effects of Flow Pattern

Using the diabatic flow pattern map presented in Chapter 4 in this thesis, the CHF data were analyzed using the exit vapor qualities to determine the local regime at CHF. According to this evaluation, all CHF data fall within the annular flow regime.

8.2 Comparison of Results to Existing CHF Methods

This sub-section shows the comparison of the current CHF data with the CHF prediction methods of Wojtan et al. [23], Qi et al. [35], Mudawar et al. [36] and Katto et al. [37]. The comparisons are illustrated in Fig. (8.9) - Fig. (8.13). As can be seen, the best method is that of Wojtan et al., Qi et al. and Katto et al. but the level of accuracy is not satisfactory when extrapolating their method to larger diameters.

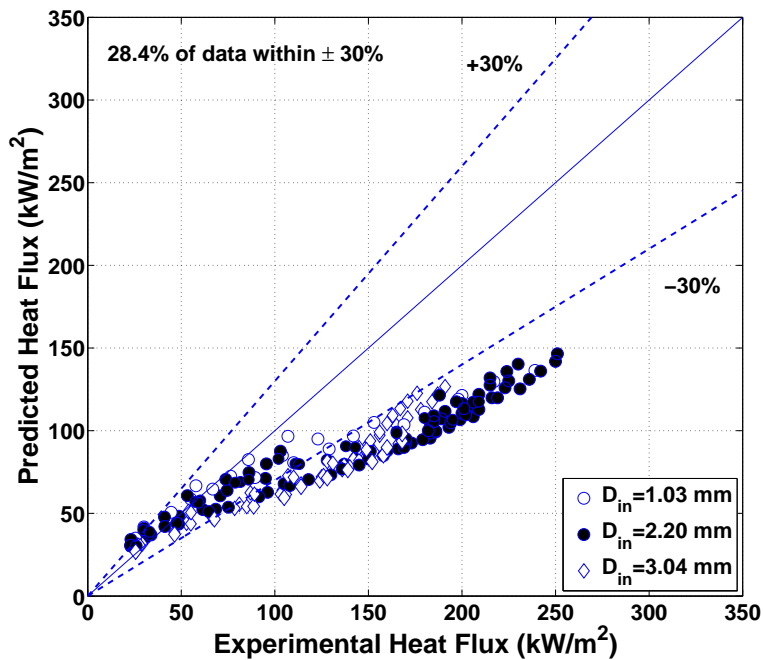


Figure 8.9: Comparison of the Wojtan et al. [23] correlation with the current experimental CHF data.

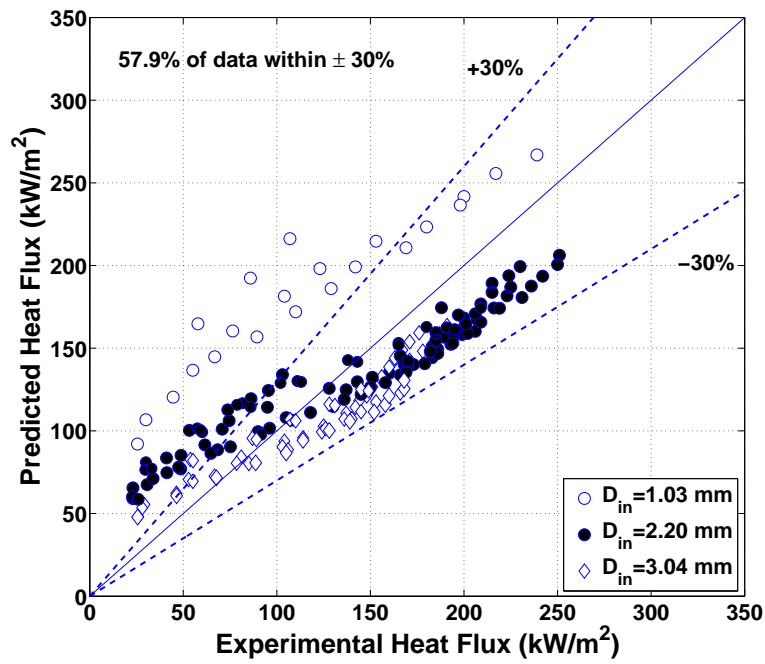


Figure 8.10: Comparison of the Qi et al. [35] correlation with the current experimental CHF data.

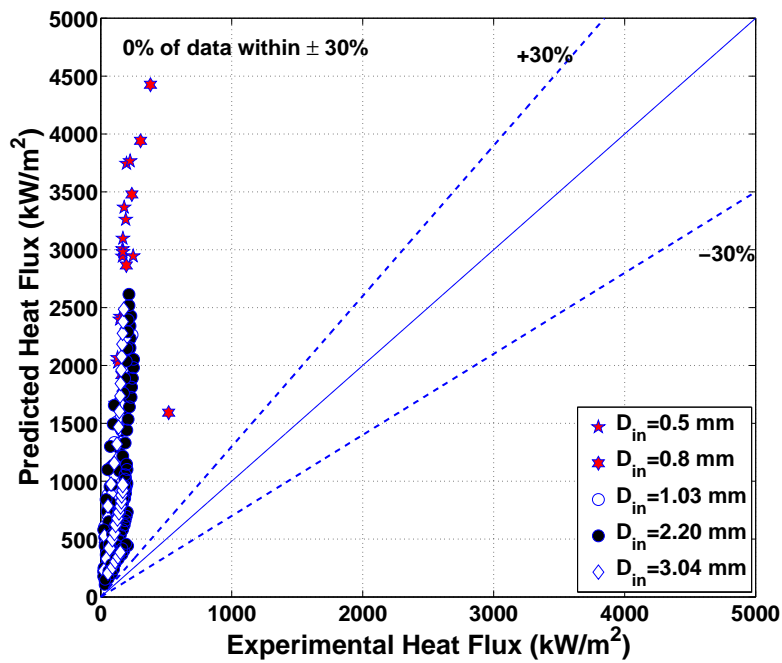


Figure 8.11: Comparison of the Mudawar et al. [36] correlation with the current experimental CHF data.

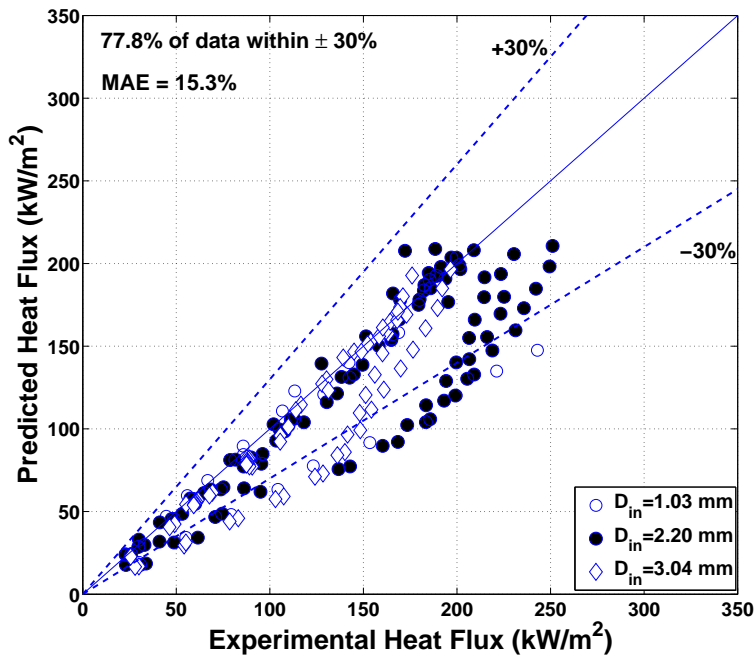


Figure 8.12: Comparison of the Katto et al. [37] correlation with the current experimental CHF data.

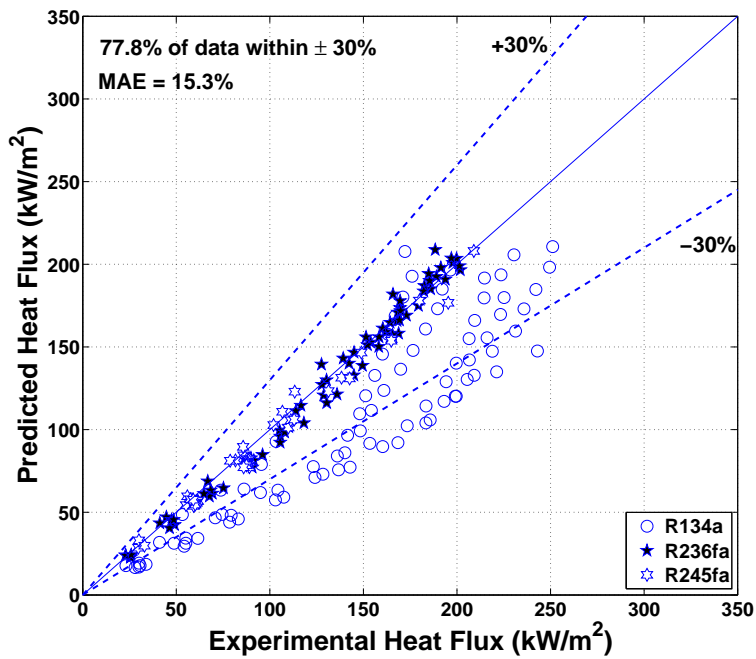


Figure 8.13: Comparison of the Katto et al. [37] correlation with the current experimental CHF data for various fluids.

8.3 New CHF correlation

The original correlation of Wojtan et al. [23] has been modified to fit the current CHF experimental data, the experimental CHF data of Wojtan et al. [23] for circular channels with $D_{in}=0.51$ and 0.79 mm and square multichannel CHF data of Park [38] for R134a, R236fa and R245fa with heated equivalent diameters of $D_{he}=0.35$ and 0.88 mm. Additional experimental CHF data for different fluid properties, channel size, shape, heated length and saturation conditions have been incorporated in the development of the new CHF correlation. The new CHF correlation proposed here is:

$$\frac{q_{CHF}}{Gh_{lv}} = 0.12 \left(\frac{\mu_{LO}}{\mu_{VO}} \right)^{0.183} \left(\frac{\rho_{VO}}{\rho_{LO}} \right)^{0.062} We_{LO}^{-0.141} \left(\frac{L_{ev}}{D_{in}} \right)^{-0.7} \left(\frac{D_{in}}{D_{th}} \right)^{0.11} \quad (8.1)$$

where $Co=0.5$ and D_{th} is defined as

$$D_{th} = \frac{1}{Co} \sqrt{\frac{\sigma}{g(\rho_{LO} - \rho_{VO})}} \quad (8.2)$$

and the Weber number is defined as

$$We_{LO} = \frac{G^2 L_{ev}}{\sigma \rho_{LO}} \quad (8.3)$$

The power constant term for density ratio, Weber number and the length/ratio have all been modified to fit the data. Two new terms, namely (D_{in}/D_{th}) and (μ_{VO}/μ_{LO}) have been introduced into the new CHF correlation to account for macro-microscale transition for channel confinement and the effects of viscosity on CHF. All the fluid properties were evaluated at the inlet of the channel. The new CHF correlation predicts the current experimental data and the experimental of Wojtan et al. [23] for all the three fluids in the $D_{in}=0.51, 0.79, 1.03, 2.20$ and 3.04 mm channels with 94.4% data within ± 30 % prediction and MAE = 13.6%, as presented in Fig. (8.14). The new CHF correlation also accurately predicts the multi-microchannel CHF data of Park [38] and the experimental CHF data of Bruno [39] for silicon multi-microchannels with good accuracy, as illustrated in Fig. (8.16) and Fig. (8.17). The new CHF correlation also successfully predicted the split flow multi-channel CHF database of Mauro et al. [40] with 100% data within ± 30 % and MAE = 20.7%, as shown in Fig. (8.18). In summary, the new CHF prediction method proposed here covers single and square multi-channels with internal diameters from 0.35 mm to 3.04 mm that spans the range above and below D_{th} . The range of applicability for the new CHF correlation is shown in Table 8.1.

D_{int} (mm)	G (kg/m ² s)	We_{LO}	$\frac{\mu_{LO}}{\mu_{VO}}$	$\frac{\rho_{VO}}{\rho_{LO}}$	$\frac{L_{ev}}{D_{in}}$
0.35 – 3.04	84 – 3736	7 – 201232	14.4 – 53.1	0.024 – 0.036	22.7 – 177.6

Table 8.1: Applicability range of the new CHF correlation.

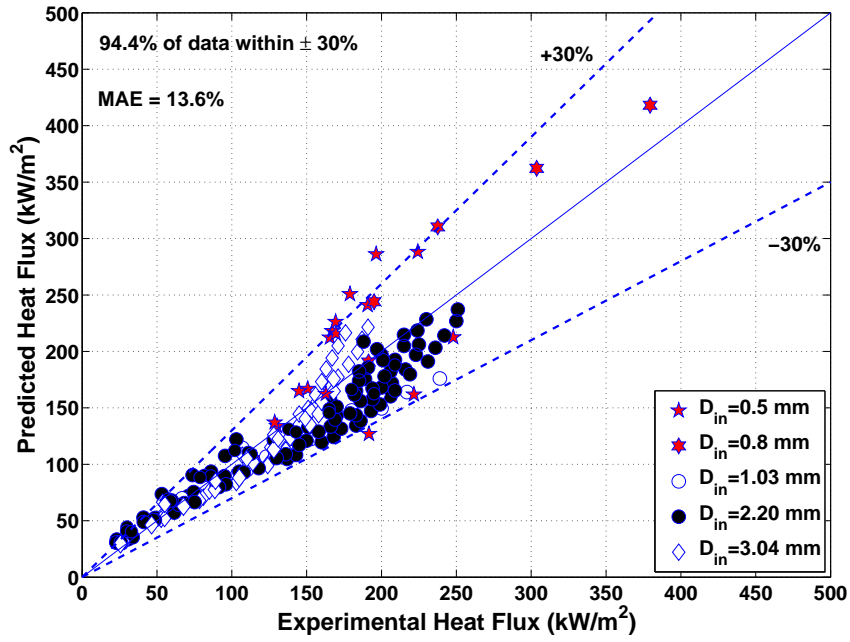


Figure 8.14: Comparison of the new CHF correlation with the experimental CHF data.

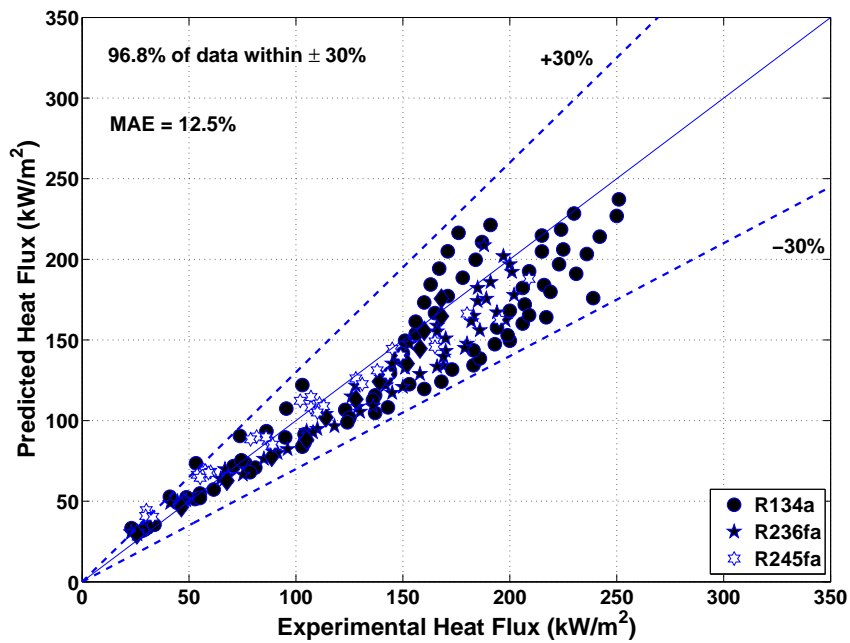


Figure 8.15: Fluid comparison with the new CHF correlation.

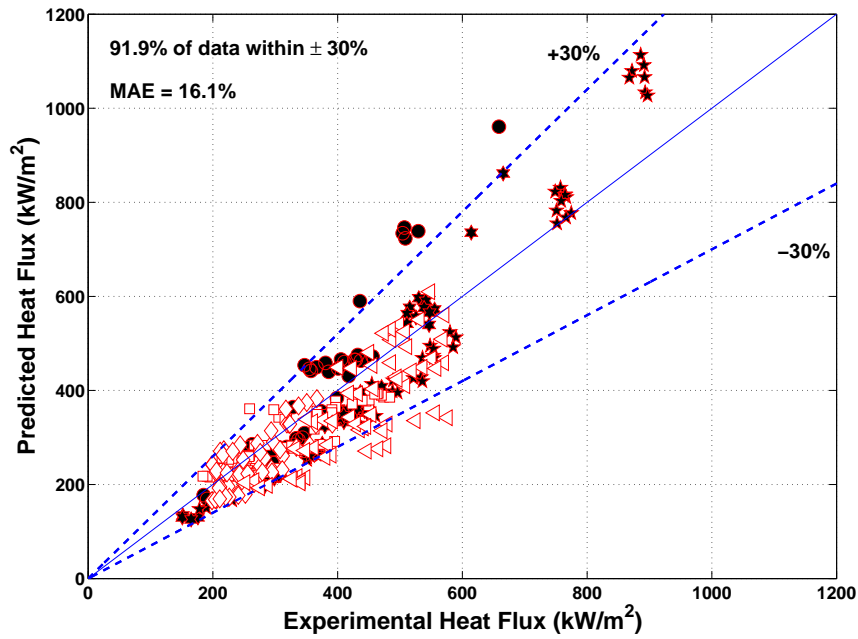


Figure 8.16: Comparison of the new CHF correlation with the experimental data of Park [38].

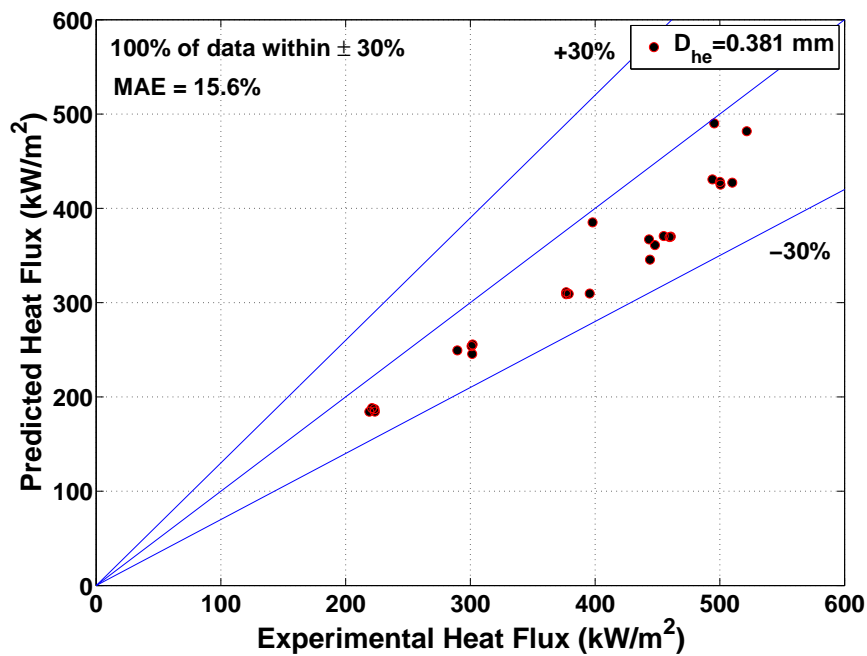


Figure 8.17: Comparison of the new CHF correlation with the CHF experimental data of Bruno et al. [39] for silicon multi micro-channels.

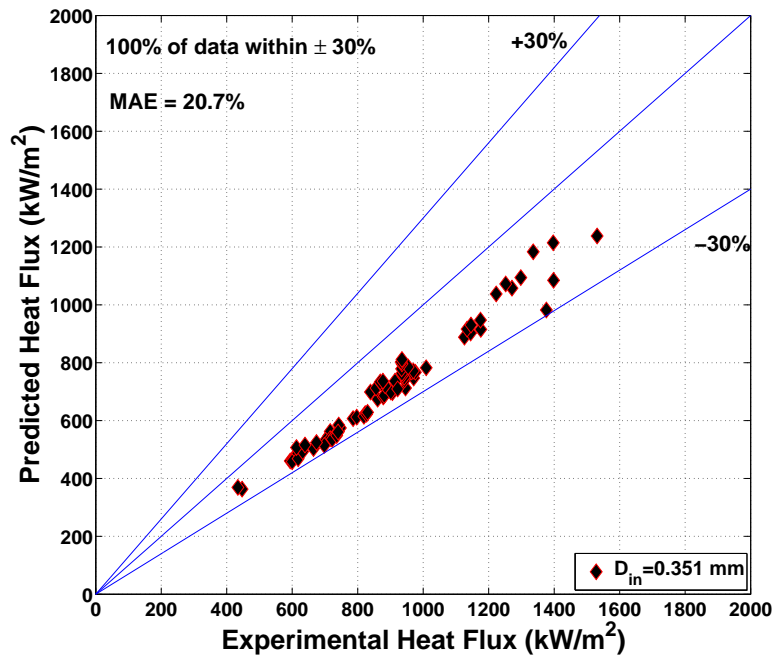


Figure 8.18: Comparison of the new CHF correlation with the split flow CHF experimental data of Mauro et al. [40].

Table 8.2 illustrates the comparative summary of the CHF predictions against the experimental CHF results for single-circular, square copper and silicon multi-microchannels and multi-microchannels with split flow configuration.

<i>CHF Data</i>	D_{int} (mm)	<i>Channel</i>	<i>data points</i>	$\pm 30\%$	<i>MAE</i>
<i>Current + Wojtan(2006)</i>	0.51 – 3.04	<i>single – circular</i>	215	94.4	13.6%
<i>Park(2008)</i>	0.35, 0.88	<i>Multichannels</i>	323	91.9	16.1%
<i>Mauro(2009)</i>	0.35, 0.88	<i>Split – multichannels</i>	78	100	20.7%
<i>Bruno(2008)</i>	0.381	<i>Silicon multichannels</i>	25	100	15.6%

Table 8.2: Experimental CHF data comparison with the newly proposed CHF correlation.

The comparison of the newly proposed CHF correlation with 2497 experimental CHF data points for water for channels of $D_{in}=0.33 - 6.23 \text{ mm}$ is shown in Fig. (8.19). Globally, the new correlation only manage to predict 34.4% of the data to within $\pm 30 \%$. This is not surprising as the new correlation was developed mainly for refrigerants. Thus, the primary reason for this lack of accuracy is related to the property of water, which poses a very small vapor density in comparison with non-aqueous fluids.

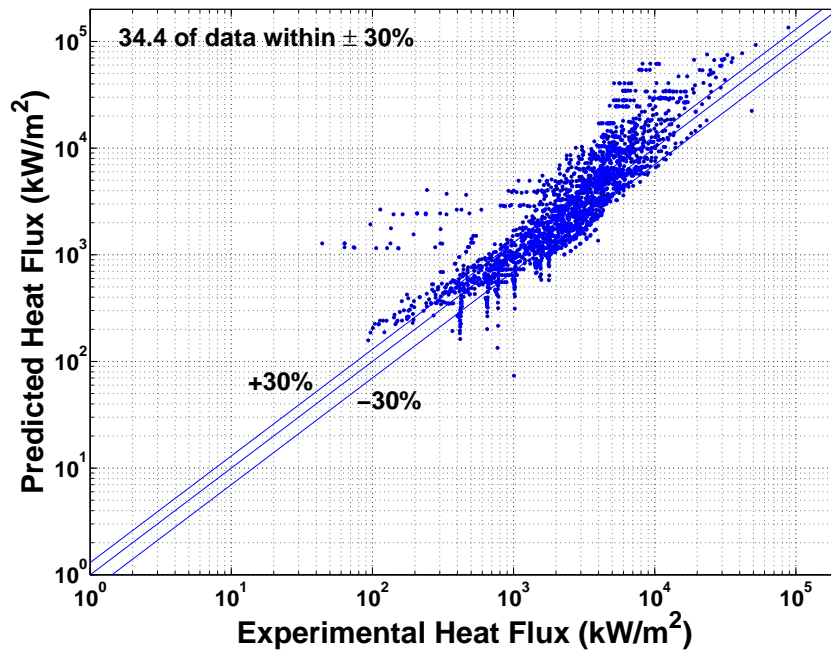


Figure 8.19: Experimental CHF data comparison for water with the new CHF correlation.

Chapter 9

Conclusions and Recommendations

9.1 Conclusions

The flow boiling experiments performed for R134a, R236fa and R245fa in the $D_{in}=1.03$, 2.20 and 3.04 mm channels showed significant influence of channel confinement on two-phase flow patterns, flow boiling heat transfer, pressure drop, critical heat flux and liquid film stratification. In summary, a total of 17485 heat transfer data points, 1152 pressure drop data points and 191 CHF data points have been acquired in this study. The two-phase flow pattern transitions have been found to be a function of channel confinement, mass velocity and saturation temperature/pressure. With the new experimental flow pattern observations, a new updated flow pattern map that is able to predict the both miniscale and microscale flows have been proposed in this study. With respect to the two-phase flow pattern observations and liquid film stratification determined through the image processing technique, an intermediate transition region exists between macroscale and microscale for Co in the range of $0.3-0.4 < Co_{transition} < 1.0$.

The work and results summary are outlined below.

9.1.1 Two-Phase Flow Patterns

The two-phase flow patterns and transitions have been observed to be a function of channel confinement, mass velocity and saturation temperature. Fluid properties such as surface tension, phase densities, and viscosity, were also found to affect the flow pattern transitions. From the experimental flow pattern observations, three distinct microscale flow regimes, i.e. Isolated bubble, Coalescing bubble and Annular flow regime were observed. Another macroscale type flow regime, i.e. the Slug-Plug flow regime was observed for the larger $D_{in}=3.04$ mm channel corresponding to $Co=0.34$. As channel confinement increases, the respective IB/CB flow pattern transition was observed to occur earlier at lower vapor qualities while an expansion of the annular flow regime towards lower vapor qualities was observed. In summary, the gravity forces were found to be more dominant when $Co < 0.34$. Fig. (9.1) illustrates the current macro-microscale transition criterion for Co : $0.3-0.4 < Co_{transition} < 1.0$ and the macro-microscale transition criterion of Li et al. [41] and Cheng et al. [42].

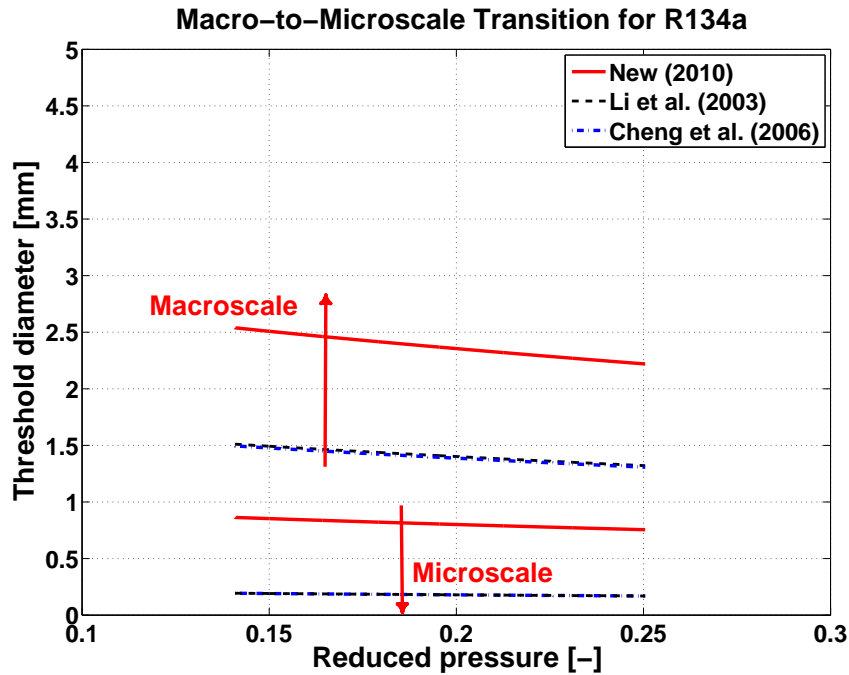


Figure 9.1: Macro-microscale transition criterion: Current study, Li et al. [41] and Cheng et al. [42].

A new macro-microscale flow pattern map has been proposed to predict both the macroscale and microscale flows. The proposed flow pattern map includes new dimensionless numbers accounting for the gravity, inertia and surface tension effects. The introduction of the confinement number, Co accounts for the confined flow boiling effect as a function of the capillary length while the Froude number accounts for the inertia and gravity forces. The liquid and vapor phase viscosity and density, Reynolds number and Weber number terms account for the viscous, surface tension and shear forces. In other words, these dimensionless numbers account for the transition from surface tension dominated flow (IB) to shear dominated flow (A).

9.1.2 Flow Boiling Heat Transfer

The flow boiling heat transfer coefficients are a significant function of the two-phase flow pattern and were observed to rise with heat flux in the sub-cooled and saturated region. From the results, the heat transfer coefficient was observed to be higher for higher saturation temperatures. The dramatic rise in heat transfer coefficients from the sub-cooled region to the saturated region coincides with the onset of saturated boiling. The monotonically increasing heat transfer coefficient at higher vapor qualities corresponded to annular flow, signifying convective boiling as the dominant heat transfer mechanism in these small scale channels in that regime. For higher channel confinement, i.e. for R245fa, the effects of heat flux on the heat transfer coefficients were only observed for lower vapor qualities, and a monotonically converging heat transfer trend at higher vapor qualities was

observed signifying convective boiling as the dominant flow boiling mechanism. Finally, the comparison of the current experimental heat transfer results with the three-zone model of Thome et al. [33, 34] yielded very good accuracy when utilizing the measured surface roughness of the individual channels as the dryout thickness.

9.1.3 Two-Phase Pressure Drops

Numerous flow boiling two-phase pressure drop data have been measured and compared to conventional macroscale and microscale prediction methods from literature. In summary, the statistical comparison showed relatively good accuracy for three prediction methods developed for macroscale flows, i.e. Baroczy-Chisholm, Friedel and the homogeneous model with the Cicchitti viscosity relation. As for the other microscale prediction methods, the Sun-Mishima and Zhang-Mishima methods yielded the best predictions of the current pressure drop data. In conclusion, there is no effect of macro-microscale transitional channel sizes on two-phase pressure drop as illustrated in the macroscale and microscale prediction comparisons presented in Chapter 6.

9.1.4 Film Thickness Measurements

From the image processing results, it was observed that the gravity forces are fully suppressed and overcome by the surface tension forces when the confinement number approaches 1, $Co \approx 1$, that is where the top and bottom liquid film thicknesses are similar in magnitude. This was observed for R245fa in the $D_{in}=1.03 \text{ mm}$ channel, as shown earlier in Chapter 7. However, there still seems to be some flow pattern effects on this threshold, with elongated bubbles still more buoyant than annular flows. In summary, the lower threshold of macroscale flow is at about $Co=0.3 - 0.4$ whilst the upper threshold of symmetric microscale flow is considered to be at $Co \approx 1$, with a transition region in between, i.e. $0.3 - 0.4 \leq Co \leq 1.0$.

9.1.5 Critical Heat Flux

The critical heat flux data acquired during this experimental campaign indicated the effect of saturation temperature, mass velocity, channel confinement and fluid properties on CHF but no effect of sub-cooling was observed for the conditions tested. The CHF was observed to rise with increasing mass velocity but decreased with increasing saturation temperature. The CHF was also the highest for R245fa, followed by R134a and then R236fa. Comparing the CHF for the $D_{in}=1.03, 2.20$ and 3.04 mm channels, the CHF was observed to be the highest for the $D_{in}=1.03 \text{ mm}$ channel, followed by the $D_{in}=2.20$ and then the 3.04 mm channel. Globally comparing the CHF database for $D_{in}=0.50, 0.79, 1.03, 2.20$ and 3.04 mm channels, a peak in CHF peak was observed lying in between the $D_{in}=0.79$ and 1.03 mm channels.

A new CHF correlation that is able to predict CHF for R134a, R236fa and R245fa in circular channels, square multichannels and split flow square multichannels has been

proposed. The introduction of the (D_{in}/D_{th}) and (μ_{VO}/μ_{LO}) terms accounts for macro-microscale transition for channel confinement and the viscous and interfacial shear effects on CHF.

9.2 Recommendations

In summary, a new database has been obtained for macro-to-microscale flow boiling in transition for three refrigerants, i.e. R134a, R236fa and R245fa, corresponding to high pressure, medium pressure and low pressure fluids. It is therefore recommended that new flow boiling and CHF experiments be extended to other refrigerant fluids, to other channel size and shapes to further investigate the macro-to-microscale flow boiling transition and thermal processes. Finally, it is therefore recommended that a new flow pattern based heat transfer model for annular flow be developed covering these macro-microscale channels.

Bibliography

- [1] J.C. Harley, Y. Huang, H.H. Bau, and J.N. Zemel. Gas flow in microchannels. *Journal of Fluid Mechanics*, 287:257–274, 1995.
- [2] S.G. Kandlikar and W.J. Grande. Evolution of microchannel flow passages - Thermohydraulic performance and fabrication technology. *Heat Transfer Engineering*, 24:3–17, 2003.
- [3] D. Steiner and J. Taborek. Flow boiling heat transfer in vertical tubes correlated by an asymptotic model. *Heat Transfer Engineering*, 13(2):43–69, 1992.
- [4] N. Kattan, J.R. Thome, and D. Favrat. Flow boiling in horizontal tubes: Part 1-Development of a diabatic two-phase flow pattern map. *Journal of Heat Transfer - Trans of the ASME*, 120:140–147, 1998.
- [5] G.M. Lazarek and S.H. Black. Evaporative heat transfer, pressure drop and critical heat flux in small vertical tube with R113. *International Journal of Heat and Mass Transfer*, 7:945–960, 1982.
- [6] S. Lin, P. A. Kew, and K. Cornwell. Flow boiling of refrigerant R141b in small tubes. *Trans IChemE*, 79, Part A:417–424, 2001.
- [7] Z.Y. Bao, D.F. Fletcher, and B.S. Haynes. Flow boiling heat transfer of Freon and HCFC123 in narrow passages. *International Journal of Heat and Mass Transfer*, 43:3347–3358, 2000.
- [8] W. Owhaib, C.M-Callizo, and B. Palm. Evaporative heat transfer in vertical circular microchannels. *Applied Thermal Engineering*, 24:1241–1253, 2004.
- [9] R. Khodabandeh. Heat transfer in the evaporator of an advanced two-phase thermosyphon loop. *International Journal of Refrigeration*, 28:190–20, 2005.
- [10] L. Consolini. *Convective boiling heat transfer in a single micro-channel*. PhD thesis, ÉCOLE POLYTECHNIQUE FÉDÉRALE DE LAUSANNE, THÈSE No 4024 (2008).
- [11] Oxford 3rd edition, Oxford University Press, editor. *J.G. Collier and J.R. Thome. Convective boiling and condensation*, 1994.
- [12] T. Sato, T. Minamiyama, M. Yanai, and T. Tokura. Study of heat transfer in boiling two-phase channel flow-Part 1: Flow patterns in a boiling channel. *Heat Transfer Japanese Research*, 1(1):1–14, 1972.

- [13] L. Wojtan, T. Ursenbacher, and J. R. Thome. Investigation of flow boiling in horizontal tubes: Part I - a new diabatic two-phase flow pattern map. *International Journal of Heat and Mass Transfer*, 48:2955–2969, 2005.
- [14] M. Kawaji and M.Y. Chung. Adiabatic gas-liquid flow in microchannels. *Microscale Thermophysical Engineering*, 8:239–257, 2004.
- [15] M. Suo. *Two-phase flow in capillary tubes*. PhD thesis, Massachusetts Institute of Technology, 1963.
- [16] M.K. Akbar, D.A. Plummer, and S.M. Ghiaasiaan. On gas-liquid two-phase flow regimes in microchannels. *International Journal of Multiphase Flow*, 29:855–865, 2003.
- [17] L. Chen, Y.S. Tian, and T.G. Karayiannis. The effect of tube diameter on vertical two-phase flow regimes in small tubes. *International Journal of Heat and Mass Transfer*, 49:4220–4230, 2006.
- [18] R. Revellin and J. R. Thome. Adiabatic two-phase frictional pressure drops in microchannels. *Experimental Thermal and Fluid Science*, 31:673–685, 2007.
- [19] C.L. Vandervort, A.E. Bergles, and M.K. Jensen. An experimental study of critical heat flux in very high heat flux subcooled boiling. *International Journal of Heat and Mass Transfer*, 37:161–173, 1994.
- [20] S.G. Kandlikar. Critical heat flux in sub-cooled flow boiling : An assesment of current understanding and future directions for research. *Multiphase Science and Technology*, 13, No. 3:207–232, 2001.
- [21] A.E. Bergles. Subcooled burnout in tubes of small diameter. *ASME Paper No. 63-WA-182*, 1963.
- [22] F. Inasaka and H. Nariai. Critical heat flux and flow characteristics of subcooled flow boiling in narrow tubes. *JSME International Journal*, Vol. 30-268:1595–1600., 1987.
- [23] L. Wojtan, R. Revellin, and J.R. Thome. Investigation of saturated critical heat flux in a single, uniformly heated microchannel. *Experimental Thermal and Fluid Science*, 30:765–774, 2006.
- [24] R. Revellin and J.R. Thome. Experimental investigation of R134a and R245fa two-phase flow in microchannels for different flow conditions. *International Journal of Heat and Fluid Flow*, 28:63–71, 2007.
- [25] C.Y. Yang and C.C. Shieh. Flow pattern of air-water and two-phase R134a in small circular tubes. *International Journal of Multiphase Flows*, 27:1163–1177, 2001.
- [26] V. Gnielinski. New equations for heat and mass transfer in turbulent pipe and channel flow. *Institution of Chemical Engineers*, 1936:359–368, 16.

- [27] T.M. Tran, M.W. Wanmbgsnass, and D.M. France. Small circular and rectangular-channel boiling with two refrigerants. *International Journal of Multiphase Flow*, 22:485–498, 1996.
- [28] S. S. Bertsch, E. A. Groll, and S. V. Garimella. A composite heat transfer correlation for saturated flow boiling in small channels. *International Journal of Heat and Mass Transfer*, 52:2110–2118, 2009.
- [29] Z. Liu and R.H.S. Winterton. A general correlation for saturated and subcooled boiling in tubes and annuli based on a nucleate pool boiling equation. *International Journal of Heat and Mass Transfer*, 11:2750–2766, 1991.
- [30] S. Saitoh, H. Daiguji, and E. Hihara. Correlation for flow boiling heat transfer of R134a in horizontal tubes including the effect of tube diameter. *International Journal of Heat and Mass Transfer*, 50:5215–5225, 2007.
- [31] L. Consolini and J.R. Thome. Micro-channel flow boiling heat transfer of R134a, R236fa and R245fa. *Microfluidics and Nanofluidics*, 6(6):731–746, 2009.
- [32] L. Consolini and J.R. Thome. A heat transfer model for evaporation of coalescing bubble in micro-channel flow. *International Journal of Heat and Fluid Flow*, 31:115–125, 2010.
- [33] J.R. Thome, V. Dupont, and A.M. Jacobi. Heat transfer model for evaporation in microchannels, part I: presentation of the model. *International Journal of Heat and Mass Transfer*, 47:3375–3385, 2004.
- [34] V. Dupont, J.R. Thome, and A.M. Jacobi. Heat transfer model for evaporation in microchannels, part II: comparison with the database. *International Journal of Heat and Mass Transfer*, 47:3387–3401, 2004.
- [35] S. Qi, P. Zhang, R. Wang, and L. Xu. Flow boiling of liquid nitrogen in microtubes: part II - heat transfer characteristics and critical heat flux. *International Journal of Heat and Mass Transfer*, 50:5017–5030, 2007.
- [36] W. Qu and I. Mudawar. Measurement and correlation of critical heat flux in two-phase microchannel heat sinks. *International Journal of Heat and Mass Transfer*, 47:2045–2059, 2004.
- [37] Y. Katto and H. Ohno. An improved version of the generalized correlation of critical heat flux for the forced convective boiling in uniformly heated vertical tubes. *International Journal of Heat and Mass Transfer*, 27(9):1641–1648, 1984.
- [38] J. E. Park. *Critical Heat Flux in Multi-Microchannel Copper Elements with Low Pressure Refrigerants*. PhD thesis, ÉCOLE POLYTECHNIQUE FÉDÉRALE DE LAUSANNE, No. 4223 (2008).
- [39] B. Agostini, R. Revellin, J.R. Thome, M. Fabbri, B. Michel, D. Calmi, and U. Kloter. High heat flux flow boiling in silicon multi-channels, part III: Saturated critical heat flux of R236fa and two-phase pressure drops. *International Journal of Heat and Mass Transfer*, 51:5426–5442, 2008.

- [40] A.W. Mauro, J.R. Thome, D. Toto, and G.P. Vanoli. Saturated critical heat flux in a multi-channel heat sink fed by a split flow system. *Experimental Thermal and Fluid Science*, in press, 2009.
- [41] J.M. Li and B.K. Wang. Size effect on two-phase flow regime for condensation in micro/mini tubes. *Heat Transfer-Asian Research*, 32:65–71, 2003.
- [42] P. Cheng and H.Y. Wu. Mesoscale and microscale phase-change heat transfer. *Advances in Heat Transfer*, 39:469–573, 2006.
- [43] L.N. Jiang, M. Wong, and Y. Zohar. Phase change in microchannel heat sinks with integrated temperature sensors. *Journal of Microelectromech. Systems*, 8:358–365, 1999.
- [44] J.M. Koo, L.N. Jiang, L. Zhang, P. Zhou, S.S. Banerjee, T.W. Kenny, J.G. Santiago, and K.E. Goodson. Modeling of two-phase microchannel heat sinks for very large scale integration VLSI chips. *IEEE*, pages 422–426, 2001.
- [45] J. R. Thome. The new frontier in heat transfer - Microscale and Nanoscale technologies. *Heat Transfer Engineering*, 27:1–3, 2006.
- [46] S. Lin, K. Sefiane, and J.R.E. Christy. Prospects of confined flow boiling in thermal management of microsystems. *Applied Thermal Engineering*, 22:825–837, 2002.
- [47] A.M. Jacobi S.S. Mehendale and R.K. Shah. Fluid flow and heat transfer at micro- and meso-scales with application to heat exchanger design. *Applied Mechanics Review*, 53:175–193, 2000.
- [48] R.K. Shah. Classification of heat exchangers. In *Heat Exchangers: Thermal Hydraulic Fundamentals and Design*, S. Kakac, A.E. Bergles, F. Mayinger, eds., Hemisphere, Washington D.C., 1986.
- [49] P.A. Kew and K. Cornwell. Correlations for prediction of flow boiling heat transfer in small-diameter channels. *Applied Thermal Engineering*, 17:8–10, 1997.
- [50] K.A. Triplett, S.M. Ghiaasiaan, S.I. Abdel-Khalik, and D.L. Sadowski. Gas liquid two-phase flow in microchannels. Part 1 - Two-phase flow patterns. *International Journal of Multiphase Flow*, 25:377–394, 1999.
- [51] N. Brauner and A. Ullmann. The prediction of flow boiling maps in minichannels. In *4th Japanese-European Two-Phase Flow Group Meeting, Kyoto*, 24-28 September, 2006.
- [52] A.M. Jacobi and J.R. Thome. Heat transfer model for evaporation of elongated bubble flows in microchannels. *Journal of Heat Transfer*, 124:1131–1136, 2002.
- [53] J.R. Thome. Engineering data book III. Technical report, www.wlv.com/products/databook/db3/DataBookIII.pdf, 2008.

- [54] W. Fritz. Berechnung des maximal volume von dampfblassen. *Physics Zeitung*, 36:379–388, 1935.
- [55] K. Nishikawa, Y. Fujita, M. Tsutsui, and K. Yoshimoto. On the nucleate boiling heat transfer from vertical surface. In *Proc. 13th National Heat Transfer Symp. Japan*, pp394-396, 1976.
- [56] K. Nishikawa, Y. Fujita, M. Tsutsui, and T. Ono. FURTHER REPORT on the nucleate boiling heat transfer from vertical surface. In *Proc. 16th National Heat Transfer Symp. Japan*, pp295-297, 1979.
- [57] S.S. Kutateladze and I.I. Grogonin. Growth rate and detachment diameter of a bubble in free convection boiling of a saturated liquid. *High Temperature (Translation)*, 17:667–671, 1979.
- [58] M.K. Jensen and G.J. Memmel. Evaluation of bubble departure diameter correlations. In *Proc. 8th International Heat Transfer Conference, San Francisco, Vol. 4*, 1986.
- [59] N. Kattan, J.R. Thome, and D. Favrat. Flow boiling in horizontal tubes: Part 2 - New heat transfer data for five refrigerants. *Journal of Heat Transfer - Trans of the ASME*, 120:148–155, 1998.
- [60] N. Kattan, J.R. Thome, and D. Favrat. Flow boiling in horizontal tubes: Part 3 - Development of a new heat transfer model based on flow pattern. *Journal of Heat Transfer - Trans of the ASME*, 120:156–165, 1998.
- [61] M. Lallemand, C. Branescu, and P. Haberschill. Local heat transfer coefficients during boiling of R22 and R407c in horizontal and smooth microfin tubes. *International Journal of Refrigeration*, 24:57–72, 2001.
- [62] J.M.S. Jabardo and E.P.B. Filho. Convective boiling of halocarbon refrigerants flowing in a horizontal copper tube - an experimental study. *Experimental Thermal and Fluid Science*, 23:93–104, 2000.
- [63] K. Moriyama and A. Inoue. The thermodynamic characteristics of the two-phase flow in extremely narrow channels. *Heat Transfer Japanese Research*, 21(8):823–856, 1992.
- [64] Y.Y. Yan and T.F. Lin. Evaporation heat transfer and pressure drop of refrigerant R134a in a small pipe. *International Journal of Heat and Mass Transfer*, 41:4183–4194, 1998.
- [65] C.M. Callizo, R. Ali, and B. Palm. New experimental results on flow boiling of R134a in a vertical microchannel. *10th UK Heat Transfer Conference, Edinburgh*, 2007.
- [66] S. Saitoh, H. Daiguji, and E. Hihara. Effect of tube diameter on boiling heat transfer of R134a in horizontal small diameter tubes. *International Journal of Heat and Mass Transfer*, 48:4973–4984, 2005.

- [67] G.F. Hewitt and D.N. Roberts. Studies of two-phase flow patterns by simultaneous x-ray and flash photography. Technical report, Atomic Energy Research Establishment, Harwell, Report No. AERE-M 2159, 1969.
- [68] O. Baker. Simultaneous flow of oil and gas. *Oil and Gas Journal*, 53:185–190, 1954.
- [69] Y. Taitel and A.E. Dukler. A model for predicting flow regime transitions in horizontal and near horizontal gas-liquid flow. *AIChE Journal*, 22:47–55, 1976.
- [70] T. Sato, T. Minamiyama, M. Yanai, T. Tokura, and Y. Ito. Study of heat transfer in boiling two-phase channel flow-Part 2: Heat transfer in the nucleate boiling region. *Heat Transfer Japanese Research*, 1(1):15–30, 1971.
- [71] C.A. Damianides and J.W. Westwater. Two-phase flow patterns in a compact heat exchanger and in small tubes. *2nd Proceedings of the UK National Conference on Heat Transfer, Glasgow, Mechanical Engineering Publications*, pages 1257–1268, Sept 1988.
- [72] T. Fukano and A. Kariyasaki. Characteristics of a gas-liquid two-phase flow in a capillary. *Nuclear Engineering Design*, 141:59–68, 1993.
- [73] A. Serizawa, Z. Feng, and Z. Kawara. Two-phase flow in microchannels. *Experimental Thermal and Fluid Science*, 26:703–714, 2000.
- [74] A. Kawahara, P.M.Y. Chung, and M. Kawaji. Investigation of two-phase flow pattern, void fraction and pressure drop in a microchannel. *International Journal of Multiphase Flow*, 28(9):1411–1435, 2002.
- [75] P.M.Y. Chung and M. Kawaji. The effect of channel diameter on adiabatic two-phase flow characteristics in microchannels. *International Journal of Multiphase Flows*, 30:735–761, 2004.
- [76] L. Zhao and K.S. Rezkallah. Gas-liquid flow patterns at microgravity conditions. *International Journal of Multiphase Flow*, 19:751–763, 1993.
- [77] K.S. Rezkallah. Weber number based flow-pattern maps for liquid-gas flow in microgravity. *International Journal of Multiphase Flow*, 22:1265–1270, 1996.
- [78] D.C. Lowe and K.S. Rezkallah. Flow regime identification in microgravity two-phase flow using void fraction signals. *International Journal of Multiphase Flow*, 25:433–457, 1999.
- [79] K.A. Triplett, S.M. Ghiaasiaan, S.I. Abdel-Khalik, A. LeMouel, and B.N. McCord. Gas liquid two-phase flow in microchannels. Part 2- Void fraction and pressure drop. *International Journal of Multiphase Flow*, 25:395–410, 1999.
- [80] J.W. Coleman and S. Garimella. Two-phase flow regimes in round, square and rectangular tubes during condensation of refrigerant R134a. *International Journal of Refrigeration*, 26:117–128, 2003.

- [81] C.L. Ong and J.R. Thome. Flow boiling heat transfer of R134a, R236fa and R245fa in a horizontal 1.030mm circular channel. *Experimental Thermal and Fluid Science*, 33:651–663, 2009.
- [82] W. Tong, A.E. Bergles, and M.K. Jensen. Pressure drop with highly subcooled flow boiling in small-diameter tubes. *Experimental Thermal and Fluid Science*, 15:202–212, 1997.
- [83] K. Pehlivan, I. Hassan, and M. Vaillancourt. Experimental study on two-phase flow and pressure drop in millimeter sized channels. *Applied Thermal Engineering*, 26:1506–1514, 2006.
- [84] D. Chisholm. A theoretical basis for the lockhart martinelli correlation for two-phase flow. *International Journal of Heat and Mass Transfer*, 10:1767–1778, 1967.
- [85] S.G. Kandlikar. Two-phase flow patterns, pressure drop and heat transfer during boiling in minichannel flow passages of compact evaporators. *Heat Transfer Engineering*, 23:5–23, 2002.
- [86] T.N. Tran, M.C. Chyu, M.W. Wambsganss, and D.M. France. Two-phase pressure drop of refrigerants during flow boiling in small channels - an experimental investigation and correlation development. *International Conference on Compact Heat Exchangers and Enhancement Technology for Process Industries, Banff, Canada*, pages 18–23, 1999.
- [87] J.M. Quibén and J.R. Thome. Flow pattern based two-phase frictional pressure drop model for horizontal tubes, Part 2-new phenomenological model. *International Journal of Heat and Fluid Flow*, 28:1060–1072, 2007.
- [88] R. Revellin and P. Haberschill. Prediction of frictional pressure drop during flow boiling of refrigerants in horizontal tubes - comparison to an experimental database. *International Journal of Refrigeration*, 32:487–497, 2009.
- [89] R. Grönnerud. Investigation of liquid hold-up, flow resistance and heat transfer in circulation type evaporators, part iv - two-phase flow resistance in boiling refrigerants. *Bull de L'inst. du Froid*, In annexe 1972-1, 1979.
- [90] G. Ribatski, L. Wojtan, and J. R. Thome. An analysis of experimental data and prediction methods for two-phase frictional pressure drop and flow boiling heat transfer in micro-scale channels. *Experimental Thermal and Fluid Science*, 31:1–19, 2006.
- [91] H. Müller-Steinhagen and K. Heck. A simple friction pressure drop correlation for two-phase flow in pipes. *Chemical Engineering Process*, 20:297–308, 1986.
- [92] K. Mishima and T. Hibiki. Some characteristics of air-water two-phase flow in small diameter vertical tubes. *International Journal of Multiphase Flow*, 22:703–712, 1996.

- [93] G.P. Celata, M. Cumo, A. Mariani, H. Niriai, and F. Inasaka. Influence of channel diameter on subcooled flow boiling burnout at high heat fluxes. *International Journal of Heat and Mass Transfer*, 36, No.13:3407–3410, 1993.
- [94] G.P. Celata, M. Cumo, and A. Mariani. Geometrical effect on the subcooled flow boiling critical heat flux. *Rev Gén Therm*, 36:807–814, 1997.
- [95] M.P. Fiori and A.E. Bergles. Model of critical heat flux in subcooled flow boiling. *Heat Transfer 70, Proceedings of the 4th International Heat Transfer Conference*, 6:Paper B6.3, 1970.
- [96] A.E. Bergles, J.H. Lienhard V, G.E. Kendall, and P. Griffith. Boiling and evaporation in small diameter channels. *Heat Transfer Engineering*, 24(1):18–40, 2003.
- [97] G.M. Roach, A.K. Abdel-Khalik, S.M. Ghiaasiaan, M.F. Dowling, and S.M. Jeter. Low flow critical heat flux in heated microchannels. *Nuclear Science Engineering*, 131:411–425, 1997.
- [98] C.H. Oh and S.B. Englert. Critical heat flux for low flow boiling in vertical uniformly heated thin rectangular channels. *International Journal of Heat and Mass Transfer*, 36, No. 2:325–335., 1993.
- [99] R. Revellin, V. Dupont, T. Ursenbacher, I. Zun, and J.R. Thome. Characterization of diabatic two-phase flows in microchannels: Flow parameter results for R134a in a 0.5 mm channel. *International Journal of Multiphase Flow*, 32:755–774, 2006.
- [100] R. Revellin. *Experimental two-phase fluid flow in microchannels*. PhD thesis, ÉCOLE POLYTECHNIQUE FÉDÉRALE DE LAUSANNE, 2005.
- [101] S.W. Churchill and H.H.S. Chu. Correlating equations for laminar and turbulent free convection from a horizontal cylinder. *International Journal of Heat and Mass Transfer*, 18:1049–1053, 1975.
- [102] P.A. Jones P.K. Maciejewski P.E. McCarthy M.L. Price J.A. Rabensteine R.B. Schumacher W.G. Steele J.S. Wyler D.A. Coutts, R.H. Dieck, editor. *Test Uncertainty, Instruments and Apparatus, Supplement to ASME performance test codes*. American Society of Mechanical Engineers, 1998.
- [103] S.J. Kline and F.A. McClintock. Describing uncertainties in single-sample experiments.
- [104] R.J. Moffat. Contributions to the theory of single-sample uncertainty analysis. *AFOSR-HTTM Conference, Turbulent flows: Comparison of Computation and Experiment*, 1981.
- [105] R.J. Moffat. Using uncertainty analysis in the planning of an experiment. *Symposium on Uncertainty Analysis*, 1983.

- [106] E.W. Weisstein. "least squares fitting.". From MathWorld—A Wolfram Web Resource. <http://mathworld.wolfram.com/LeastSquaresFitting.html>.
- [107] W.S. Bousman, J.B. MacQuillen, and L.C. Witte. Gas-liquid flow patterns in microgravity - effects of tube diameter, liquid viscosity and surface tension. *International Journal of Multiphase Flow*, 22:1035–1053, 1996.
- [108] A. Tabatabai and A. Faghri. A new two-phase flow pattern map and transition boundary accounting for surface tension effects in horizontal miniature and microtubes. *Journal of Heat Transfer*, 123:959–967, 2001.
- [109] F.W. Dittus and L.M.K. Boelter. *Publications of Engineering, University of California, Berkeley*, 2:443, 1930.
- [110] J. Petterson. Flow vaporization of CO₂ in microchannel tubes. *Experimental Thermal and Fluid Science*, 28:111–121, 2004.
- [111] H.-K. Oh, M. Katsuta, and K. Shibata. Heat transfer characteristics of R134a in a capillary tube heat exchanger. *Proceedings of 11th IHTC*, 6:131–136, 1998.
- [112] J.Y. Shin, M.S. Kim, and S.T. Ro. Experimental study on forced convective boiling heat transfer of pure refrigerants and refrigerant mixtures in a horizontal tube. *International Journal of Refrigeration*, 20(4):267–275(9), 1997.
- [113] R.K. Shah and A.L. London. *Laminar Flow Forced Convection in Ducts, Supplement 1 to Advances in Heat Transfer*. New York Academic Press, 1978.
- [114] R.J. Phillips. Forced convection, liquid cooled, microchannel heat sinks. Master's thesis, Department of Mechanical Engineering, Massachusetts Institute of Technology, Cambridge, MA, 1987.
- [115] R.W. Lockhart and R.C. Martinelli. Proposed correlation of data for isothermal two-phase, two-component flow in pipes. *Chemical Engineering Process*, 45, No. 1:39–48, 1949.
- [116] C.J. Baroczy. A systematic correlation for two-phase pressure drop (2nd ed.). *Chem. Eng. Prog. Symp. Ser 62*, 44:232–249, 1966.
- [117] D. Chisholm. Pressure gradients due to friction during the flow of evaporating two-phase mixtures in smooth tubes and channels. *International Journal of Heat and Mass Transfer*, 16:347–358, 1973.
- [118] L. Friedel. Improved friction pressure drop correlations for horizontal and vertical two-phase pipe flow. *3R Int.*, 18:485–492, 1979.
- [119] W. Zhang, T. Hibiki, and K. Mishima. Correlations of two-phase frictional pressure drop and void fraction in mini-channel. *International Journal of Heat and Mass Transfer*, Volume 53, Issues 1-3:453–465, 2010.
- [120] L. Sun and K. Mishima. Evaluation analysis of prediction methods for two-phase flow pressure drop in mini-channels. *International Journal of Multiphase Flow*, Volume 35, Issue 1:47–54, 2009.

-
- [121] A.P. Roday, T. Borca-Tasçuic, and M.K. Jensen. The critical heat flux condition with water in a uniformly heated microtube. *Journal of Heat Transfer*, 130, 2008.
- [122] D.E. Kamidis and T.S. Ravigururajan. Single and two-phase refrigerant flow in minichannels. In *Proceedings of NHTC2000: 33rd National Heat Transfer Conference, Albuquerque, NM*, pp. 1-8, 2000.
- [123] W. Yu, D.M. France, W.M. Wambugnass, and J.R. Hull. Two-phase pressure drop, boiling heat transfer and critical heat flux to water in a small diameter horizontal tube. *International Journal of Multiphase Flow*, 28:927–941, 2002.
- [124] A.P. Ornatskii and L.S. Vinyarskii. Critical heat transfer in forced motion of underheated water-alcohol mixtures in tubes of diameter 0.5mm. *Teplofizika Vysokikh Temperatur (High Temp.)*, 3(6):881–883, 1965.

Curriculum Vitae

PERSONAL DATA

Name **Chin Lee ONG**
Date of birth 23rd April, 1978
Birthplace Kuala Lumpur, Malaysia
Nationality Malaysian

EDUCATION

2005–2010 **Doctoral Student and Assistant**, Laboratory of Heat and Mass Transfer, Swiss Federal Institute of Technology Lausanne (EPFL), Switzerland.
2001–2002 **Master of Aerospace Engineering**, RMIT University, Melbourne, Australia.
1997–2000 **Bachelor of Aerospace Engineering**, RMIT University, Melbourne, Australia.
1996 **Monash University Foundation Year**, Taylors College, Melbourne, Australia.

WORKING EXPERIENCE

2003–2004 **Citibank Malaysia, Kuala Lumpur, Malaysia:**

- Sales Manager, Bankcards Marketing Department and Acquisition Department.

2002 **Applied Physics Department, Robert Bosch GmbH, Stuttgart, Germany:**

- Thermal analysis of a urea-water injector for exhaust after treatment for diesel motor engines.

2000 **Jujurbina Construction Pte. Ltd., Kuala Lumpur, Malaysia:**

- Assistant to civil engineers involved in the company's construction projects.

Journal Publications

1. Chin. L. Ong, John. R. Thome, Flow boiling heat transfer of R134a, R236fa and R245fa in a horizontal 1.030 *mm* circular channel, *Experimental and Thermal Fluid Science*, **33**, 651-663 (2009).
2. A. Cioncolini, John. R. Thome, L. Consolini, Chin. L. Ong, Microscale adiabatic gas-liquid annular two-phase flow: Analytical model description, void fraction and pressure gradient predictions, *Heat Transfer Engineering*, **31**(4), 310-320 (2009).